ACS SYMPOSIUM SERIES 1094

Advances in Quantum Monte Carlo

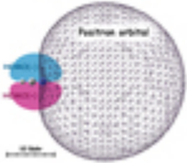
Positron orbital

EDITED BY

Shigenori Tanaka, Stuart M. Rothstein,
and William A. Lester, Jr.

Downloaded by 89.163.35.42 on May 27, 2012 | http://pubs.acs.org
Publication Date (Web): February 6, 2012 | doi: 10.1021/bk-2012-1094.fw001

Advances in Quantum Monte Carlo

In Advances in Quantum Monte Carlo; Tanaka, S., et al.;
ACS Symposium Series; American Chemical Society: Washington, DC, 2012.

Downloaded by 89.163.35.42 on May 27, 2012 | http://pubs.acs.org
Publication Date (Web): February 6, 2012 | doi: 10.1021/bk-2012-1094.fw001

Downloaded by 89.163.35.42 on May 27, 2012 | http://pubs.acs.org
Publication Date (Web): February 6, 2012 | doi: 10.1021/bk-2012-1094.fw001

ACS SYMPOSIUM SERIES **1094**

Advances in Quantum Monte Carlo

Shigenori Tanaka, Editor
Kobe University
Kobe, Hyogo, Japan

Stuart M. Rothstein, Editor
Brock University
St. Catharines, Ontario, Canada

William A. Lester, Jr., Editor
University of California, Berkeley
Berkeley, California, United States

Sponsored by the
ACS Division of Physical Chemistry

American Chemical Society, Washington, DC

Distributed in print by Oxford University Press, Inc.

Downloaded by 89.163.35.42 on May 27, 2012 | http://pubs.acs.org
Publication Date (Web): February 6, 2012 | doi: 10.1021/bk-2012-1094.fw001

Library of Congress Cataloging-in-Publication Data

Advances in quantum Monte Carlo / Shigenori Tanaka, Stuart M. Rothstein, William A. Lester, Jr., editor[s] ; sponsored by the ACS Division of Physical Chemistry.
p. cm. -- (ACS symposium series ; 1094)
Includes bibliographical references and index.
ISBN 978-0-8412-2750-7 (alk. paper)
1. Monte Carlo method--Congresses. 2. Quantum chemistry--Congresses. 3. Quantum theory--Congresses. I. Tanaka, Shigenori. II. Rothstein, Stuart M. III. Lester, W. A. IV. American Chemical Society. Division of Physical Chemistry.
QD462.6.M66A382 2012
541′.28--dc23
2012001702

The paper used in this publication meets the minimum requirements of American National Standard for Information Sciences—Permanence of Paper for Printed Library Materials, ANSI Z39.48n1984.

Copyright © 2012 American Chemical Society

Distributed in print by Oxford University Press, Inc.

All Rights Reserved. Reprographic copying beyond that permitted by Sections 107 or 108 of the U.S. Copyright Act is allowed for internal use only, provided that a per-chapter fee of $40.25 plus $0.75 per page is paid to the Copyright Clearance Center, Inc., 222 Rosewood Drive, Danvers, MA 01923, USA. Republication or reproduction for sale of pages in this book is permitted only under license from ACS. Direct these and other permission requests to ACS Copyright Office, Publications Division, 1155 16th Street, N.W., Washington, DC 20036.

The citation of trade names and/or names of manufacturers in this publication is not to be construed as an endorsement or as approval by ACS of the commercial products or services referenced herein; nor should the mere reference herein to any drawing, specification, chemical process, or other data be regarded as a license or as a conveyance of any right or permission to the holder, reader, or any other person or corporation, to manufacture, reproduce, use, or sell any patented invention or copyrighted work that may in any way be related thereto. Registered names, trademarks, etc., used in this publication, even without specific indication thereof, are not to be considered unprotected by law.

PRINTED IN THE UNITED STATES OF AMERICA

Foreword

The ACS Symposium Series was first published in 1974 to provide a mechanism for publishing symposia quickly in book form. The purpose of the series is to publish timely, comprehensive books developed from the ACS sponsored symposia based on current scientific research. Occasionally, books are developed from symposia sponsored by other organizations when the topic is of keen interest to the chemistry audience.

Before agreeing to publish a book, the proposed table of contents is reviewed for appropriate and comprehensive coverage and for interest to the audience. Some papers may be excluded to better focus the book; others may be added to provide comprehensiveness. When appropriate, overview or introductory chapters are added. Drafts of chapters are peer-reviewed prior to final acceptance or rejection, and manuscripts are prepared in camera-ready format.

As a rule, only original research papers and original review papers are included in the volumes. Verbatim reproductions of previous published papers are not accepted.

ACS Books Department

Downloaded by 89.163.35.42 on May 27, 2012 | http://pubs.acs.org
Publication Date (Web): February 6, 2012 | doi: 10.1021/bk-2012-1094.fw001

In Advances in Quantum Monte Carlo; Tanaka, S., et al.;
ACS Symposium Series; American Chemical Society: Washington, DC, 2012.

Downloaded by 89.163.35.42 on May 27, 2012 | http://pubs.acs.org
Publication Date (Web): February 6, 2012 | doi: 10.1021/bk-2012-1094.pr001

Preface

The chapters in this monograph are contributions from the *Advances in Quantum Monte Carlo* symposium held at Pacifichem 2010, International Chemical Congress of Pacific Basin Societies. The symposium was dedicated to celebrate the career of James B. Anderson, a notable researcher in the field.

Quantum Monte Carlo provides an *ab initio* solution to the Schroedinger equation by performing a random walk through configuration space in imaginary time. Benchmark calculations suggest that its most commonly-used variant, “fixed-node” diffusion Monte Carlo, estimates energies with an accuracy comparable to that of high-level coupled-cluster calculations. These two methods, each having advantages and disadvantages, are complementary “gold-standards” of quantum chemistry.

There are challenges facing researchers in the field, several of which are addressed in the chapters in this monograph. These include improving the accuracy and precision of quantum Monte Carlo calculations; understanding the exchange nodes and utilizing the simulated electron distribution; extending the method to large and/or experimentally-challenging systems; and developing hybrid molecular mechanics/dynamics and Monte Carlo algorithms.

We extend special thanks to the Physical Chemistry Division of the American Chemical Society and Silicon Graphics, Inc. that sponsored the symposium and provided partial financial support to offset travel expenses of some of its participants.

Shigenori Tanaka
Kobe, Hyogo, Japan

Stuart M. Rothstein
St. Catharines, Ontario, Canada

William A. Lester, Jr.
Berkeley, California, United States

In Advances in Quantum Monte Carlo; Tanaka, S., et al.;
ACS Symposium Series; American Chemical Society: Washington, DC, 2012.

Downloaded by OHIO STATE UNIV LIBRARIES on May 27, 2012 | http://pubs.acs.org
Publication Date (Web): February 6, 2012 | doi: 10.1021/bk-2012-1094.ot001

Editors' Biographies

Shigenori Tanaka

Shigenori Tanaka received his B.S. degree in physics from University of Tokyo in 1982 and his Ph.D. degree in physics from University of Tokyo (S. Ichimaru) in 1986. After a Young Research Fellow of Japan Society for the Promotion of Science and serving two years as a Research Associate at University of Tokyo, he joined in 1989 Toshiba Research and Development Center. As a Visiting Associate, Tanaka also did research at the California Institute of Technology (R.A. Marcus) from 1995−1996. Since 2004, he is a professor at Kobe University.

Stuart M. Rothstein

Stuart M. Rothstein received his B.S. degree in chemistry from the University of Illinois in 1964 and his Ph.D. degree in chemistry from the University of Michigan (S.M. Blinder) in 1968. After a one year post-doc at Johns Hopkins University (H.J. Silverstone) and serving one year as an Assistant Professor at Swarthmore College, in 1970 he joined the Department of Chemistry at Brock University. While on sabbatical leaves, Rothstein has done research at Uppsala University (P.O. Löwdin), the University of Southern California (H.S. Taylor), the University of California at Berkeley (W.A. Lester, Jr.), and Kobe University (S. Tanaka).

William A. Lester, Jr.

William A. Lester, Jr. was awarded a B.S. degree in 1958 and a M.S. degree in 1959 in chemistry from the University of Chicago. He received his Ph.D. in chemistry in 1964 from The Catholic University of America while employed at the National Bureau of Standards. He has held appointments at the Theoretical Chemistry Institute, University of Wisconsin, the Department of Chemistry, UW Madison, and the IBM San Jose Research Laboratory. He was Director of the U.S. National Resource for Computation in Chemistry and Professor of Chemistry at the University of California, Berkeley. He is presently Professor of the Graduate School, Department of Chemistry, University of California, Berkeley.

In Advances in Quantum Monte Carlo; Tanaka, S., et al.;
ACS Symposium Series; American Chemical Society: Washington, DC, 2012.

Downloaded by 89.163.35.42 on May 27, 2012 | http://pubs.acs.org
Publication Date (Web): February 6, 2012 | doi: 10.1021/bk-2012-1094.ch001

Chapter 1

Correlated Sampling for Energy Differences in Diffusion Quantum Monte Carlo

James B. Anderson[*]

Department of Chemistry, Pennsylvania State University,
University Park, Pennsylvania 16802
[*]E-mail: jba@psu.edu

We describe a method using correlated sampling in fixed-node *diffusion* QMC calculations to determine differences in energies for similar molecular systems. The method is based on an earlier scheme for calculating corrections to trial wave functions applied to two or more systems with correlated calculations in fixed-node QMC. The result is a significant reduction in the statistical error in comparing the energies of similar molecular structures.

Introduction

The statistical error inherent in Quantum Monte Carlo calculations leads to difficulties in calculating differences in energies for similar systems. Analytic variational calculations, for example, are free of this problem. In *variational* QMC the statistical error in energy differences may be reduced with use of correlated sampling, but correlated sampling in *diffusion* QMC has been problematical. We report here a new method which is successful for correlated sampling in diffusion QMC and produces accurate energy differences for similar systems at the diffusion QMC level.

We have described previously several versions of a quantum Monte Carlo method for the direct calculation of corrections to trial wave functions (*1*, *2*). This method gives - for fixed nodes - the difference δ between a true wave function Ψ and a trial wave function Ψ_0, as well as the difference between the true energy E and the expectation value of the energy E_{var} for the trial wave function. The statistical or sampling errors associated with the Monte Carlo procedures as well as any systematic errors occur only in the corrections. Thus very accurate wave

In Advances in Quantum Monte Carlo; Tanaka, S., et al.;
ACS Symposium Series; American Chemical Society: Washington, DC, 2012.

functions and energies may be corrected with very simple calculations. The nodes are unchanged and the wave functions and energies for these systems are corrected to the fixed-node values - those corresponding to the exact solutions for the fixed nodes of the trial wave functions.

We have also described previously some correlated diffusion QMC calculations for similar structures of the H_3^+ ion (*3*). These took advantage of scaled length and energy parameters, but were only mildly successful because the initial correlation of electron positions was diminished as the calculations proceeded.

In the work reported here we have combined the latest version of the correction method (*2*) with the correlated sampling in diffusion QMC (*3*). We have carried out *correction* calculations for cases of two similar systems with correlated sampling of electron positions, moves, and multiplications wherever possible. Since the two systems are slightly different, the initial similarity in walker positions and weights is not maintained exactly, but the correction calculation is fairly short, and the systems remain nearly similar over the length of the calculation.

Downloaded by 89.163.35.42 on May 27, 2012 | http://pubs.acs.org
Publication Date (Web): February 6, 2012 | doi: 10.1021/bk-2012-1094.ch001

Theoretical Basis

The derivation of the latest version of our correction scheme is given in Ref. (*2*). We give a brief description here. The basic equation is that for QMC with importance sampling (*4–7*) where $f = \Psi\Psi_0$, the product of the true wave function and a trial wave function, and E_{ref} is a reference energy,

$$\frac{\partial f}{\partial \tau} = \frac{1}{2}\nabla^2 f - \nabla \cdot \left(f \nabla \ln \Psi_0\right) - \left(\frac{H\Psi_0}{\Psi_0} - E_{\mathrm{ref}}\right) f \qquad (1)$$

Making use of the difference $\delta = \Psi - \Psi_0$ and defining another function $g = \delta\Psi_0 = (\Psi - \Psi_0)\,\Psi_0$ we obtain

$$\frac{\partial g}{\partial \tau} = \frac{1}{2}\nabla^2 g - \nabla \cdot \left(g \nabla \ln \Psi_0\right) - \left(\frac{H\Psi_0}{\Psi_0} - E_{\mathrm{ref}}\right) g + \left[-\left(\frac{H\Psi_0}{\Psi_0} - E_{\mathrm{ref}}\right) \Psi_0^{\,2} \right] \qquad (2)$$

The term $H\Psi_0/\Psi_0$ is the local energy E_{loc} for the trial wave function. The last term in Eq. (2) is a distributed source term S, which may be positive or negative. It is convenient to introduce the expectation value of the energy E_{var} for the trial function and write S as a collection of terms

$$S = S_p + S_n + S_q \quad , \qquad (3)$$

where

$$S_p = \left[-\left(E_{\mathrm{loc}} - E_{\mathrm{var}} \right) \Psi_0^2 \right]_p$$

$$S_n = \left[-\left(E_{\mathrm{loc}} - E_{\mathrm{var}} \right) \Psi_0^2 \right]_n$$

$$S_q = \left[-\left(E_{\mathrm{var}} - E_{ref} \right) \Psi_0^2 \right]_q \quad ,$$

and where the subscript p indicates a region $E_{\mathrm{loc}} < E_{\mathrm{var}}$ and a positive particle feed, the subscript n indicates a region of $E_{\mathrm{loc}} > E_{\mathrm{var}}$ and a negative particle feed, and the subscript q indicates an additional particle feed, normally negative.

We consider the integrals of each of the terms in Eq. (2) over all accessible space. Thus we define the integrals

$$I_g = \int g dV, \quad I_p = \int S_p dV, \quad I_n = \int S_n dV, \quad I_q = \int \Psi_0^2 dV, \qquad (4)$$

and Eq. (2) becomes

$$\frac{\partial I_g}{\partial \tau} = \int \frac{1}{2} \nabla^2 g dV - \int \nabla \cdot \left(g \nabla \ln \Psi_0 \right) dV$$

$$- \int \left(E_{\mathrm{loc}} - E_{\mathrm{ref}} \right) g dV + I_p + I_n - \left(E_{\mathrm{var}} - E_{\mathrm{ref}} \right) I_q \ . \qquad (5)$$

Since the diffusion and drift terms merely move particles within the volume and the drift term prevents their crossing a nodal surface, they make no contribution to changes in Ig , and they are zero and may be eliminated. The multiplication term containing ($E_{\mathrm{loc}} - E_{\mathrm{ref}}$) is applicable to each particle fed to the system. An average growth factor $\overline{f_p}$, $\overline{f_n}$, $\overline{f_q}$ for each type of particle during its lifetime in the system may be combined with the feed terms. Thus we obtain

$$\frac{\partial I_g}{\partial \tau} = I_p \overline{f_p} + I_n \overline{f_n} - \left(E_{\mathrm{var}} - E_{\mathrm{ref}} \right) I_q \overline{f_q} \quad . \qquad (6)$$

Since particles fed at any point in the system tend to the same distribution with increased time in the system, those of sufficient age may be cancelled in equal weights, positive with negative, regardless of their locations. For a steady state and for a complete cancellation of positive and negative particles at a fixed age we have $\partial Ig/\partial\tau = 0$, and the energy E is equal to E_{ref} which is given by (after rearrangement)

$$E = E_{\mathrm{ref}} = E_{\mathrm{var}} - \frac{\frac{I_p}{I_q} \overline{f_p} + \frac{I_n}{I_q} \overline{f_n}}{\overline{f_q}} \qquad (7)$$

Downloaded by 89.163.35.42 on May 27, 2012 | http://pubs.acs.org
Publication Date (Web): February 6, 2012 | doi: 10.1021/bk-2012-1094.ch001

Downloaded by 89.163.35.42 on May 27, 2012 | http://pubs.acs.org
Publication Date (Web): February 6, 2012 | doi: 10.1021/bk-2012-1094.ch001

To determine the energy one then needs to obtain only the ratios of the integrals I_p/I_q and I_n/I_q rather than the individual values. Also needed are the values of $\overline{f_p}$, $\overline{f_n}$ and $\overline{f_q}$ as well as E_{var}.

The ratios of the integrals may be determined by numerical integration, typically by Metropolis sampling of Ψ_0^2 with accumulation of average values of I_p/I_q and I_n/I_q. Their definition in terms of E_{var} ensures that the absolute values of these ratios be equal and uncertainty in their relative values is eliminated. Since an accurate value of E_{var} is required, an analytic integration to determine E_{var} is preferred. The values of $\overline{f_p}$, $\overline{f_n}$ and $\overline{f_q}$ are determined for sample feed particles obtained in the Metropolis integrations. These are selected with probabilities proportional to (in addition to Ψ_0^2) the absolute values of the quantities $[-(E_{\mathrm{loc}} - E_{\mathrm{var}})]_p$ for p, $[-(E_{\mathrm{loc}} - E_{\mathrm{var}})]_{\mathrm{n}}$ for n, and unity for q. The particles are subjected to diffusion, drift, and multiplication (weight increase or decrease) for a period (age) sufficiently long to produce no further change in their average weights. Positive particles of type p, fed in regions of $E_{\mathrm{loc}} < E_{\mathrm{var}}$, give values of $\overline{f_p} > 1$. Negative particles of type n, fed in regions of $E_{\mathrm{loc}} < E_{\mathrm{var}}$, give values of $\overline{f_n} < 1$. Particles of type q normally give a value $\overline{f_q}$ very close to unity.

The energy E is given by the known value of E_{var} and a correction term. When Ψ_0 is a good approximation to the true wave function, the correction term is small and any error in the correction term is correspondingly small. As Ψ_0 approaches the true wave function the ratios $I_{\mathrm{p}}/I_{\mathrm{q}}$ and $I_{\mathrm{n}}/I_{\mathrm{q}}$ approach zero and the values of $\overline{f_p}$, $\overline{f_n}$ and $\overline{f_q}$ approach unity.

Introducing Correlation

To calculate the difference in diffusion QMC energies for two systems A and B the variational energies E_{varA} and E_{varB} for the two systems and their difference are determined in correlated variational QMC calculations using Metropolis sampling. Electron positions may be identical for the two systems or scaled in one way or another to maintain similarity. The sampling may be carried out with a value (or weight) function W given by $W_{\mathrm{A}} + W_{\mathrm{B}}$, the sum of squares of the two trial wave functions. In this case the energy for each system is given by the weighted average of its local energies using weights proportional to W_{A} or W_{B}. If the two systems are nearly the same the statistical error in the difference $E_{\mathrm{varA}} - E_{\mathrm{varB}}$ will be much smaller than the statistical error in the individual values E_{varA} and E_{varB}. The values of I_p, I_n, and I_q as well as sample configurations of type p, n, and q are retained.

The next step is a correction calculation for each of the trial wave functions carried out as described in the section above using the correlated type p, n, and q samples to determine values of $\overline{f_p}$, $\overline{f_n}$ and $\overline{f_q}$ for each of the systems. For these correlated diffusion QMC calculations the initial electron positions correspond but the initial weights as found in the variational calculations may vary for the two systems. The drift terms and the multiplication terms may also vary, but if the systems are similar the differences will be small. The diffusion terms and the points of multiplication are matched for the two systems, so that electron movements and multiplications are correlated as much as possible. Since the initial configurations p and q are deviations from typical configurations, their local energies also deviate, and the changes in weights and contributions to the values of $\overline{f_p}$ and $\overline{f_n}$ are large at the start of a run. To avoid time-step error the time-step size must be very small at the start. As the run proceeds the walkers approach normal behavior and the values of $\overline{f_p}$ and $\overline{f_n}$ approach their asymptotic values.

A Simple Test: Neon vs. Neon (moved slightly)

To test the method we calculated the difference in diffusion QMC energies for two systems A and B which are known to have the same energy: a neon atom in each case (non-interacting) with the first located at the origin of coordinates and the second displaced a short distance from the origin. The displacement was 0.02 bohr. Each had a trial function consisting of a fairly good SCF function and a Schmidt-Moscowitz (*8*) Jastrow function centered on its nucleus. The two trial functions were identical except for positioning. In the variational calculation the sampling value for walker moves was taken as the sum of the squares of the trial functions. The results are shown in Table 1.

Table 1. Correlated DQMC: Ne vs. Ne shifted 0.02 bohr

Energies (hartrees)			
	Ne #1		*Ne #2*
E_{var}	–128.867 504		–127.867 268
(VQMC)	± 0.000 090		± 0.000 086
E_{cor}	–128.924 310		–128.924 195
(DQMC)	± 0.001 100		± 0.001 100
E_{cor} difference		–0.000 115	
		±0.000 077	
E_{exact} [a]	–128.9376		–128.9376

[a] Reference (*9*).

It may be seen that the uncertainty in the difference for variational energies is 16 microhartrees and that for diffusion energies is 77 microhartrees, while the corresponding uncertainties in the individual values are about 90 and 1100 microhartrees, respectively. The 77-microhartree error in the calculated difference in diffusion energies is about the same as the indicated statistical error in that quantity. This is the desired result. That is, the known difference in

Downloaded by 89.163.35.42 on May 27, 2012 | http://pubs.acs.org
Publication Date (Web): February 6, 2012 | doi: 10.1021/bk-2012-1094.ch001

DQMC energies (zero) is reproduced (as 0.000 115 ± 0.000 077 hartrees) despite uncertainties of 0.001 100 hartrees in the individual values.

Comparison of Two H_2 Molecules

A second example, for which the energy difference is known nearly exactly, is the case of two ground-state H_2 moleculas with slightly different internuclear distances, the first with R = 1.4000 bohr and the other with R = 1.4011 bohr. In this case the wave function is nodeless. The trial function was a high quality single-determinant function with an optimized Jastrow term. The time-step and distance parameters for the diffusion calculations were scaled to place electrons in geometrically similar positions – in effect by placing the nuclei in identical positions in the scaled systems. The results are shown, together with those of accurate analytic variational calculations by Cencek and Szalewicz (*10*) for comparison, in Table 2.

The table shows the desired effect: the uncertainty in the calculated difference in the DQMC energies (0.040 microhartrees) is much lower than the uncertainties (4.800 and 5.300 microhartrees) in the DQMC energies of the calculations considered separately.

Table 2. Correlated DQMC: H_2 with R = 1.4000 bohr vs. H_2 with R = 1.4011 bohr

Energies (hartrees)			
	R = 1.4000		*R = 1.4011*
E_{var}	–1.173 434 517		–1.173 433 737
(VQMC)	±0.000 000 130		±0.000 000 130
E_{cor}	–1.174 470 644		–1.174 470 901
(DQMC)	±0.000 004 800		±0.000 005 300
E_{cor} difference		–0.000 000 257	
		±0.000 000 040	
E_{exact} difference[a]		0.000 000 217	
E_{exact} [a]	–1.174 475 714		–1.174 475 931

[a] Reference (*10*).

The table shows the desired effect: the uncertainty in the calculated difference in the DQMC energies (0.040 microhartrees) is much lower than the uncertainties (4.800 and 5.300 microhartrees) in the DQMC energies of the calculations considered separately.

Downloaded by 89.163.35.42 on May 27, 2012 | http://pubs.acs.org
Publication Date (Web): February 6, 2012 | doi: 10.1021/bk-2012-1094.ch001

Comparison of Two C_{10} Rings

A third example, for which the energy difference is not known exactly, is the case of two C_{10} rings of slightly different radii. The ten carbon atoms were placed evenly on circles, one with a radius of 2.04 bohr, the other with a radius of 2.08 bohr. The circles were centered on the origin, and the length and time scales of the second were adjusted to obtain geometric and dynamic similarity. The trial wave function was a single determinant function with a Jastrow term, the same for both systems. The effect of geometric scaling was to give different values for the wave functions and local energies for corresponding electron configurations. The results are shown in Table 3.

Table 3. Correlated DQMC: C_{10} circle (R = 2.04 bohr) vs. C_{10} circle (R = 2.08 bohr)

Energies (hartrees)			
	R = 2.04		*R = 2.08*
E_{var}	–379.4307		–379.4319
(VQMC)	± 0.0067		± 0.0053
E_{cor}	–379.4485		–379.4500
(DQMC)	± 0.0130		± 0.0130
E_{cor} difference		+ 0.0015	
		± 0.0013	

Again the results show significantly lower statistical errors for the differences in variational QMC energies and the differences in diffusion QMC energies than for the individual values of these energies. The uncertainty in the diffusion QMC difference is approximately equal to the indicated difference as expected for a minimum in the energy. Additional calculations for slightly different geometries indicate a minimum at a radius of about 2.08 bohr. Independent analytical calculations (MP2, with substantially different trial functions) indicate a minimum in the range of 2.08 to 2.12 bohr.

The Neon Dimer

The neon dimer represents a special challenge to quantum mechanics in general, and this challenge might be met by correlated diffusion QMC calculations. One should expect significant cancellations in calculations for separated neon atoms (Ne + Ne) vs. the Ne dimer (Ne-Ne) at or near its equilibrium separation distance of about 5.8 bohr. The trial function used was the product of two single atom functions (as used for the Ne atom above) with additional cross terms in the Jastrow function. The results are shown in Table 4.

Downloaded by 89.163.35.42 on May 27, 2012 | http://pubs.acs.org
Publication Date (Web): February 6, 2012 | doi: 10.1021/bk-2012-1094.ch001

Table 4. Correlated DQMC: (Ne + Ne) vs. Ne_2 (R = 5.8 bohr)

Energies (hartrees)			
	Ne + Ne		*Ne_2*
E_{var}	–257.538 127		–257.538 261
(VQMC)	± 0.000 200		± 0.000 200
E_{cor}	–257.845 542		–257.846 338
(DQMC)	± 0.000 500		± 0.000 400
E_{cor} difference		– 0.000 796	
		± 0.000 700	

In this case we were successful in demonstrating the effectiveness of correlated variational QMC and obtained a well depth of 0.000134 +/- 0.000009 hartrees, in good agreement with accepted values derived from experiment (*11*). But, for the correlated diffusion QMC the indicated well depth was 0.000796 +/- 0.000700 hartrees. With this large value of the statistical error, we conclude that a much better trial function is required for this difficult case. We expect to pursue this case further.

Discussion

It is clear that correlated sampling provides significant improvements in the determination of differences in diffusion QMC energies of similar molecular systems. Of course, the accuracy in the differences in calculated energies depends strongly on the degree of similarity of the systems compared. For closely similar systems the difference method can provide (loosely) the derivative in energy with respect to a variable describing the difference in the systems.

We note that the method of correlated sampling in diffusion QMC described here can be applied, in a similar fashion, to the optimization of a trial wave functions. In this case, we compute the difference in *diffusion* QMC energies for the same system and two similar wave functions. Since the difference in energies depends only on the node locations, the node structure may be optimized, thereby providing a solution to the so-called ‘sign problem of quantum Monte Carlo’. We are encouraged by our early investigations.

Acknowledgments

Support by the National Science Foundation (IGERT Award No. 9987589) and by the Research Computing and Cyber Infrastructure (a unit of ITF) of the Pennsylvania State University is gratefully acknowledged

Downloaded by 89.163.35.42 on May 27, 2012 | http://pubs.acs.org
Publication Date (Web): February 6, 2012 | doi: 10.1021/bk-2012-1094.ch001

References

1. Anderson, J. B.; Freihaut, B. H. *J. Comput. Phys.* **1979**, *31*, 425.
2. Anderson, J. B. *J. Chem. Phys.* **2000**, *112*, 9699.
3. Traynor, C. A.; Anderson, J. B. *Chem. Phys. Lett.* **1988**, *147*, 389.
4. Metropolis, N.; Ulam, S. *J. Am. Stat. Assoc.* **1949**, *44*, 335.
5. Anderson, J. B. *J. Chem. Phys.* **1975**, *63*, 1499.
6. Grimm, R. C.; Storer, R. G. *J. Comput. Phys.* **1971**, *7*, 134.
7. Mentch, F.; Anderson, J. B. *J. Chem. Phys.* **1981**, *74*, 6307.
8. Schmidt, K. E.; Moscowitz, J. W. *J. Chem. Phys.* **1990**, *93*, 4172.
9. Chakravorty, S. J.; Gwaltney, S. R.; Davidson, E. R.; Parpia, F. A.; Fischer, C. F. *Phys. Rev. A* **1993**, *47*, 3649.
10. Cencek, W.; Szalewicz, K. *Int. J. Quantum Chem.* **2008**, *108*, 2191.
11. Aziz, R. A.; Slaman, M. J. *Chem. Phys.* **1989**, *180*, 187.

Downloaded by 89.163.35.42 on May 27, 2012 | http://pubs.acs.org
Publication Date (Web): February 6, 2012 | doi: 10.1021/bk-2012-1094.ch001

Chapter 2

Population Control Bias with Applications to Parallel Diffusion Monte Carlo

Jaron T. Krogel*,1,2 and David M. Ceperley1,2

1Department of Physics, University of Illinois, Urbana-Champaign, Urbana, Illinois 61801
2National Center for Supercomputing Applications (NCSA), University of Illinois, Urbana-Champaign, Urbana, Illinois 61801
***E-mail: jkrogel2@illinois.edu**

The future of scientific computing will be driven by highly distributed parallel machines with millions of compute nodes. In order to take advantage of this already arriving wave of computing capability we must identify and remove the remaining barriers to parallel scaling in the Diffusion Monte Carlo algorithm. To address these scaling issues in a simple way, we propose that a time delay be introduced into the population control feedback. In order to assess this algorithm, we investigate the behavior of population fluctuations and the population control bias (which will emerge into greater relevance with larger physical systems and requirements of higher accuracy) in a model system for both the standard and time delayed DMC algorithms. We then condense our findings into a simple set of recommendations to improve the scaling of DMC while managing the population control bias.

The Future of Parallel DMC

Modern parallel machines are composed of tens of thousands of SMP nodes which will rapidly increase into the millions in coming years. Keeping pace with such developments is crucial to the success of scientific computing. Monte Carlo methods are particularly well suited to make use of this ever increasing computing power since they contain low serial dependency. In Markov Chain Monte Carlo, a function is evaluated along a large chain of randomly generated

In Advances in Quantum Monte Carlo; Tanaka, S., et al.;
ACS Symposium Series; American Chemical Society: Washington, DC, 2012.

particle configurations to obtain its mean. Conceptually, we think of the chain as a random walk, meaning that it is formed by a walker which steps from configuration to configuration. Typically, straightforward replication of Monte Carlo random walks allows near perfect scaling, however a central feature of any Monte Carlo algorithm will limit the practical efficiency gains realized when scaling to millions of processors: the equilibration time of the random walks.

The bottleneck due to equilibration time arises from the pursuit to simulate ever larger systems. Since the time to obtain new configurations is increased, the equilibration time consumes a larger fraction of the fixed serial run time. A direct way to minimize the ratio of serial equilibration time and total run time is to minimize the number of walkers per SMP node. For many Monte Carlo algorithms it is possible to achieve the exact minimum of just one walker per node; however this is not the case for the standard Diffusion Monte Carlo (DMC) method.

DMC is a Monte Carlo procedure to solve the many-body time independent Schrödinger equation (*1*, *2*). It is currently the most widely used Quantum Monte Carlo algorithm for chemical and condensed matter systems. In the standard algorithm, the population of walkers fluctuates through a birth-death process known as branching and so load balancing challenges arise in the limit of few walkers per node. For example, a set of nodes each running with a single walker will quickly evolve into a situation where nodes contain zero, one, or two or more walkers each. In this circumstance, the overall efficiency can fall since all walkers must complete a step before the trial energy is collected and branching is performed. In typical implementations, current codes use on the approximately one hundred walkers per node to avoid load balancing inefficiency, however this leads to equilibration inefficiency as mentioned above. Though load balancing operations cannot perfectly redistribute the load for arbitrary population sizes, they will have to be performed frequently to prevent the situation from becoming even worse. Since most implementations of load balancing rely on operations within the Message Passing Interface (which impose synchronization at some level), parallel efficiency will further suffer with increasing machine size. At the same time, the branching process must be tightly regulated to prevent chronic shortages of walkers which could leave large numbers of nodes idle.

Demanding smaller fluctuations in the DMC walker population (greater stability) increases a systematic error within DMC as we detail below. However, with the advent of larger machines, a greater level of accuracy will inevitably be pursued, requiring parallel algorithms with greater robustness and less bias. Thus the population control bias, which has largely been neglected in the past, could become increasingly relevant to future applications.

In this work, we explore the relationship between the population control parameters and the stability and accuracy of the standard DMC method. Using a simple and efficient model problem, the simple harmonic oscillator, we obtain empirical formulas describing the behavior of population stability and the population control bias over a range of control parameters. Since we expect population dynamics (and hence stability and bias) to depend more strongly on the control method used than the particular details of the physical system, these results should apply broadly to current DMC practice.

Looking ahead to the rapidly approaching parallel efficiency difficulties outlined above, we move on to a possible solution to the scaling problem. We propose the introduction of a feedback delay in the population control mechanism which removes synchronization requirements from the algorithm and allows load balancing techniques that capitalize on keeping the time averaged load constant rather than the instantaneous load. These features ease the tradeoff between serial and parallel efficiency. As we must be cautious not to introduce unmanageable instability or bias into the simulation, we repeat the model analysis on cases with delayed feedback. These results are then consolidated into a brief set of practical recommendations to improve the parallel efficiency and reduce the population control bias in typical DMC simulations.

Other types of Quantum Monte Carlo, such as Reptation (*3*) and Path Integral Monte Carlo (*4*), do not suffer from population control bias. However, those methods have not been systematically applied to systems of many electrons, and in particular, there have been no studies of their relative efficiency, e.g. how their errors scale with computer time and number of electrons. In addition, these methods have other difficulties in scaling to very large number of processors. For these reasons, we limit the discussion to Diffusion Monte Carlo.

Review of the DMC Method

The Diffusion Monte Carlo algorithm (*1*, *2*) can be viewed as a technique to iteratively refine the standard variational method (*5*). In the variational method, an *ansatz* for the many-body wavefunction (ψ_T) is optimized to be as close as possible to the true ground state, usually by minimizing a combination of its energy moments, $\mu_n = \langle \psi_T | \hat{H}^n | \psi_T \rangle$. The Hamiltonian operator, Ĥ, is given by

$$\hat{H} = -\frac{\hbar^2}{2m}\nabla^2 + V \tag{1}$$

The variational energy obtained by integrating the local energy ($E_L = \psi_T^{-1}\hat{H}\psi_T$) over the trial probability density ($f_0 = |\psi_T|^2$) is a strict upper bound on the ground state energy of the system.

$$E_V = \frac{\int dR\, f_0(R) E_L(R)}{\int dR\, f_0(R)} \geq E_0 \tag{2}$$

In DMC, the variational probability density is evolved forward in imaginary time through the iterative application of a short time Green's function.

$$f_{t+\tau}(R') = \int dR\, G(R', R; \tau) f_t(R) \tag{3}$$

The importance sampled (*1*, *2*, *6*, *7*) form of this propagator

$$G(R',R;\tau) = \psi_T(R')\langle R'|e^{-\tau(\hat{H}-E_T)}|R\rangle/\psi_T(R) \tag{4}$$

optimally guides the trial probability density toward the mixed distribution ($\psi_T\psi_0$) which is composed of the trial and exact ground state wavefunctions. In fact, the probability density evolves toward the mixed distribution exponentially fast in imaginary time.

$$f_t \xrightarrow[t\to\infty]{} \psi_T\psi_0 e^{-t(E_0-E_T)} \tag{5}$$

The exponential factor on the right hand side of equation 5 provides the first glimpse of an instability in the DMC algorithm which will be addressed in the context of population control. The trial energy, E_T, is selected as close to the ground state energy (E_0) as possible to prevent the norm of the distribution from vanishing or diverging within the timescales of interest. The rapid evolution of the probability density similarly means that the DMC energy

$$E_{DMC}(t) = \frac{\int dR\, f_t(R)E_L(R)}{\int dR\, f_t(R)} \tag{6}$$

will also experience exponential convergence from the variational energy at zero time to the exact ground state energy at large imaginary times.

Thus far, we have considered only the formal outline of the DMC algorithm. The conversion of the formal method into a Monte Carlo sampling process introduces the practical issues of efficiency, stability, and accuracy. In practice, the short time Green's function is approximately factorized into a product of diffusion and branching terms.

$$\begin{aligned} G_d(R',R) &= \exp\left(-\tfrac{1}{4\tau}\left[R' - R - 2\tau\psi_T^{-1}(R)\nabla\psi_T(R)\right]^2\right) \\ G_b(R',R) &= \exp\left(-\tfrac{\tau}{2}\left[E_L(R') + E_L(R)\right]\right) \end{aligned} \tag{7}$$

Here the magnitude of the timestep, τ, is determined by the acceptable level of error in the breakup; later on τ will take on a meaning which differs from this standard usage. The diffusion term determines the spatial motion of the random walks, causing them to undergo Brownian motion which is biased toward regions of high probability as represented by the trial wavefunction. The branching term acts as a configurational weight, which is typically implemented as a birth-death process of the walkers.

The walker population at finite imaginary time is represented by the norm of the mixed distribution:

$$P_t = \int dR f_t(R) \tag{8}$$

Recalling the large time limit of the probability density in equation 5, it is clear that the walker population will perish or diverge, depending on the value of the trial energy. Yet, even if the trial energy is exact, local fluctuations in the branching weights (eq 7) will cause the dynamic population to vary in an unbounded fashion as imaginary time progresses. This is evident from the fact that the integral in equation 8 is approximated by a sum over all Monte Carlo trajectories (prior walker populations) which involve products of the branching weights up to time t-τ. Thus the future weight of a single walker, represented by the number of its descendants, will exponentially disappear or diverge depending on the local energy along its future trajectory. The collective effect of unhindered branching is an instability in the walker population, which is clearly intolerable from a practical perspective.

Several procedures have been invented to restrict the fluctuations of the walker population at the expense of introducing additional bias into the calculation. Such procedures generally fall into one of two camps: fixed population methods, such as the "comb" (*8*, *9*) and reconfiguration algorithms (*10*, *11*), or the dynamic adjustment of the trial energy (*1*, *2*, *12*, *13*). In this work, our attention will be restricted to the latter, as it is the most widely used method for population control in the DMC community. In the standard population control procedure, the trial energy is modified in the following way:

$$E_T(t) = \langle E_L \rangle_t - \frac{1}{g\tau} \log \frac{P_t}{P_0} \tag{9}$$

Here, the average indicates the current best estimate of the total energy and P_t and P_0 are the current and target populations, respectively.

The calculation of the total energy and population is what binds together the otherwise independent walkers, and causes a parallel bottleneck. The control parameter, g, is somewhat arbitrary and equals the typical number of generations (or branching steps) required for the population to return to its target value. In the absence of fluctuations, the population will return to its target value in exactly $g\tau$ units of imaginary time. These population control adjustments perturb the branching weights and hence introduce bias into any estimators. If the control parameter is too large, the population fluctuations will be hard to control; if it is too small, there could be a large bias on the estimated energy.

The population control bias has been addressed in only a handful of studies to date, possibly because its magnitude has been small for the typical range of physical system sizes (*14*). Though it has been known for some time that this bias ultimately scales exponentially with physical system size (*13*, *15*), it seems that this fact is only becoming appreciated more recently (*16*, *17*). It has been shown that the bias will decrease linearly with target population size (*12*, *13*, *15*, *18*) and will decrease if the uncontrolled population fluctuations are small (*10*). The population control bias can be systematically reduced by updating the trial energy less often (*12*), increasing the target population size, loosening the dynamic control (*13*) (increasing g), or using importance sampling (*12*, *13*, *18*) with a better trial wavefunction. Attempts to completely correct for the bias include extrapolation in $1/P_0$ (*12*, *13*) which requires many runs, and reweighting samples over a partial history (*13*, *15*) in a single run, though this is not always more efficient than the extrapolation approach (*19*).

Delayed Feedback DMC

The pursuit of higher accuracy is one of the main reasons larger machines are developed for computational science. In the context of Quantum Monte Carlo this means that continual effort must be given to minimize statistical error and systematic biases. In order to meet these goals, we wish to reformulate Diffusion Monte Carlo in a simple way that removes the bottleneck to parallel efficiency and does not exacerbate the population control bias. Any modifications to the DMC algorithm should also maintain the stability of the algorithm, i.e. the population fluctuations must be controllable. Finally, we require that reproducibility be maintained, specifically that simulation results should not depend on machine conditions such as the number of nodes used or interruptions from background daemon processes.

A simple way of meeting these requirements is to introduce a time delay, or lag, in the population control feedback. Thus the trial energy used at time *t* only requires information from all walkers at time *t-L*. The opening of this window in "time" postpones any synchronization demands, and may remove them entirely provided that a load balancing can be done within this time window. This opens the possibility of near perfect parallel scaling even for a very small number of walkers per node. Introducing a feedback delay clearly satisfies the requirement of reproducibility since information from different imaginary times is not mixed. Its impact on stability and bias is not as obvious and requires further consideration and testing.

In general, the introduction of a feedback delay should decrease the stability of the simulation, meaning that fluctuations of the walker population should grow larger. Crudely speaking, the effect of the time delay is to increase the population control parameter (g) by the length of the delay (L), since it will take L more steps to reign in population fluctuations than it would otherwise. This loosening of control will allow larger fluctuations, increasing the probability that the population will explode, vanish, or simply become too volatile for effective load balancing.

The impact of a feedback delay on the population control bias is somewhat more subtle. To see its effect, consider walkers entering a region of very low local energy. Without a feedback delay, the population will immediately rise, causing a sharp response from the population control mechanism and hence a large bias. Introducing a time delay will allow walkers to diffuse back out of this biasing region before branching, thus smoothing out its effect and reducing the bias. The effect may or may not be large, but at the very least the introduction of delayed feedback should not increase the population control bias.

Dependence of Stability and Accuracy on DMC Parameters

The impact of delayed population feedback on stability and accuracy needs to be studied and quantified, with attention given to its interrelationship with other parameters used in DMC. Relevant parameters include the target population size, population control parameter, branching frequency, and trial energy update frequency. In order to probe these relationships empirically, we have developed a model that implements DMC for one of the simplest possible systems, the one-dimensional harmonic oscillator. This model is justified because the bias and population fluctuations should depend more strongly on the control method used than the actual details of the physical system.

Model System

The simple harmonic oscillator has the advantage that its imaginary time propagator is known exactly. This fact can be exploited to eliminate the timestep error typically incurred by the breakup into diffusion and branching terms (see eq 7). With the timestep error removed, the only bias remaining is due to the population control procedure, allowing us to study it in isolation and hence much more accurately. In order to mimic DMC, the importance sampled propagator is again factored into diffusion (G_d) and branching (G_b) terms:

$$\begin{aligned} G(R',R) &= G_d(R',R)G_b(R') \\ G_b(R') &\equiv \int dR\, G(R',R) \end{aligned} \qquad (10)$$

In the limit of small imaginary time, the results in equation 7 are recovered.

Though the resulting DMC algorithm has no timestep error, the timestep used here still has an important connection to typical DMC simulation. In standard DMC, there are three timescales which are relevant to the discussion of population control bias. The first is the Trotter timestep, τ_t, which appears in the standard breakup given in eq 7. This timescale relates to the timestep error and it has been purposefully removed from our model. The other timescales are the branching period, τ_b, which is the time between branching operations, and τ_u, the time between updates of the trial energy (E_T). Branching more often without adjusting the trial energy should have no adverse effect on the bias, and so we set $\tau_b = \tau_u$ in our simulations. For the remainder of the work, we refer to this timescale as the timestep or the update period and will write it as τ. The bias will increase with more aggressive population control, and thus we expect to see a larger population control bias at small timesteps in our results.

The potential and trial wavefunction used for the model system are given by

$$V(x) = x^2 \qquad\qquad \psi_T(x) = e^{-\frac{1}{2}ax^2} \qquad (11)$$

with all quantities listed in dimensionless units ($\hbar = 1$, $m = 1/2$). The exact ground state energy for this system is equal to 1 and the ground state wavefunction is obtained when $a = 1$. Since a poor trial wavefunction will increase the branching rate, and thus more strongly manifest the population control bias, we use a trial function with $a = 0.1$ which badly oversamples low probability regions.

The exact importance sampled propagator, or Green's function, is given by

$$G(x',x;\tau) = (2\pi s)^{-\frac{1}{2}} e^{\tau E_T} e^{-\frac{1}{2}a\left(x'^2 - x^2\right)} e^{-\frac{1}{2s}\left[c\left(x'^2 + x^2\right) - 2xx'\right]} \quad (12)$$

Where c and s are defined as

$$c \equiv \cosh(2\tau) \qquad s \equiv \sinh(2\tau) \quad (13)$$

The Green's function is then integrated, as in equation 10, to obtain the effective branching weight and diffusion transition probability.

$$\begin{aligned} G_d(x',x) &= \left(\frac{c+as}{2\pi s}\right)^{1/2} \exp\left(-\frac{c+as}{2s}\left[x' - \frac{x}{c+as}\right]^2\right) \\ G_b(x') &= e^{\tau E_T}(c+as)^{-1/2} \exp\left(-\frac{1}{2s}\left[c - as - \frac{1}{c+as}\right]x'^2\right) \end{aligned} \quad (14)$$

The transition probability can be sampled exactly using a Gaussian random number generator.

Definitions of Stability and Bias

Let us define exactly what we mean by stability and bias in DMC. Defining bias is straightforward: it is simply the deviation away from the exact ground state energy.

$$b \equiv \langle E \rangle - E_0 \quad (15)$$

Stability is most easily quantified in terms of its opposite: the volatility of the walker population. Here we define volatility as

$$v \equiv \langle f^2 \rangle - \langle f \rangle^2 \qquad f \equiv \log(P_t/P_0) \quad (16)$$

which is the magnitude of population fluctuations.

Perhaps a more direct measure of stability is the probability that a simulation will not fail, meaning that the population remains within a practical range (we have used $P_0/10 < P < 10P_0$). Given the inexpensive nature of our calculations, we also explore this quantity by repeating runs many times in volatile areas of parameter space (which is spanned by g, P_0, and τ). These quantities are linked in the sense that isosurfaces of the volatility closely match those of the stability. The reason for this close relationship is that both quantities are determined by the width of the population distribution. Thus conclusions drawn from the volatility are valid reflections of how viable, or stable, DMC simulations will be.

Results with Zero Feedback Delay

A series of long simulations (3.34 x 10^8 samples) were performed over a range of control parameters (g = 1, 2, 4, 8, 16, 32, 64, 128), population sizes (P_0 = 8, 16, 32, 64), and update periods (τ = 0.0025, 0.005, 0.01, 0.02, 0.04). These population targets are very small, but were chosen so that the volatility and bias would be increased and thus computed more accurately.

The relationship between volatility (v), control parameter (g), target population size (P_0), and update period (τ) can be inferred from figure 1. The data for various population sizes (differentiated by symbol) largely lie on top of one another, demonstrating the inverse relationship between volatility and population size. Simulations with P_0 = 8 were largely unstable and have been excluded from the fits (though the 1/ P_0 relationship still clearly held for these runs). The data also support a power law relationship between the volatility and $g\tau$. Slight deviations from power law behavior were found for $g < 4$ (data not shown). As g is taken below the critical threshold of 1, the population feedback overcorrects, causing the population to oscillate within an exponentially growing envelope. Thus, g can be regarded as an independent parameter only as this instability is approached (small g). To summarize, we find that:

$$v \propto \frac{g\tau}{P} \qquad (17)$$

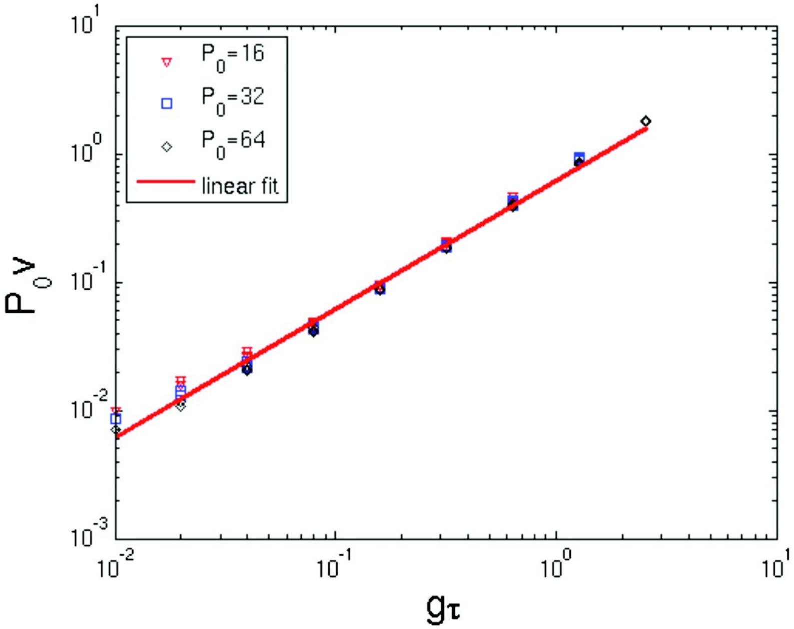

Figure 1. Population volatility vs. combined population control parameter and update period.

A similar relationship can be obtained for the population control bias. Figure 2 displays results for the bias over the same range of parameters in Figure 1. Again, it is immediately clear that the bias scales inversely with target population size. The bias is clearly not a power law in $g\tau$, but a logarithmic fit conforms to the data almost perfectly. The bias then approximately satisfies the empirical relation

$$b \propto \frac{1}{P} \log \frac{t_f}{g\tau} \tag{18}$$

where t_f is a constant roughly equal to 3.0. It should be noted that this form cannot hold in the limit of large $g\tau$ because the bias must strictly vanish in this regime. A simple analysis of DMC using continuous weights rather than branching reveals that the bias must transition to an inverse relationship in the large $g\tau$ limit.

$$b \xrightarrow[g\tau \to \infty]{} \frac{1}{Pg\tau} \tag{19}$$

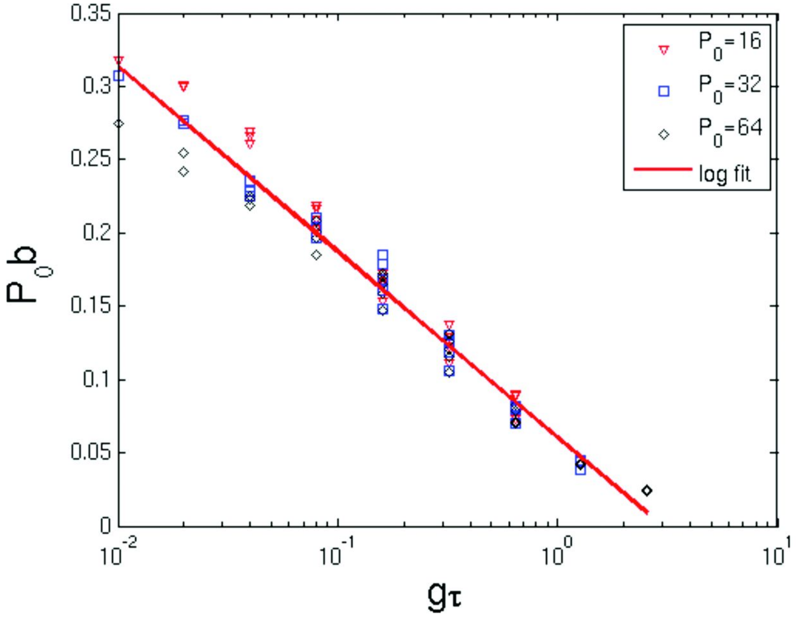

Figure 2. Population control bias vs. combined population control parameter and update period.

Alhough we have studied the bias in a simple model problem, our results should hold for other systems of typical interest involving singular potentials or the fixed node constraint. These complicating factors will indeed affect the bias, since they change the local energy distribution. However, the central limit theorem implies that these local energies, if averaged over enough steps, will converge to the same distribution as the model case, but with a different variance. Therefore the effects of nodes and singular potentials should be contained only within the fit constants in eq 18, and not in its functional form. Though this argument is fairly general, explicit tests of such systems should be made to fully confirm its validity.

Results with Finite Feedback Delay

For the introduction a finite feedback delay (*L*), we expect that most of the prior results will simply be modified by replacing *g* with *g*+*L*. This expectation is largely borne out by the data, especially in the case of the volatility. Figure 3 shows filled stability contours of a 64 walker simulation with unstable regions becoming increasingly dark. Though the stability (probability of a successful run) is shown here, the essential features are identical to the inverse volatility. A dramatic effect of the feedback delay is seen in the region of tight control (small *g*) and finite delay.

The strong instability seen in this region is a manifestation the critical instability discussed earlier, only here the system becomes unstable for all $g < L+1$. In this regime, population fluctuations are overcorrected, similar to the feedback experienced when a microphone is placed next to a loudspeaker. The upper solid line in the plot marks the expected isostability curve $g_{eff} = g + L$ shown along the boundary between stability and instability. For systems with smaller target populations, the stable (white) region becomes narrower and the predicted contour matches well with the observed stability until the critical instability is approached. Thus equation 17 is extended to obtain eq 20 as long as the time delay satisfies eq 21.

$$v \propto \frac{(g + L)\tau}{P} \tag{20}$$

$$L < g - 1 \tag{21}$$

Provided *L* is chosen somewhat below this bound, the time delayed method should be as stable as the standard algorithm with a control parameter of $g + L$. Though the triangular stability region narrows as *L* increases, it should be noted that its size will increase proportional to the target population size.

Results for the population control bias demonstrate that a feedback delay does reduce the bias, though the beneficial effects are partially checked by an increase in volatility. Figure 4 illustrates this situation by showing the real decrease in the bias after the increased volatility is accounted for. Time delayed simulations were performed with a fixed control parameter ($g = 32$) over a range of delays (from 0 to 32). The time delayed data are plotted at an effective control parameter (*g*+*L*), so that data displayed at a particular value of *g* have the same volatility. It appears at first that adding a time delay equal to the control parameter halves the bias relative to the undelayed case. However, after the data are shifted to reflect the loss of stability, the actual gains are smaller. Still, increasing the feedback delay can be an effective means for reducing the population control bias provided the increased volatility is acceptable.

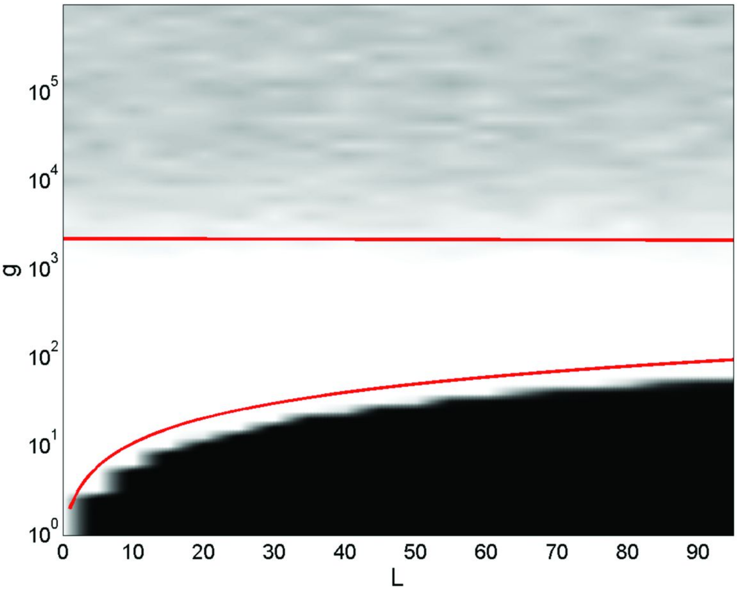

Figure 3. Stability vs. feedback delay and population control parameter shown with instability lines for P_0=64 and τ=0.01. Brighter regions are more stable.

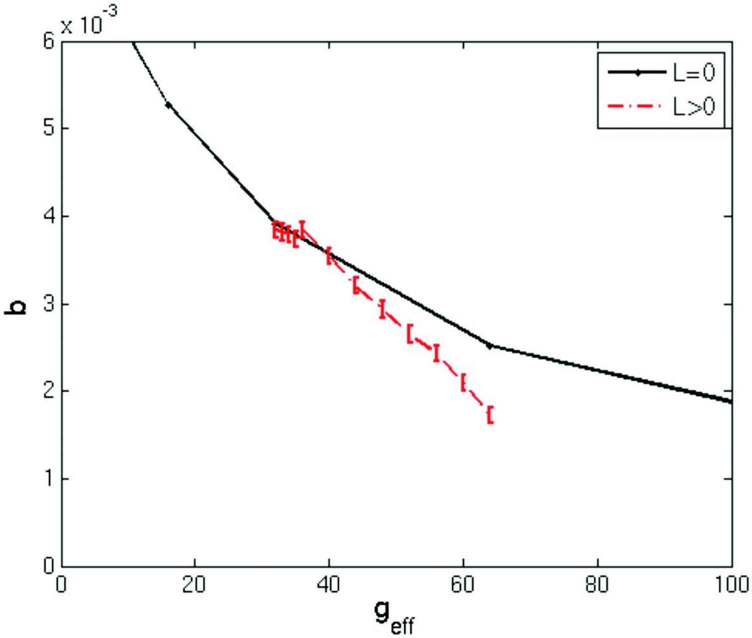

Figure 4. Population control bias vs. effective control parameter for standard (black) and time delayed (red) DMC at τ=0.01 and P_0=32.

Practical Recommendations for DMC Simulations

Optimizing the balance between efficiency and accuracy is a significant goal of any discipline which employs large scale simulation. Finding the right tradeoffs in DMC is a case of selecting optimal values for the control parameters. Using the insight gained from the model system, we are now in a position to effectively navigate the parameter space toward the optimal solution.

A natural benefit of increasing machine size is that the target walker population must scale in the same way, providing an added reservoir of stability to the simulation and damping the bias. The increase in the size of the simulated physical system requires a decrease of the number of walkers per node in order to restore the serial efficiency lost from longer equilibration times. The low walker count per node increases the total idle time due to more interactions with synchronization barriers and strains load balancing algorithms, further reducing the parallel efficiency.

Introducing a population control feedback delay of sufficient length should push back the synchronization barriers inherent in standard DMC. Though the time delay will increase the volatility of the walker population, and thus require frequent attention from the load balancer, there will be more time to get the balance right before the energy must be accumulated. The load should be defined in this case as the amount of time required to advance all walkers to a specific point in imaginary time, such as L steps beyond the average projection time of the walkers.

The population control parameter (g) should be selected so as to satisfy the lower bound in equation 21 while keeping it as small as is necessary to reign in the population fluctuations. If the population control bias is a primary concern, the population correction in the trial energy could be updated less often and/or standard correction methods such extrapolation (*12*) or reweighting (*13*) could be employed.

Conclusion

We have established empirical relationships which reveal the dependence of the population control bias and population volatility on the trial energy update period, population control parameter, and target population size. Though established by a thorough investigation of a simple model system, we expect that these relationships will apply generally to Diffusion Monte Carlo. We have proposed a simple modification to the DMC algorithm, namely the use of delayed feedback in the population control mechanism, which should increase the parallel performance of DMC simulations. This modification, which requires minimal change to existing codes, should function well with only a few walkers per node which will reduce the fraction of CPU time spent on walker equilibration. Model results have shown that the introduction of a feedback delay moderately reduces the population control bias after the increase in population volatility has been accounted for. Finally, we have provided general recommendations to improve serial and parallel efficiency while reducing bias by adjusting only the trial energy update frequency, population control parameter, and feedback delay. Future work will investigate the population control bias in real physical systems to assess the adequacy of conclusions drawn from the model system.

Acknowledgments

We gratefully acknowledge support from the U.S. Department of Energy under contract No. DE-F605-080R2335 and the National Science Foundation under grant OCI-0904572. Helpful comments and suggestions made by Jeongnim Kim and Bryan Clark have aided our work and we express our gratitude for their insights and encouragement.

References

1. Ceperley, D. M.; Alder, B. J. *Phys. Rev. Lett.* **1980**, *45*, 566.
2. Reynolds, P. J.; Ceperley, D. M.; Alder, B. J.; Lester, W. A. *J. Chem. Phys.* **1982**, *77*, 5593–5603.
3. Baroni, S.; Moroni, S. *Phys. Rev. Lett.* **1999**, *82*, 4745–4748.
4. Ceperley, D. M. *Rev. Mod. Phys.* **1995**, *67*, 279–355.
5. McMillan, W. L. *Phys. Rev.* **1965**, *138*, A442.
6. Kalos, M. H.; Levesque, D.; Verlet, L. *Phys. Rev. A* **1974**, *9*, 2178.
7. Mentch, F.; Anderson, J. B. *J. Chem. Phys.* **1981**, *74*, 6307–6311.
8. Davis, D. H. Lawrence Radiation Laboratory Report No. UCRL-6707, 1961.
9. Booth, T. E.; Gubernatis, J. E. *Phys. Rev. E.* **2009**, *80*, 046704.
10. Buonaura, M. C.; Sorella, S. *Phys. Rev. B* **1998**, *57*, 11446–11456.
11. Assaraf, R.; Caffarel, M.; Khelif, A. *Phys. Rev. E* **2000**, *61*, 4566.
12. Ceperley, D. M. *J. Comput. Phys.* **1983**, *51*, 404–422.
13. Umrigar, C. J.; Nightingale, M. P.; Runge, K. J. *J. Chem. Phys.* **1993**, *99*, 2865–2890.
14. Drummond, N. D.; Needs, R. J.; Sorouri, A.; Foulkes, W. M. C. *Phys. Rev. B* **2008**, *78*, 125106.
15. Hetherington, J. H. *Phys. Rev. A* **1984**, *30*, 2713.
16. Warren, G. L.; Hinde, R. J. *Phys. Rev. E* **2006**, *73*, 056706.
17. Nemec, N. *Phys. Rev. B* **2010**, *81*, 035119.
18. Cerf, N.; Martin, O. C. *Phys. Rev. E* **1995**, *51*, 3679.
19. Drummond, N. D.; Radnai, Z.; Trail, J. R.; Towler, M. D.; Needs, R. J. *Phys. Rev. B* **2004**, *69*, 085116.

Chapter 3

Enhancement of Sampling Efficiency in *ab Initio* Monte Carlo Simulations Using an Auxiliary Potential Energy Surface

Akira Nakayama* **and Tetsuya Taketsugu**

Division of Chemistry, Graduate School of Science, Hokkaido University,
Sapporo 060-0810, Japan
***E-mail: akira-n@sci.hokudai.ac.jp**

Downloaded by UNIV OF GUELPH LIBRARY on May 28, 2012 | http://pubs.acs.org
Publication Date (Web): February 6, 2012 | doi: 10.1021/bk-2012-1094.ch003

An approach is developed to enhance sampling for *ab initio* Monte Carlo and *ab initio* path integral Monte Carlo calculations of molecular clusters by utilizing an approximate potential as a guide to move in the configuration space more efficiently. Two methods are introduced in this chapter, where the first one utilizes the interpolated potential energy surface obtained by the moving least-squares method, and the second one employs the molecular dynamics scheme to update the system configuration in the context of hybrid Monte Carlo method in which potential energy gradients are evaluated by computationally less expensive *ab initio* electronic structure methods. The sampling efficiencies in both methods are demonstrated for a water molecule and hydronium cation.

I. Introduction

Computer simulations via molecular dynamics (MD) and Monte Carlo (MC) methods are widely used in a variety of fields ranging from drug design to materials science (*1*). Instead of using empirical force fields, *ab initio* molecular dynamics or *ab initio* Monte Carlo methods, which solve the electronic Schrödinger equation for nuclear potential energy (or its derivatives) as needed, are now being widely used to investigate static and also dynamic properties of molecular systems from first principles. The computational cost for such *ab initio* simulations is, however, still highly expensive when combined with statistical simulations since 10^5-10^6

In Advances in Quantum Monte Carlo; Tanaka, S., et al.;
ACS Symposium Series; American Chemical Society: Washington, DC, 2012.

simulation steps are usually required, thus limiting their applicability to relatively small system sizes.

A Monte Carlo simulation is efficient in empirical force fields, especially when the total potential is represented by a sum of the additive interactions. In each MC step, the pair interactions only between the 'chosen' atom and other atoms are needed to evaluate, *i.e.* it is not necessary to evaluate the potential of the whole system. If one employs the primitive approach for *ab initio* Monte Carlo calculations, *ab initio* potential energy must be calculated in each step even if only one atom is chosen to move, which does not seem to be efficient compared to simulations with empirical force fields. In contrast to *ab initio* Monte Carlo calculations, *ab initio* molecular dynamics has the advantage that the whole molecular configuration is updated in each time step. However, the evaluation of the *ab initio* potential energy gradients requires additional computational cost, which could be several times more than that of energy calculation. Furthermore, the module for the analytical energy gradients is not available for some highly correlated methods such as CCSD(T).

In this chapter we demonstrate that sampling efficiency for *ab initio* Monte Carlo calculations is realized by utilizing an approximate potential as a guide to move in the configuration space more effectively. An auxiliary Markov chain is generated on this approximate potential, and as an approximate potential, we adopt an interpolated potential energy surface that is constructed by the moving least-squares method (*2*). Also we introduce another simple scheme in the context of *ab initio* hybrid Monte Carlo (HMC) calculations, which also enhances sampling efficiency by utilizing the potential energy gradients of an approximate potential for updating the system configurations (*3*).

These schemes are applied to a water molecule and hydronium cation (H_3O^+) and the effectiveness of the present approach is analyzed in detail. Since quantum effects of nuclei are important for hydrogen atoms, we also perform *ab initio* path integral Monte Carlo (PIMC) calculations for these systems and the efficiency of the method is again discussed.

This chapter is organized as follows: Section II presents details of the simulation methods including a short review of the path integral Monte Carlo method for the quantum treatment of nuclei. In Sec III the results obtained by these methodologies are presented, along with the detailed analysis of the efficiency of the method. Section IV contains the conclusions of this work.

II. Methodologies

Approximate Potential Method

The multiple Markov chain methods (MMC) (*4*) are originally developed to enhance sampling in which Markov chains running at a higher temperature are used to promote transition among different regions of high probability density. The approximate potential (AP) method exploits this idea and uses an auxiliary Markov chain that moves on the approximate and computationally less expensive potential. In this method, a Monte Carlo importance sampling is performed on this approximate potential, and after a fixed number of steps, the difference between the

Downloaded by UNIV OF GUELPH LIBRARY on May 28, 2012 | http://pubs.acs.org
Publication Date (Web): February 6, 2012 | doi: 10.1021/bk-2012-1094.ch003

original and approximate potential is used as a criterion to restore sampling with respect to the original potential. With this method, correlation in the Markov chain on the original potential is significantly reduced. Since the approximate potential is chosen such that the computational cost for evaluation is much less expensive than the original one, significant computational saving is attained. Iftimie *et.al.* utilized this idea in the *ab initio* simulation of proton transfer reactions and used molecular mechanics potentials as an approximate potential (*5*, *6*). Gelb applied this scheme to Lennard-Jones fluids and showed that the speedups by almost a factor of four are obtained (*7*). Bandyopadhyay showed that this method can be used to determine stationary points on the potential energy surface of molecular systems (*8*).

In the AP method, the key to efficient sampling is finding a suitable approximate potential. It is desirable that the approximate potential is close to the original potential within a region of configuration space accessible at a given temperature. This results in a high acceptance ratio and ensures an effective sampling. When the approximate potential is identical to the original potential, the acceptance ratio is always one. On the other hand, if the approximate potential is appreciably different from the original one, the Markov chain on the approximate potential may spend long periods of time in the region that is less significant for the system. In some cases this could lead to less efficient sampling than the conventional MC method.

We briefly describe the AP method for a canonical ensemble of classical system, whose probability density is given as

$$\rho(\mathbf{R}) = \frac{1}{Z}\exp\left[-\beta V(\mathbf{R})\right] \tag{1}$$

where $\beta = 1/k_B T$ is the reciprocal temperature in units of the Boltzmann constant. Here **R** is the configuration of the system and Z is the partition function. The extension to quantum systems using imaginary time path integral formulation, which will be described below, is straightforward. The procedure for the AP method is as follows. Suppose that the current configuration of the system is $\mathbf{R}^{(i)}$. An auxiliary Markov chain is generated from $\mathbf{R}^{(i)}$ with the probability density proportional to $\exp\left[-\beta V_{\text{ap}}(\mathbf{R})\right]$ where V_{ap} is the approximate potential. After a fixed number of updates on the approximate potential, one attempts to move the system configuration $\mathbf{R}^{(i)}$ to the final configuration of the auxiliary Markov chain ($\mathbf{R}^{(j)}$) with probability

$$\min\left[1, \exp\left\{-\beta\left[\left(V(\mathbf{R}^{(j)}) - V_{\text{ap}}(\mathbf{R}^{(j)})\right) - \left(V(\mathbf{R}^{(i)}) - V_{\text{ap}}(\mathbf{R}^{(i)})\right)\right]\right\}\right]. \tag{2}$$

One can see that the transition from $\mathbf{R}^{(i)}$ to $\mathbf{R}^{(j)}$ is performed based on the difference between the original and approximate potentials. With this criterion the microscopic reversibility for the system configuration

$$\rho(\mathbf{R}^{(i)})P(\mathbf{R}^{(i)} \to \mathbf{R}^{(j)}) = \rho(\mathbf{R}^{(j)})P(\mathbf{R}^{(j)} \to \mathbf{R}^{(i)}) \tag{3}$$

Downloaded by UNIV OF GUELPH LIBRARY on May 28, 2012 | http://pubs.acs.org
Publication Date (Web): February 6, 2012 | doi: 10.1021/bk-2012-1094.ch003

is satisfied (*5*, *7*), where P is the transition probability. The acceptance probability given in eq. (2) is closely related to that of the parallel tempering method (*4*, *9*, *10*) (also known as the replica exchange method (*11*)). If the above move is accepted, another auxiliary Markov chain is generated from $\mathbf{R}^{(j)}$, and if the move is rejected, the current configuration of the system goes back to the original configuration $\mathbf{R}^{(i)}$ and another attempt is made. It is noted that the limiting distribution for the system does not depend on the form of the approximate potential, provided that the updating scheme on the approximate potential is ergodic. In the current implementation of *ab initio* MC, *ab initio* calculation is performed at the final configuration of the auxiliary Markov chain on the approximate potential.

Downloaded by UNIV OF GUELPH LIBRARY on May 28, 2012 | http://pubs.acs.org
Publication Date (Web): February 6, 2012 | doi: 10.1021/bk-2012-1094.ch003

The IMLS Approach

The approximate potential energy surface is constructed by the interpolation method using the moving least-squares approach (*12*, *13*). The modified Shepard interpolation method (*14*) is widely used for construction of potential energy surface and it is usually more efficient than the IMLS method. The modified Shepard interpolation method requires the derivatives normally up to the second order to obtain a reliable potential energy. The *ab initio* calculations of these derivatives at reference points are computationally expensive for some highly sophisticated electronic structure methods. The IMLS method, on the other hand, yields a sufficiently accurate potential only with the potential energy. The IMLS is relatively expensive since one needs to solve a weighted-least-squares equation at each evaluation point, but still much less expensive than *ab initio* calculations by several orders of magnitude.

The interpolated potential energy at a nuclear configuration $\mathbf{Z}$ is represented by a linear combination of linearly independent basis functions $b_i(\mathbf{Z})$ as

$$V(\mathbf{Z}) = \sum_{i=1}^{M} a_i b_i(\mathbf{Z}) \qquad (4)$$

where M is the total number of basis functions. The coefficients a_i are obtained by minimizing the following weighted deviations:

$$D[V(\mathbf{Z})] = \sum_{i=1}^{N_d} w_i(\mathbf{Z}) \left[\sum_{j=1}^{M} a_j b_j(\mathbf{Z}^{(i)}) - V_{\mathrm{ref}}(\mathbf{Z}^{(i)}) \right]^2 . \qquad (5)$$

Here, N_d is the number of reference data points and $V_{\mathrm{ref}}(\mathbf{Z}^{(i)})$ is the energy value at point $\mathbf{Z}^{(i)}$ in the dataset. The weight function $w_i(\mathbf{Z})$ decays with distance $\left|\mathbf{Z} - \mathbf{Z}^{(i)}\right|$ so that the closer data points have a larger weight than the more distant ones. Note that the coefficients a_i are implicitly dependent on $\mathbf{Z}$ because of the weight function. In this study, the coordinates are taken to be the reciprocal internuclear distances (*i.e.*, $Z_k = 1/r_{ij}$), which is commonly used in the context of the IMLS interpolations and also in the modified Shepard interpolations.

The minimization condition with respect to a_i leads to the following equation:

$$\mathbf{B}^T\mathbf{W}\mathbf{B}\mathbf{a} = \mathbf{B}^T\mathbf{W}\mathbf{V} \tag{6}$$

where $\mathbf{a} = \left(a_1, a_2, \cdots, a_M\right)^T$, $\mathbf{V} = \left(V(\mathbf{Z}^{(1)}), V(\mathbf{Z}^{(2)}), \cdots, V(\mathbf{Z}^{(N_d)})\right)^T$, and $\mathbf{W}$ is a diagonal matrix whose elements are $W_{ij} = w_i(\mathbf{Z})\delta_{ij}$. $\mathbf{B}$ is composed of values of the basis functions at $\mathbf{Z}^{(i)}$ and given by

$$\mathbf{B} = \begin{pmatrix} b_1(\mathbf{Z}^{(1)}) & b_2(\mathbf{Z}^{(1)}) & \cdots & b_M(\mathbf{Z}^{(1)}) \\ b_1(\mathbf{Z}^{(2)}) & b_2(\mathbf{Z}^{(2)}) & \cdots & b_M(\mathbf{Z}^{(2)}) \\ \cdots & \cdots & \cdots & \cdots \\ b_1(\mathbf{Z}^{(N_d)}) & b_2(\mathbf{Z}^{(N_d)}) & \cdots & b_M(\mathbf{Z}^{(N_d)}) \end{pmatrix}. \tag{7}$$

The interpolated potential for a given configuration $\mathbf{Z}$ is obtained by solving the normal equation Eq. (6), which is implemented by using the singular value decomposition (SVD).

In this work, we use polynomials up to the second order of each component of $\mathbf{Z}$ as the basis functions. The weight function of the form

$$w_i(\mathbf{Z}) = 1\Big/\left|\mathbf{Z} - \mathbf{Z}^{(i)}\right|^2 \tag{8}$$

is employed throughout this study.

Path Integral Monte Carlo Method

The imaginary time path integral formulation of quantum statistics provides a conceptual and computationally practical route for studying the quantum nature of systems at thermal equilibrium (*15*). Based on Feynman's notion that a quantum system can be mapped onto a classical model of interacting "polymers" with path integrals, the path integral Monte Carlo method has proven to be extremely useful for studying finite temperature properties of many-particle systems. Quantum effects such as zero-point motion and tunneling as well as thermal fluctuations are included rigorously in this method and it is now seeing widespread use in a variety of applications to chemical systems. A combination of path integral techniques with *ab initio* calculations has been realized for systems where the empirical force fields is not available.

Downloaded by UNIV OF GUELPH LIBRARY on May 28, 2012 | http://pubs.acs.org
Publication Date (Web): February 6, 2012 | doi: 10.1021/bk-2012-1094.ch003

Downloaded by UNIV OF GUELPH LIBRARY on May 28, 2012 | http://pubs.acs.org
Publication Date (Web): February 6, 2012 | doi: 10.1021/bk-2012-1094.ch003

In the path integral Monte Carlo calculations, the expectation value of an operator $\hat{A}$ corresponding to an observable at thermal equilibrium can be expressed as

$$\begin{aligned}\left\langle \hat{A} \right\rangle &= \frac{1}{Z}\prod_{j=1}^{N}\left(\frac{m_j P}{2\pi\beta h^2}\right)^{\frac{3P}{2}} \\ &\times \int d\mathbf{R}_1 \int d\mathbf{R}_2 \cdots \int d\mathbf{R}_P A(\mathbf{R}_1)\exp\left[-\sum_{j=1}^{N}\frac{m_j P}{2\beta h^2}\sum_{i=1}^{P}\left|\mathbf{r}_i^{(j)} - \mathbf{r}_{i+1}^{(j)}\right|^2 - \frac{\beta}{P}\sum_{i=1}^{P}V(\mathbf{R}_i)\right]\end{aligned} \tag{9}$$

where P is the number of time slices and $Z = \mathrm{Tr}(e^{-\beta\hat{H}})$ is the canonical partition function. Here we assume that the system of interest consists of N atoms with the Cartesian positions $\mathbf{R} = \left\{\mathbf{r}^{(1)}, \mathbf{r}^{(2)}, \cdots, \mathbf{r}^{(N)}\right\}$. In the above equation, $\hat{A}$ is assumed to be a function of the position operator and cyclic periodic boundary condition $\mathbf{R}_{P+1}=\mathbf{R}_1$ is imposed. A Monte Carlo sampling is performed according to the distribution function given by

$$w(\mathbf{R};\beta) = \exp\left[-\sum_{j=1}^{N}\frac{m_j P}{2\beta h^2}\sum_{i=1}^{P}\left|\mathbf{r}_i^{(j)} - \mathbf{r}_{i+1}^{(j)}\right|^2 - \frac{\beta}{P}\sum_{i=1}^{P}V(\mathbf{R}_i)\right] \tag{10}$$

The staging PIMC algorithm (*16*, *17*) is highly efficient as a sampling method in PIMC, thus we employ this technique in a MC sampling on the approximate potential. When applying the AP method to PIMC simulations, the acceptance probability for the update of the system configuration from **R** to **R′** is given by

$$\min\left[1, \exp\left\{-\frac{\beta}{P}\left[\sum_{i=1}^{P}\left(V(\mathbf{R}'_i) - V_{\mathrm{ap}}(\mathbf{R}'_i)\right) - \sum_{i=1}^{P}\left(V(\mathbf{R}_i) - V_{\mathrm{ap}}(\mathbf{R}_i)\right)\right]\right\}\right]. \tag{11}$$

Note that the harmonic spring terms cancel out. Therefore, the acceptance criterion is based on the difference between the *ab initio* and approximate potential at the current and trial configurations.

Hybrid Monte Carlo

The hybrid Monte Carlo method combines the advantages of both the MD and MC methods, allowing the global update of the system configuration with reasonable acceptance ratio (*18*, *19*). It is an exact method and does not suffer from the finite step-size errors of MD simulations. In an update process of the system configuration, the time-reversible and area-preserving MD algorithm needs to be used to ensure the detailed balance and the commonly used velocity Verlet algorithm satisfies this requirement. The initial momenta $\mathbf{P}^{(i)}$ are drawn randomly from the Boltzmann distribution at the given inverse temperature β and after a fixed number of MD steps, the final configuration $\mathbf{R}^{(f)}$ is accepted according to the following criterion

$$\min\left[1,\frac{\rho(\mathbf{R}^{(j)})\exp(-\beta T(\mathbf{P}^{(j)}))}{\rho(\mathbf{R}^{(i)})\exp(-\beta T(\mathbf{P}^{(i)}))}\right]=\min\left[1,\frac{\exp(-\beta H(\mathbf{P}^{(j)},\mathbf{R}^{(j)}))}{\exp(-\beta H(\mathbf{P}^{(i)},\mathbf{R}^{(i)}))}\right] \quad (12)$$

where $\mathbf{P}^{(j)}$ are momenta at the final configuration and ρ is the target distribution. In this study, ρ is given as $\exp(-\beta V)$, therefore the acceptance probability is rewritten as in the right-hand side of eq. (12).

Here we propose a method which employs a computationally inexpensive (approximate) potential energy surface V_{ap} and its gradient for an MD update part, but uses the same acceptance probability given above to ensure that the target distribution is still determined under the potential V. Note that $\mathbf{P}^{(j)}$ are the momenta which evolve under the potential V_{ap} from initial phase space variables $\mathbf{P}^{(i)}$ and $\mathbf{R}^{(i)}$. In the context of *ab initio* simulations, one can use energy gradients of less expensive *ab initio* potentials for an MD update part. The numerical evaluation of the energy gradients requires additional computational cost, which could be several times higher than that of the energy calculation, thus there would be a great saving in computational effort if the above approach is utilized. For example, the potential energies are calculated at the level of CCSD(T)/cc-pVTZ, but energy gradients of HF/cc-pVDZ level are used for an MD update. It nevertheless gives the correct distribution determined by CCSD(T)/cc-pVTZ.

Downloaded by UNIV OF GUELPH LIBRARY on May 28, 2012 | http://pubs.acs.org
Publication Date (Web): February 6, 2012 | doi: 10.1021/bk-2012-1094.ch003

III. Results and Discussion

Simulations Using Interpolated Potential Energy Surface

Ab Initio Simulations on H_2O

'On-the-fly' *ab initio* Monte Carlo calculations were performed on an H_2O molecule. The *ab initio* calculations were performed at the MP2 level of theory using the MOLPRO2008.1 package (*20*). The segmented DZP basis set augmented with diffuse functions (*21*) was employed. The reference points for interpolation were sampled by classical molecular dynamics calculations at a constant temperature of 300 K with the massive Nosé-Hoover thermostat chains. The time step of 1.0 fs was employed and all configurations and potential energies along the trajectory were stored as the reference data. This time step is not appropriate from the viewpoint of the energy conservation, but it can explore the configuration space more quickly. A total of 100 reference points were stored. The *ab initio* MC calculation with $N_s = 10$ and $N_p = 100$ was performed for a total of 1,000,000 steps.

Table I shows the obtained average of the geometrical parameters and potential energies along with these statistical errors and relative efficiencies. The statistical errors are estimated by block averages. The result of the conventional MC calculation (without using AP) is also displayed for comparison. The zero of the potential energy corresponds to the energy at the equilibrium structure. The *ab initio* PIMC calculations were also carried out for a total of 100,000 steps. Reference points were generated by the *ab initio* molecular dynamics simulation at $T = 2700$ K as described above. A Monte Carlo sampling on the approximate potential was performed with $N_s = 96$ and $N_p = 100$ using the staging algorithm with path length $L = 6$.

The obtained results are summarized in Table I, along with the result of the conventional PIMC method (without using AP) employing the staging algorithm with $L = 6$. Since we used the primitive form for the kinetic energy estimator, the large statistical error for kinetic energy was observed in comparison to the potential energy. The virial estimator is preferable for the kinetic energy, but since it requires potential energy derivatives, we have not employed it here. The acceptance ratio for the update of the system configuration is around 0.91 with a current set of parameters, which is also a measure of the accuracy of the IMLS potential.

In this example on H_2O, an increase in efficiency, which is propotional to the inverse of the square of the statistaical error (the relative value with respect to the conventional method is shown in the table), by roughly an order of magnitude is obtained for both the classical and quantum simulations. It is noted that the above AP simulations take only around 1-2% more in cpu time than that of the corresponding conventional calculations.

Downloaded by UNIV OF GUELPH LIBRARY on May 28, 2012 | http://pubs.acs.org
Publication Date (Web): February 6, 2012 | doi: 10.1021/bk-2012-1094.ch003

Table I. Average of geometrical parameters and energies along with these statistical errors and relative efficiencies for ab initio classical MC (1,000,000 steps) and ab initio PIMC (100,000 steps) calculations on an H_2O molecule. AP is the result of calculation with the approximate potential. The equilibrium geometrical parameters are $R_{OH} = 0.9640$ Å and $\theta = 104.00$ degree. The efficiency is relative to its value without using AP.

	classical MC (AP)	*classical MC (without AP)*	*PIMC (AP)*	*PIMC (without AP)*
$\langle R_{OH} \rangle$ (Å)	0.9669	–	0.9817	–
$\langle \theta \rangle$ (deg)	103.95	–	103.79	–
$\langle V \rangle$ (K)	454.0	452.4	3180.1	3170.7
σ_V (K)	0.6	1.9	3.4	10.5
efficiency	8.9	1.0	9.9	1.0
$\langle K \rangle$ (K)	–	–	3960.8	4077.6
σ_K (K)	–	–	23.4	73.3
efficiency	–	–	9.8	1.0

Downloaded by UNIV OF GUELPH LIBRARY on May 28, 2012 | http://pubs.acs.org
Publication Date (Web): February 6, 2012 | doi: 10.1021/bk-2012-1094.ch003

Ab Initio Simulations on H_3O^+

The hydronium cation H_3O^+ has been studied extensively in relation to Eigen's proton transfer mechanism in water. This cation is a floppy molecule and involves the Walden inversion between pyramidal structures in the C_{3v} symmetry. Previous calculations by *ab initio* path integral molecular dynamics showed that the Walden inversion is enhanced significantly by the inclusion of quantum effects of nuclei (*22*).

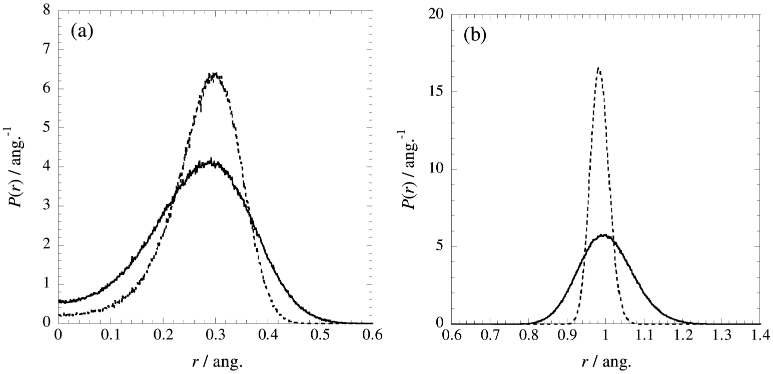

Figure 1. Distribution functions of the distance between (a) the O atom and H-H-H plane and (b) the O and H atoms. The solid and dashed lines are the results of PIMC and classical MC calculations, respectively.

The *ab initio* MC and PIMC calculations were performed with $N_s = 20$ and $N_s = 96$ for a total of 1,000,000 and 100,000 steps, respectively. A total of 500 reference points were generated by the molecular dynamics simulation at $T = 2700$ K and the nearest $N_p = 100$ points were used for the fitting. Figure 1 shows the distribution function of the distance between the O atom and H-H-H plane and between the O and H atoms. The increased value at zero for quantum simulation in Figure 1(a) reflects the fact that the inversion is enhanced significantly by the quantum treatment of nuclei.

Again, in order to demonstrate the effectiveness of our method, the conventional MC and staging PIMC calculations were performed for 1,000,000 and $100{,}000 \times P/(L\text{-}1)$ steps, respectively. Table II summarizes the obtained geometrical parameters and energies, along with these statistical errors and relative efficiencies. As seen in the table, an increase in efficiency by an order of magnitude is obtained for the expectation values of energy. The acceptance ratio for the update of the system configuration was ~ 0.81 and ~ 0.82 for classical MC and PIMC simulations, respectively. It is noteworthy that simulation with the acceptance ratio of around 0.8 still gives a significant reduction in computational cost. One can improve this rate further by increasing reference points. With the current set of parameters, the computational cost is increased by only 1-2% compared to the conventional calculation.

Table II. Average of geometrical parameters and energies, along with these statistical errors (in kelvin) and relative efficiencies for ab initio simulations on H_3O^+. AP is the result of calculation with the approximate potential. The efficiency is relative to its value without using AP.

	classical MC (AP)	*Classical MC (without AP)*	*PIMC (AP)*	*PIMC (without AP)*
$<R_{OH}>$ (Å)	0.9845	–	1.0007	–
$<\theta>$ (deg)	112.08	–	112.31	–
$<V>$ (K)	928.2	932.9	5194.5	5183.5
σ_V (K)	1.1	3.8	4.7	13.7
efficiency	12.9	1.0	8.4	1.0
$<K>$ (K)	–	–	5826.1	6035.8
σ_K (K)	–	–	28.4	93.4
efficency	–	–	10.8	1.0

Downloaded by UNIV OF GUELPH LIBRARY on May 28, 2012 | http://pubs.acs.org
Publication Date (Web): February 6, 2012 | doi: 10.1021/bk-2012-1094.ch003

Hybrid Monte Carlo and Hybrid Path Integral Monte Carlo Simulations

As a simple illustration of the method, we first show the results of *ab initio* HMC calculations on an H_2O molecule at $T = 300$ K. The target level of *ab initio* method is set to MP2/cc-pVDZ. For simplicity, a single step was used for an MD part in one MC cycle and a total of 50,000 MC steps were taken. *Ab initio* MD calculations at a constant temperature of 300 K were also carried out for comparison at the level of MP2/cc-pVDZ.

Figure 2(a) shows the acceptance ratio as a function of a time step by employing various auxiliary potentials obtained from different (low-level) *ab initio* methods and basis sets. It is seen that good acceptance ratio is obtained even when the time step is increased to 1.5 ~ 2.0 fs. Figure 2(b) shows the statistical errors of potential energies (σ_V) and OH bond lengths (σ_R) as a function of acceptance ratio. A good convergence is achieved when the acceptance ratio is around 40 ~ 60 %. The statistical errors are reduced in most cases in comparison to *ab initio* MD simulations with $\Delta t = 0.1$ fs. Considering that the CPU time decreases dramatically as a level of *ab initio* calculations is lowered for computing gradients and that the efficiency of the method is proportional to the inverse of the square of statistical errors, a significant computational saving is achieved. Note that increasing a time step of *ab initio* MD calculations will certainly reduce the statistical errors, but will induce large systematic errors due to finite step-size. In *ab initio* MD, the total energy deviates from its initial value by ~ 1.2 kcal/mol for the entire run when the time step is increased to 0.5 fs.

Ab initio path integral hybrid Monte Carlo calculations (*23*) were also performed for H_2O and H_3O^+ molecules with 16 imaginary-time slices and compared with the *ab initio* path integral MD simulations (*24*) (MP2/cc-pVDZ) at a constant temperature of 300 K. The normal mode coordinates (*25*) were used in all calculations and a total of 50,000 steps were taken for both path integral HMC and path integral MD calculations. The results obtained are shown in Table III and the performance is essentially similar to that obtained in *ab initio* HMC simulations. Again, *ab initio* path integral HMC calculations with auxiliary potentials offered a significant increase in computational efficiency.

Downloaded by UNIV OF GUELPH LIBRARY on May 28, 2012 | http://pubs.acs.org
Publication Date (Web): February 6, 2012 | doi: 10.1021/bk-2012-1094.ch003

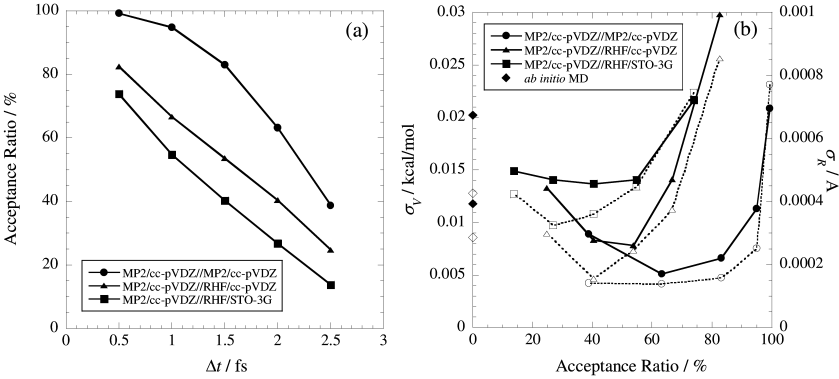

Figure 2. (a) Acceptance ratio as a function of time step in ab initio HMC simulation. MP2/cc-pVDZ//RHF/STO-3G indicates that the target distribution is calculated at the level of MP2/cc-pVDZ and the energy gradients are obtained by RHF/STO-3G for an MD update. (b) Statistical errors of potential energies (filled symbols) and OH bond lengths (hollow symbols) as a function of acceptance ratio. The errors are estimated by the block averages using 50 blocks in both the ab initio HMC and MD simulations. The errors of ab initio MD calculations are shown at zero, where the higher (lower) values correspond to simulations with Δt = 0.2 fs (Δt = 0.1 fs). The average values of potential energy and OH bond length taken from the run of minimum errors are <V> = 0.906 kcal/mol and <R> = 0.9678 Å, respectively.

Downloaded by UNIV OF GUELPH LIBRARY on May 28, 2012 | http://pubs.acs.org
Publication Date (Web): February 6, 2012 | doi: 10.1021/bk-2012-1094.ch003

Table III. Acceptance ratio and statistical errors of potential energies (σ_V in units of kcal/mol) and OH bond lengths (σ_R in units of Å) for H_2O and H_3O^+ molecules in ab initio path integral HMC and MD simulations. The average values of potential energy and OH bond length taken from the run of minimum errors are <V> = 6.022 kcal/mol and <R> = 0.9811 Å for H_2O, and <V> = 10.013 kcal/mol and <R> = 1.0019 Å for H_3O^+.

H_2O	Δt	%	$\sigma_V \times 10^{-2}$	$\sigma_R \times 10^{-4}$
MP2/cc-pVDZ//MP2/cc-pVDZ	1.0	94.4	3.0	3.2
	2.0	58.4	1.8	1.7
MP2/cc-pVDZ//RHF/cc-pVDZ	1.0	67.2	3.8	3.9
	2.0	38.6	2.8	2.5
MP2/cc-pVDZ//RHF/STO-3G	1.0	57.0	4.3	4.3
	2.0	29.5	3.0	3.2
path integral MD	0.1	–	12.5	5.9
	0.2	–	4.6	4.5
H_3O^+				
MP2/cc-pVDZ//MP2/cc-pVDZ	1.0	93.8	4.7	3.3
	2.0	55.8	3.2	2.6
MP2/cc-pVDZ//RHF/cc-pVDZ	1.0	65.5	6.4	6.5
	2.0	35.2	3.7	2.1
MP2/cc-pVDZ//RHF/STO-3G	1.0	73.1	5.6	4.6
	2.0	43.0	3.6	2.7
path integral MD	0.1	–	15.8	5.7
	0.2	–	9.5	4.5

IV. Concluding Remarks

In this chapter, we demonstrated that the efficiency of *ab initio* Monte Carlo and *ab initio* path integral Monte Carlo calculation is enhanced significantly using a suitable approximate potential. In the first part, the interpolated potential energy obtained by the IMLS method was used as an approximate potential and this scheme was applied to a water molecule and small protonated water clusters. It was observed that the statistical errors were reduced by almost a factor of three in most of the calculations presented in this work, which translates into a reduction of the computational cost by an order of magnitude. One of the attractive features of the method is that potential energy gradients are not required in the calculations, which enables one to perform *ab initio* simulations with highly correlated electronic structure methods such as CCSD(T), where the evaluation of energy gradients is highly demanding or the module for analytical gradients is not available. This will open the door for quantum simulations with highly accurate *ab initio* potential. Another feature is that one can use any form of the Monte Carlo sampling on the approximate potential. If the system has the multiple minima separated by high energy barriers, it usually exhibits a quasi-ergodic behavior. This problem can be circumvented by employing the advanced sampling method, such as J-walking (*26*), multicanonical sampling (*27*), and parallel tempering method (*4*, *9*, *10*).

In the second part, we introduce a simple scheme in the context of hybrid Monte Carlo and hybrid path integral Monte Carlo methods, where the energy gradients are obtained from the computationally less expensive method, and in this chapter, we employ a lower level *ab initio* method for updating system configurations. Again, a significant increase in computational efficiency is obtained. It is noted that the similarity of the target and auxiliary potentials is of course a key factor which determines the efficiency of the method. One needs to find a compromise between accuracy of an auxiliary potential and computational cost for evaluating energy gradients. One of the notable advantages of the present method is again that it does not require energy gradients calculations for target (high-level) *ab initio* potentials.

Ab initio simulations have the strength in which one can have direct access to the electronic property of molecules. The detailed understanding of these properties, such as electronic charge or dipole moment, will provide deeper insight into the microscopic structure of complex molecular systems.

Acknowledgments

A.N. acknowledges financial support by a Grant-in-Aid for Young Scientists from the Ministry of Education, Culture, Sports, Science and Technology (MEXT, Japan). The authors thanks Dr. Motoyuki Shiga for fruitful discussions and part of the present work is a collaboration with him.

References

1. Frenkel, D.; Smit, B. *Understanding Molecular Simulation*: Academic Press: San Diego, 1996.
2. Nakayama, A.; Seki, N.; Taketsugu, T. *J. Chem. Phys.* **2009**, 130.
3. Nakayama, A.; Taketsugu, T.; Shiga, M. *Chem. Lett.* **2009**, 38.
4. Geyer, C. J.; Thompson, E. A. *J. Am. Stat. Assoc.* **1995**, 90.
5. Iftimie, R.; Salahub, D.; Wei, D. Q.; Schofield, J. *J. Chem. Phys.* **2000**, 113.
6. Iftimie, R.; Schofield, J. *J. Chem. Phys.* **2001**, 114.
7. Gelb, L. D. *J. Chem. Phys.* **2003**, 118.
8. Bandyopadhyay, P. *J. Chem. Phys.* **2005**, 122.
9. Lyubartsev, A. P.; Martsinovski, A. A.; Shevkunov, S. V.; Vorontsov-Velyaminov, P. N. *J. Chem. Phys.* **1992**, 96.
10. Marinari, E.; Parisi, G. *Europhys. Lett.* **1992**, 19.
11. Hukushima, K.; Nemoto, K. *J. Phys. Soc. Jpn.* **1996**, 65.
12. Maisuradze, G. G.; Thompson, D. L.; Wagner, A. F.; Minkoff, M. *J. Chem. Phys.* **2003**, 119.
13. Kawano, A.; Guo, Y.; Thompson, D. L.; Wagner, A. F.; Minkoff, M. *J. Chem. Phys.* **2004**, 120.
14. Ischtwan, J.; Collins, M. A. *J. Chem. Phys.* **1994**, 100.

Downloaded by UNIV OF GUELPH LIBRARY on May 28, 2012 | http://pubs.acs.org
Publication Date (Web): February 6, 2012 | doi: 10.1021/bk-2012-1094.ch003

15. Feynman, R. P. *Statistical Mechanics*; Addison-Wesley: Redwood City, CA, 1972.
16. Pollock, E. L.; Ceperley, D. M. *Phys. Rev. B* **1984**, 30.
17. Sprik, M.; Klein, M. L.; Chandler, D. *Phys. Rev. B* **1985**, 31.
18. Duane, S.; Kennedy, A. D.; Pendleton, B. J.; Roweth, D. *Phys. Lett. B* **1987**, 195.
19. Mehlig, B.; Heermann, D. W.; Forrest, B. M. *Phys. Rev. B* **1992**, 45.
20. Werner, H.-J.; Knowles, P. J.; Lindh, R.; Manby, F. R.; Schütz, M.; et al. *MOLPRO*, version 2008.1; a package of *ab initio* programs.
21. Segmented Gaussian Basis Set. http://setani.sci.hokudai.ac.jp/sapporo/.
22. Tachikawa, M.; Shiga, M. *J. Chem. Phys.* **2004**, 121.
23. Tuckerman, M. E.; Berne, B. J.; Martyna, G. J.; Klein, M. L. *J. Chem. Phys.* **1993**, 99.
24. Shiga, M.; Tachikawa, M.; Miura, S. *J. Chem. Phys.* **2001**, 115.
25. Cao, J.; Martyna, G. J. *J. Chem. Phys.* **1996**, 104.
26. Frantz, D. D.; Freeman, D. L.; Doll, J. D. *J. Chem. Phys.* **1990**, 93.
27. Berg, B. A.; Neuhaus, T. *Phys. Lett. B* **1991**, 267.

Downloaded by UNIV OF GUELPH LIBRARY on May 28, 2012 | http://pubs.acs.org
Publication Date (Web): February 6, 2012 | doi: 10.1021/bk-2012-1094.ch003

Chapter 4

Recent Results in the Exact Treatment of Fermions at Zero and Finite Temperature

Norm M. Tubman,*,1,2 Jonathan L. DuBois,[1] and Berni J. Alder[1]

[1]Lawrence Livermore National Laboratory, Livermore, CA 94550
[2]Department of Physics, University of Illinois, Urbana-Champaign,
Champaign, Illinois 61820
***E-mail: normantubman2015@u.northwestern.edu**

We present release-node quantum Monte Carlo simulations of the first row diatomic molecules and assess how accurately their ground state energies can be obtained with current computational resources. An explicit analysis of the fermion-boson energy difference shows a strong dependence on the nuclear charge, Z, which in turn determines the growth of the variance of the release-node energy. We show that efficiency gains from maximum entropy analysis are modest and that extrapolation to the ground state is tractable only for the low Z elements. For finite temperatures we discuss what can be gleaned from the structure of permutation space for interacting Fermi systems. We then demonstrate improved efficiency in the exact path integral Monte Carlo treatment of liquid ^{3}He by using importance sampling to deemphasize the contribution of long permutation cycles to the partition function.

Exact Methods at T=0

The fundamental goal in the field of *ab initio* simulations is to perform electronic calculations to high accuracy or, even better, exactly. To simulate exact methods an exponentially increasing amount of resources seems to be needed, and thus in practice system sizes are often severely restricted. For example, two well-known methods which are in principle exact are configuration interaction and density functional theory. Here, the exponential computational complexity is manifest in the formulation of configuration interaction (*1*), and is less obvious in

In Advances in Quantum Monte Carlo; Tanaka, S., et al.;
ACS Symposium Series; American Chemical Society: Washington, DC, 2012.

DFT where it arises as a problem in generating exact functionals (*2*). As a result, practical uses of these algorithms do not yield exact results.

Release-node quantum Monte Carlo (RN-QMC) is a simulation method that allows the eigenstates of a Hamiltonian to be sampled without any systematic bias. The method is computationally expensive, however, and there are significant limitations to what can feasibly be simulated. For quantum Monte Carlo (QMC) calculations this has lead to the development of the popular but approximate fixed-node diffusion Monte Carlo (FN-DMC). Despite the possibility of improved accuracy, RN-QMC has only been used in a relatively limited number of simulations. Nonetheless there have been some notable applications and algorithmic developments.

One such application in which RN-QMC has been successful is the electron gas (*3*) where hundreds of electrons have been simulated without convergence problems. Convergence of a RN-QMC calculation is dependent on two decay parameters given by $\tau_1 = E^F_0, E^B_0$, which determines the imaginary-time growth of the variance, and $\tau_2 = E^F_1, E^B_0$, which determines the slowest imaginary-time decay of the excited antisymmetric components relative to the fermion ground state. The energies E^F_0, E^B_0, and E^F_1 are the fermion ground state, the boson ground state and the first excited fermion state, respectively. Hamiltonians in which the fermion-boson energy gap is small are well suited for RN-QMC simulations, and the free electron gas is one such Hamiltonian. Nuclear charge centers change the situation significantly such that relatively small atoms have large fermion-boson energy gaps. The largest molecular RN-QMC calculations to date have been performed on systems of around 10 electrons. However, even in these cases, convergence is not always attained. In the first RN-QMC calculations of molecules (*4*) several systems were simulated including H_2O and Li_2 molecules. Later RN-QMC calculations included systems such as HF (*5*) , LiH (*6*), and H_2+H (*7*) in which RN-QMC was able to reach higher accuracies as a result of algorithmic modifications and increased computational resources. Our goal is to consider the range of Hamiltonians that can be practically simulated with RN-QMC with current computational power and modern algorithms. In particular we have applied the method to the simulation of the first row dimers with an accuracy goal of 10^{-3} [a.u.].

Released Node Quantum Monte Carlo

We can understand how RN-QMC achieves exact results by considering the eigenfunction expansion of the imaginary time propagator

$$e^{-t(H-E_T)} = \sum_i e^{-t(E_i-E_T)} |\Phi_i\rangle\langle\Phi_i|. \tag{1}$$

For $E_T = E_0$ the asymptotic, $t \longrightarrow \infty$, limit of this operator gives the ground state of the Hamiltonian. Technically a RN-QMC calculation is only converged in this limit, however in practice we consider a RN-QMC calculation converged when the slope of the release-node energy estimator is zero to within the statistical error. This occurs when the standard error of our energy estimate at a given imaginary time is larger than the final energy difference to be decayed in the asymptotic limit. As imaginary time increases with repeated application of the propagator in equation (*1*), all excited states decay relative to the ground state. If a trial function, $\Psi_T(X)$, is used for importance sampling, the asymptotic distribution will be:

$$\lim_{t\to\infty}\sum_i e^{-t(E_i-E_T)}|\Phi_i\rangle\langle\Phi_i|\psi_T\rangle \approx e^{-t(E_0-E_T)}|\Phi_0\rangle\langle\Phi_0|\psi_T\rangle. \qquad (2)$$

For a standard molecular Hamiltonian the ground state wave function is a boson state and the fermion ground state is an excited state of the Hamiltonian. Like all other excited states, it decays exponentially relative to the ground state with application of the imaginary-time propagator. In certain cases we can accurately measure the fermion ground state as it decays in imaginary time. To determine the fermion ground state we can make a projection onto the antisymmetric subspace during this decay process.

The antisymmetric projection is problematic for many Hamiltonians. The release-node method is an example of a transient algorithm since the fermion ground state is decaying exponentially in the limit of large imaginary time. The release process is initiated with the introduction of a nodeless guide wave function, $\Psi_G(X)$, such that the walkers will equilibrate to the boson ground state. During this process an antisymmetric trial wave function is used to project out the antisymmetric signal. This causes a sign problem that manifests in the simulation as exponentially growing noise in the release-node energy estimate.

The release-node energy can be calculated in a similar form to the FN-DMC

$$E_0^{RN} = \frac{\sum_i W_i R(\mathbf{X}_i) E_L^T(\mathbf{X}_i)}{\sum_i W_i R(\mathbf{X}_i)}. \qquad (3)$$

This estimator involves the sum of positive and negative terms, given by the sign of the trial wave-function as seen in the term $R = \Psi_T(X)/\Psi_G(X)$, which is the reweighting factor for the guiding wave function. The weight of the *i*th walker is calculated as

$$W = \prod_j e^{-t/2(E_L^G(\mathbf{R}_j)+E_L^G(\mathbf{R}_{j+1}))} \qquad (4)$$

where the product is over all previous positions the walker has traversed. The terms E_L^T and E_L^G are the local energies of the trial wave-function and the guiding function respectively. The form of the local energy is given by $E_L^{G,T} = \Psi^{-1}_{G,T} H\Psi_{G,T}$. It can be shown that the variance of the transient energy E_0^{RN} is proportional to a growing exponential with imaginary time (*8*, *9*):

$$\sigma^2(E_0^{RN}) \propto e^{2t(E_0^F - E_0^B)}. \qquad (5)$$

The release-node estimate for the energy will start decaying from the FN-DMC energy, and eventually it will become flat, while the variance will continue to grow as given in equation (4). The convergence rate from the FN-DMC energy to the fermion ground state energy is different for each of the component eigenstates present in the fixed-node wave function. Ideally one would like a fast decay of the fermion excited states, and a slow increase of the variance, i.e. $(E_1^F - E_0^F) \gg (E_0^F - E_0^B)$. In this ideal situation one can hope to sample E_0^F at a large imaginary time with relatively small variance.

Fermion-Boson Gaps

The actual cost of a RN-QMC calculation is somewhat complicated by the introduction of a trial wave function. A good trial wave function can significantly decrease the contamination from the excited states, improving the convergence of the release algorithm. In the limit that the trial wave function has the correct nodal structure, FN-QMC gives the ground state energy and RN-QMC will be flat as a function of imaginary time. Therefore generating high quality RN-QMC results involves a balance of computing the best wave function possible and running release-node for as much imaginary time as possible. Once a trial wave function is optimized and put into a release-node calculation it is the growth of the variance as a function of imaginary time that prevents a calculation from converging. It can be seen from equation (5) that this is independent of the trial wave function.

With this behavior of the variance it is important that the excited states decay away before the simulation is overwhelmed with noise. For the first-row dimers, excluding Li_2, we have estimated the amount of time needed to converge our starting FN-DMC starting wave functions[11] to an accuracy greater than 10^{-3} [a.u.] will be greater than 1 [a.u.]$^{-1}$. A more accurate estimate of the convergence times is dependent on the magnitude of the excited state components of the FN-DMC wave function. Since the rate of growth of the variance is determined by the fermion-boson energy gap, it is important to understand how a Hamiltonian influences this energy gap. We recently made some calculations of the fermion-boson energy differences for the first-row dimers shown in Table I. The fermion energies are calculated from FN-DMC and the boson energies are calculated with unrestricted Diffusion Monte Carlo (DMC) using nodeless guiding wave functions. The boson energies are measured without any systematic errors, while the fermion energies have systematic errors corresponding to errors in the nodal surfaces. These systematic errors are estimated to be much smaller than 1 [a.u.] and are much smaller than the scale of the fermion-boson energy differences. The fermion-boson energy differences cover a range of about two orders of magnitude across the first-row dimers. As previously mentioned, we would like to simulate at least 1 [a.u.]$^{-1}$ of imaginary time during the release process, however the size of these fermion-boson gaps imply that the variance will grow to intractable sizes for most of the first row dimers well before 1 [a.u.]$^{-1}$ of simulation time.

In a recent RN-QMC study of the first row dimers (*10*), for a given set of trial wave functions (*11*), we were able to achieve an accuracy of 10^{-4} [a.u.] for Li_2, however we were not able to achieved our desired accuracy of 10^{-3} for any of the other first row dimers.

Table I. Fermion-Boson energy gaps for the second row dimers. Boson ground states are measured without any systematic errors with DMC, while the fermion energies are taken as the estimated exact values from reference (*11*). All energies are in Hartree.

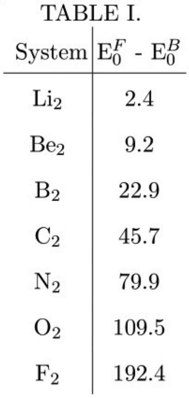

TABLE I.

System	E_0^F - E_0^B
Li_2	2.4
Be_2	9.2
B_2	22.9
C_2	45.7
N_2	79.9
O_2	109.5
F_2	192.4

Improving Release Node

While performing RN-QMC on better wave functions will always lead to better results, there are several methods have been proposed to reduce the computational cost of RN-QMC – some of which have the promise of removing the exponential scaling of the algorithm. In this section we consider a few of the more promising techniques which are imaginary time projections and walker cancellation.

Projection techniques are based on sampling quantities during the release process, other than the RN-QMC energy estimator, to project out the ground state energy. It is known that some of these quantities, which are called imaginary time correlators, have simple imaginary-time dependence of the eigenvalue spectrum. After generating samples of a correlator of interest, we can fit the data and extract out the ground-state energy. The benefit of such an approach is that a highly accurate estimate of the ground-state energy might be possible with a limited amount of imaginary-time data. The idea of fitting imaginary time data is a general concept that has been applied very broadly in computational physics and other fields (*12*). As far as applications of this for RN-QMC calculations, only the LiH molecule and various model Hamiltonians have tested these ideas (*6*, *13*, *14*).

Projecting out the ground state energy with this imaginary time data is equivalent to performing an inverse Laplace transform. The inverse Laplace transform is known to be sensitive to noisy data and we used a Maximum Entropy technique in our calculations to reduce our sensitivity to noise. We showed significantly better results than our standard release-node calculations (*10*), as we were able to generate ground state energies for Li_2, Be_2, and B_2 with this approach. However, due to the nature of the inverse Laplace transform, our results were too noisy to properly project out ground state energies for the rest of the first row dimers. Our analysis suggests that these projection techniques that rely on inverse Laplace techniques, although more efficient that standard RN-QMC, do not get around the exponential scaling of the problem and practically can not be applied to larger systems.

Cancellation techniques provide an alternative route to improving on the efficiency of the RN-QMC method. It has been demonstrated that, by allowing walkers of opposite sign to annihilate each other, cancellation can slow down the growth rate of the error. To date, this approach has been applied to a number of problems with varying success (*15*). In addition, cancellation has also been applied in molecular calculations for linear H-H-H and H_2 (*16*). A recent study demonstrating promising behavior of the technique in high dimensional systems is worth noting (*17*).

Exact Methods at Finite Temperature

Path integral quantum Monte Carlo (PIMC) methods have provided significant insights into the low temperature properties of bosonic quantum liquids and solids (see e.g. (*18*)). And while the approach can, in principle, be applied to simulate the full many-body partition function for fermions as well, a sign problem occurs for temperatures below the $T \rightarrow \infty$ limit. As a result, enforcement of Fermi symmetry for all but the smallest finite temperature systems has in practice required the invocation of an uncontrolled approximation in the form of a restriction on the phase space of the path integral in order to prevent sign changes (*19*, *20*). In this section we discuss what is known about the nature of the sign problem at finite T and describe an approach for reducing its effects.

PIMC methods work by sampling a product of approximate high temperature (short imaginary time) density matrices (Green functions) $\exp[-\beta\hat{H}] = \exp[-(\beta/M)\hat{H}]^M$ just as in ground state QMC methods like DMC. The differences between the methods arise mainly from the fact that sampling of a fixed finite temperature ensemble imposes a periodicity on the permuted coordinates in β, i.e.

$$\rho(\mathbf{R};\beta) \propto \sum_{\mathcal{P}} (-1)^{\mathcal{P}} \langle \mathbf{R}|e^{-\frac{\beta}{M}\mathcal{H}}|\mathbf{R}_1\rangle\langle \mathbf{R}_1|e^{-\frac{\beta}{M}\mathcal{H}}|\mathbf{R}_2\rangle \ldots \langle \mathbf{R}_{M-1}|e^{-\frac{\beta}{M}\mathcal{H}}|\mathcal{P}[\mathbf{R}]\rangle. \tag{6}$$

where the sum is over the symmetric group and $P[\mathbf{R}]$ represents a permutation of the many-body coordinate $\mathbf{R}$. In ground state methods this periodicity formally only exists at $\mathbf{R}_{\beta\rightarrow\infty}$, and antisymmetry may be imposed by an explicit projection at each time slice as described above. In canonical PIMC, however, the β periodicity of $P[\mathbf{R}]$ requires that permutations be sampled explicitly and so configuration space typically consists of complete paths $Y=\{\mathbf{R},\mathbf{R}_1,\mathbf{R}_2,\ldots,\mathbf{R}_{M-1}\}$ where $\mathbf{R}_{M-1}$ must be connected to $P[\mathbf{R}]$ by the high temperature density matrix $\exp[-(\beta/M)\hat{H}]$. The sum over permutations in e.q. (6) is clearly the source of the sign problem in finite temperature PIMC. However, the explicit representation of permutations as linked polymers and in particular the connection between the length of a permutation (i.e. the number of particles participating in a single closed loop) and the kinetic energy leads to some interesting and useful observations about the structure of permutation space and, consequently, the finite T sign problem as well.

The Structure of Permutation Space

While there are N! possible permutations of N particles, the symmetry group can be further organized into subsets of topologically equivalent diagrams (*21*, *22*). Figure 1 shows representative members from the five equivalences classes of the Symmetric group for four particles, S_4. It is easy to see that if each of these classes was equally probable, the sum over all of them would indeed be zero and, as a result, the antisymmetric 'signal' embedded in the partition function would disappear. At any finite temperature, however, each equivalent permutation sector will have a different mean energy and therefore a different probability and the total contribution to the antisymmetrized partition function will be nonzero. For this reason one might be so bold as to say that at finite temperature there is not a sign problem but merely a "sign annoyance."

In practice, while the number of equivalence classes grows roughly as $N^{7/2}$ (*23*) – much more slowly than the N! number of enumerated permutations -- the contribution to the partition function of neighboring high order sectors (i.e. those consisting of long permutation cycles) becomes nearly identical at even moderately low temperatures. As a result, if the partition function is sampled directly, most of the simulation time will be spent generating configurations that will ultimately cancel each other out.

In addition to recognizing the relative importance of low order permutation sectors, it is instructive to examine the connection between the order of a permutation sector and the mean kinetic energy. Intuitively, long permutations impose a weaker constraint on the paths of participating particles since a path consisting of ν particles only need return to its starting point after imaginary time $\nu\beta$. As a consequence, in an isotropic system longer permutation cycles will, on average, have lower kinetic energy than short ones. For the noninteracting gas this connection is especially clear as the contribution to the partition function from ν permuting particles is equivalent to the single particle partition function at a lower temperture $Z_1(\nu/T)$. As a result, the mean energy of paths in each permutation sector is monotonically decreasing with the order of the sector. For fixed particle number, the virial theorem tells us that this trend must hold for systems with pairwise interactions as well.

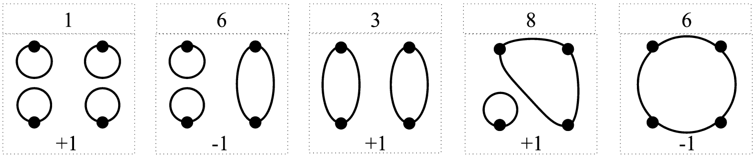

Figure 1. Diagramatic representation of the equivalence classes of the symmetric group for 4 particles, S_4, the number of elements in each class (top), and the sign of the contribution of members of each class to the partition function (bottom).

Motivated by these observations we have recently explored the possibility of improving the efficiency of PIMC simulations applied to Fermi systems by using importance sampling to limit the time spent evaluating nearly degenerate permutation classes. The approach is relatively straightforward. Starting with the recently developed continuous-space worm algorithm (*24*, *25*) to efficiently sample permutation space, we employ standard importance sampling techniques to modify the probability of moves that change the permutation sector. Sampling of long permutation cycles is penalized by reducing the probability of attempting moves that will extend the length of a permutation while the acceptance probability of such moves is increased to maintain detailed balance. The net result is that low order permutation sectors (those with only a few short permutation cycles) are sampled a great deal and high orders very rarely. In addition, the energy of each equivalence class is binned separately so that the final expectation value for the energy is taken by summing over the mean energy in each class multiplied by the probability of being in the class

$$\langle E\rangle = \sum_g \mathrm{S}gn[g](\bar{E}_g+\sigma_E)(\bar{n}_g+\sigma_n) \approx \sum_g \mathrm{S}gn[g]\tilde{E}[g]\tilde{n}[g] + \tilde{\sigma}_E\tilde{\sigma}_n. \qquad (7)$$

Finally, using the knowledge that both the mean energy per sector E_g and the probability of occupying each sector n_g are monotonically decreasing functions, an improved estimate of the mean energy is obtained by fitting E_g and n_g to smoothly decaying functions E[g] and n[g]. The $\tilde{\sigma}_{E,n}$ in eq (7) represent the statistical error in the energy and probability density respectively in each sector while $\tilde{\sigma}_{E,n}$ are the error resulting from fitting energies and probability density over all sectors using a model. This step can in principle introduce a systematic error but it is not strictly necessary. We also note that since sampling is performed in the grand canonical ensemble, the chemical potential, μ, is a parameter. In the results for ^{3}He below we have fixed μ so as to match the known experimental density. A more detailed account of this "exchange truncated grand canonical PIMC method" will be presented elsewhere (*26*).

Results of a simulation of N=66 ^{3}He particles using the Aziz potential (*27*) and the approach outlined above are shown in Figure 2. Our results for the temperature dependence of the energy are in very good agreement with experiment. In contrast, it can be seen that the restricted path approach (*19*) suffers from a comparatively large systematic error. Also of note is that we are able to obtain results well below the Fermi temperature of ^{3}He despite the fact that, in principle, exact treatment of the partition function requires sampling of $66! \sim 10^{92}$ permutations and ~6000 equivalent permutation groups.

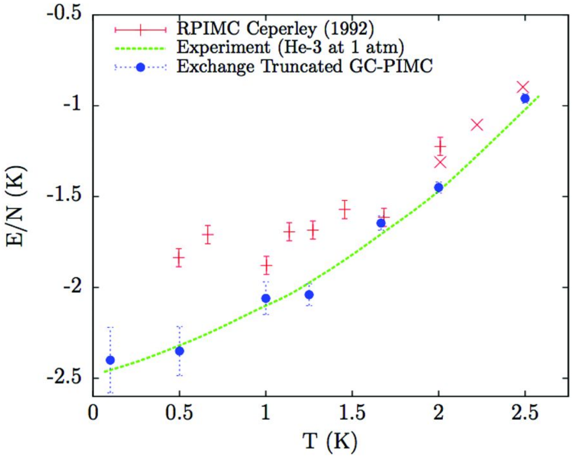

Figure 2. Results of Exchange Truncated Grand Canonical PIMC applied to liquid ^{3}He. Our results (solid circles) agree well with experimental data (dashed line) down to temperatures well below the ^{3}He Fermi temperature. The improvement over the approximate restricted path integral method (+ symbols), a 25% difference in energy per particle at 0.5 K, is evident.

Conclusion

We have applied the RN-QMC method to the first row dimmers in an attempt to quantify the level of accuracy obtainable for all-electron chemical systems with this approach using current resources. Our results indicate that release node projections can be converged for up to ~ 10 electrons with an accuracy of at least 10^{-3}. We find that while maximum entropy analysis of the imaginary time decay significantly improves estimates of the ground state energy, it does directly not solve the problem of the poor scaling of the computational cost of RN-QMC for a fixed error bar with Z. For finite temperatures we reviewed some of what is known about the nature of the sign problem and presented results of a new scheme for taking advantage of the structure in permutation space by neglecting contributions from long permutation cycles. An open area for future research in this area involves the generalization of our approach to inhomogeneous systems.

References

1. Szabo, A.; Ostlund, N. *Modern Quantum Chemistry*; Dover Publications: Mineola, New York, 1982.
2. Schuch, N.; Verstraete, F. *Nat. Phys.* **2009**, *5*, 732.
3. Ceperley, D. M.; Alder, B. J. *Phys. Rev. Lett.* **1980**, *45*, 566.
4. Ceperley, D. M.; Alder, B. J. *J. Chem. Phys.* **1984**, *81*, 5833.
5. Lüchow, A.; Anderson, J. B. *J. Chem. Phys.* **1996**, *105*, 4636.
6. Caffarel, M.; Ceperley, D. M. *J. Chem. Phys.* **1992**, *97*, 8415.
7. Diedrich, D. L.; Anderson, J. B. *J. Chem. Phys.* **1994**, *100*, 8089.

8. Assaraf, R.; Caffarel, M.; Khelif, A. *J. Phys. A* **2007**, *40*, 1181.
9. Morgenstern, I. *Z. Phys. B* **1989**, *77*, 267.
10. Tubman, N. M.; DuBois, J. L; Hood, R. Q.; Alder, B. J. *J. Chem. Phys.* **2011**, *135*, 184109.
11. Filippi, C.; Umrigar, C. J. *J. Chem. Phys.* **1996**, *105*, 213.
12. Jarrell, M.; Gubernatis, J. E. *Phys. Rep.* **1996**, *269*, 133.
13. Caffarel, M.; Gadea, M.; Ceperley, D. M. *Europhys. Lett.* **1991**, *16*, 249.
14. Blume, D.; Lewerenz, M.; Niyaz, P.; Whaley, K. B. *Phys. Rev. E* **1997**, *55*, 3664.
15. (a) Arnow, D. M.; Kalos, M. H. *J. Chem. Phys.* **1982**, *77*, 5562. (b) Kalos, M. H. *Phys. Rev. E* **1996**, *53*, 5420. (c) Zhang, S.; Kalos, M. H. *Phys. Rev. Lett.* **1991**,*67*, 3074. (d) Kalos, M. H.; Pederiva, F. *Phys. Rev. Lett.* **2000**, *85*, 3547.
16. Anderson, J. B.; Traynor, C. A.; Boghosian, B. M. *J. Chem. Phys.* **1991**, *95*, 7418.
17. Arias de Saavedra, F.; Kalos, M. H.; Pederiva, F. *Mol. Phys.* **2011**, *109*, 2797.
18. Ceperley, D. M. *Rev. Mod. Phys.* **1995**, *67*, 279.
19. Ceperley, D. M. *Phys. Rev. Lett.* **1992**, *69*, 331.
20. Ceperley, D. M. In *Monte Carlo and Molecular Dynamics of Condensed Matter Systems*; Binder, K., Ciccotti, G., Eds.; Editrice Compositori: Bologna, Italy, 1996.
21. Feynman, R. P. *Statistical Mechanics*; W. A. Benjamin: New York, 1972.
22. Elliot, J. P.; Dawber, P. G. *Symmetry in Physics*; Macmillan: London, 1979.
23. Lyubartsev, A. P.; Vorontsov-Velyaminov, P. N. *Phys. Rev. A* **1993**, *48*, 4075.
24. Boninsegni, M.; Prokof'ev, N. V.; Svistunov, B. V. *Phys. Rev. Lett.* **2006**, *96*, 070601.
25. Boninsegni, M.; Prokof'ev, N. V.; Svistunov, B. V. *Phys. Rev. E* **2006**, *74*, 036701.
26. DuBois, J. L; Alder, B. J. **2012**, in preparation.
27. Aziz, R. A.; Nain, V. P. S.; Carley, J. S.; Taylor, W. L.; McConville, G. T. *J. Chem. Phys.* **1979**, *70*, 4330.

Downloaded by CORNELL UNIV on May 27, 2012 | http://pubs.acs.org
Publication Date (Web): February 6, 2012 | doi: 10.1021/bk-2012-1094.ch005

Chapter 5

Quantum Monte Carlo Facing the Hartree-Fock Symmetry Dilemma: The Case of Hydrogen Rings

Peter Reinhardt,*,[1] Julien Toulouse,[1] Roland Assaraf,[1] C. J. Umrigar,[2] and Philip E. Hoggan[3]

**[1]Laboratoire de Chimie Théorique,
Université Pierre et Marie Curie and CNRS, 4 place Jussieu,
75252 Paris, France
[2]Laboratory of Atomic and Solid State Physics, Cornell University,
Ithaca, New York 14853, U.S.A.
[3]LASMEA, Université Blaise Pascal and CNRS, 24 avenue des Landais,
63177 Aubière, France
*E-mail: Peter.Reinhardt@upmc.fr. Fax: +33 1 44 27 41 17.**

When using Hartree-Fock (HF) trial wave functions in quantum Monte Carlo calculations, one faces, in case of HF instabilities, the HF symmetry dilemma in choosing between the symmetry-adapted solution of higher HF energy and symmetry-broken solutions of lower HF energies. In this work, we have examined the HF symmetry dilemma in hydrogen rings which present singlet instabilities for sufficiently large rings. We have found that the symmetry-adapted HF wave function gives a lower energy both in variational Monte Carlo and in fixed-node diffusion Monte Carlo. This indicates that the symmetry-adapted wave function has more accurate nodes than the symmetry-broken wave functions, and thus suggests that spatial symmetry is an important criterion for selecting good trial wave functions.

In Advances in Quantum Monte Carlo; Tanaka, S., et al.;
ACS Symposium Series; American Chemical Society: Washington, DC, 2012.

I. Introduction

It is well known that the symmetry-adapted solution of the nonlinear Hartree-Fock (HF) equations of an electronic system is sometimes unstable. An unstable solution corresponds to a saddle point of the energy as a function of the orbital parameters, and breaking of space and/or spin symmetries of the wave function then necessarily leads to one or several lower-energy HF solutions. The stability conditions of the HF equations were first formulated by Thouless (*1*), and the different instabilities were first categorized by Čiček and Paldus (*2–7*). For closed-shell systems, one may encounter "singlet instabilities" when only space symmetry is broken, and "triplet (or nonsinglet) instabilities" when spin symmetry is also broken. There is thus a symmetry dilemma (*8*) in choosing between the symmetry-adapted wave function of higher HF energy and a symmetry-broken wave function of lower HF energy, in particular as a reference for a post-Hartree-Fock calculation.

A particularly spectacular example is provided by closed-shell hydrogen rings H_{4n+2} with equal bond lengths (*9*) (see, also, ref. (*10*)). The metallic symmetry-adapted HF solution exhibits singlet instabilities for sufficiently large numbers of hydrogen atoms, and one can obtain insulating symmetry-broken HF solutions with orbitals localizing on either the atoms or the bonds. However, both Møller-Plesset perturbation theory or linearized coupled cluster doubles theory (also called CEPA--0 or DMBPT–∞) give a lower total energy when starting from the symmetry-adapted solution than when starting from the symmetry-broken solutions, which casts doubts on the physical significance of the symmetry-broken solutions. Of course, the symmetry dilemma would be removed with a full configuration-interaction calculation which must give one unique solution, independent of the orbitals used.

Quantum Monte Carlo (QMC) approaches are alternatives to the traditional quantum chemistry methods (*11–13*). The two most commonly used variants are variational Monte Carlo (VMC) which simply evaluates the energy of a flexible trial wave function by stochastic sampling, and diffusion Monte Carlo (DMC) which improves upon VMC by projecting the trial wave function onto the exact ground state, while keeping the nodes of the wave function fixed. The most common form of the trial wave function is a Jastrow factor multiplied by a fixed HF determinant. If a system exhibits HF instabilities, then QMC also faces the symmetry dilemma in choosing between different HF wave functions. Indeed, different HF wave functions necessarily lead to different energies in VMC, but also in DMC since the nodes of these HF wave functions are generally different. This symmetry dilemma in DMC is only due to the fixed-node approximation, since without this approximation DMC would give one unique solution, independent of the orbitals used.

In this work, we study the impact of the HF symmetry dilemma for QMC in hydrogen rings H_{4n+2}. In Sec. II, we recall the HF symmetry-breaking problem in these systems, and discuss the effect of using a Slater basis versus a Gaussian basis. In Sec. III, we explain the QMC methodology and report our VMC and DMC results. Our conclusions are summarized in Sec. IV.

Downloaded by CORNELL UNIV on May 27, 2012 | http://pubs.acs.org
Publication Date (Web): February 6, 2012 | doi: 10.1021/bk-2012-1094.ch005

Downloaded by CORNELL UNIV on May 27, 2012 | http://pubs.acs.org
Publication Date (Web): February 6, 2012 | doi: 10.1021/bk-2012-1094.ch005

II. Hartree-Fock Symmetry Breaking

In previous studies (*9*, *14*), the electronic structure of periodic rings of 4n+2 evenly spaced hydrogen atoms (with a fixed distance of $r_{H-H} = 0.74747$ Å) has been investigated. The number of hydrogen atoms is restricted to 4n+2 in order to obtain a possible closed-shell single-determinant solution with 2n+1 occupied orbitals. The symmetry-adapted HF wave function has a metallic character and can be expressed with either delocalized canonical orbitals or localized Wannier orbitals. The canonical orbitals are doubly degenerate, except for the lowest-energy one, and in a minimal basis the orbital coefficients are fixed by the cyclic symmetry. Besides the symmetry-adapted (SA) solution, two different symmetry-broken HF solutions of lower energy can be obtained beyond critical ring sizes, when using unit cells of 2 hydrogen atoms. One solution corresponds to orbitals localized on hydrogen atoms and is referred to as the symmetry-broken atom-centered (SB-AC) solution, while the other corresponds to orbitals localized on bonds and is referred to as the symmetry-broken bond-centered (SB-BC) solution. The SB-BC solution is the lowest one in energy and corresponds to a true minimum. The three solutions can be schematically described as ···H···H···, $\cdots H^{+}\cdots H^{-}\cdots$, and ···H–H···. In each case, the symmetry breaking is accompanied by an opening of an energy gap between occupied and virtual orbitals, and orbitals decay much more rapidly than for the symmetry-adapted solution, in agreement with the theoretical result of Kohn (*15*).

In order to distinguish the three different wave functions, one may look at the one-particle density matrix P

$$P_{\alpha\beta} = 2\sum\nolimits_{i \in occ.} c_{\alpha i}\, c_{\beta i}$$

This equation contains the expansion coefficients $c_{\alpha i}$ of the occupied molecular orbitals $\varphi_i(\vec{r})$

$$\varphi_i(\vec{r}) = \sum\nolimits_{\alpha.} c_{\alpha i}\ \chi_\alpha(\vec{r})$$

expanded in a minimal set of atom-centered basis functions, i.e. one single basis function $\chi_\alpha(\vec{r})$ per hydrogen atom. As depicted in Figure 1, for the SA solution, we see equal elements on the diagonal and the sub-diagonals of the density matrix. For the SB-AC solution, an alternation of element values on the diagonal of the density matrix is obtained, but equal elements on the first sub-diagonal, and for the SB-BC solution we have equality of the diagonal elements and alternation on the first sub-diagonal.

Downloaded by CORNELL UNIV on May 27, 2012 | http://pubs.acs.org
Publication Date (Web): February 6, 2012 | doi: 10.1021/bk-2012-1094.ch005

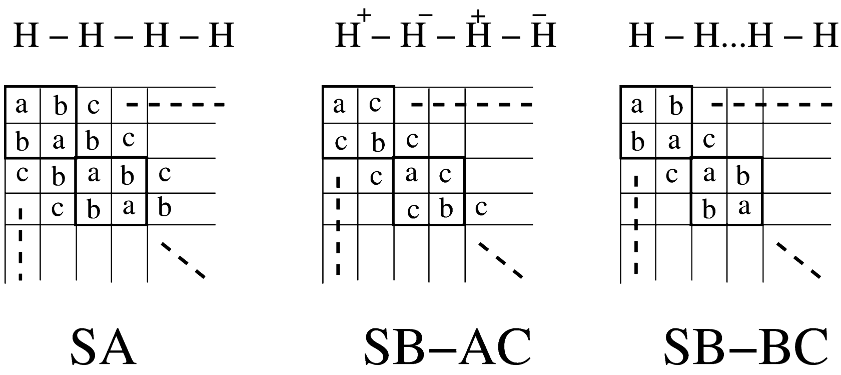

Figure 1. Structure of the one-particle density matrix for the HF symmetry-adapted (SA) and symmetry-broken (SB-AC and SB-BC) solutions.

In ref. (*9*), a minimal Gaussian basis set (five *s* Gaussian functions contracted to one single basis function for each hydrogen atom) was used. However, Gaussian basis functions are not appropriate for all-electron QMC calculations. They give large statistical fluctuations due to their incorrect vanishing gradient at the nuclear positions. It is thus much preferable to use Slater basis functions which correctly have a non-zero gradient on the nuclei and an exponential decay at large distance. In this work, we use a minimal Slater basis set (one *1s* Slater function on each hydrogen atom) with an exponent of 1.17, which is smaller than the optimal exponent of 1.24 for an isolated H_2 molecule as we aim at describing systems with diffuse electron distributions and still keep a single fixed exponent. Spin-restricted HF (and MP2) calculations were performed with an experimental code for ring systems, employed already for the previous studies (*16*). The necessary integrals over Slater functions have been calculated with the program SMILES (*17*). In order to obtain the symmetry-broken HF solutions, we start from a set of localized Wannier orbitals describing either an ionic situation or an explicit bond in the two-atom unit cell, and use an iterative configuration interaction procedure using singly excited determinants (*18*, *19*) instead of diagonalizing a Fock operator to avoid complete delocalization of the molecular orbitals.

Table I reports the HF energy differences between the symmetry-broken solutions and the symmetry-adapted one for the Gaussian basis set of ref. (*9*) and the Slater basis set of the present study. With the Gaussian basis set, the departure of the SB-BC and SB-AC solutions from the SA solution occurs for H_{46} and H_{54} rings, respectively. With the Slater basis set, the onset of symmetry breaking takes place for larger rings, i.e. for H_{50} and H_{62} for SB-BC and SB-AC, respectively. In addition, for a fixed ring size, the lowering in energy of the symmetry-broken solutions is smaller with the Slater basis set. This is an indication that the Slater basis is better than the Gaussian basis, since the amount of symmetry breaking is usually larger for poorer wave functions. The HF total energies are indeed lower with the Slater basis, for example for H_{42}, the (SA) energy is –0.950252 hartree with the Gaussian basis and –0.997003 hartree with the Slater basis. As an additional verification of the usefulness of Slater functions, we can look at Kato's cusp condition (*20*) at the nuclear positions $\vec{r_n}$:

$$\frac{1}{2}\ \frac{|\vec{\nabla}\rho(\vec{r}_n)|_{av.}}{\rho(\vec{r}_n)} = Z_n$$

where $\rho(\vec{r}_n)$ and $|\vec{\nabla}\rho(\vec{r}_n)|_{av.}$ are the density and the spherical average of density gradient at the nuclear positions, and Z is the nuclear charge. For example, for the H_{86} ring, we find 1.009 for SA, 1.012 for SB-BC, and 1.034 and 0.980 for SB-AC, close to the ideal value of Z = 1.

Table I. HF energy differences of H_{4n+2} rings, per H_2 cell in mhartree, between the symmetry-broken solutions (SB-AC and SB-BC) and the symmetry-adapted (SA) one, for the Gaussian and Slater basis sets

	Gaussian basis		*Slater basis*	
4n+2	$E_{SB\text{-}AC} - E_{SA}$	$E_{SB\text{-}BC} - E_{SA}$	$E_{SB\text{-}AC} - E_{SA}$	$E_{SB\text{-}BC} - E_{SA}$
42	—	—	—	—
46	—	−0.00258	—	—
50	—	−0.03555	—	−0.00199
54	−0.00115	−0.08933	—	−0.02739
58	−0.01900	−0.15116	—	−0.06961
62	−0.04980	−0.21440	−0.00080	−0.11914
66	−0.08678	−0.27565	−0.01223	−0.17074

Downloaded by CORNELL UNIV on May 27, 2012 | http://pubs.acs.org
Publication Date (Web): February 6, 2012 | doi: 10.1021/bk-2012-1094.ch005

III. Quantum Monte Carlo Study

QMC methods are considered as producing benchmarks in quantum chemistry, approaching the electronic-structure problem through a drastically different way than common wave-function-based methods or density-functional theory. As QMC methods often rely of a HF trial wave function, it is interesting to check their sensitivity to HF symmetry breaking. We start by giving a brief overview of the VMC and DMC methods employed in this work.

A. Brief Overview of VMC and DMC

We consider Jastrow-Slater trial wave function of the form

$$\Psi_T(\mathbf{R}) = \mathrm{J}(\mathbf{R})\,\Phi\,(\mathbf{R})$$

where **R** designates the electron coordinates, $\Phi\,(\mathbf{R})$ is a HF determinant and $\mathrm{J}(\mathbf{R}) = e^{f(r_{ij},r_{Ii})}$ is a Jastrow correlation factor depending explicitly on the electron-electron distances r_{ij} and the nuclei-electron distances r_{Ij} . In VMC, one

Downloaded by CORNELL UNIV on May 27, 2012 | http://pubs.acs.org
Publication Date (Web): February 6, 2012 | doi: 10.1021/bk-2012-1094.ch005

calculates the energy as the expectation value of the Hamiltonian *H* over the wave function $\Psi_T(\mathbf{R})$ by stochastic sampling

$$E_{VMC} = \int \Psi_T(\mathbf{R})\, H\, \Psi_T(\mathbf{R}) d\mathbf{R} = \int \Psi_T(\mathbf{R})\, H\, \Psi_T(\mathbf{R}) d\mathbf{R}$$

$$= \int \Psi_T(\mathbf{R})\, E_L(\mathbf{R}) d\mathbf{R} \approx \frac{\mathbf{1}}{\boldsymbol{M}} \sum_{i=0}^{M} \boldsymbol{E_L}(\mathbf{R}_i)$$

$E_L(\mathbf{R}) = \frac{H\, \Psi_T(\mathbf{R})}{\Psi_T(\mathbf{R})}$ is the local energy, and the *M* points $\mathbf{R}_i$ are sampled from $(\Psi_T(\mathbf{R}))^2$ by a Metropolis algorithm. In DMC, one improves over the distribution $(\Psi_T(\mathbf{R}))^2$ by generating another distribution: $f(\mathbf{R}, \tau)$, obtained by evolving the importance-sampling Schrödinger equation in imaginary time $\tau = it$

$$-\frac{\partial}{\partial \tau} f(\mathbf{R}, \tau) = -\frac{1}{2}\nabla^2 f(\mathbf{R}, \tau) + \vec{\nabla} \cdot \left(f(\mathbf{R}, \tau) \frac{\vec{\nabla} \Psi_T(\mathbf{R})}{\Psi_T(\mathbf{R})} \right) + (E_L(\mathbf{R}) - E_T) f(\mathbf{R}, \tau)$$

This equation resembles an ordinary diffusion equation with diffusion, drift and source terms on the right-hand side. This diffusion process is simulated stochastically with a population of walkers representing the distribution $f(\mathbf{R}, \tau)$. The trial energy E_T is adjusted in the course of the calculation in order to maintain a stable population of walkers. After some iterations the stationary distribution is obtained from $f(\mathbf{R}, \tau \rightarrow \infty) = \Psi_{FN}(\mathbf{R})\, \Psi_T(\mathbf{R})$ where $\Psi_{FN}(\mathbf{R})$ is the fixed-node (FN) wave function, i.e. the best approximation to the ground-state wave function having the same nodes as the trial wave function. In practice, this fixed-node approximation is automatically enforced by using $\Psi_{FN}(\mathbf{R})\, \Psi_T(\mathbf{R})$ as a positive probability density, meaning that $\Psi_{FN}(\mathbf{R})$ must necessarily be of the same sign as $\Psi_T(\mathbf{R})$. The DMC energy is then calculated as the statistical average of the local energy of the trial wave function over the mixed distribution: $\Psi_{FN}(\mathbf{R})\, \Psi_T(\mathbf{R})$.

The nodes of the wave function are the locations of the points $\boldsymbol{R}$ where the wave function vanishes. For a system of *N* electrons in 3 dimensions, they form (*3N-1*)–dimensional hypersurfaces. A subset of these nodes is given by the antisymmetry property of the fermionic wave function with respect to the exchange of two electrons, which implies that the wave function vanishes when two same-spin electrons are at the same point in space. However, these "Pauli" (or exchange) nodes form only (*3N-3*)–dimensional hypersurfaces, and are therefore far from sufficient to determine the full nodal hypersurfaces (see, e.g., ref. (*21*) for examples on simple atomic systems). Likewise, space symmetry is generally far from sufficient to specify the nodes (*22*). For a given system, different HF wave functions (of different space symmetries) share the same Pauli nodes, but otherwise generally have very different nodal hypersurfaces, and thus lead to different fixed-node errors on DMC energies.

Downloaded by CORNELL UNIV on May 27, 2012 | http://pubs.acs.org
Publication Date (Web): February 6, 2012 | doi: 10.1021/bk-2012-1094.ch005

B. Computational Details

The QMC calculations have been performed with the program CHAMP (*23*) on a massively parallel IBM BlueGene architecture using up to 4096 processors. The trial wave functions are constructed by multiplying the previously obtained HF wave functions by a Jastrow factor consisting of the exponential of the sum of electron-nucleus, electron-electron and possibly electron-electron-nucleus terms, written as systematic polynomial and Padé expansions (*24*) (see also refs. (*25*, *26*)). Some Jastrow parameters are fixed by imposing the electron-electron cusp condition, and the others are optimized with the linear energy minimization method in VMC (*27–29*), using an accelerated Metropolis algorithm (*30*, *31*). The orbital and basis exponent parameters are kept fixed in this work. Once the trial wave functions have been optimized, we perform DMC calculations within the short-time and fixed-node approximations (see, e.g., refs. (*32–36*)). We use an imaginary time step of $\Delta\tau = 0.01$ hartree^{-1} in an efficient DMC algorithm having very small time-step errors (*37*). We use a target population of 100 walkers per processor, and estimate statistical uncertainties with blocks of 1000 iterations, for an energy autocorrelation time of about 50 iterations. The statistical uncertainty on the average energy per H_2 cell is decreased to smaller than 2×10^{-5} hartree.

The computational cost of the VMC calculations grows with the third power of the number of hydrogen atoms when optimizing all the two-body and three-body terms in the Jastrow factor. When restricting the Jastrow factor to the two-body terms only, the computational cost scales quadratically with the number of hydrogen atoms, suggesting that it is the evaluation of the Jastrow factor which dominates the computational cost and not the evaluation of the Slater determinant. The large reduction of computational cost achieved by removing the three-body terms comes without too much a loss on the VMC energy, and in principle no loss at all on the DMC energy. For example, for the H_{26} ring system, we find a VMC energy of -13.8894 ± 0.0005 hartree with the three-body term, and -13.8430 ± 0.0005 hartree without the three-body term. The computational effort is about 20 times more time consuming in the former case. We thus use a two-body Jastrow only.

As the variance V of the local energy of a ring of n H_2 molecules is approximately n times the variance V for one H_2 molecule, the statistical uncertainty on the energy grows with the square root of n

$$\sigma\big(E(H_{2n})\big) \sim \sqrt{\frac{V\big(E_L(H_{2n})\big)}{M}} \sim \sqrt{\frac{n\,V\big(E_L(H_2)\big)}{M}}$$

Here M is the number of Monte Carlo iterations. Therefore, the statistical uncertainty on the energy per H_2 cell decreases as $1/\sqrt{n}$, and thus calculations aiming at a given statistical uncertainty on this quantity demand fewer steps for increasing ring sizes.

In Advances in Quantum Monte Carlo; Tanaka, S., et al.;
ACS Symposium Series; American Chemical Society: Washington, DC, 2012.

C. Results

Figure 2 reports the VMC total energies of the hydrogen rings, per H_2 cell, for the three HF solutions from 46 to 102 hydrogen atoms. Like in Møller-Plesset perturbation theory or linearized coupled cluster doubles theory, the energy ordering of the three solutions are reversed in comparison to HF, the SA wave function giving now the lowest total energy and the SB-BC solution giving the highest one. For the case of H_{86}, we show in Table II the QMC total energies and energy differences of the symmetry-adapted and symmetry-broken solutions. For comparison, we also report MP2 energies calculated with the same Slater basis set. The VMC total energy per H_2 cell lie about 50 mhartree below the MP2 energies, and the energy splittings between the different solutions are also smaller than those in MP2, which shows the Jastrow factor better describes electron correlation.

Figure 3 reports the corresponding DMC results. The energy ordering is the same as in VMC and MP2, the SA wave function giving the lowest DMC total energy, and thus the smallest fixed-node error. As shown in Table II, the energy splittings between the different solutions are much smaller in DMC. This indicates that DMC is less sensitive to symmetry breaking than other correlation methods. It is an interesting feature for cases where symmetry breaking cannot be avoided.

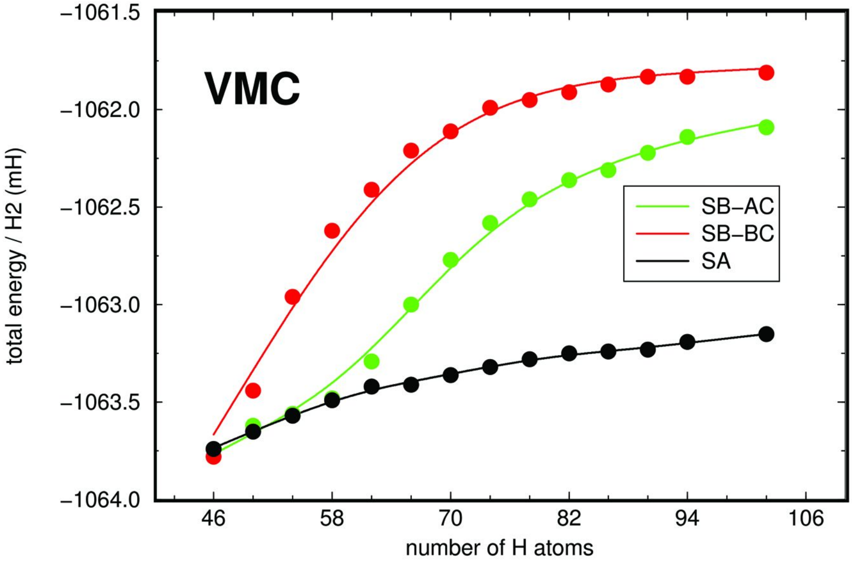

Figure 2. VMC total energies of H_{4n+2} rings, per H_2 cell in mhartree, for the symmetry-adapted (SA) and the two symmetry-broken (SB-AC and SB-BC) HF solutions from 46 to 102 hydrogen atoms. The statistical uncertainty is about the size of the point.

Downloaded by CORNELL UNIV on May 27, 2012 | http://pubs.acs.org
Publication Date (Web): February 6, 2012 | doi: 10.1021/bk-2012-1094.ch005

Table II. Total energy and energy differences, per H_2 cell in mhartree, of the symmetry-adapted (SA) and the symmetry-broken (SB-AC and SB-BC) HF solutions, for the H_{86} ring, with the Slater basis set

Method	*E(SA)*	*E(SB-AC)-E(SA)*	*E(SB-BC)-E(SA)*
HF	−996.15	−0.14	−0.39
MP2	−1016.22	1.37	1.55
VMC	−1063.24	0.93	1.36
DMC	−1077.57	0.31	0.70

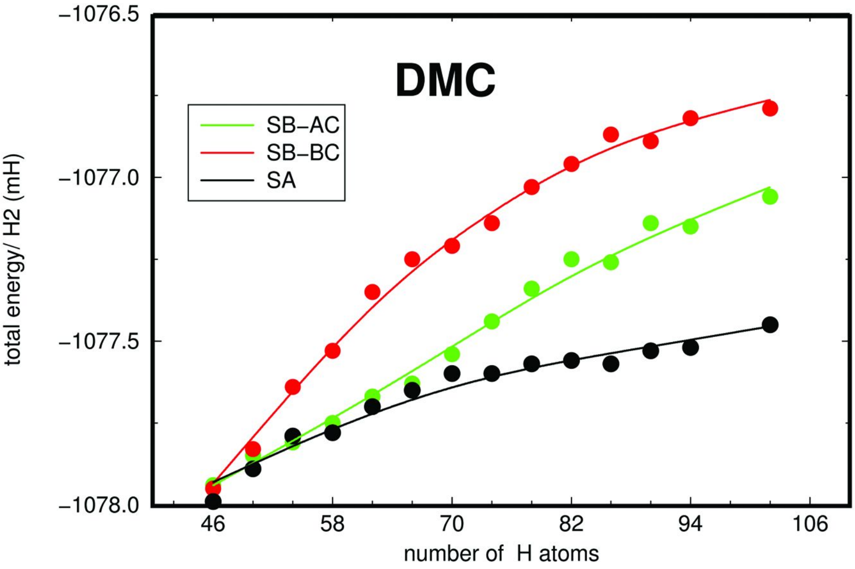

Figure 3. DMC total energies of H_{4n+2} rings, per H_2 cell in mhartree, for the symmetry-adapted (SA) and the two symmetry-broken (SB-AC and SB-BC) HF solutions from 46 to 102 hydrogen atoms. The statistical uncertainty is about the size of the point.

IV. Conclusion

When HF trial wave functions are used in QMC calculations, in case of HF instabilities QMC faces the HF symmetry dilemma in choosing between the symmetry-adapted solution of higher HF energy and symmetry-broken solutions of lower HF energies. In this work, we have examined the HF symmetry dilemma in hydrogen rings H_{4n+2} which present HF singlet instabilities for sufficiently large ring sizes. We have shown that using a Slater basis set, instead of a Gaussian basis set, delays the onset of HF symmetry breaking until larger rings and slightly reduces the energy splittings between the symmetry-adapted and symmetry-broken wave functions. When using these different HF wave functions

Downloaded by CORNELL UNIV on May 27, 2012 | http://pubs.acs.org
Publication Date (Web): February 6, 2012 | doi: 10.1021/bk-2012-1094.ch005

in VMC and DMC, we have found that the energy ordering is reversed, the symmetry-adapted wave function always giving the lowest energy. This confirms previous post-Hartree-Fock studies in showing that these symmetry-broken solutions are bad starting wave functions for correlated calculations. The fact that the symmetry-adapted wave function gives the lowest DMC energy indicates that this wave function has more accurate nodes than the symmetry-broken wave functions. The present experience thus suggests that spatial symmetry is an important criterion for selecting good trial wave functions.

Acknowledgments

This work has been financed mainly through the DEISA network, project STOP-Qalm. All QMC calculations have been performed on the IBM Bluegene machines in Jülich and Munich (Germany). The authors thank the staff of IDRIS (Orsay, France) for technical assistance to install, test and run the QMC program CHAMP on these machines. We also acknowledge the possibility of using the Slater integral code SMILES (Madrid, Spain) for preparing the HF starting wave functions. Discussions with P. Gori-Giorgi (Amsterdam, Netherlands) and J.-P. Malrieu (Toulouse, France) were very helpful for the project.

Downloaded by CORNELL UNIV on May 27, 2012 | http://pubs.acs.org
Publication Date (Web): February 6, 2012 | doi: 10.1021/bk-2012-1094.ch005

References

1. Thouless, D. J. *The Quantum Mechanics of Many Body Systems*; Academic Press: New York, 1961.
2. Čiček, J.; Paldus, J. *J. Chem. Phys.* **1967**, *47*, 3976.
3. Paldus, J.; Čiček, J. *J. Chem. Phys.* **1970**, *52*, 2919.
4. Čiček, J.; Paldus, J. *J. Chem. Phys.* **1970**, *53*, 821.
5. Paldus, J.; Čiček, J. *J. Chem. Phys.* **1971**, *54*, 2293.
6. Čiček, J.; Paldus, J. *Phys. Rev. A* **1971**, *3*, 525.
7. Paldus, J.; Čiček, J. *Phys. Rev. A* **1970**, *2*, 2268.
8. Löwdin, P.-O. *Rev. Mod. Phys.* **1963**, *35*, 496.
9. Reinhardt, P.; Malrieu, J. P. *J. Chem. Phys.* **1999**, *110*, 775.
10. Bénard, M.; Paldus, J. *J. Chem. Phys.* **1980**, *72*, 6546.
11. Hammond, B. L.; W. A. Lester, J.; Reynolds, P. J. *Monte Carlo Methods in Ab Initio Quantum Chemistry*; World Scientific: Singapore, 1994.
12. Nightingale, M. P., Umrigar, C. J., Eds.; *Quantum Monte Carlo Methods in Physics and Chemistry*; NATO ASI Ser. C 525; Kluwer: Dordrecht, 1999.
13. Foulkes, W. M. C.; Mitas, L.; Needs, R. J.; Rajagopal, G. *Rev. Mod. Phys.* **2001**, *73*, 33.
14. Reinhardt, P.; Malrieu, J. P. *J. Chem. Phys.* **1998**, *109*, 7632.
15. Kohn, W. *Chem. Phys. Lett.* **1993**, *208*, 167.
16. Reinhardt, P. *Different Programs To Perform Ab-Initio Calculations within Highly Localized Orbitals*; Toulouse-Dresden-Paris, 1998, unpublished.
17. Fernández Rico, J.; López, R.; Aguado, A.; Ema, I.; Ramírez, G. *Int. J. Quantum Chem.* **2001**, *81*, 148.
18. Daudey, J.-P. *Chem. Phys. Lett.* **1974**, *24*, 574.

19. Reinhardt, P.; Malrieu, J.-P.; Povill, A.; Rubio, J. *Int. J. Quantum Chem.* **1997**, *70*, 167.
20. Kato, T. *Commun. Pure Appl. Math.* **1957**, *10*, 151.
21. Bressanini, D.; Ceperley, D. M.; Reynolds, P. *In Recent Advances in Quantum Monte Carlo Methods, II*; Lester, W. A., Rothstein, S. M., Tanaka, S., Eds.; World Scientific: Hackensack, NJ, 2001; p 3.
22. Bressanini, D.; Morosi, G.; Tarasco, S. *J. Chem. Phys.* **2005**, *123*, 204109.
23. Umrigar, C. J.; Filippi, C.; Toulouse, J. CHAMP (Cornell-Holland Ab-initio Materials Package). http://pages.physics.cornell.edu/~cyrus/champ.html.
24. Umrigar, C. J., unpublished.
25. Filippi, C.; Umrigar, C. J. *J. Chem. Phys.* **1996**, *105*, 213.
26. Güçlü, A. D.; Jeon, G. S.; Umrigar, C. J.; Jain, J. K. *Phys. Rev. B* **2005**, *72*, 205327.
27. Toulouse, J.; Umrigar, C. J. *J. Chem. Phys.* **2007**, *126*, 084102.
28. Umrigar, C. J.; Toulouse, J.; Filippi, C.; Sorella, S.; Hennig, R. G. *Phys. Rev. Lett.* **2007**, *98*, 110201.
29. Toulouse, J.; Umrigar, C. J. *J. Chem. Phys.* **2008**, *128*, 174101.
30. Umrigar, C. J. *Phys. Rev. Lett.* **1993**, *71*, 408.
31. Umrigar, C. J. *In Quantum Monte Carlo Methods in Physics and Chemistry*; Nightingale, M. P., Umrigar, C. J., Eds.; NATO ASI Ser. C 525; Kluwer: Dordrecht, 1999; p 129.
32. Grimm, R.; Storer, R. G. *J. Comput. Phys.* **1971**, *7*, 134.
33. Anderson, J. B. *J. Chem. Phys.* **1975**, *63*, 1499.
34. Anderson, J. B. *J. Chem. Phys.* **1976**, *65*, 4121.
35. Reynolds, P. J.; Ceperley, D. M.; Alder, B. J.; Lester, W. A. *J. Chem. Phys.* **1982**, *77*, 5593.
36. Moskowitz, J. W.; Schmidt, K. E.; Lee, M. A.; Kalos, M. H. *J. Chem. Phys.* **1982**, *77*, 349.
37. Umrigar, C. J.; Nightingale, M. P.; Runge, K. J. *J. Chem. Phys.* **1993**, *99*, 2865.

Downloaded by CORNELL UNIV on May 27, 2012 | http://pubs.acs.org
Publication Date (Web): February 6, 2012 | doi: 10.1021/bk-2012-1094.ch005

Chapter 6

Single Electron Densities from Quantum Monte Carlo Simulations

Arne Lüchow* **and René Petz**

Institute of Physical Chemistry, RWTH Aachen University,
52056 Aachen, Germany
***E-mail: luechow@rwth-aachen.de**

Downloaded by CORNELL UNIV on May 28, 2012 | http://pubs.acs.org
Publication Date (Web): February 6, 2012 | doi: 10.1021/bk-2012-1094.ch006

In this contribution, quantum Monte Carlo is used to construct strongly localized single electron densities from all-electron correlated wavefunctions. They allow interpretations in terms of core, bond or lone pair electrons. It is demonstrated that single electron densities can be obtained efficiently within the variational quantum Monte Carlo (VMC) method. Results for LiH, ethane, ethene, and water are shown.

Introduction

Quantum Monte Carlo is a technique that allows both accurate and favorably scaling electron structure calculations. While other electron structure methods such as the density functional theory employ an effective one-electron Hamiltonian the variational and the diffusion quantum Monte Carlo method (VMC and DMC) are based on the full-dimensional electronic wavefunction ψ. More precisely, VMC and DMC construct samples of the distributions $|\psi|^2$ and $\psi\psi_0$, respectively, by means of Monte Carlo methods where ψ denotes an approximate wavefunction or trial function and ψ the exact ground state wavefunction. The efficiency of these methods is due to importance sampling, i.e. many sample points describe regions with large values of $|\psi|^2$ or $\psi\psi_0$ while few points are used for small values. The distributions are usually built to calculate the total energy as expectation of the local energy $E_L = H\psi/\psi$. Sometimes other quantum mechanical expectations such as multipole moments are calculated similarly. Details to these methods are found in other chapters of this book, or in recent review articles (*1*, *2*).

The full-dimensional wavefunction contains of course much more information than that obtained from a few expectation values. In fact, it contains all information

In Advances in Quantum Monte Carlo; Tanaka, S., et al.;
ACS Symposium Series; American Chemical Society: Washington, DC, 2012.

Downloaded by CORNELL UNIV on May 28, 2012 | http://pubs.acs.org
Publication Date (Web): February 6, 2012 | doi: 10.1021/bk-2012-1094.ch006

about the chemistry and physics of a molecule or a molecular system. Therefore, is should be possible to extract information about the delocalization or localization of electrons, about where the electrons or electron pairs can be found in the molecule, and about exchange or effects due to the antisymmetry from the wavefunction. Finally, it should be possible to extract transferable chemical entities such as bond electron pairs and lone pairs, or even transferable groups such as a methyl group from the wavefunction.

Many methods for a chemically oriented analysis of wavefunctions and densities that are based on DFT or other ab initio methods are well known and will not be discussed here, but only a few quantum Monte Carlo (QMC) techniques have been presented up to date. Most notably are the electron pair localization method (EPLF) by Scemama et. al. (*3*, *4*) and the density analysis by Alexander and Coldwell (*5*). The compact analytical form of the many-body wavefunction ψ employed in QMC allows in addition for the determination of the local maxima of $|\psi|^2$. These represent the most likely arrangements of all electrons and contain therefore considerable information about many-body properties of the system.

In a very recent publication, the current authors have presented a new method for analyzing $|\psi|^2$ which is given as a sample (*6*). It is demonstrated that it is possible to extract strongly localized single-electron densities representing bonds, cores, and lone pairs without use of atomic or molecular orbitals. The main idea is the assignment of the electrons in the $|\psi|^2$ sample to reference positions. In this contribution, we briefly review the method and elaborate on details of the assignment procedure. In addition, we suggest an alternative choice of reference positions.

Single Electron Densities

The variational quantum Monte Carlo method can construct efficiently large samples of $|\psi|^2$ which is observable and describes the probability density of all electrons at once. Such samples can be obtained experimentally (at least in principle) by determining repeatedly all electron positions at once. This does not violate the Heisenberg uncertainty principle as long as no momentum information is available. In the quantum simulation of this experiment, the spin state (up or down) is available for each electron as well. Contrary to measurements or calculations of spin densities it is possible to extract information about electron distances and angles.

Chemists have rationalized very successfully the electronic structure of molecules since the advent of the ingenious “Lewis” electron pair by G. N. Lewis in terms of bond electron pairs, lone pairs, core electrons and so on. Quantum mechanics does not allow to distinguish between “lone pair” and “core” electrons, but chemists do not maintain that there are distinct lone pair electrons, only that there are two electrons in a “lone pair” region. The Loge theory of R. Daudel is an example for the definition of disjunct domains that are constructed such as to contain e.g. two electrons in the mean (*7*). The availability of $|\psi|^2$ samples enables the opposite approach: the two lone pair, core, bond electrons, and so on are identified in each electron arrangement of the sample and collected

Downloaded by CORNELL UNIV on May 28, 2012 | http://pubs.acs.org
Publication Date (Web): February 6, 2012 | doi: 10.1021/bk-2012-1094.ch006

to *single electron densities*, one density for spin up and one for spin down electrons. It should be noted that such single electron densities are related to squared localized molecular orbitals, but are defined for arbitrary wavefunctions, including multireference wavefunctions.

In many cases, it is obvious which electrons are core, which are bond electrons, but in other cases the assignment is not obvious. For an automatic construction of single electron densities a unique algorithm for the assignment is required. It is desirable to devise an algorithm that does not rely on "chemical knowledge" but on properties of the electron distribution itself.

The current authors have suggested to assign electrons to single electron densities based on a reference electron arrangement. Each electron has to be assigned uniquely to one electron of the reference. The reference can be the *most probable electron arrangement*, i.e. the maximum of $|\psi|^2$ (*6*). The relation of this maximum to the chemical structure has been discussed recently by Scemama et al. (*8*). Here we suggest an alternative reference, iterated centers of charge of the single electron densities. The construction of this reference is discussed below. First, the efficient assignment of the electrons of an electron arrangement during a VMC calculation is analyzed. In the following section, the new reference electron arrangement is discussed in detail.

The Assignment of Electrons

In VMC, electron positions are sampled efficiently. During the VMC run, independent electron positions shall be assigned to a reference electron arrangement. This is, in principle, a simple problem. In mathematical terms, positions of individual electrons are denoted $\mathbf{r}_i$ with index i of the electron. In QMC, spin up and spin down electrons are distinguished and treated here separately. Let $\mathbf{R}^u = (\mathbf{r}_1, \ldots, \mathbf{r}_{nu})$ and $\mathbf{R}^d = (\mathbf{r}_1, \ldots, \mathbf{r}_{nd})$ collect the electron positions to a vector with all (*nu*) up-spin electrons and all (*nd*) down-spin electrons, respectively. Both vectors can be combined to $\mathbf{R} = (\mathbf{r}_1, \ldots, \mathbf{r}_n)$. The reference electron arrangement is described by such a vector $\mathbf{R}_{ref}$. Same-spin electrons are indistinguishable, which is accounted for by the Slater determinant form of the wavefunction, but have nonetheless assigned indices.

The identification of, for instance, the electron of a certain lone pair requires finding the *index* of the electron closest to the reference position of the lone pair. In practical terms, the assignment of an index in the electron position vector $\mathbf{R}$ to an index of the reference vector $\mathbf{R}_{ref}$ describes the identification of an electron. The assignment of all electrons in $\mathbf{R}$ to the reference $\mathbf{R}_{ref}$ has the obvious limitation that all electrons must be assigned and no two electrons are allowed to be assigned to the same reference position. Furthermore, up and down-spin electrons are assigned separately. The assignment of both types of electrons are obviously permutations of the indices, and finding the best assignment of the electrons amounts to finding the best permutation. This requires a cost function that determines which of two permutations is better.

The assignment of all electrons to the closest reference position is not possible in all cases due to the uniqueness requirement. A cost function that retains this assignment if possible is the Euklidian distance d of the $3n$ dimensional position vectors. Its square is

$$d^2 = \left|\mathbf{R} - \mathbf{R}_{ref}\right|^2 = \sum_{i=1}^{n} \left|\mathbf{r}_i - \mathbf{r}_i^{\mathrm{ref}}\right|^2$$

This cost function has been suggested previously (*6*). The assignment requires finding the permutations (separately for spin up and spin down electrons) that minimize the cost function.

A naïve implementation of the assignment would evaluate d for all permutations requiring $n_u! + n_d!$ evaluations. This approach would render the method inapplicable to all but the smallest molecules. Luckily, the electron assignment with the squared Euklidian distance is a special case of the linear sum assignment problem, well known in computer science (*9*). The Munkres or Hungarian algorithm solves this problem efficiently with a complexity of $O(N^3)$ (*10*, *11*). The assignment has to be carried out for independent electron arrangements during the VMC run. Since the local energy calculations have a complexity of $O(N^3)$ as well, the single electron density calculations do not have a higher complexity as the VMC calculation itself. Because of the importance of the assignment complexity for the usability the Munkres algorithm is presented here with an emphasis on the flexibility with respect to the cost function.

The assignment of (the indices of) the vector $\mathbf{R}$ to $\mathbf{R}_{\mathrm{ref}}$, both of length n, is described by an n x n assignment matrix $\mathbf{X}$ whose elements are zero except when $\mathbf{r}_i$ is assigned to $\mathbf{r}_j$ when $x_{ij} = 1$. Possible assignments, i.e. permutations have one and only one “1” in each row and each column. There are $n!$ possible assignments or permutations, here denoted $\mathbf{X}^{(k)}$.

The cost function is evaluated based on a n x n cost matrix $\mathbf{C} = (c_{ij})$ whose elements contain the “cost” for the assignment of $\mathbf{r}_i$ to $\mathbf{r}_j$ which is

$$c_{ij} = \left|\mathbf{r}_i - \mathbf{r}_j\right|^2$$

The cost function $C(k)$ is constructed from the two matrices

$$C(k) = \sum_{i,j=1}^{n} x_{ij}^{(k)} c_{ij} \quad .$$

The structure of the $\mathbf{X}$ matrices ensures that the cost function is indeed the Euklidean distance of a permutation of $\mathbf{R}$ and $\mathbf{R}_{\mathrm{ref}}$.

The Munkres algorithm is able to find the assignment $\mathbf{X}$ that minimizes $C(k)$ in $O(N^3)$ steps provided that the c_{ij} are non-negative integer. Non-negative real numbers can be converted approximately to integers by multiplication with a large number and retaining the integer part.

The Munkres algorithm consists of the following three steps acting on the cost function matrix C (see Figure 1). First, from each row of C the smallest value in the row is subtracted. Second, from each column the smallest value is subtracted. Afterwards the algorithm looks for the minimal number of rows and columns to cover all zeros of the matrix C. Third, the smallest value which is not covered

Downloaded by CORNELL UNIV on May 28, 2012 | http://pubs.acs.org
Publication Date (Web): February 6, 2012 | doi: 10.1021/bk-2012-1094.ch006

Downloaded by CORNELL UNIV on May 28, 2012 | http://pubs.acs.org
Publication Date (Web): February 6, 2012 | doi: 10.1021/bk-2012-1094.ch006

after step two is subtracted from all uncovered values. If the number of rows or columns necessary to cover all zeros of *C* now equals the total number of rows or columns the assignment can be found from the zeros of the matrix. Otherwise the algorithm goes back to step three. For details see references (*10*, *11*).

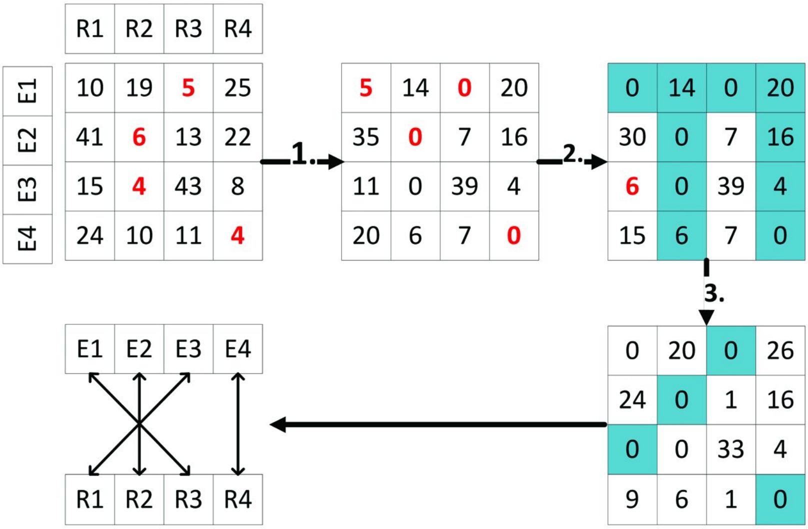
R1 R2 R3 R4
E1 E2 E3 E4
10 19 5 25
41 6 13 22
15 4 43 8
24 10 11 4
1.
5 14 0 20
35 0 7 16
11 0 39 4
20 6 7 0
2.
0 14 0 20
30 0 7 16
6 0 39 4
15 6 7 0
3.
0 20 0 26
24 0 1 16
0 0 33 4
9 6 1 0
E1 E2 E3 E4
R1 R2 R3 R4

Figure 1. Simplified illustration of the steps taken by the Munkres algorithm to find the correct assignment.

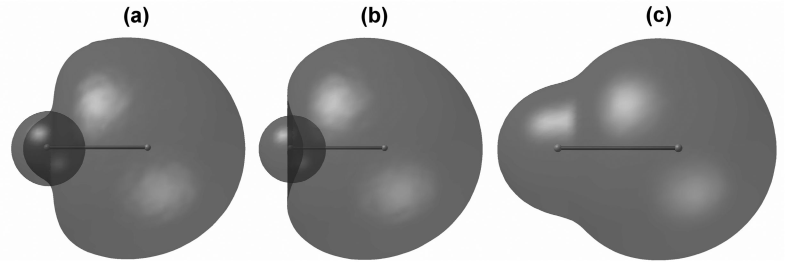

Figure 2. Isosurfaces (60%) for the single electrons of LiH, with the SD (a) and the CD assignment (b). (c) Isosurface of the total spin up density.

From the knowledge of the algorithm one can deduce that more general cost functions can replace the simple distance criterion although not arbitrary ones. The cost function has to be a sum of matrix elements of the *C* matrix. One possible generalization to improve the assignment is the introduction of weights such as

$$c_{ij} := w_{ij}\left|\mathbf{r}_i - \mathbf{r}_j\right|^2$$

with weights depending only on $\mathbf{r}_i$ and $\mathbf{r}_j$.

The assignment with respect to the simple squared distance works very well, but has the unwanted effect that the electrons closest to the nuclei are not always assigned to the core even though the reference position for the core electrons are at the nucleus position (for K shell cores). This is due to the fact that the small core electron-nucleus distance contributes only little to the overall cost function. For best transferability and interpretation the closest up and down spin electrons should be assigned to the “core”.

Rather than constructing an appropriate weight function we have suggested in reference (*6*) to assign the closest electron of each spin to the core of atoms heavier than Helium while all valence electrons are assigned with the Munkres algorithm using the squared distance cost matrix. This algorithm will be denoted CD (for core-distance) while the simple algorithm with the squared distance only is denoted SD. One should note that the valence electrons can still come arbitrarily close to the nucleus even with the CD algorithm.

The difference of the algorithms is demonstrated for LiH. This is not only a simple molecule but also an excellent test case as it has a large core and only two valence electrons that are strongly drawn toward the H atom. The single electron densities are shown here as isosurfaces that enclose a given percentage of the single electron density. In Figure 2 the spin up single electron densities are shown with 60% isosurfaces obtained with both algorithms from a HF wave function. The value of 60% is arbitrary. Smaller or larger values would simply shrink or enlarge, respectively, the surfaces. The global maximum of $|\psi|^2$ is used here as reference for the assignment. In both cases the total density is exactly partitioned into two single electron densities (up and down spin densities are identical). The CD variant leads to stronger localization and to a slightly more compact core while the valence density appears to contain core contribution in the SD case. This example also demonstrates how the construction of isosurfaces for the single electron densities emphasizes the chemical structure of the system. While the two single electron densities add up exactly to the total density, the two isosurfaces do not add up to the isosurface of the total density. Regions where electrons are partly assigned to the core and partly to the valence density may be within the isosurface of the total density but outside the isosurfaces of both core and valence densities.

Downloaded by CORNELL UNIV on May 28, 2012 | http://pubs.acs.org
Publication Date (Web): February 6, 2012 | doi: 10.1021/bk-2012-1094.ch006

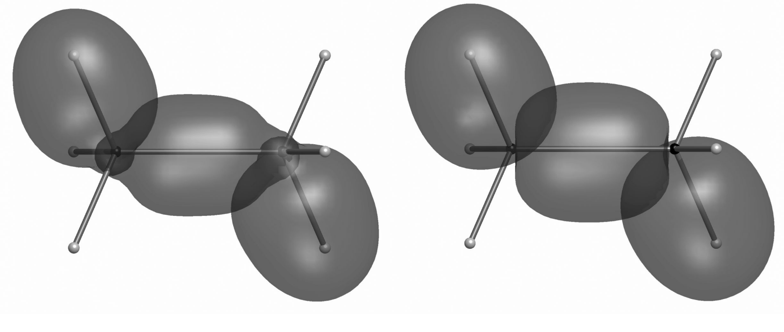

Figure 3. Isosurfaces (60%) of spin up valence densities ethane with the SD (left) and CD assignment (right).

Figure 3 shows a similar difference for single electron densities of ethane obtained from a HF wavefunction. The C-H and C-C bond densities based on the global maximum reference are shown with a clear separation of core and valence only with the preassignment of the core electrons.

The better localization and separation of core and valence densities is obtained by first assigning the electrons closest to the core and then all other electrons efficiently with the Munkres algorithm and the distance cost function. This assignment algorithm is easily extended to larger cores.

Downloaded by CORNELL UNIV on May 28, 2012 | http://pubs.acs.org
Publication Date (Web): February 6, 2012 | doi: 10.1021/bk-2012-1094.ch006

Optimal Reference Positions: Self-Consistent Centers of Charge

The single electron densities are to a large extent fairly independent of the chosen reference positions. In previous work, the maxima of $|\psi|^2$ have been utilized for the reference. The maxima itself contain considerable information about the many-body structure of the wavefunction but have a few drawbacks as reference positions. First, the spin up and spin down position do not coincide for correlated wavefunctions due to the Coulomb repulsion. This leads to apparent "spin polarization" and single electron densities that are not identical for spin up and spin down electrons. No observable spin polarization arises because the reverse spin polarization is as likely in closed shell systems and all possible spin polarizations cancel exactly (*6*). Therefore, an unpolarized reference that is obtained from the wavefunction itself (like the maxima) without any assumption about the "chemical structure" is desirable. Second, many local maxima exist with similar values of $|\psi|^2$, and it is not always obvious that the global maximum is the best reference. Finally, finding the maxima is a global optimization procedure which becomes quite time consuming for large molecules.

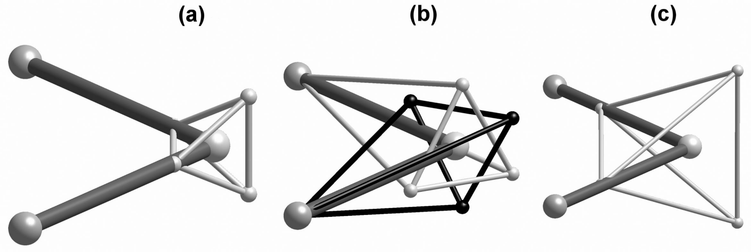

Figure 4. (a) Maxima for the uncorrelated and (b) correlated water wavefunction together with the (c) self-consistent centers of charge of the correlated water wavefunction.

Downloaded by CORNELL UNIV on May 28, 2012 | http://pubs.acs.org
Publication Date (Web): February 6, 2012 | doi: 10.1021/bk-2012-1094.ch006

The construction of self-consistent centers of charge is a way to avoid many drawbacks of the maximum reference. These points result from an iteration of reference points that are obtained as centers of charge of the single electron distribution. Let **c** denote the center of a charge density ρ(**r**) with a total charge *q*. The center is obtained with

$$\mathbf{c} = \frac{1}{q} \int \rho(\mathbf{r})\mathbf{r}\, dV$$

The integration is easily carried out during the VMC run for each single electron density after the assignment step. If a certain statistical accuracy of **c** is obtained, the center of charges of all single electron densities are defined as new references for renewed calculations of single electron densities. This process is iterated until the centers of charge are converged. It is more time consuming than the density determination with given reference points, but still efficient.

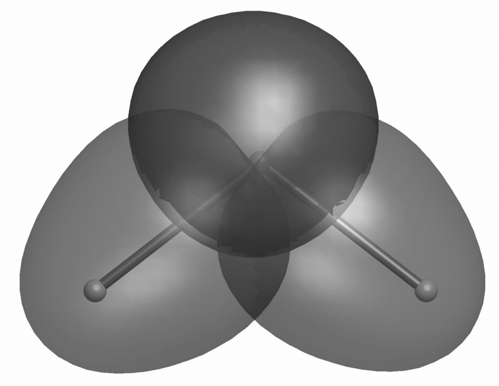

Figure 5. Isosurfaces (60%) for the spin up single electron densities obtained with self-consistent center of charge reference for a correlated water wavefunction.

In Figure 4 first results for the self-consistent centers of charge are presented and compared with the global maximum reference. The uncorrelated and correlated maxima of water as well as the self-consistent centers of charge are shown. In case of the uncorrelated maximum the positions of the electrons with different spin within the maxima are equal and both form a tetrahedron around the oxygen atom. When dynamical correlation is added, here with a Jastrow factor, the positions of electrons with different spin differ. Now the electrons of different spin form two distorted tetrahedra which are rotated against each other. This reference causes the single electron densities of spin up and down electrons to differ slightly. These differences are arbitrary due to indistinguishability of the electrons in a closed shell system with $M_S = 0$ and can be cancelled by building electron pair densities. This is demonstrated for water in the previous publication of the authors (*6*). In Figure 4c the self-consistent center-of-charge reference positions are shown. Spin up and spin down centers of charge converge to the same positions even if the initial reference positions are the maxima of Figure 4b. The four positions form again a regular tetrahedron around the oxygen atom. The reference positions are now close to the middle of the bond. The reference position is determined by the electronegativity difference of the two atoms and the size of their cores.

Downloaded by CORNELL UNIV on May 28, 2012 | http://pubs.acs.org
Publication Date (Web): February 6, 2012 | doi: 10.1021/bk-2012-1094.ch006

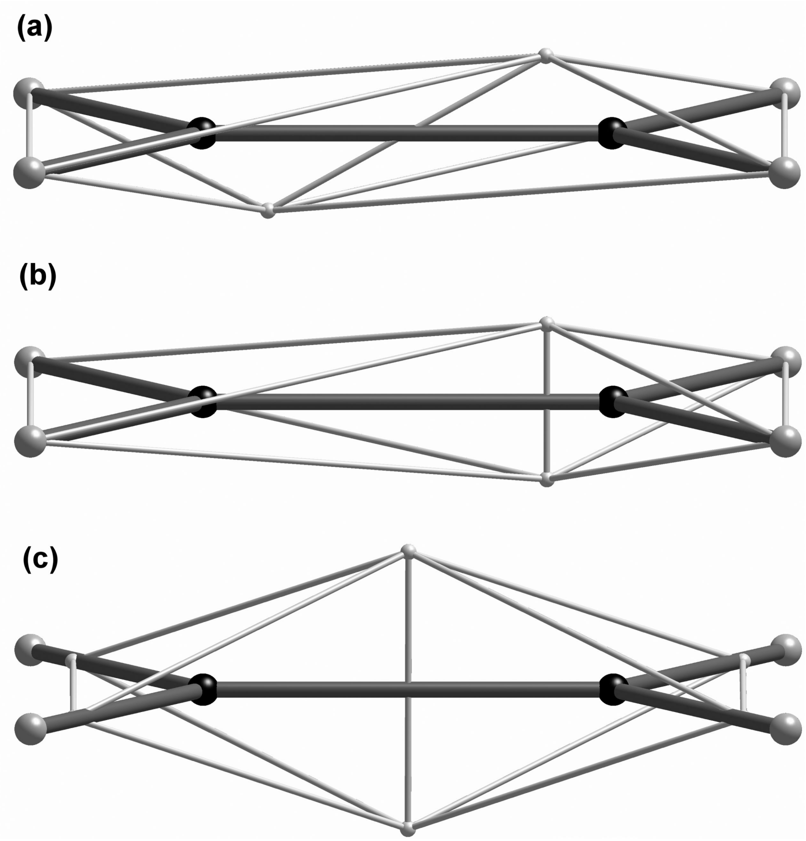

Figure 6. Two maxima for the uncorrelated ethene wavefunction (a-b), together with the self-consistent centers of charge (c).

Since spin up and spin down electrons have the same reference position in closed shell systems the corresponding single electron densities agree as well. The electron pair density is then simply twice the single electron density. In Figure 5 the single electron densities based on the center-of-charge reference points are shown and may be compared with the single electron densities from the maximum reference in ref. (*6*).

Downloaded by CORNELL UNIV on May 28, 2012 | http://pubs.acs.org
Publication Date (Web): February 6, 2012 | doi: 10.1021/bk-2012-1094.ch006

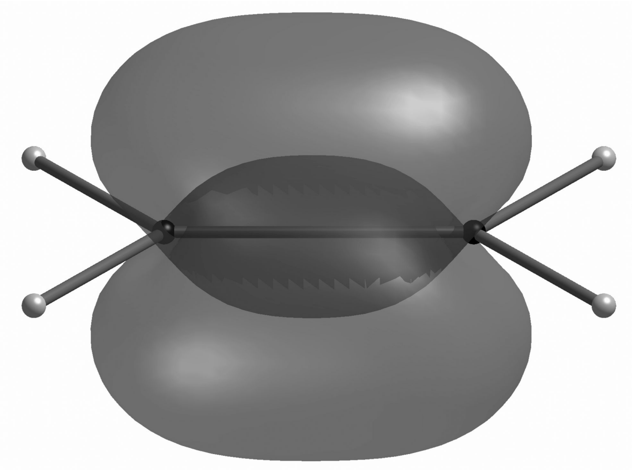

Figure 7. Isosurfaces (60%) for the spin up single electron densities of the double bond obtained with self-consistent centers of charge of the uncorrelated ethene wavefunction.

The advantages of self-consistent center-of-charges are obvious in the ethene molecule. For the uncorrelated ethene wavefunction it is possible to obtain four different maxima with the same value of $|\psi|^2$. Two of these four maxima are shown in Figure 6. They differ only in the positions of the electrons along the C=C bond axis. In case of the two maxima shown in Figure 6a and 6b the spin up and spin down electrons take the same positions and form two distorted tetrahedra linked by one edge. Two additional maxima are formed by filling all four positions along the C=C bond and thus by separating spin up and down electrons. These invariant maxima result in qualitatively different single electron densities. While the possible maximum positions contain considerable chemical information about the double bond, it is desirable to have a unique description of the double bond. This is achieved with the self-consistent centers of charge because the same set of self-consistent centers of charge is obtained for all equivalent maxima as starting point. The converged centers of charge are in the middle of the C=C bond above and below the ethene plane. The corresponding single electron densities show a banana bond-like shape (Figure 7).

This and other calculations show that much fewer self-consistent centers of charge are obtained than maxima. They converge for a wide range of starting points. The centers of charges of the localized molecular orbitals are a particularly simple and sensible starting point for the iteration. Due to favorable scaling behavior and easy parallelization of the VMC method and the SED partitioning it is possible to study much large molecules than considered in this study.

Finally, we note that the proposed density analysis is quite distinct from the well-known quantum theory of atoms and molecules (QTAIM) of R. W. Bader (*12*, *13*). In this method, the mathematical properties of the total electron density are investigated. This allows the determination of so-called bond critical paths that may be identified as chemical bonds and domains that are identified as the atoms in the molecule. In contrast to QTAIM, the single electron density analysis described in this paper employs the mathematical properties of the 3n-dimensional all-electron probability density $|\psi|^2$ which is projected into ordinary space. As in QTAIM, the total density is exactly partitioned, but into single electron densities and not into atoms, allowing the distinction of, for instance, bond electrons and lone pair electrons. Furthermore, the single electron densities overlap whereas the QTAIM partitioning results in disjunct atomic domains. The concept of overlapping electron densities is closer to traditional bonding concepts in chemistry.

Concluding, we have shown that strongly localized single electron densities are obtained when core electrons are assigned prior to the valence electrons. The flexibility of the efficient assignment algorithm has been discussed. Finally, it has been shown that iterated centers of charge of the single electron densities form a chemically more reasonable reference for electron assignments than maxima of $|\psi|^2$. With this reference strongly localized single electron densities are obtained that describe core electrons, bond electrons, and lone pair electrons. These transferable units are obtained directly from the many-electron distribution $|\psi|^2$ without the need of any “chemical insight”. Any wavefunction such as VB or MO-based functions including multireference ones can be employed to obtain single electron densities. Most efficient are the Slater-Jastrow functions usually employed in QMC.

Downloaded by CORNELL UNIV on May 28, 2012 | http://pubs.acs.org
Publication Date (Web): February 6, 2012 | doi: 10.1021/bk-2012-1094.ch006

Acknowledgments

Helpful discussions with Andreas Savin on suitable reference points are gratefully acknowledged.

References

1. Lester, W. A., Jr.; Mitas, L.; Hammond, B. *Chem. Phys. Lett.* **2009**, *478*, 1.
2. Lüchow, A. *WIREs Comput. Mol. Sci.* **2011**, *1*, 388.
3. Scemama, A.; Caffarel, M.; Chaquin, P. *J. Chem. Phys.* **2004**, *121*, 1725.
4. Amador-Bedolla, C.; Salomon-Ferrer, R.; Lester, W. A., Jr.; Vazquez-Martinez, J. A.; Aspuru-Guzik, A. *J. Chem. Phys.* **2007**, *126*, 204308.
5. Alexander, S. A.; Coldwell, R. L. *Int. J. Quantum Chem.* **2008**, *109*, 385.
6. Lüchow, A.; Petz, R. *J. Comput. Chem.* **2011**, *32*, 2619.
7. Daudel, R.; Georges, L.; Peeters, D.; Sana, M. *Quantum Chemistry*; Wiley: Chichester, 1983.
8. Scemama, A.; Caffarel, M.; Savin, A. *J. Comput. Chem.* **2007**, *28*, 442.
9. Burkard, R.; Dell’Amico, M., Martello, S. SIAM, Philadelphia, 2009.
10. Munkres, J. *J. Soc. Ind. Appl. Math.* **1957**, *5*, 32.
11. Silver, R. *Commun. ACM* **1960**, *3*, 605.
12. Bader, R. W. F.; Nguyen-Dang, T. T. *Adv. Quantum Chem.* **1981**, *14*, 63.
13. Bader, R. W. F. *Atoms in Molecules*; Oxford University Press: Oxford, 1990.

Downloaded by PENNSYLVANIA STATE UNIV on May 28, 2012 | http://pubs.acs.org
Publication Date (Web): February 6, 2012 | doi: 10.1021/bk-2012-1094.ch007

Chapter 7

Many-Body Nodal Hypersurface and Domain Averages for Correlated Wave Functions

Shuming Hu, Kevin Rasch,[*] and Lubos Mitas

**Department of Physics, North Carolina State University,
Raleigh, North Carolina 27695
[*]E-mail: kmrasch@ncsu.edu**

We outline the basic notions of nodal hypersurface and domain averages for antisymmetric wave functions. We illustrate their properties, analyze the results for few-electron explicitly solvable cases, and discuss possible further developments.

Quantum Monte Carlo is one of the most effective many-body methodologies for the study of quantum systems. It is based on a combination of analytical insights, robustness of stochastic approaches, and performance of parallel architectures (*1–10*). The approach has been applied to a variety of challenging problems in electronic structure of atoms, small molecules, clusters, solids, ultracold condensates, and beyond (*1–15*). The two most commonly used QMC methods are variational Monte Carlo and diffusion Monte Carlo (DMC). Let us briefly recapitulate the basics of the DMC method.

It is straightforward to show that for $\tau \to \infty$, the operator $\exp(-\tau H)$ projects out the ground state of a given symmetry from any trial function with nonzero overlap. We assume that the Hamiltonian H is time-reversal symmetric so that the eigenstates can be chosen to be real. This projection is most conveniently carried

In Advances in Quantum Monte Carlo; Tanaka, S., et al.;
ACS Symposium Series; American Chemical Society: Washington, DC, 2012.

out by solving the Schrödinger equation in an imaginary time integral form so that the product

$$f(\vec{R},t) = \Phi(\vec{R},t)\Psi_T(\vec{R})$$

obeys

$$f(\vec{R},t+\tau) = \int G(\vec{R},\vec{R}',\tau) f(\vec{R}',t)\, d\vec{R}'.$$

The Green's function is given by

$$G(\vec{R},\vec{R}',\tau) = \frac{\Psi_T(\vec{R})}{\Psi_T(\vec{R}')} \langle \vec{R} \,|\, e^{-\tau(H-E_T)} \,|\, \vec{R}' \rangle$$

where

$$\vec{R} = (\vec{r}_1, \cdots, \vec{r}_N)$$

denotes positions of N particles and E_T is an energy offset. In the DMC method, the function $f(\mathbf{R},t)$ is represented by a set of 10^2-10^4 random walkers (sampling points) in the $3N$-dimensional space of electron configurations. The walkers are propagated for a time slice τ by interpreting the Green's function as a transition probability from $\mathbf{R}' \rightarrow \mathbf{R}$. The kernel is known for small τ, and the large time t limit is obtained by iterating the propagation. The method is formally exact provided that the boundary conditions, i.e. the *fermion nodes* of the antisymmetric solution defined as $\Phi(\mathbf{R},\infty) = 0$, are known (*1*, *5*, *14*).

Unfortunately the antisymmetry does not specify the nodes completely, and currently we have to use approximations. The commonly used fixed-node approximation (*14*) enforces the nodes of $f(\mathbf{R},t)$ to be identical to the nodes of $\psi_T(\mathbf{R})$ which then implies that

$$f(\vec{R},t) \geq 0$$

everywhere. It is therefore clear that the accuracy of the fixed-node DMC is determined by the quality of the trial wave function nodes. The commonly used form for ψ_T is the Slater-Jastrow wave function given as

$$\Psi_T(\vec{R}) = \sum_n d_n \cdot \det{}_n^{\uparrow}[\{\varphi_\alpha\}] \quad \det{}_n^{\downarrow}[\{\varphi_\beta\}] \quad \exp[U_{corr}]$$

where U_{corr} is the correlation factor explicitly depending on interparticle distances thus describing pair or higher order correlations explicitly. The typical number of Slater determinants is between 1 and 10^3, and the corresponding weights d_n are usually estimated in multi-reference Hartree-Fock (HF) or Configuration Interaction (CI) calculations and then re-optimized in the variational framework.

In Advances in Quantum Monte Carlo; Tanaka, S., et al.;
ACS Symposium Series; American Chemical Society: Washington, DC, 2012.

Downloaded by PENNSYLVANIA STATE UNIV on May 28, 2012 | http://pubs.acs.org
Publication Date (Web): February 6, 2012 | doi: 10.1021/bk-2012-1094.ch007

Downloaded by PENNSYLVANIA STATE UNIV on May 28, 2012 | http://pubs.acs.org
Publication Date (Web): February 6, 2012 | doi: 10.1021/bk-2012-1094.ch007

It is quite remarkable that the nodes of such Slater-Jastrow wave functions (often with a single-determinant product only) lead to unexpectedly small errors and that the typical amount of obtained correlation energy in fixed-node DMC is ≈95%. This is true for essentially all systems we have studied: atoms, molecules, clusters and solids (*1–15*).

The fixed-node approximation is perhaps the single most important unsolved problem which hampers the progress in further improvement of accuracy and efficiency of the QMC calculations. One of the key difficulties is that the fixed-node bias is actually very small on the scale of the total energy. A comparison of the total energy components for a typical electronic structure problem is given in Table I.

Table I. Energy components as percentages of the total energy in Coulombic systems[a]

Energy Component	*% of E_{total}*
Kinetic	100
Exchange	≈8
Correlation	≈3
Δ_{FN}	≈2

[a] $\Delta_{FN} = E_{exact} - E_{FNDMC/HF}$ is the fixed-node (FN) bias corresponding to the Hartree-Fock nodes.

Considering the typical fluctuations of the DMC energy per stochastic sample (which is of the order of a few percent of the total energy), the node-related "signal" is very weak. Unfortunately a few percent of the correlation energy can influence the energy differences we are interested in.

The optimization methods (despite a number of recent developments) have difficulties picking up the nodal bias signal as it appears buried in the noise which is inherent to the QMC methodology. Recent developments in the nodal optimization using the self-healing method (*16*) enable the filtering of some of the noise quite effectively, however, the performance of the method has to be tested on more systems. However, this is not the only problem. Another key issue is that our knowledge of the nodal properties is very limited. At present we simply have no clear idea how to improve the nodal hypersurfaces for general cases in an efficient manner (for example, in systems which might require an exponential number of Slater determinants just to describe the correct spin and spatial symmetries).

We simply have to develop other measures which can provide more targeted information about the nodal shapes. It is straightforward to show that the total energy or its components are not selective enough in this respect. Let us consider a few simple illustrations. For example, the two non-interacting two-electron atomic states $^3S(1s2s)$ and $^3P(1s2p)$ have the same total, kinetic, and potential energies, but different nodal shapes. Since the symmetries in this case are different, one might argue that the symmetry should be used to distinguish and, possibly, classify the nodal shapes in this case. Consider another case: non-interacting four-electron atomic states ${}^1S(1s^22s^2)$ and ${}^1S(1s^22p^2)$. These degenerate states have the same symmetry, however, the nodes are different, both in topology and in the shape. Clearly, we would like to measure and distinguish the nodes in such cases.

Characterization of the nodes can be of significant interest in another context. Recently, an interesting scenario was suggested for systems in quantum critical point, namely, that the nodes in such a state might exhibit fractal (scale-invariant) character (*16*). For this purpose it would be very useful to measure the smoothness of the nodal surfaces.

Let us now consider the stationary Schrödinger equation

$$-\frac{1}{2}\nabla^2_{\vec{R}}\Psi(\vec{R})+V(\vec{R})\Psi(\vec{R})=E\Psi(\vec{R}).$$

The exact fermionic eigenstate ψ determines the nodal domains

$$\Omega^+=\{\vec{R};\Psi(\vec{R})>0\},\quad \Omega^-=\{\vec{R};\Psi(\vec{R})<0\}$$

and the corresponding node $\partial\Omega$. We integrate the equation over the Ω^+ domain *only*, and using the Gauss-Stokes-Green theorem we get

$$\int_{\Omega^+}(V(\vec{R})-E)\Psi(\vec{R})\,d\vec{R}-\frac{1}{2}\int_{\partial\Omega}\nabla_{\vec{R}}\Psi(\vec{R})\cdot d\vec{S}_n=0.$$

Similarly, we can integrate over the Ω^- domain and if we put it together (assuming either free or periodic boundary conditions) then we get

$$\int_{\partial\Omega}|\nabla_{\vec{R}}\Psi(\vec{R})|d\vec{S}+\int V(\vec{R})|\Psi(\vec{R})|d\vec{R}=E\int|\Psi(\vec{R})|d\vec{R}.$$

The obtained equation shows that the total energy is given as a sum of kinetic and potential components, which we call nodal (hypersurface) and domain averages (nda, in short). They are defined as follows

$$E^{nda}_{kin}=\int_{\partial\Omega}|\nabla_{\vec{R}}\Psi(\vec{R})|d\vec{S}\Big/\int|\Psi(\vec{R})|d\vec{R}$$

and

$$E^{nda}_{pot}=\int V(\vec{R})|\Psi(\vec{R})|d\vec{R}\Big/\int|\Psi(\vec{R})|d\vec{R},$$

so that

$$E=E^{nda}_{kin}+E^{nda}_{pot}.$$

This derivation and the definitions deserve some comment. First, we tacitly assumed that there is only one positive and one negative nodal domain, however, this generically applies only to fermionic ground states. Generalization to more domains is straightforward: one integrates domain by domain and sums the

Downloaded by PENNSYLVANIA STATE UNIV on May 28, 2012 | http://pubs.acs.org
Publication Date (Web): February 6, 2012 | doi: 10.1021/bk-2012-1094.ch007

results. It therefore applies to *any eigenstate* including excitations, both fermionic and bosonic (the bosonic ground state is an exception since it is nodeless). It is important that $E_{\mathrm{kin}}^{\mathrm{nda}}$ depends solely on the gradient of the wave function on the node (domain boundary) and not on the wave function values inside the domain. The key idea is that these expressions measure properties of the quantum amplitudes more directly than the expectation values. In fact, the expectations *supress* the nodal signal since both the square of the exact eigenstate and also its Laplacian vanish at the node. Note that although the sum of kinetic and potential nda components produces the total energy, the expression has no variational property, i.e. it is not quadratic in the wave functions as is the usual expectation value. It is rather a "one-sided expectation" which enables one to probe the nodal structure as we will show in what follows.

The nda values are not trivial to calculate, and for illustration we will present just a few simple cases. Let us first consider a toy model, an electron in a *2p* orbital so that the state is ^{2}P(*2p*). For the Coulomb potential $V(r)=-Z/r$ we have

$$\Psi = z\rho_{2p}(r) = z\, e^{-Zr/2},$$

and we can write

$$E_{pot}^{nda}(2p) = \frac{\iint V(r)\rho_{2p}(r)\, r\,|\cos(\vartheta)|\, r^2 \sin(\vartheta)\, d\vartheta dr}{\iint \rho_{2p}(r) r\,|\cos(\vartheta)|\, r^2 \sin(\vartheta)\, d\vartheta dr} = \frac{-Z^2}{6}.$$

Since the node is the plane given by $z=0$ and

$$|\nabla\Psi|_{z=0} = \rho_{2p}(r),$$

we can easily evaluate the kinetic energy part

$$E_{kin}^{nda}(2p) = \frac{\iint \rho_{2p}(r)\, dxdy}{2\pi \iint \rho_{2p}(r) r\,|\cos(\vartheta)|\, r^2 \sin(\vartheta)\, d\vartheta dr} = \frac{Z^2}{24}.$$

Note that the integral in the numerator is over the plane while the integration domain of the denominator is the full 3D volume. One can also verify that the sum of the two components gives $E=-Z^2/8$ as expected.

Cases with more than one particle are much more interesting. We mentioned the two excitations of the He atom, namely ^{3}S(*1s2s*) and ^{3}P(*1s2p*), and also the corresponding four-particle singlets ^{1}S($1s^2 2s^2$) and ^{1}S($1s^2 2p^2$). Actually, these are quite nontrivial to calculate even in noninteracting cases. The state ^{3}S(*1s2s*) is straightforward but rather involved, and one ends up with numerous integrals. The states with *2p* orbitals are even more complicated since the node is given by a combination of exponentials and linear functions so that the integration domains become complicated. Therefore for this case we have used Monte Carlo integration. The resulting values are listed in Table II.

Downloaded by PENNSYLVANIA STATE UNIV on May 28, 2012 | http://pubs.acs.org
Publication Date (Web): February 6, 2012 | doi: 10.1021/bk-2012-1094.ch007

Downloaded by PENNSYLVANIA STATE UNIV on May 28, 2012 | http://pubs.acs.org
Publication Date (Web): February 6, 2012 | doi: 10.1021/bk-2012-1094.ch007

Table II. Energy components for two- and four-electron atoms: standard expectations and nda values[a,b]

States	E_{tot}	E_{kin}	E_{pot}	E_{kin}^{nda}	E_{pot}^{nda}
^{3}S(*1s2s*)	-5/8	5/8	-5/4	10/221	-1185/168
^{3}P(*1s2p*)	·	·	·	1/20 (ε)	-27/40 (ε)
^{1}S($1s^22s^2$)	5/4	5/4	-5/2	20/221	-1185/884
^{1}S($1s^22p^2$)	·	·	·	1/10 (ε)	-27/20 (ε)

[a] The energies in a.u. are proportional to Z^2. The results are exact except for the values with the error bars $\varepsilon \approx 1.10^{-5}$ in the brackets. [b] The dot means that the value is the same as in the row above.

The values show clearly that one can distinguish the states and the nodes by the nodal and domain averages. For example, the $E_{\text{kin}}^{\text{nda}}$ differ by more than 10 (0.002)% between the corresponding degenerate rows. Note that if one would consider the interaction, then the two four-electron states would mix. Clearly, the nda components will depend on the mixing and thus reflect the node change under interactions. If fact, there is an optimal mixing which provides the best node within the functional form as shown previously in calculations of the Be atom (*17*, *18*).

It is interesting to analyze another case: two noninteracting electrons in $2p^2$ configuration which can couple into the three states ^{3}P, ^{1}S, ^{1}D. For example, the wave function for the state ^{3}P($2p^2$) is given by

$$\Psi(1,2) = \rho_{2p}(r_1)\rho_{2p}(r_2)(x_1 y_2 - x_2 y_1),$$

and the nda potential energy can be written as

$$E_{pot}^{nda}(2p^2) = 2\frac{\iint V(r_1)\rho_{2p}(r_1)\rho_{2p}(r_2)\,|\,x_1 y_2 - x_2 y_1\,|\,dr_1\,dr_2}{\iint \rho_{2p}(r_1)\rho_{2p}(r_2)\,|\,x_1 y_2 - x_2 y_1\,|\,dr_1\,dr_2}$$

The integrals can be factored into radial and angular components. Since the angular parts cancel out, we get

$$E_{pot}^{nda}(2p^2) = 2E_{pot}^{nda}(2p).$$

It is perhaps somewhat unexpected that we also get the same result for the other two states ^{1}S($2p^2$) and ^{1}D($2p^2$), all of which are summarized in Table III.

Table III. Energy components for *2p²* states for Coulomb potential: standard expectations and nda values

States	E_{tot}	E_{kin}	E_{pot}	E_{kin}^{nda}	E_{pot}^{nda}
^{3}P, ^{1}S, ^{1}D	-1/4	1/4	-1/2	1/12	-1/3

We therefore conclude that all the components are the same for all three states, although two of them are singlets and one is triplet and also have different spatial symmetries. Note that this is strictly true only for the *noninteracting* system. This implies that the states might have equivalent nodes, and a little bit of analysis actually shows that. One can find that the node for the ^{3}P state can be described from the perspective of one of the two electrons as the plane defined by the angular momentum axis and the second electron. Similarly, the node of the ^{1}D state looks to one of the electrons as the plane which contains the angular momentum axis and is orthogonal to a plane defined by the second electron and the angular momentum axis. Finally, for ^{1}S states one of the electrons sees a plane which is orthogonal to the position vector of the second electron. In all three cases the node subset is therefore a plane which passes through the origin. Although these are only subsets of the complete 5D node, which is a hyperbolic hypersurface in 6D, the construction enables us to get an insight into their properties. In fact, this shows that there are only two nodal domains in all three cases: the scanning electron is either on one or the other side of the considered plane. Let us further define the equivalency for a set of nodes. By equivalency we mean that the nodes in the given set can be transformed to each other by coordinate transforms which are unitary (the determinant of the transformation matrix is equal to +1 or -1). This includes not only rotations but also reflections around the origin since otherwise the triplet nodes cannot be transformed to the singlet nodes. This can be inspected, for example, by transforming the node of one of the ^{1}D states

$$\Psi(1,2) = \rho_{2p}(r_1)\rho_{2p}(r_2)(x_1 y_2 + x_2 y_1),$$

to the node of ^{3}P state using the reflection of one coordinate component, say, $x_2 \rightarrow -x_2$ (see the wave function above). With some effort one could find that the nodes of the singlets are also equivalent. For this the reader might find it useful to consult our previous papers on related topics of nodal structure and analysis (*9*).

Note that for two *interacting* electrons in these states the nda components will *not* be identical since the e-e Coulomb repulsion will distort the wave function gradients in different ways for different states, and energetically, it will favor the triplet over the singlets.

The previous case of two non-interacting electrons can be further generalized to a given subshell *l=n-1* for any *n* and for any possible spin symmetry and occupations up to the maximum *2(2l+1).* The energies can be evaluated the same way as above, and it is revealing to explore the quasiclassical limit of the

Downloaded by PENNSYLVANIA STATE UNIV on May 28, 2012 | http://pubs.acs.org
Publication Date (Web): February 6, 2012 | doi: 10.1021/bk-2012-1094.ch007

Downloaded by PENNSYLVANIA STATE UNIV on May 28, 2012 | http://pubs.acs.org
Publication Date (Web): February 6, 2012 | doi: 10.1021/bk-2012-1094.ch007

nda estimates. Consider the class of atomic (excited) states such that *k* electrons occupy subshell *l=n-1* with any allowed spatial and spin symmetry. The state is $^{2S+1}L[\varphi_l^k]$ where *k* is the occupation. One can find:

$$E_{kin}^{nda}(k,l) = kZ^2 \frac{l}{2(l+1)^2(l+2)}$$

and

$$E_{pot}^{nda}(k,l) = -kZ^2 \frac{l}{(l+1)(l+2)},$$

so that all the non-interacting nodes for various symmetries are equivalent. By checking out the quasiclassical limit *l*→∞, we find

$$\lim_{l\to\infty} E_{kin}^{nda}(k,l) = \lim_{l\to\infty} E_{kin}(k,l)$$

and

$$\lim_{l\to\infty} E_{pot}^{nda}(k,l) = \lim_{l\to\infty} E_{pot}(k,l)$$

Clearly, averages over ψ^2 and $|\psi|$ become identical since the quantum effects become irrelevant for *l*→∞.

Let us now turn to the case of a system with interactions. Consider the two-particle 3D harmonic problem with the Coulomb interaction. The Hamiltonian is given by

$$H = (P_1^2 + P_2^2)/2 + \omega^2(r_1^2 + r_2^2)/2 + g_0/r_{12}$$

where g_0 is the interaction strength. For certain values of g_0 and ω, combined with particular symmetry, one can find simple analytical eigenstates. For $g_0=1$ and ω=1/4, the lowest triplet of P symmetry $^3P(sp)$ is given exactly as (*19*)

$$\Psi_{exact} = \Psi_0(1 + r_{12}/4)$$

where the noninteracting solution ψ_0 (i.e. $g_0=0$) is as usual

$$\Psi_0 = e^{-(r_1^2+r_2^2)\omega/2}(z_1 - z_2).$$

The noninteracting energy for this particular state ($n_1=n_2=l_1=0,\ l_2=1$) can be expressed as

$$E_0 = (2n_1 + 2n_2 + l_1 + l_2 + 3)\omega = 4\omega = 1$$

while the interacting exact eigenvalue is

$$E_{exact} = E_0 + 1/4.$$

These analytical solutions are sufficiently simple so that we can evaluate the nda components for various combinations of Hamiltonians and wave functions.

a. Noninteracting Hamiltonian and Noninteracting Wave Function

It is straightforward to find out that for $g_0=0$, we get

$$E_{pot}^{nda} = \frac{7\omega}{2} = \frac{7}{8},$$

and correspondingly

$$E_{kin}^{nda} = \frac{\omega}{2}.$$

b. Interacting Hamiltonian with g$_0$=1 and the Exact Eigenstat

After making transformation to center of mass and relative coordinates, one can find

$$E_{pot}^{nda} = \frac{7\omega}{2} + \frac{3}{8}\frac{\sqrt{\pi}}{4+3\sqrt{\pi}} + \frac{1+\sqrt{\pi}/2}{4+3\sqrt{\pi}},$$

and using the exact result above, we find

$$E_{kin}^{nda} = E - E_{pot}^{nda}.$$

c. Interacting Hamiltonian and Noninteracting Wave Function with the Correct Node

It is interesting to find out the estimation energy considering an approximate wave function which has the exact node. Let us first consider the noninteracting wave function. This will give quite a poor estimate since the potential and kinetic energy will be “unbalanced,” but it will still be instructive. Taking ψ_0 above, we get

$$E_{pot}^{nda} = \frac{7\omega}{2} + \frac{\sqrt{\pi\omega}}{4}$$

Downloaded by PENNSYLVANIA STATE UNIV on May 28, 2012 | http://pubs.acs.org
Publication Date (Web): February 6, 2012 | doi: 10.1021/bk-2012-1094.ch007

Downloaded by PENNSYLVANIA STATE UNIV on May 28, 2012 | http://pubs.acs.org
Publication Date (Web): February 6, 2012 | doi: 10.1021/bk-2012-1094.ch007

and

$$E_{kin}^{nda} = \frac{\omega}{2}.$$

This provides a clear demonstration that the energy obtained as nda sum is not necessarily an upper bound since

$$E_{kin}^{nda} + E_{pot}^{nda} \cong \frac{9.77\ldots\omega}{2} < E_{exact} = \frac{10\omega}{2},$$

which gives 1.226 ... vs. the exact value 5/4. Actually, the error is not very large considering how crude the trial state is. The dominant error is in the potential part, which comes out lower. This is caused by two effects: the noninteracting value of the exponent in the gaussian is not optimal and a secondary impact comes also from the absence of the correlation. The kinetic energy component is the same as in the noninteracting Hamiltonian, i.e. slightly larger than the exact. This results from the missing exchange hole which affects the gradient of the wave function on the nodal surface. Obviously, these ideas should be explored further and such investigations are currently in progress.

Conclusions

We have introduced the nodal hypersurface and domain averages, dubbed "nda," as a tool for characterization of the nodes of trial wave functions. We have demonstrated their properties on a number of few-particle cases and analyzed implications of these results. For example, we were able to distinguish the nodal differences between degenerate states of the same and different symmetries. These characteristics enabled us to identify the equivalence of nodes in unexpected situations such as between noninteracting singlets and triplets. Clearly, the results show interesting potential and deserve further investigation. The theory can be further explored with much more powerful developments which will be presented elsewhere.

This work is supported by ARO, DOE and by the NSF grants DMR-0804549 and OCI-0904794. Discussions with Wei Ku on topics related to this paper are gratefully acknowledged.

References

1. (a) Ceperley, D. M.; Kalos, M. H. Quantum Many-Body Problems. In *Monte Carlo Methods in Statistical Physics*; Binder, K., Ed.; Springer: Berlin, 1979; pp 145−194. (b) Schmidt, K. E.; Ceperley, D. M. Monte Carlo Techniques for Quantum Fluids, Solids and Droplets. In *Monte Carlo Methods in Statistical Physics II*; Binder, K., Ed.; Springer: Berlin, 1984; pp 279−355.
2. Hammond, B. L.; Lester, W. A., Jr.; Reynolds, P. J. *Monte Carlo Methods in ab initio Quantum Chemistry*; World Scientific: Singapore, 1994.

3. Anderson, J. B. Exact Quantum Chemistry by Monte Carlo Methods. In *Understanding Chemical Reactivity*; Langhoff, S. R., Ed.; Kluwer: Dordrecht, 1995; pp 1−45.
4. Ceperley, D. M.; Mitas, L. Quantum Monte Carlo Methods in Chemistry. In *Advances in Chemical Physics*; Prigogine, I., Rice, S. A., Eds.; Wiley: New York, 1996; Vol. XCIII, pp 1−38.
5. Foulkes, W. M. C.; Mitas, L.; Needs, R. J.; Rajagopal, G. Quantum Monte Carlo for solids. *Rev. Mod. Phys.* **2001**, *73*, 33–83.
6. Schmidt, K. E.; Moskowitz, J. W. Correlated Monte Carlo wave functions for the atoms He through Ne. *J. Chem. Phys.* **1990**, *93*, 4172.
7. Kolorenc, J.; Mitas, L. Quantum Monte Carlo calculations of structural properties of FeO solid under pressure. *Phys. Rev. Lett.* **2008**, *101*, 185502.
8. (a) Bajdich, M.; Wagner, L. K.; Drobny, G.; Mitas, L.; Schmidt, K. E. Pfaffian wave functions for electronic structure quantum Monte Carlo. *Phys. Rev. Lett.* **2006**, *96*, 130201. (b) See also *Phys. Rev. B* **2008**, *77*, 115112.
9. (a) Mitas, L. Structure of fermion nodes and nodal cells. *Phys. Rev. Lett.* **2006**, *96*, 240402. (b) Bajdich, M.; Mitas, L.; Drobny, G.; Wagner, L. K. Approximate and exact nodes of fermionic wavefunctions: Coordinate transformations and topologies. *Phys. Rev. B* **2005**, *72*, 075131.
10. Kolorenc, J.; Mitas, L. Applications of quantum Monte Carlo in condensed systems. *Rep. Prog. Phys.* **2011**, *74*, 026502.
11. Grossman, J. C.; Rohlfing, M.; Mitas, L.; Louie, S. G.; Cohen, M. L. High accuracy many-body calculational approaches for excitations in molecules. *Phys. Rev. Lett.* **2001**, *86*, 472.
12. Wagner, L. K.; Bajdich, M.; Mitas, L. QWalk: Quantum Monte Carlo code for electronic structure. *J. Comput. Phys.* **2009**, *228*, 3390.
13. (a) Bajdich, M.; Mitas, L. Electronic structure quantum Monte Carlo. *Acta Phys. Slovaca* **2009**, *59*, 81−168. (b) Mitas, L. Electronic structure by Quantum Monte Carlo: Atoms, molecules and solids. *Comp. Phys. Commun.* **1996**, *97*, 107.
14. Anderson, J. B. Quantum chemistry by random walk. *J. Chem. Phys.* **1976**, *65*, 4121.
15. Ceperley, D. M.; Alder, B. J. Quantum Monte Carlo. *Science* **1986**, *231*, 555.
16. Kruger, F.; Zaanen, J. Fermionic quantum criticality and the fractal nodal surface. *Phys. Rev. B* **2008**, *78*, 035104.
17. Umrigar, C. J.; Wilson, K. G.; Wilkins, J. W. Optimized trial wave functions for quantum Monte Carlo calculations. *Phys. Rev. Lett.* **1988**, *60*, 1719.
18. Bressanini, D.; Ceperley, D. M.; Reynolds, P. J. In *Recent Advances in Quantum Monte Carlo Methods*; Lester, W. A., Ed.; World Scientific: Singapore, 2002; Part II, p 1.
19. Taut, M. Two electrons in an external oscillator potential: Particular analytic solutions of a Coulomb correlation problem. *Phys. Rev. A* **1993**, *48*, 3561.

Downloaded by PENNSYLVANIA STATE UNIV on May 28, 2012 | http://pubs.acs.org
Publication Date (Web): February 6, 2012 | doi: 10.1021/bk-2012-1094.ch007

Downloaded by UNIV OF GUELPH LIBRARY on May 28, 2012 | http://pubs.acs.org
Publication Date (Web): February 6, 2012 | doi: 10.1021/bk-2012-1094.ch008

Chapter 8

A Quantum Monte Carlo Study of the Ground State Chromium Dimer

Kenta Hongo[1,2] and Ryo Maezono[*,1]

[1]Japan Advanced Institute of Science and Technology, 1-1 Asahidai, Nomi, Ishikawa 923-1282, Japan
[2]The Institute of Statistical Mathematics, 10-3 Midori-cho, Tachikawa, Tokyo 190-8562, Japan
[*]E-mail: rmaezono@mac.com

We take variational and diffusion quantum Monte Carlo (VMC and DMC) methods to investigate the chemical binding of the ground state chromium dimer, employing various single determinant (SD) or multi-determinant (MD) wavefunctions multiplied by a Jastrow factor as a trial/guiding wavefunction. The molecular orbitals (MOs) entering the SD wavefunction were calculated using restricted or unrestricted Hartree-Fock or density functional theory (DFT) calculations where five commonly-used local (SVWN5), semi-local (PW91 and BLYP), and hybrid (B1LYP and B3LYP) functionals were examined. The MD expansions were obtained from the complete-active space self-consistent field, generalized valence bond, and unrestricted configuration interaction methods. We also adopted the UB3LYP MOs to construct the MD expansion and optimized their coefficients at the VMC level. The DMC binding curves have a minimum indicating a bound state, but the comparison of atomic and molecular energies gives rise to a negative binding energy for the DMC simulations.

In Advances in Quantum Monte Carlo; Tanaka, S., et al.;
ACS Symposium Series; American Chemical Society: Washington, DC, 2012.

Downloaded by UNIV OF GUELPH LIBRARY on May 28, 2012 | http://pubs.acs.org
Publication Date (Web): February 6, 2012 | doi: 10.1021/bk-2012-1094.ch008

The chromium dimer (Cr_2) has been a notorious molecular system long known for its chemical binding mechanism involving a highly complicated blend of 4*s*-4*s* and 3*d*-3*d* interactions with antiferromagnetic coupling. The ground state is experimentally found to be a singlet state ${}^1\Sigma_g^+$, but up- and down-spin electrons in Cr_2 are antiferromagnetically localized on each of the Cr atom. A tremendous number of experimental and theoretical studies have been devoted toward understanding such a complicated mechanism so far. A comprehensive list of the literatures as well as a detailed description of the binding mechanism are found in Ref. (*1*).

To summarize its binding nature, Cr_2 can be regarded as a ‘near-degenerate’ system having metallic multiple bonds in terms of traditional molecular orbital (MO) theories. To describe such a system properly, multi-reference theories such as multi-reference configuration interaction (MRCI), coupled-cluster (MRCC), and second-order perturbation (CASPT2) methods are essential beyond restricted or unrestricted Hartree-Fock (RHF/UHF) as well as the generalized valence bond (GVB) or complete active space self-consistent field (CASSCF) methods. Although sophisticated multi-reference methods have recently provided a good evaluation of the equilibrium bond length ($R_{\rm e}$) comparable with experiment, there is still room to improve further the accuracy of the binding energy ($D_{\rm e}$); for instance, recent spectroscopic experiments reported $R_{\rm e}$ = 1.6788 Å (*2*) and $D_{\rm e}$ = 1.56 ± 0.05 eV (*3*), while the latest MRCC (CBS extrapolation) values of $R_{\rm e}$ and $D_{\rm e}$ deviate from experiment by 0.2% and 10%, respectively ($R_{\rm e}$ = 1.675 Å and $D_{\rm e}$ = 1.400 eV) (*4*). In density functional theory (DFT), though various exchange-correlation (XC) functionals are available such as the localized density approximation (LDA), generalized gradient approximation (GGA) as well as the hybrid XC functionals (e.g., B3LYP) in both restricted and unrestricted treatments, qualitatively satisfactory results have not been achieved as well, implying that a delicate and subtle balance between exchange and correlation should be involved in XC functionals in order to appropriately describe the chemical binding in Cr_2.

Quantum Monte Carlo (QMC) methods (*5*, *6*) are one of the most accurate techniques in state-of-the-art *ab initio* calculations for quantitative descriptions of electronic structures. There are two typical QMC calculations, *i.e.*, variational and diffusion Monte Carlo (VMC and DMC) methods. VMC is not usually accurate enough since its result strongly depends on the correlated trial wavefunction adopted. DMC is a technique for numerically solving the many-electron Schrödinger equation for stationary states using imaginary time evolution. The fixed-node approximation is usually assumed to maintain the fermionic anti-symmetry in DMC. Although the fixed-node DMC can accurately evaluate the ground state energy of many atoms and molecules using only the trial node from a single determinant (SD), it sometimes fails, especially for near-degenerate systems such as the Be atom. This implies that the fixed-node DMC method can work well for the dynamic correlation, but not for the static (or non-dynamic) correlation which should be included at the stage of choosing the fixed-node guiding wavefunction. Hence Cr_2 can be regarded as a good challenge to QMC.

In our previous study (*1*) we applied VMC and DMC methods to the ground state Cr_2 using various choices of Slater-Jastrow trial wavefuntions in both single- and multi-determinant forms. The MOs in the single determinant were obtained using restricted or unrestricted HF and DFT calculations including SVWN5 LDA, PW91 and BLYP GGA, B1LYP and B3LYP hybrid functionals. The multideterminant expansions were obtained from the GVB and (truncated) unrestricted CISD methods. In this article we shall review our previous study and report our QMC results obtained using additional multideterminant calculations.

Quantum Monte Carlo Methods

We take standard variational and fixed-node diffusion Monte Carlo (VMC and DMC) methods with various choices of trial/guiding wavefunctions to calculate the ground state energy and binding curve of Cr_2. Quality of the guiding wavefunctions in DMC is examined according to the variational principle with respect to the fixed node (*5*, *6*), while practical DFT calculations do not necessarily satisfy the variational principle because of their approximate XC functionals. Note that one cannot therefore compare the QMC total energies with the DFT (SCF) ones. Gaussian03 (*7*) was used for SCF calculations, while we used CASINO ver.3.0 (*8*) for QMC calculations. Some calculations (HF and GVB) were carried out using GAMESS (*9*) for SCF and QWalk (*10*) for QMC. General and detailed references about the methods themselves are available in the form of the textbooks and review papers (*5*, *6*) as well as in this book. Here we give a brief description of our pseudopotential and trial wavefunctions. More detailed information is found in our previous study (*1*).

The inner Neon core (10 core electrons) of the Cr atom were replaced with a small core norm-conserving pseudopotential which is constructed from Dirac-Fock atomic solutions, *i.e.*, Lee-Needs (LN) soft pseudopotential (*11*) using Troullier-Martins construction. The ground state Cr_2 molecule has 14 up- and 14 down-spin electrons. The present non-local pseudopotentials were evaluated by the T-move scheme (*12*) which is devised to reduce the instability and bias due to the locality approximation (*13*).

We adopted the many-body (trial) wavefunction in the form of Slater-Jastrow type. The Slater part was expanded in terms of direct products of up- and down-spin Slater determinants, associated with expansion coefficients. The single determinant wavefunction corresponds to taking only one expansion term. The orbital functions in the determinants were expanded with a contracted Gaussian basis set (17s18p15d6f)/[8s8p7d3f] (whose contraction exponents and contraction coefficients are available in the Supplementary Materials of Ref. (*1*)). Variety of the XC functionals are examined to construct orbital functions including restricted or unrestricted HF, SVWN LDA, PW91 and BLYP GGA, B1LYP and B3LYP hybrid functionals. In addition to a single-determinant form of the many-body wavefunction, we also tried several multi-determinant (MD) forms. The multideterminant expansions were obtained from the CASSCF, GVB, and truncated unrestricted CISD (UCISD). For all the SD and the best MD trial/guiding wavefunctions, we also take into account the backflow transformation (*14*), which is introduced to modify the nodal surface variationally (*15*, *16*). It consists of electron-nucleus and electron-electron terms whose

Downloaded by UNIV OF GUELPH LIBRARY on May 28, 2012 | http://pubs.acs.org
Publication Date (Web): February 6, 2012 | doi: 10.1021/bk-2012-1094.ch008

parameters were optimized by the filtered reweighted variance minimization scheme (*17*) allowing spin polarized degrees of freedom. As for the Jastrow part (*18*), we employed one-, two-, and three-body terms (*19*) which take into account the dynamical correlation due to electron-nucleus, electron-electron, and electron-electron-nucleus coalescence, respectively. The electron-electron cusp condition (*20*) is imposed in the two-body term. Variational parameters in the Jastrow part are designed to be able to include spin-polarized case. They were optimized individually at each bond length by the variance minimization (*17*) as well as the energy minimization (*21*) procedures.

Downloaded by UNIV OF GUELPH LIBRARY on May 28, 2012 | http://pubs.acs.org
Publication Date (Web): February 6, 2012 | doi: 10.1021/bk-2012-1094.ch008

Single Determinant Calculations

We shall first summarize our findings in QMC calculations within the SD treatment, according to Ref. (*1*). UB3LYP turns out to give the variationally best total energy. Except for HF, the unrestricted DFT nodes are found to be better than the corresponding restricted ones. At the SCF level, RHF gives a much higher energy than UHF, which is a well-known failure of restricted treatments for a spin-polarized system (*22*). In DMC, however, the amplitude of the many-body wavefunction is automatically adjusted by the projection operation and is not directly governed by the XC approximation. The results show that the RHF nodal surface is superior to the UHF one, leading us to examine restricted methods for generating the trial nodal surface.

Any choice of trial nodes gives a binding curve with an energy minimum, but unrestricted trial nodes end up with a much larger R_e and smaller D_e in the QMC final results, compared with the experimental values. Though ULDA and UGGA reproduce a proper R_e, it is found that the QMC calculations with these trial nodes overestimate R_e. The restricted nodes recover fairly well R_e even at QMC, but they give a higher energy than the unrestricted ones. At the experimental R_e, we could not get a stable molecular energy lower than twice the atomic energy (zero-binding energy) at the QMC level.

Multi-Determinant Calculations

Within restricted multideterminant treatments, CASSCF and GVB are both expected to give a proper description of the spin polarized Cr_2 (*23*), due to their multideterminant expansions with near-degenerate orbitals. As for the CAS trial wavefunction, we attempted to use CAS(12,12) arising from the 4s(1)3d(5) atomic orbitals, but it has too many determinants for QMC to be performed. Instead, we employed CAS(2,4) and CAS(2,7), though they do not have a significant physical meaning. CAS(12,12) has 427,350 configuration state functions (CSFs), while CAS(2,4) and CAS(2,7) have 16 and 49 CSFs, respectively. In contrast to CAS, GVB properly describes a spin polarization in Cr_2 with more compact form of the MD expansion. Our GVB wavefunction was constructed from 12 active occupied MOs up to level 20 near HOMO-LUMO level, similar to CAS(12,12). This provides a very compact form of the MD expansion with only 64 terms. An explicit form of the present GVB wavefunction is given in Ref. (*1*). In this study the GVB binding curves were not evaluated because we could not obtain reliably converged results at stretched geometries.

Table I. HF, UB3LYP, CASSCF, GVB, UCISD, and QMC energies at the experimental bond length (R_e = 1.68 Å)

Methods	*SCF*	*VMC*	*DMC*
UHF	-171.701	-172.665(6)	-172.903(2)
RHF	-171.097	-172.584(4)	-172.911(2)
UB3LYP	-172.974	-172.756(2)	-172.954(2)
CAS(2,4)	-171.403	-172.548(2)	-172.727(3)
CAS(2,7)	-171.405	-172.559(2)	-172.743(3)
GVB	-171.624	-172.698(6)	-172.861(2)
GVBopt		-172.723(2)	-172.933(2)
UCISD(UHF)	-172.599	-172.772(2)	-172.926(3)
UCISD(HOMO-LUMO±6)	-172.599	-172.744(2)	-172.901(2)
UCISD(UB3LYP+3)		-172.794(2)	-172.968(2)
UCISD(UB3LYP+10)		-172.747(2)	-172.950(2)
Best ZBE		-172.931(2)	-173.012(3)

NOTE: Energies are in units of hartree (a.u.). The number in the parenthesis refers to the estimated error in the last digit. Except for the RHF and UHF trial/guiding wavefunctions, the QMC results are those without the backflow transformation. ZBE stands for the zero-binding energy, and 'GVBopt' for GVB with coefficients optimized further by VMC (see text).

The CAS(2,4) and CAS(2,7) wavefunctions give rise to a higher energy than the RHF wavefunction at the VMC and DMC levels. The GVB wavefunction achieves a better (lower) VMC energy than using the HF one, while the former turns out to give a higher DMC energy than the latter. Then we tried to optimize the coefficients further at the VMC level using a mixed scheme between energy and variance minimization (*21*) with 95% weight on the former. Using this (shown as 'GVBopt' in Table I), we obtained a better DMC value than when using HF, but still above the best zero-binding energy.

Figure 1 shows (a) SCF, (b) VMC, and (c) DMC binding curves using CAS(2,4), CAS(2,7) and UB3LYP. Though CAS(2,4) and CAS(2,7) could not achieve a lower DMC energy than UB3LYP, several interesting behaviors are found as follows: At the SCF level, CAS(2,7) gives a binding curve with a similar shape to UB3LYP, though overestimating R_e. The VMC and DMC values of R_e, in turn, get shorter, and their shapes of the binding curve are similar to the restricted SD cases. This implies that the CAS nodal structure is essentially the same as the restricted SD one, but the terms involved in the CAS expansion well describe the localized amplitude similar to the unrestricted SD cases.

Downloaded by UNIV OF GUELPH LIBRARY on May 28, 2012 | http://pubs.acs.org
Publication Date (Web): February 6, 2012 | doi: 10.1021/bk-2012-1094.ch008

Downloaded by UNIV OF GUELPH LIBRARY on May 28, 2012 | http://pubs.acs.org
Publication Date (Web): February 6, 2012 | doi: 10.1021/bk-2012-1094.ch008

(a) SCF/CASSCF and B3LYP

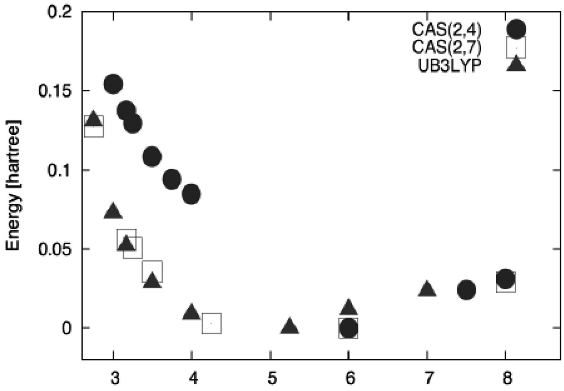

(b) VMC/CASSCF and UB3LYP (w/o Backflow)

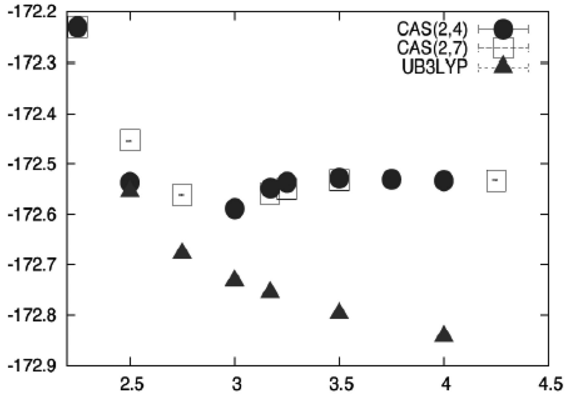

(c) DMC/CASSCF and UB3LYP (w/o Backflow)

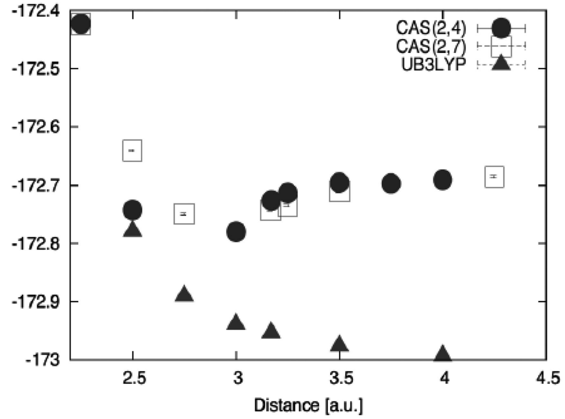

Figure 1. (a) SCF, (b) VMC, and (c) DMC binding curves using CAS(2,4), CAS(2,7), and UB3LYP. Note that in (a) SCF energies are shifted so that each minimum, -171.540 , -171.461, and -173.026 hartree to be zero. In QMC simulations, (b) and (c), error bars are within symbol size.

Since our restricted treatments could not give better results than UB3LYP, we tried UCISD (unrestricted CI singles and doubles) methods. Using a UHF reference, the UCISD expansion gives 7,521,823 terms, all of which cannot be taken into account in a QMC calculation. We truncated this expression into 35 determinants, removing those terms with coefficients $|c_i| < 0.01$. The coefficients were optimized further at the VMC level, first by weight-limited variance minimizations (*8*), followed by energy minimizations. This wavefunction is referred to as 'UCISD(UHF)' in Table I. Using this, we achieved a lower VMC energy than when using UB3LYP, indicating that our VMC optimization of the CI coefficients was successful. At DMC, however, UCISD(UHF) turned out to give a worse result than UB3LYP. We also tried another choice of expansion: 67 excited configurations, in which the active space was HOMO±6 and the single and double excitations of occupied orbitals were restricted to virtual orbitals with the same symmetry [UCISD(HOMO-LUMO±6)]. This gives, however, a worse result than UB3LYP even at the VMC level.

As can be seen in Table I, the above CI treatments could not give any variationally better trial node than UB3LYP. The easiest way to go beyond those treatments would be to add UCISD expansions to UB3LYP because it is the best starting point. By considering the UB3LYP orbital symmetry near the HOMO level, we made two different sizes of CI expansions: The first one took into account only 3 virtual orbitals above the LUMO, including only σ and π symmetries [UCISD(UB3LYP+3)], and the second was a larger one with 10 virtual orbitals in which σ, π, and δ symmetries were included [UCISD(UB3LYP+10)]. In both cases we considered only such excited configurations between the orbitals with the same symmetry, resulting in around 50 and 650 determinants for UCISD(UB3LYP+3) and UCISD(UB3LYP+10), respectively (the numbers of determinants vary a little amount depending on *R*).

VMC using the UCISD(UB3LYP+3) trial wavefunction gives a better result than when using the UB3LYP one because the former includes more variational degrees of freedom to be optimized. As for UCISD(UB3LYP+10), however, we could not achieve a satisfactory optimization, giving a higher VMC energy [-172.747(2) hartree] than the initial UB3LYP calculation [-172.756(2) hartree]. The UCISD(UB3LYP+3) node gives a lower DMC energy than the UB3LYP node. Focusing on UCISD(UB3LYP+3), we further introduced the backflow transformation. The DMC with the backflow transformation gives a lower energy [-172.992(3) hartree] than that without the backflow transformation [-172.968(2) hartree], but still above the best ZBE [-173.012(3) hartree].

Summary and Perspective

We studied the chemical binding of the ground state Cr_2 molecule using the fixed node DMC method. Various different types of nodal structures were compared based on the variational principle with respect to the node of the DMC guiding function. We tested various choices of XC functionals in restricted or unrestricted forms. In addition to the single determinant form, we also tried several multi-determinant wavefunction obtained from the CASSCF, GVB, and

Downloaded by UNIV OF GUELPH LIBRARY on May 28, 2012 | http://pubs.acs.org
Publication Date (Web): February 6, 2012 | doi: 10.1021/bk-2012-1094.ch008

Downloaded by UNIV OF GUELPH LIBRARY on May 28, 2012 | http://pubs.acs.org
Publication Date (Web): February 6, 2012 | doi: 10.1021/bk-2012-1094.ch008

UCISD methods. Our best guiding wavefunction was found to be the UCISD one with the UB3LYP orbitals, whose expansion coefficients were optimized at the VMC level. Although our best DMC result even using the backflow transformation cannot reproduce the binding of Cr_2 at the experimental R_e, we believe that our benchmark on various choices of the trial/guiding wavefunctions would be helpful to calibrate the performance of current QMC methods as well as to exploit more accurate trial/guiding wavefunctions.

We also attempted to use another many-body wavefunction form, Pfaffian (*24*), which is available in QWalk. However we failed to optimize the off-diagonal elements of the Pfaffian and then we could not obtain reliable results, so not reported here. Our work on the Cr_2 molecule is still in progress for obtaining the Pfaffian wavefunction as well as exploiting which levels of MOs are to be included in the multideterminant wavefunction.

References

1. Hongo, K.; Maezono, R. *Int. J. Quantum Chem.* **2011**, DOI: 10.1002/qua.23113.
2. Bondybey, V. E.; English, J. H. *Chem. Phys. Lett.* **1983**, *50*, 1451.
3. Simard, B.; Lebeault-Dorget, M.-A.; Marijnissen, A.; ter Meulen, J. J. *J. Chem. Phys.* **1998**, *108*, 9668.
4. Müller, T. *J. Phys. Chem. A* **2009**, *113*, 12729.
5. Hammond, B. L.; Lester, W. A., Jr.; Reynolds, P. J. *Monte Carlo Methods in ab Initio Quantum Chemistry*; World Scientific: Singapore, 1994.
6. Foulkes, W. M. C.; Mitas, L.; Needs, R. J.; Rajagopal, G. *Rev. Mod. Phys.* **2001**, *73*, 33.
7. Frisch, M. J.; Trucks, G. W.; Schlegel, H. B.; Scuseria, G. E.; Robb, M. A.; Cheeseman, J. R.; Montgomery, J. A. Jr.; Vreven, T.; Kudin, K. N.; Burant, J. C.; Millam, J. M.; Iyengar, S. S.; Tomasi, J.; Barone, V.; Mennucci, B.; Cossi, M.; Scalmani, G.; Rega, N.; Petersson, G. A.; Nakatsuji, H.; Hada, M.; Ehara, M.; Toyota, K.; Fukuda, R.; Hasegawa, J.; Ishida, M.; Nakajima, T.; Honda, Y.; Kitao, O.; Nakai, H.; Klene, M.; Li, X.; Knox, J. E.; Hratchian, H. P.; Cross, J. B.; Bakken, V.; Adamo, C.; Jaramillo, J.; Gomperts, R.; Stratmann, R. E.; Yazyev, O.; Austin, A. J.; Cammi, R.; Pomelli, C.; Ochterski, J. W.; Ayala, P. Y.; Morokuma, K.; Voth, G. A.; Salvador, P.; Dannenberg, J. J.; Zakrzewski, V. G.; Dapprich, S.; Daniels, A. D.; Strain, M. C.; Farkas, O.; Malick, D. K.; Rabuck, A. D.; Raghavachari, K.; Foresman, J. B.; Ortiz, J. V.; Cui, Q.; Baboul, A. G.; Clifford, S.; Cioslowski, J.; Stefanov, B. B.; Liu, G.; Liashenko, A.; Piskorz, P.; Komaromi, I.; Martin, R. L.; Fox, D. J.; Keith, T.; Al-Laham, M. A.; Peng, C. Y.; Nanayakkara, A.; Challacombe, M.; Gill, P. M. W.; Johnson, B.; Chen, W.; Wong, M. W.; Gonzalez, C.; Pople, J. A. *Gaussian 03*, Revision E.01; Gaussian: Wallingford, CT, 2004.
8. Needs, R. J.; Towler, M. D.; Drummond, N. D.; Rios, P. L. *J. Phys.: Condens. Matter* **2010**, *22*, 023201.

9. Schmidt, M. W.; Baldridge, K. K.; Boatz, J. A.; Elbert, S. T.; Gordon, M. S.; Jensen, J. H.; Koseki, S.; Matsunaga, N.; Nguyen, K. A.; Su, S. J.; Windus, T. L.; Dupuis, M.; Montgomery, J. A. *J. Comput. Chem.* **1993**, *14*, 1347.
10. Wagner, L. K.; Bajdich, M.; Mitas, L. *J. Comput. Phys.* **2009**, *228*, 3390.
11. (a) Lee, Y. Private communication. (b) See also Lee, Y.; Kent, P. R. C.; Towler, M. D.; Needs, R. J.; Rajagopal, G. *Phys. Rev. B* **2000**, *62*, 13347, for large-core version of these pseudopotentials.
12. Casula, M. *Phys. Rev. B* **2006**, *74*, 161102.
13. Mitas, L.; Shirley, E. L.; Ceperley, D. M. *J. Chem. Phys.* **1991**, *95*, 3467.
14. Feynman, R. P.; Cohen, M. *Phys. Rev. Lett.* **1956**, *102*, 1189.
15. Drummond, N. D.; Rios, P. L.; Ma, A.; Trail, J. R.; Spink, G. G.; Towler, M. D.; Needs, R. J. *J. Phys. Chem.* **2006**, *124*, 224104.
16. Rios, P. L.; Ma, A.; Drummond, N. D.; Towler, M. D.; Needs, R. J. *Phys. Rev. E* **2006**, *74*, 066701.
17. Drummond, N. D.; Needs, R. J. *Phys. Rev. B* **2005**, *72*, 085124.
18. Jastrow, R. J. *Phys. Rev.* **1995**, *98*, 1479.
19. Drummond, N. D.; Towler, M. D.; Needs, R. J. *Phys. Rev. B* **2004**, *70*, 235119.
20. Kato, T. *Commun. Pure Appl. Math.* **1957**, *10*, 151.
21. Umrigar, C. J.; Filippi, C. *Phys. Rev. Lett.* **2005**, *94*, 150201.
22. Szabo, A.; Ostlund, N. S. *Modern Quantum Chemistry*; McGraw-Hill: New York, 1989.
23. Bauschlicher, C. W., Jr. *J. Chem. Phys.* **1980**, *72*, 880.
24. Bajdich, M.; Mitas, L.; Drobn, G.; Wagner, L. K.; Schmidt, K. E. *Phys. Rev. Lett.* **2006**, *96*, 130201.

Downloaded by UNIV OF GUELPH LIBRARY on May 28, 2012 | http://pubs.acs.org
Publication Date (Web): February 6, 2012 | doi: 10.1021/bk-2012-1094.ch008

Downloaded by PENNSYLVANIA STATE UNIV on May 28, 2012 | http://pubs.acs.org
Publication Date (Web): February 6, 2012 | doi: 10.1021/bk-2012-1094.ch009

Chapter 9

A Benchmark Quantum Monte Carlo Study of Molecular Crystal Polymorphism: A Challenging Case for Density-Functional Theory

Mark A. Watson,*,[1] Kenta Hongo,[1,2] Toshiaki Iitaka,[3] and Alán Aspuru-Guzik[1]

**[1]Department of Chemistry and Chemical Biology, Harvard University,
12 Oxford Street, Cambridge, Massachusetts 02138, U.S.A.
[2]The Institute of Statistical Mathematics, 10-3 Midori-cho,
Tachikawa, Tokyo 190-8562, Japan
[3]Computational Astrophysics Laboratory, RIKEN, 2-1 Hirosawa,
Wako, Saitama 351-0198, Japan
*E-mail: mark.watson@cantab.net**

We have applied the diffusion Monte Carlo method to determine the relative stabilities of the two polymorphs of the *para*-diiodobenzene organic molecular crystal. Our result predicts the α phase to be more stable than the β phase at zero temperature (with a 2% statistical uncertainty) in agreement with experiment. We used the result to benchmark eight commonly-used local, semi-local and hybrid density functionals. The semi-local and hybrid functionals incorrectly predict the β phase to be the most stable using the experimental crystal structures, while the addition of an empirical dispersion correction was found to strongly over-compensate this error. The local functionals are the most consistent, but this is almost certainly due to fortuitous error cancellation. We conclude that there is a real need for efficient, accurate many-body methods, or improved density-functionals, which can accurately capture electron correlation and dispersion interactions in molecular crystals.

In Advances in Quantum Monte Carlo; Tanaka, S., et al.;
ACS Symposium Series; American Chemical Society: Washington, DC, 2012.

Downloaded by PENNSYLVANIA STATE UNIV on May 28, 2012 | http://pubs.acs.org
Publication Date (Web): February 6, 2012 | doi: 10.1021/bk-2012-1094.ch009

1. Introduction

Recent progress in the understanding and synthesis of advanced structural and functional materials (*1–6*) presents exciting challenges to the fields of electronic structure theory and computational materials science. For example, much attention has recently been devoted to the discovery and assessment of organic molecular crystals for the fabrication of nanoelectronic devices and organic semiconductors (*7–11*). Theoretical methods can aid in the first-principles characterization and design of such materials *in silico*, but their potential has yet to be fully realized. The major obstacle is the steep growth in computational cost of the most accurate *ab initio* methods when treating macromolecules or solid-state systems compared to simpler gas-phase calculations. In practice, therefore, significant compromises are usually made between the level of theory and the computational feasibility, and most often the only practical method available is a variation of density-functional theory (DFT) (*12*). The purpose of this work is to therefore benchmark the performance of DFT against an accurate, reliable, but expensive many-body method. We have chosen a particularly challenging result - the relative stabilities of the crystal polymorphs of *para*-diiodobenzene (DIB) - in order to demonstrate the limitations of many commonly-used DFT exchange-correlation functionals.

DIB is remarkable among organic molecular semiconductors because of its excellent charge-transport properties, reflected in its unusually high room-temperature hole mobility, which is greater than 10 cm$_2$/(Vs) (*13*). It has therefore attracted much interest in the field of organic electronics. A particularly interesting feature of DIB is the fact that it exists in two different crystal phases, known as the α and β polymorphs. Polymorphism is the ability of a material to exist in more than one crystalline state while retaining the same chemical composition, but displaying different crystal packing motifs, physical and chemical properties (*14*, *15*). In many cases, only one polymorph will be useful as the active ingredient of a drug (*16–18*) or as the component of a functional material. Brillante *et al.* were the first to investigate the polymorphism of DIB theoretically (*19*). They used density-functional theory and found that the α phase is less stable than the β phase by about 96 meV per unit cell at zero temperature. Unfortunately, this contradicts experiment, which shows that the α phase is the most stable up to about 326 K (*20*, *21*). A detailed understanding of polymorphism can therefore be of great importance, but the treatment of this phenomenon is a major challenge for first-principles methods. Indeed, the rigorous treatment of crystalline materials, or the *ab initio* prediction of crystal structures, is a well-known and long-standing problem in general (*22*, *23*). Theoretical studies of polymorphism (*24*) are particularly difficult due to the very small energy changes that need to be accurately captured; in the case of DIB, on the order of 1 meV per atom.

Currently, DFT is the method of choice for performing *ab initio* calculations on solid-state materials or molecular crystals because it is an effective independent-particle theory and is highly competitive in terms of the balance between computational cost and accuracy. As a result, DFT studies have been routinely used by several groups to explore the properties of DIB, such as

Downloaded by PENNSYLVANIA STATE UNIV on May 28, 2012 | http://pubs.acs.org
Publication Date (Web): February 6, 2012 | doi: 10.1021/bk-2012-1094.ch009

hole mobility (*25*, *26*). However, the accuracy and reliability of conventional exchange-correlation functionals for studying sensitive phenomena such as polymorphism is questionable. Indeed, despite its success, DFT has some well-known weaknesses. For example, conventional functionals often fail to accurately capture dispersion interactions, as was comprehensively shown in the recent benchmark study of Zhao and Truhlar (*27*). In molecular crystal calculations, especially when comparing polymorphs, it is reasonable to expect that an accurate treatment of these interactions is important. Even for some covalent clusters, such as C_{20} or B_{20}, several commonly used functionals have been shown to be highly unreliable in predicting geometries and relative ground-state energies (*28*). Nevertheless, in most cases, DFT is essentially the most accurate *ab initio* method available due to the prohibitive computational cost of the alternatives.

In gas-phase molecular quantum chemistry, there is a systematic hierarchy of well-established, convergent approximations to the many-body solution of the electronic Schrödinger equation (*29*). For small or medium-sized systems, highly accurate predictions can be made, and using local correlation methods, their high computational cost can be reduced to allow applications on systems with as many as one thousand atoms (*30–33*). There is much to be done, however, to extend these successes to the solid-state regime. Hartree-Fock (HF) theory is the lowest order wavefunction approximation, and like DFT it is a single-particle theory. As a result, efficient implementations have been realized in terms of crystalline orbital theory (*34*, *35*). In contrast, higher-order wavefunction methods show a much less favorable scaling of computational cost as one moves to infinite systems, since they are unable to exploit the translational symmetry of the periodic lattice in the same way (*36*, *37*). For example, the HF (or DFT) method usually scales like $O(n^{2\text{-}3})$ in the size of the basis n, and in a crystalline orbital implementation, the computational cost grows as $O(n^{2\text{-}3}K)$, where K is the total number of **k**-points in the first Brillouin zone. In contrast, the coupled-cluster singles and doubles (CCSD) method usually scales like $O(n^6)$, but has a much more expensive cost which grows like $O(n^6K^4)$ in a crystalline calculation. Nevertheless, considerable effort has been devoted to this problem in recent years and interesting progress is being made (*36–42*). For example, a cluster-expansion method has been used to successfully apply many-body wavefunctions routinely to molecular crystals (*43*), albeit with additional approximations.

As an alternative to the above wavefunction hierarchy, we consider in this work the quantum Monte Carlo (QMC) method. QMC methods can evaluate the total energy of many-electron systems to high accuracy (*44–46*) because they can explicitly take into account electron correlation effects at reasonable cost by means of a stochastic approach. Here, we employ one of the most accurate QMC methods, namely, diffusion Monte Carlo (DMC), which has been shown to have an accuracy comparable to the CCSD(T) (CCSD with perturbative triple excitations) wavefunction method in a cc-pVQZ basis set (*47*). However, while CCSD(T) scales like $O(n^7)$, DMC has a more modest cost, which grows linearly to cubicly with the size of the system, albeit with a larger prefactor (*48*). Nevertheless, while DMC offers an attractive alternative, the issue of computational scaling with respect to the number of **k**-points in crystalline systems remains. Here we do not

Downloaded by PENNSYLVANIA STATE UNIV on May 28, 2012 | http://pubs.acs.org
Publication Date (Web): February 6, 2012 | doi: 10.1021/bk-2012-1094.ch009

attempt to solve this problem, but instead take the pragmatic approach of only computing the DMC energy at a single k-point. We then estimate the resulting finite-size error using a DFT-based correction scheme as described in Sec. 2.

In summary, let us reiterate our motivation. DFT is currently the most feasible method available for the general treatment of molecular crystal systems, but it introduces significant uncontrolled approximations, and its reliability is therefore questionable for highly sensitive properties. In contrast, DMC is one of the most accurate many-body methods available in practice, but it is computationally very expensive and can only readily provide an estimate of the total energy. We therefore take the view that the DMC results can be used as a cornerstone to benchmark the more approximate methods, such as DFT, and to assess their reliability for the prediction of more interesting physical properties.

2. Methodology

We now outline the computational details of the DFT and QMC methods used in this work. First, we describe the crystal geometries we use for the two *para*-DIB polymorphs. In the DMC case, due to the high computational cost and difficulty of DMC geometry optimization (*49*), it was only feasible to perform the calculations at the experimental crystal geometries, which we obtained from the Cambridge Structural Database (http://www.ccdc.cam.ac.uk). The records of the lattice constants and unit cell atomic positions for the α and β phases are identified by the codes ZZZPRO03 and ZZZPRO04, respectively. The two polymorphs are packed into orthorhombic crystal lattices, with space group symmetry *Pbca* for the α phase, and *Pccn* for the β phase (*21*). As shown in Figure 1, both structures have four DIB molecules (48 atoms, 584 electrons) per unit cell, and the qualitative difference between the α and β packing motifs can be clearly seen in terms of the orientation of the individual molecules. At the DFT level, we were also able to perform geometry optimizations of the crystal structure, relaxing both the atomic positions and lattice constants, and we therefore report results for both experimental and optimized structures.

All the DFT calculations were performed using the CRYSTAL09 program package (*35*), with a 1×3×4 Monkhorst-Pack **k**-point mesh. For the Gaussian basis, we used the standard 6-31G** set for the carbon and hydrogen atoms (incorporating one contracted function for each core orbital and two contracted functions for the valence orbitals, in addition to one polarization function per atom) and the 3-21G set (which has no polarization functions) for the iodine atoms. As we discuss later, the non-trivial choice of basis set is crucial for accurate and stable calculations, and we will explore this issue more rigorously in a future publication.

Concerning exchange-correlation functionals, we considered eight different approximations. Within the local density approximation (LDA), we employed: [1] Dirac-Slater exchange (*50*) combined with the Vosko-Wilk-Nusair #5 parameterization (*51*) of the correlation functional, LDA(SVWN); [2] Dirac-Slater exchange with the Perdew-Zunger '81 parameterization (*52*) of the correlation functional, LDA(PZ); [3] von Barth-Hedin (*53*) exchange and correlation,

In Advances in Quantum Monte Carlo; Tanaka, S., et al.;
ACS Symposium Series; American Chemical Society: Washington, DC, 2012.

LDA(VBH). We employed four generalized-gradient approximation (GGA) functionals: [1] Perdew-Wang ′91 exchange and correlation (PW91) (*54*); [2] Perdew-Burke-Ernzerhof exchange and correlation (PBE) (*55*); [3] Becke ′88 exchange (*56*) and Perdew ′86 correlation (*57*) (BP86); [4] Becke ′88 exchange and Lee-Yang-Parr correlation (*58*) (BLYP). In addition, we considered one hybrid functional, B3LYP (*59*), which is one of the most widely-used and generally accurate functionals for studying isolated molecular systems. Finally, to explore the effect of dispersion, which is not accurately recovered by the above functionals, we also employed a London-type empirical correction scheme proposed by Grimme (*60*). In those cases, we augment our functional notation to give, for example, “PBE+D”.

Downloaded by PENNSYLVANIA STATE UNIV on May 28, 2012 | http://pubs.acs.org
Publication Date (Web): February 6, 2012 | doi: 10.1021/bk-2012-1094.ch009

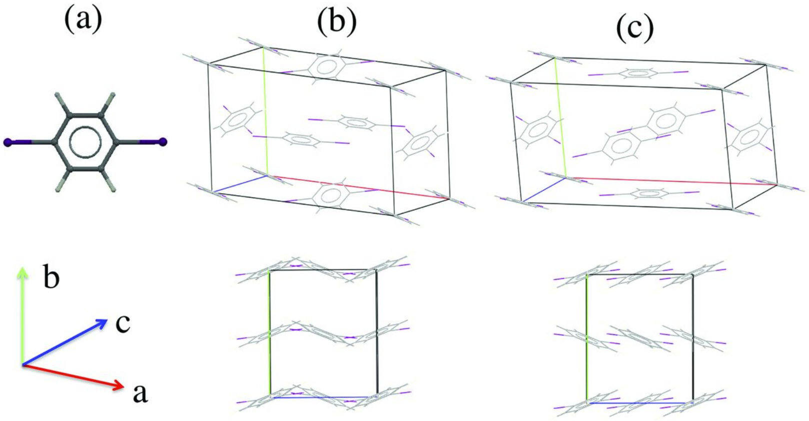

Figure 1. (a) Chemical structure of the para-DIB molecule and orientation of the unit cell lattice vectors, ***a, b,*** *and* ***c****. (b) The α phase unit cell, with experimental lattice constants: a = 17.000, b = 7.323, c = 6.168. (c) The β phase unit cell, with experimental lattice constants: a = 17.092, b = 7.461, c = 6.154; all units in Angstroms; taken from the online Cambridge Structural Database (www.ccdc.cam.ac.uk).*

All the QMC calculations were performed using the QMCPACK program suite (*61*), starting with a Slater-Jastrow trial wavefunction. The Jastrow factor (*62*) included one- and two-body Pade-type functions, which have six and four adjustable parameters, respectively, and were optimized using a variance minimization procedure (*63*). We obtained the one-electron orbitals comprising the Slater determinant from DFT calculations using the program package ABINIT (*64*, *65*) with a plane wave basis set, a cut-off energy of 40 hartree, and the Perdew-Wang (1992) LDA functional (*54*). In all the QMC calculations, the core electrons of the carbon and iodine atoms were replaced with a nonlocal Trail-Needs pseudopotential, obtained from the CASINO pseudopotential library (*66*, *67*). (The final number of correlated electrons per unit cell was therefore 168).

The corresponding DMC calculations were performed within the fixed-node approximation (*44*) using the nodes of these trial wavefunctions. To obtain reasonably converged results, we accumulated statistics over 3.2×10^7 time steps, with a step size of 0.001 a.u., and a target population of 16384 walkers. Due to the high computational expense of the DMC calculations, we took a pragmatic approach towards the treatment of finite-size errors (FSE). In fact, we only computed the DMC energy at the Γ point using a single unit cell. While it may be possible to use either twisted boundary conditions (*68*) or a larger supercell to reduce the FSE, we decided in this case to employ the *a posteriori* correction scheme of Kwee *et al.* (*69*) to estimate the finite-size error at the DFT level. For this purpose, we performed the calculations with an LDA functional, plane waves and Fritz-Haber-Institute (FHI) pseudopotentials with a cut-off energy of 50 hartree using the Quantum Espresso package (*70*). More discussion is given in Sec. 3.3.

For the accuracy required in this study, we also considered it important to include an estimate of zero-point energies (ZPE). We provide estimates only at the DFT level, computed with the CRYSTAL09 suite using the 'FREQCALC' keyword, which estimates the ZPE within a simple harmonic approximation. Further details can be found in Refs. (*71*, *72*).

Downloaded by PENNSYLVANIA STATE UNIV on May 28, 2012 | http://pubs.acs.org
Publication Date (Web): February 6, 2012 | doi: 10.1021/bk-2012-1094.ch009

3. Results and Discussion

To accurately and reliably predict the small energy differences we observe between the *para*-DIB polymorphs, many factors must be carefully included in the calculation, such as: [1] choice of first-principles method; [2] accurate crystal geometry; [3] treatment of finite size effects; and [4] inclusion of zero-point energies (ZPE). In Sec. 3.1, we report our benchmark DMC calculation and use it to evaluate several commonly-used DFT functionals. All computations are done using the experimental crystal structures. In Sec. 3.2, we investigate the geometric effects, and evaluate the ability of DFT to optimize the crystal structure accurately. Finally, in Sec. 3.3, we discuss the significance of ZPE and finite-size effects.

3.1. DFT and DMC Predictions

Here we report our results of the polymorph stabilities computed at the experimental geometries using DMC and DFT. Table I and Figure 2 summarize our findings in terms of the computed energy differences, $\Delta E \equiv E(\alpha) - E(\beta)$, between the α and β phases. Results from eight different exchange-correlation functionals are shown, including in some cases the dispersion correction scheme proposed by Grimme (denoted "+D" in the functional labels).

Our benchmark DMC result predicts the α phase to be more stable than the β phase by 48 meV per unit cell, with a statistical uncertainty of ±24 meV. This result is composed of an energy difference of $\Delta E = -98$ meV and a finite-size correction of +50 meV, estimated using the method of Kwee *et al.* described in Sec. 2. It should be stressed that $\Delta E = -48$ meV/cell is a very small energy difference of only 1 meV per atom. In other words, the question of polymorph stability in *para*-DIB is clearly an extremely difficult challenge for quantum chemistry.

Table I. Energy differences in meV/unit cell, $\Delta E \equiv E(\alpha) - E(\beta)$, between the α and β phases of *para*-DIB molecular crystals, at the experimental (expt) and DFT-optimized (opt) geometries using various functionals, including Grimme's dispersion correction (denoted "+D"). The DMC result at the experimental geometry, including the estimated finite-size correction (FSC), is also shown.

Method	*ΔE(expt)*	*ΔE(opt)*
LDA(SVWN)	-122	-128
LDA(PZ)	-123	-129
LDA(VBH)	-132	-142
PW91	29	-165
PBE	25	-12
BP86	30	-75
BLYP	93	12
B3LYP	68	-16
PBE+D	-134	-141
BP86+D	-192	-226
BLYP+D	-162	-172
B3LYP+D	-155	-163
DMC+FSC	-48 +/- 24	n/a

Indeed, turning to the DFT results, the inadequacy of conventional exchange-correlation functionals to reliably predict the correct energy ordering is immediately apparent. The DFT results in Figure 2 are grouped into three clear classes: (1) LDA ($\Delta E < 0$); (2) GGA and hybrid ($\Delta E > 0$); and (3) dispersion corrected ($\Delta E < 0$). The three LDA functionals give similar results, predicting the α phase to be clearly more stable than the β phase by approximately 125 meV per unit cell. In contrast, the four GGA functionals all predict the β phase to be the most stable, by an amount ranging from 25 meV (PBE) to 93 meV (BLYP). The addition of exact exchange does not have a major impact on the results, and the B3LYP hybrid functional also predicts the β phase to be the most stable (by 68 meV). The effect of Grimme's dispersion scheme is much more dramatic, however. In the cases we report, ΔE decreases by at least 150 meV on adding the dispersion correction. For BLYP, the 'correction' is more than 250 meV!

Downloaded by PENNSYLVANIA STATE UNIV on May 28, 2012 | http://pubs.acs.org
Publication Date (Web): February 6, 2012 | doi: 10.1021/bk-2012-1094.ch009

Downloaded by PENNSYLVANIA STATE UNIV on May 28, 2012 | http://pubs.acs.org
Publication Date (Web): February 6, 2012 | doi: 10.1021/bk-2012-1094.ch009

DMC is one of the most accurate methods currently available for this kind of calculation, and yet the size of the error bar in Figure 2 highlights the computational challenge at hand. We chose a time step of 0.001 a.u., which is small enough to make time-step error negligible, but as a result, significant computer time was required to reduce the statistical error. In fact, to achieve an error bar of ±24 meV, our DMC calculation consumed approximately 75,000 CPU-hours. A larger time step would facilitate faster convergence, but could introduce unknown systematic errors due to a failure of the short time approximation. The DMC+FSE result correctly predicts the experimental observation that the α phase is more stable than the β phase at zero temperature. The error bar implies that the probability of an incorrect energy ordering due to poor statistics is at the 2σ level, or approximately 2%. However, while we are confident of the DMC statistics, the issues of trial wavefunction (fixed-node approximation) and finite-size errors are still a point of concern. Of these, the most significant is almost certainly the latter. We discuss this more in Sec. 3.3.

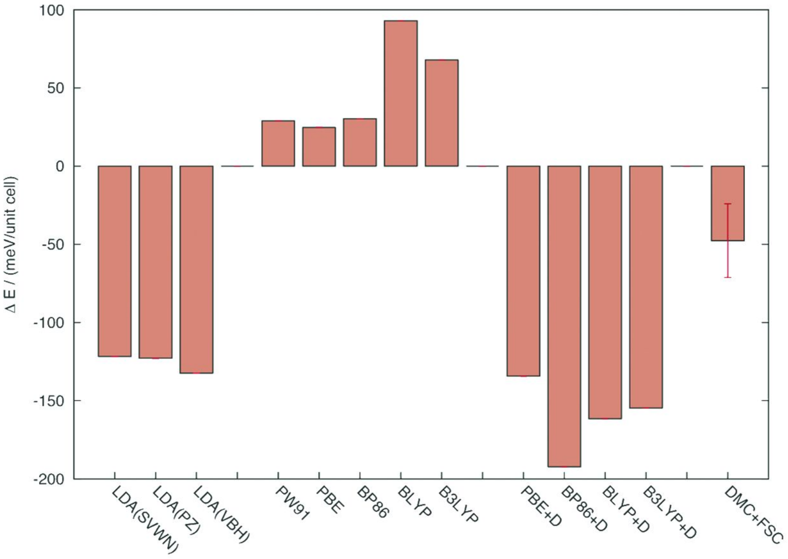

Figure 2. Computed energy differences, ΔE ≡ E(α) – E(β), between the α and β phases of para-DIB molecular crystals, at the experimental (expt) geometries using DFT and DMC. Results for eight different exchange-correlation functionals, including Grimme's dispersion correction (denoted "+D") are shown. The DMC result includes a finite-size correction (FSC) of 50 meV/unit cell, and we also display the statistical error bar.

DFT is the most widely used method for the *ab initio* treatment of molecular crystals, but it is striking that all the GGA functionals considered here incorrectly predict the β phase to be the most stable, while the cruder LDA's correctly yield $\Delta E < 0$. B3LYP, which is perhaps the most widely used functional in chemistry, also predicts the β phase to be the most stable. The addition of exact exchange only marginally improves the poor BLYP result, which is the worst of all the tested functionals. A partial understanding of the discrepancy between the LDA's and GGA's becomes clear when we look at the geometric effects in the next subsection. However, first, we will comment on the results of the dispersion correction (denoted "+D").

As we already noted, the effect of the dispersion correction is dramatic. It is not surprising that an accurate treatment of dispersion interactions is important in this system, especially when we compare the energies of the polymorphs. In the calculation of ΔE, the intramolecular energy components will largely cancel out. The resulting small energy difference will have large relative contributions from the (usually weak) intermolecular interactions, including the dispersion energy. The DFT dispersion correction successfully shifts the GGA results in the right direction, resulting in a large negative ΔE in all cases. But if we take the DMC result as a benchmark, the resulting magnitudes of the 'corrected' GGA results are much too large, by factors of approximately 3 or 4, suggesting that the dispersion scheme is not well balanced. It would be extremely interesting to test alternative dispersion-corrected functionals or other wavefunction-based methods.

Downloaded by PENNSYLVANIA STATE UNIV on May 28, 2012 | http://pubs.acs.org
Publication Date (Web): February 6, 2012 | doi: 10.1021/bk-2012-1094.ch009

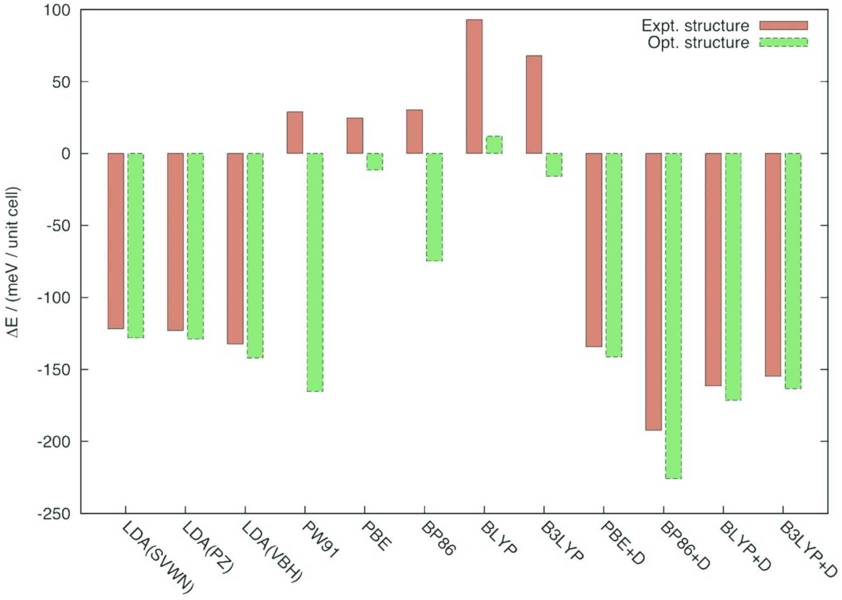

Figure 3. Computed energy differences, $\Delta E \equiv E(\alpha) - E(\beta)$, between the α and β phases of para-DIB molecular crystals, using eight different exchange-correlation functionals, including Grimme's dispersion correction (denoted "+D") are shown. Energies at the experimental and optimized geometries are compared in red and green, respectively.

Downloaded by PENNSYLVANIA STATE UNIV on May 28, 2012 | http://pubs.acs.org
Publication Date (Web): February 6, 2012 | doi: 10.1021/bk-2012-1094.ch009

3.2. DFT Structure Optimization

Due to the relatively low computational cost compared to QMC, it was also possible at the DFT level to explore the sensitivity of the results to changes in the crystal geometry. For each functional tested, we therefore optimized not only the atomic positions in the unit cell, but also the crystal lattice constants, to obtain a fully relaxed structure. We then recomputed the energy difference of the polymorphs and the results are shown in Table I and Figure 3. In all cases, the relaxed geometry lowers ΔE compared to calculations at the experimental geometry, but the change is a relatively small percentage in the case of the LDA and dispersion-corrected ("+D") functionals. Perhaps surprisingly, the effect of geometry relaxation is much more dramatic when applied to the GGA functionals and B3LYP, particularly in the case of PW91 where ΔE changes from +29 meV at the experimental geometry to −165 meV after optimizing the structures! Although this dramatic change may be surprising, the relaxed geometries give the correct qualitative prediction of the relative energies (i.e. that the α phase is more stable than the β phase) for all functionals tested, except BLYP (where ΔE remains slightly positive).

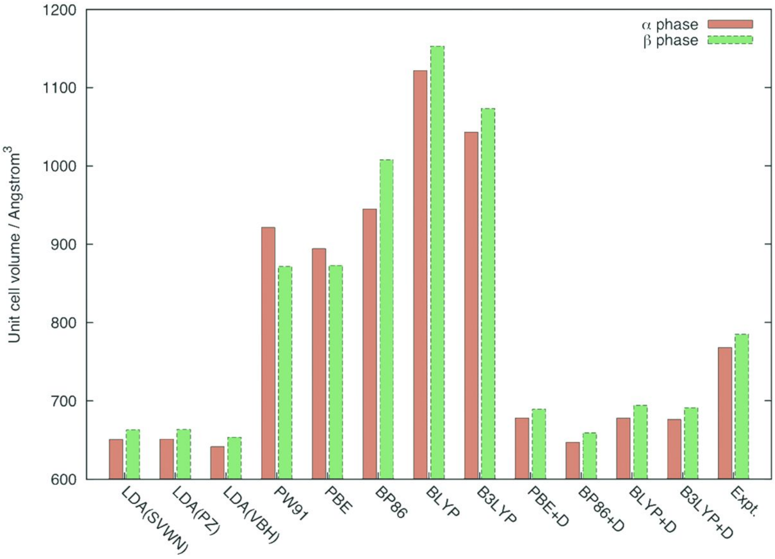

Figure 4. Optimized unit cell volumes for the α and β polymorphs evaluated using eight DFT functionals, including Grimme's dispersion correction (denoted "+D"), compared with experiment in the final column.

Downloaded by PENNSYLVANIA STATE UNIV on May 28, 2012 | http://pubs.acs.org
Publication Date (Web): February 6, 2012 | doi: 10.1021/bk-2012-1094.ch009

Table II. Optimized lattice constants and unit cell volumes, *V*, for the two polymorphs of DIB evaluated using eight DFT functionals, including Grimme's dispersion correction (denoted "+D"), compared with experiment[a]

	α phase				*β phase*			
	a	*b*	*c*	*V*	*a*	*b*	*c*	*V*
LDA(SVWN)	16.289	6.708	5.956	650.8	16.387	6.783	5.966	663.2
LDA(PZ)	16.300	6.706	5.957	651.2	16.391	6.788	5.964	663.6
LDA(VBH)	16.225	6.662	5.936	641.6	16.320	6.725	5.955	653.6
PW91	18.721	8.993	5.473	921.5	17.506	8.175	6.091	871.7
PBE	18.748	8.589	5.555	894.5	18.498	8.116	5.815	873.0
PBE+D	16.748	6.780	5.971	678.0	16.841	6.789	6.028	689.2
BP86	18.799	9.331	5.387	945.1	18.487	9.864	5.527	1007.9
BP86+D	16.465	6.560	5.991	647.1	16.646	6.596	6.003	659.1
BLYP	18.281	10.073	6.093	1122.0	18.461	10.40	6.005	1153.0
BLYP+D	16.622	6.716	6.071	677.7	17.085	6.796	5.978	694.0
B3LYP	18.620	9.733	5.756	1043.2	18.502	9.948	5.831	1073.3
B3LYP+D	16.610	6.731	6.046	676.0	16.966	6.791	5.998	691.1
Expt.	17.000	7.323	6.168	767.9	17.092	7.461	6.154	784.8

[a] Length and volume are in units of Å and Å^3, respectively.

The optimized lattice constants and unit cell volumes are reported in detail in Table II for the eight DFT functionals, including Grimme's dispersion corrections and the experimental values. To make the interpretation clearer, we plot the results of the optimized unit cell volumes for both phases in Figure 4. In addition, we plot the α phase lattice constants in Figure 5 and the β phase lattice constants in Figure 6. Looking at the unit cell volumes first, we note that experimentally the α phase has the most compact crystal structure, and it is also energetically the most stable polymorph at low temperature. Physically, the stability associated with the more compact structure is expected to be driven by a net increase in attractive interactions due to van der Waals and other noncovalent interactions. The conventional functionals cannot describe these energies accurately, and hence the GGA functionals, and B3LYP, fail to recover these compact structures. This is very clear in Figure 4, where the unit cell volumes predicted by these functionals are much too large in all cases. For PW91 and PBE, even the ordering of the α and β volumes is wrong. On the other hand, although the unit cell volumes are too compact, the LDA optimized structures are much closer to experiment, even though the LDA cannot describe dispersion either. It is well known, however, that the LDA overbinds in molecular calculations and it is likely that this tendency is compensating for the lack of dispersion. Overall, this cancellation of errors is probably a major reason why the LDA structures and ΔE values are qualitatively correct and much better than the GGA results. However, the poor quantitative accuracy of the LDA results (e.g. $\Delta E = -122$ meV for SVWN) confirms the unreliability of these predictions.

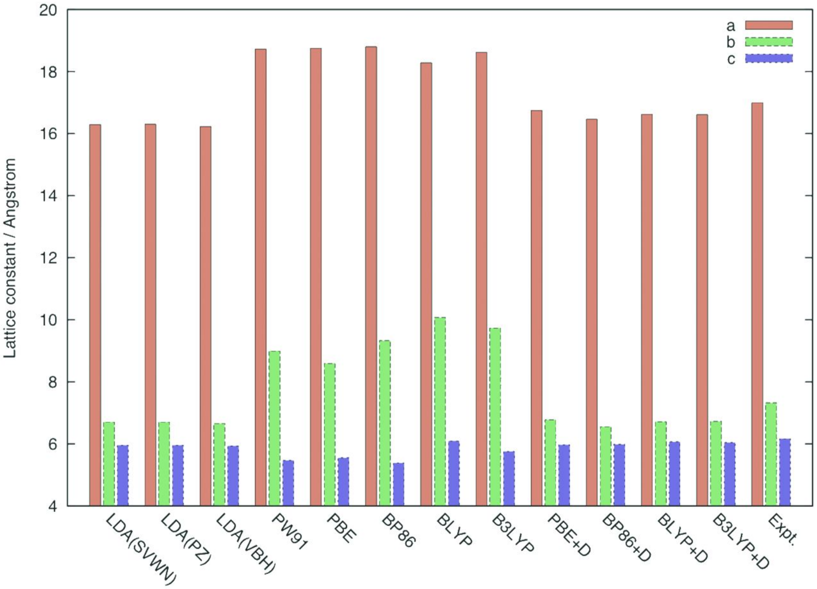

Figure 5. Optimized lattice constants for the α polymorph evaluated using eight DFT functionals, including Grimme's dispersion correction (denoted "+D"), compared with experiment.

This argument is reinforced if we consider the effect of Grimme's dispersion correction. Looking at Figure 4, it is clear that the addition of dispersion interactions into the DFT calculations strongly favors the more compact crystal structures. In fact, the dispersion-corrected functionals give the best cell volumes of all the functionals and this is reflected in much improved ΔE values, probably for the right reasons in this case. In fact, the differences between specific GGA's are insignificant compared to the addition (or not) of the dispersion correction. Nevertheless, the correction over-compensates, and the volumes actually become *too* small compared with experiment. Indeed, as with the LDA results, this correlates directly with ΔE values that are significantly too low compared to the DMC benchmark of −48±24 meV. For the LDA and dispersion-corrected functionals, there is a clear correlation between the overly compact unit cell volumes, compared to experiment, and the too-low ΔE values.

Overall, the poor structural predictions of the GGA's and B3LYP confirm the unreliability of these functionals for predicting the polymorph stabilities. For example, the PW91 ΔE(opt) value (−165 meV) has the correct sign and is comparable with the values from the dispersion-corrected functionals. However, it is apparent from Figure 4 that the favorable result is most likely due to fortuitous

Downloaded by PENNSYLVANIA STATE UNIV on May 28, 2012 | http://pubs.acs.org
Publication Date (Web): February 6, 2012 | doi: 10.1021/bk-2012-1094.ch009

error cancellation, since the optimized structures give α and β unit cell volumes which are incorrectly ordered compared with experiment.

Finally, it is interesting to take a closer look at Figures 5 and 6. Overall, we see the same trends as we already noted in Figure 4, such as the generally poor GGA results. However, it also seems that some of the lattice constants are more sensitive to errors than others. For example, it appears that the *b* lattice constant is particularly badly reproduced by the GGA's and B3LYP. Recalling Figure 1, we might hypothesize why this is. It is well known that the dispersion interaction is important for the accurate description of π-π stacking interactions. Although the geometry is slightly distorted in *para*-DIB, it can be seen that this interaction will be significant along the **b** lattice vector.

Downloaded by PENNSYLVANIA STATE UNIV on May 28, 2012 | http://pubs.acs.org
Publication Date (Web): February 6, 2012 | doi: 10.1021/bk-2012-1094.ch009

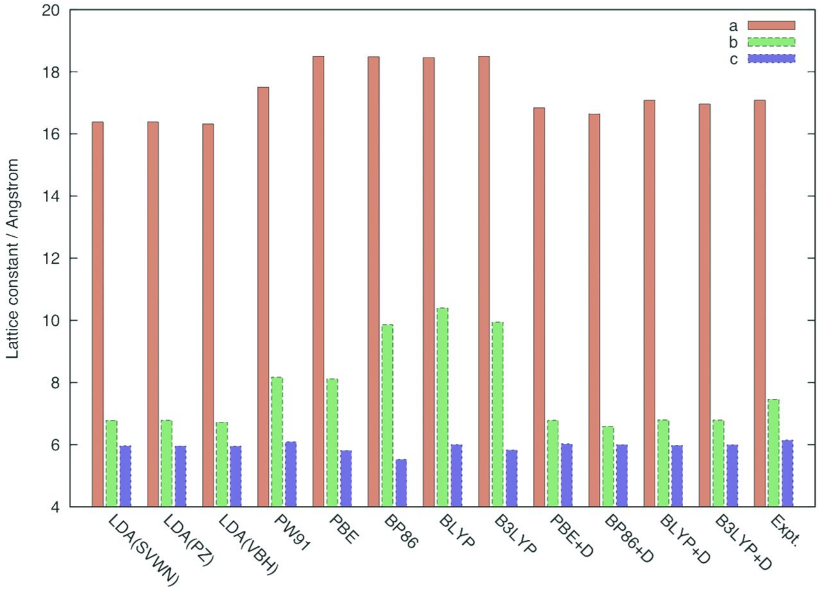

Figure 6. Optimized lattice constants for the β polymorph evaluated using eight DFT functionals, including Grimme's dispersion correction (denoted "+D"), compared with experiment.

3.3. Zero-Point and Finite-Size Effects

Due to the very small energy differences, a rigorous study of the polymorph stabilities should include an analysis of not only finite-size errors, but also zero-point energy (ZPE) contributions, which could easily be significant on an energy scale of 10 meV. For a relatively weakly bound molecular crystal such as *para*-DIB, the majority of the ZPE should come from intramolecular contributions, which we expect to be approximately the same for both polymorphs. In other words, we would not expect the ZPE to qualitatively change our predictions of polymorph stabilities. Nevertheless, a careful treatment of ZPE effects is known

Downloaded by PENNSYLVANIA STATE UNIV on May 28, 2012 | http://pubs.acs.org
Publication Date (Web): February 6, 2012 | doi: 10.1021/bk-2012-1094.ch009

to be necessary in some studies. Recently, Rivera *et al.* have emphasized the importance of accurately including ZPE's when estimating the enthalpy difference between the α and γ polymorphs of glycine (*73*).

To investigate these issues in *para*-DIB, we therefore performed DFT calculations using three exchange-correlation functionals to estimate the ZPE in the α and β phases using the methodology described in Sec. 2. At the optimized crystal geometries, the computed ZPE energy *differences* [i.e. ZPE(α) − ZPE(β)] using LDA(SVWN), B3LYP and B3LYP+D, were 8.6 meV, 4.4 meV and −1.0 meV per unit cell, respectively. These results broadly confirm our assumption that the ZPE is less important than other effects, especially if we believe the B3LYP+D value to be the most reliable. Note that a correction of 1 meV is an order of magnitude smaller than the statistical error bar of our benchmark DMC calculation.

Analogous arguments based on the structural similarity of the two phases can also be made regarding the finite-size errors. That is, we may also expect the majority of the finite-size errors to approximately cancel out when computing the polymorph energy difference ΔE. In our DFT calculations, we used a 1×3×4 **k**-point mesh which was found to converge the energies to within 10 meV. However, the differences between the Γ-point energies and those computed with more **k**-points suggest that the finite-size error in our DMC result could be large on the scale of ΔE, even though the above argument suggests it might be small in general. Due to the computational expense of DMC, however, we decided to estimate the DMC finite-size error using the DFT-based *a posteriori* correction scheme of Kwee *et al.* described in Sec. 2. As reported in Sec. 3.1, the correction was found to be +50 meV, which is significant and of the same order of magnitude as the Γ-point ΔE. We are currently performing further QMC calculations to explore the finite-size effect more rigorously and we will report our findings in a future publication

4. Conclusion

We have studied the relative stabilities of the α and β polymorphs of the *para*-diiodobenzene molecular crystal using several DFT approximations and the diffusion Monte Carlo method. The work is an extension of our preliminary study (*74*), including more accurate DMC statistics and a more comprehensive testing of different exchange-correlation functionals. Our DMC result predicts the α phase to be more stable than the β phase at zero temperature with a 2% statistical uncertainty, in agreement with experimental observation. In contrast, the DFT results using eight commonly-used functionals were inconsistent and showed large variations in the predicted polymorph energy differences. The semi-local and hybrid functionals incorrectly predict the β phase to be the most stable using the experimental crystal structures. The LDA functionals give qualitatively the correct result, but significantly overestimate the energy difference compared to the DMC benchmark. The addition of an empirical dispersion correction to the GGA and hybrid functionals corrects their behaviour and consistently predicts the α phase to be the most stable, but again the energy differences are significantly over-estimated. We also explored the effects of crystal geometry and found that the GGA and B3LYP functionals were unable to find the experimental structure. Again, we rationalized this failure in terms of the poor description of dispersion interactions, evidenced by the dramatic changes we observed when adding the dispersion correction.

In summary, we conclude that there is a real need for efficient many-body methods or improved density-functionals which can accurately and reliably capture electron correlation and dispersion interactions in molecular crystals. In addition to benchmarking the DFT results, we hope that our work demonstrates the possibility of applying DMC to challenging chemical problems in the solid phase where a rigorous treatment of electron correlation is essential.

Downloaded by PENNSYLVANIA STATE UNIV on May 28, 2012 | http://pubs.acs.org
Publication Date (Web): February 6, 2012 | doi: 10.1021/bk-2012-1094.ch009

Acknowledgments

Calculations have been performed using the Odyssey computing cluster at Harvard University's High Performance Technical Computing Center and the RIKEN Integrated Cluster of Clusters at RIKEN's Advanced Center for Computing and Communication, Japan. The authors thank Dr. Kenneth Esler and Dr. Jeongnim Kim for their helpful support with QMCPack. M.A.W and A.A-G. acknowledge financial support from NSF "Cyber-Enabled Discoveries and Innovations" (CDI) Initiative Award PHY-0835713. T.I. was supported by KAKENHI (No. 20103005 and No. 19310083) from MEXT.

References

1. Perepichka, I. F.; Perepichka, D. F.; Meng, H.; Wudl, F. *Adv. Mater.* **2005**, *17*, 2281–2305.
2. Argun, A. A.; Aubert, P.-H.; Thompson, B. C.; Schwendeman, I.; Gaupp, C. L.; Hwang, J.; Pinto, N. J.; Tanner, D. B.; MacDiarmid, A. G.; Reynolds, J. R. *Chem. Mater.* **2004**, *16*, 4401–4412.
3. Smela, E. *Adv. Mater.* **2003**, *15*, 481–494.
4. Heeger, A. J. *J. Phys. Chem. B* **2001**, *105*, 8475–8491.
5. McQuade, D. T.; Pullen, A. E.; Swager, T. M. *Chem. Rev.* **2000**, *100*, 2537–2574.
6. Brabec, C. J.; Sariciftci, N. S.; Hummelen, J. C. *Adv. Funct. Mater.* **2001**, *11*, 15–26.
7. Dimitrakopoulos, C.; Malenfant, P. *Adv. Mater.* **2002**, *14*, 99–117.
8. Anthony, J. E. *Angew. Chem., Int. Ed.* **2008**, *47*, 452–83.
9. Anthony, J. E. *Chem. Rev.* **2006**, *106*, 5028–48.
10. Coropceanu, V.; Cornil, J.; da Silva Filho, D. A.; Olivier, Y.; Silbey, R.; Brédas, J.-L. *Chem. Rev.* **2007**, *107*, 926–52.
11. Jurchescu, O.; Mourey, D.; Subramanian, S.; Parkin, S; Vogel, B; Anthony, J.; Jackson, T.; Gundlach, D. *Phys. Rev. B* **2009**, *80*, 085201.
12. Parr, R. G.; Yang, W. *Density-Functional Theory of Atoms and Molecules*; Oxford University Press: New York, 1989.

13. Schwartz, L.; Ingersoll, H.; Hornig, J. *Mol. Cryst. Liq. Cryst.* **1967**, *2*, 379–384.
14. Davey, R. J. *Cryst. Growth Des.* **2002**, *2*, 675–676.
15. Moulton, B.; Zaworotko, M. J. *Chem. Rev.* **2001**, *101*, 1629–1658.
16. Bond, A. D.; Boese, R.; Desiraju, G. R. *Angew. Chem., Int. Ed.* **2007**, *46*, 618–22.
17. Ouvrard, C.; Price, S. L. *Cryst. Growth Des.* **2004**, *4*, 1119–1127.
18. Li, T.; Feng, S. *Pharm. Res.* **2006**, *23*, 2326–32.
19. Brillante, A.; Della Valle, R. G.; Farina, L.; Venuti, E.; Cavazzoni, C.; Emerson, A. P. J.; Syassen, K. *J. Am. Chem. Soc.* **2005**, *127*, 3038–43.
20. Aliev, A. E.; Harris, K. D. M.; Alcobé, X.; Estop, E. J. *Chem. Soc., Faraday Trans.* **1993**, *89*, 3797–3800.
21. Alcobé, X.; Eugenia, E.; Aliev, A. E.; Harris, K. D. M.; Rodriguez-Carvajal, J.; Rius, J. *J. Solid State Chem.* **1994**, *110*, 20–27.
22. Hawthorne, F. C. *Nature* **1990**, *345*, 297.
23. Neumann, M. A.; Leusen, F. J. J.; Kendrick, J. *Angew. Chem., Int. Ed.* **2008**, *47*, 2427–30.
24. Price, S. L. *Adv. Drug Delivery Rev.* **2004**, *56*, 301–19.
25. Sánchez-Carrera, R. S.; Coropceanu, V.; Kim, E.-G.; Bredas, J.-L. *Chem. Mater.* **2008**, *20*, 5832–5838.
26. Ellman, B. *J. Chem. Phy.* **2006**, *125*, 074702.
27. Zhao, Y.; Truhlar, D. G. *J. Chem. Theory Comput.* **2007**, *3*, 289–300.
28. Hsing, C.; Wei, C.; Drummond, N.; Needs, R. *Phys. Rev. B* **2009**, *79*, 1–5.
29. Helgaker, T.; Jorgensen, P. J.; Olsen, J. *Molecular Electronic-Structure Theory*; Wiley: Chichester, U.K., 2000; p 336.
30. Ayala, P. Y.; Scuseria, G. E. *J. Chem. Phys.* **1999**, *110*, 3660.
31. Doser, B.; Lambrecht, D. S.; Kussmann, J.; Ochsenfeld, C. *J. Chem. Phys.* **2009**, *130*, 064107.
32. Werner, H.-J.; Manby, F. R.; Knowles, P. J. *J. Chem. Phys.* **2003**, *118*, 8149.
33. Yang, J.; Kurashige, Y.; Manby, F. R.; Chan, G. K.-L. *J. Chem. Phys.* **2011**, *134*, 044123.
34. Kertész, M. *Advances in Quantum Chemistry*, 15th ed.; Elsevier, New York, 1982; Vol. 15, Electronic Structure of Polymers, pp 161–214.
35. Dovesi, R.; Saunders, V. R.; Roetti, C.; Orlando, R.; Pascale, F.; Civalleri, B.; Doll, K.; Harrison, N. M.; Bush, I. J.; Llunell, M. *CRYSTAL09*; 2010.
36. Zgid, D.; Chan, G. K.-L. *J. Chem. Phys.* **2011**, *134*, 094115.
37. Hirata, S. *Phys. Chem. Chem. Phys.* **2009**, *11*, 8397–412.
38. Manby, F. R.; Alfè, D.; Gillan, M. J. *Phys. Chem. Chem. Phys.* **2006**, *8*, 5178–80.
39. Marsman, M.; Grüneis, A.; Paier, J.; Kresse, G. *J. Chem. Phys.* **2009**, *130*, 184103.
40. Ayala, P. Y.; Kudin, K. N.; Scuseria, G. E. *J. Chem. Phys.* **2001**, *115*, 9698.
41. Paulus, B. *Phys. Rep.* **2006**, *428*, 1–52.
42. Pisani, C.; Maschio, L.; Casassa, S.; Halo, M.; Schütz, M.; Usvyat, D. *J. Comput. Chem.* **2008**, *29*, 2113–24.
43. Sode, O.; Keceli, M.; Hirata, S.; Yagi, K. *Int. J. Quantum Chem.* **2009**, *109*, 1928–1939.

Downloaded by PENNSYLVANIA STATE UNIV on May 28, 2012 | http://pubs.acs.org
Publication Date (Web): February 6, 2012 | doi: 10.1021/bk-2012-1094.ch009

Downloaded by PENNSYLVANIA STATE UNIV on May 28, 2012 | http://pubs.acs.org
Publication Date (Web): February 6, 2012 | doi: 10.1021/bk-2012-1094.ch009

44. Foulkes, W. M. C.; Needs, R. J.; Rajagopal, G. *Rev. Mod. Phys.* **2001**, *73*, 33–83.
45. Aspuru-Guzik, A.; Lester, W. A. In *Handbook of Numerical Analysis. Special Volume: Computational Chemistry*; Le Bris, C., Ed.; Elsevier Science & Technology: New York, 2003; Vol. X, p 485.
46. Needs, R. J.; Towler, M. D.; Drummond, N. D.; López Ríos, P. *J. Phys: Condens. Matter* **2010**, *22*, 023201.
47. Grossman, J. C. *J. Chem. Phys.* **2002**, *117*, 1434.
48. Aspuru-Guzik, A.; Salomón-Ferrer, R.; Austin, B.; Lester, W. A. *J. Comput. Chem.* **2005**, *26*, 708–15.
49. Badinski, A.; Haynes, P.; Trail, J. R.; Needs, R. J. *J. Phys: Condens. Matter* **2010**, *22*, 074202.
50. Dirac, P. A. M. *Proc. Cambridge Philos. Soc.* **1930**, *26*, 376.
51. Vosko, S. J.; Wilk, L.; Nusair, M. *Can. J. Phys.* **1980**, *58*, 1200.
52. Ceperley, D.; Alder, B. *Phys. Rev. Lett.* **1980**, *45*, 566–569.
53. von Barth, U.; Hedin, L. *J. Phys. C: Solid State Phys.* **1972**, *5*, 1629–1642.
54. Perdew, J.; Wang, Y. *Phys. Rev. B* **1992**, *45*, 13244–13249.
55. Perdew, J.; Burke, K.; Ernzerhof, M. *Phys. Rev. Lett.* **1996**, *77*, 3865–3868.
56. Becke, A. *Phys. Rev. A* **1988**, *38*, 3098–3100.
57. Perdew, J. *Phys. Rev. B* **1986**, *33*, 8822–8824.
58. Lee, C.; Yang, W.; Parr, R. G. *Phys. Rev. B* **1988**, *37*, 785.
59. Becke, A. D. *J. Chem. Phys.* **1993**, *98*, 1372.
60. Grimme, S. *J. Comput Chem.* **2006**, *27*, 1787–99.
61. QMCPACK, 2010. http://qmcpack.cmscc.org.
62. Jastrow, R. *Phys. Rev.* **1955**, *98*, 1479–1484.
63. Umrigar, C.; Wilson, K.; Wilkins, J. *Phys. Rev. Lett.* **1988**, *60*, 1719–1722.
64. Gonze, X.; Rignanese, G.-M.; Verstraete, M.; Beuken, J.-M.; Pouillon, Y.; Caracas, R.; Jollet, F.; Torrent, M.; Zerah, G.; Mikami, M.; et al. *Z. Kristallogr.* **2005**, *220*, 558–562.
65. Gonze, X.; Amadon, B.; Anglade, P.-M.; Beuken, J.-M.; Bottin, F.; Boulanger, P.; Bruneval, F.; Caliste, D.; Caracas, R.; Côté, M. *Comput. Phys. Commun.* **2009**, *180*, 2582–2615.
66. Trail, J. R.; Needs, R. J. *J. Chem. Phys.* **2005**, *122*, 14112.
67. Trail, J. R.; Needs, R. J. *J. Chem. Phys.* **2005**, *122*, 174109.
68. Lin, C.; Zong, F. H.; Ceperley, D. M. *Phys. Rev. E* **2001**, *64*, 1–12.
69. Kwee, H.; Zhang, S.; Krakauer, H. *Phys. Rev. Lett.* **2008**, *100*, 126404.
70. Giannozzi, P. *J. Phys.: Condens. Matter* **2009**, *21*, 395502.
71. Zicovich-Wilson, C. M.; Pascale, F.; Roetti, C.; Saunders, V. R.; Orlando, R.; Dovesi, R. *J. Comput. Chem.* **2004**, *25*, 1873–81.
72. Pascale, F.; Zicovich-Wilson, C. M.; López Gejo, F.; Civalleri, B.; Orlando, R.; Dovesi, R. *J. Comput. Chem.* **2004**, *25*, 888–97.
73. Rivera, S. A.; Allis, D. G.; Hudson, B. S. *Cryst. Growth Des.* **2008**, *8*, 3905–3907.
74. Hongo, K.; Watson, M. A.; Sánchez-Carrera, R. S.; Iitaka, T.; Aspuru-Guzik, A. *J. Phys. Chem. Lett.* **2010**, *1*, 1789–1794.

Chapter 10

Quantum Monte Carlo in Presence of Spin-Orbit Interaction

A. Ambrosetti,[1] F. Pederiva,[*,2] E. Lipparini,[2] and L. Mitas[3]

[1]Dipartimento di Fisica, University of Padova, via Marzolo 8, I-35131, Padova, Italy
[2]Dipartimento di Fisica and INFN - Gruppo collegato di Trento, University of Trento, via Sommarive 14, I-38123 Trento, Italy
[3]Department of Physics, North Carolina State University, Raleigh, North Carolina 27695, U.S.A.
[*]E-mail: pederiva@science.unitn.it

The combined recent interest in nanoscale systems and spintronics has led to a renewed attention on spin orbit (SO) effects in solid state physics. Among the several numerical approaches available, Quantum Monte Carlo Methods (QMC) are probably best suited in order to achieve the elevated accuracy standards, required for disentangling the very small spin-orbit effects in relatively large system. Unfortunately, standard QMC algorithms are unable of correctly describing SO interacting systems. More sophisticated implementations are thus required both for Variational (VMC) and Diffusion Monte Carlo (DMC), implying a dynamical use of the spin degrees of freedom and, for DMC in particular, an imaginary propagator showing non trivial dependence on spin operators. Both DMC and VMC extensions will be briefly discussed, together with applications on the two dimensional electron gas with Rashba interaction and isolated atoms.

In Advances in Quantum Monte Carlo; Tanaka, S., et al.;
ACS Symposium Series; American Chemical Society: Washington, DC, 2012.

Introduction

The spin-orbit (SO) interaction is a relativistic quantum effect induced by non-uniform electric fields and resulting in a coupling of angular momentum to spin. Its understanding and its correct description through the Dirac equation (*1*) dates back to the beginning of the last century and, thereafter, intensive studies have been performed (*2*) on isolated atoms (*3*), achieving theoretical estimates in remarkable agreement with spectroscopic measurements.

Solid theoretical frameworks have been developed in order to satisfactorily explain, for instance, the limits of weak and strong SO couplings usually referred to as LS and jj couplings, and state of the art many body methods were also applied in order to treat the problem (*4*).

Despite the elevated accuracy of theoretical calculations of single atoms SO splittings, the effects of the SO interaction in solid state systems was, up to recently, largely unexplored.

The recent interest on spintronics and nanoscale systems such as quantum dots, quantum wires, etc. led to a renewed interest in SO interactions due to the discovery of the Rashba (*5*, *6*) and Dresselhaus (*7*) interactions. The combined experimental (*8–12*) and theoretical (*13–16*) efforts resulted in a good degree of understanding of SO effects in nanostructures, and to the proposal of devices for spin control (*17*). Due to its typically very weak strength, an efficient theoretical description of the SO interaction necessarily requires an extremely elevated degree of accuracy, only achievable by means of a restricted number of quantum many body methods. Among the several numerical method available, QMC algorithms certainly represent ideal candidates for addressing SO problems: a favorable combination of computational costs and elevated accuracy proves indeed essential for capturing tiny SO effects in relatively extended systems.

In the present paper both VMC and DMC methods will be considered. Because their standard implementations are not directly applicable to SO interacting systems, an extension of both methods is required. In both cases, the spin degrees of freedom will be explicitly accounted for and integrated similarly to space coordinates. However, due to the intrinsic differences between VMC and DMC, the two methods will be modified according to two separate schemes. DMC, in particular, will require the implementation of a specific imaginary time propagator carrying an explicit dependence on spin operators.

VMC+SO: C and Pb Atoms

Method

VMC is a robust and efficient method for the investigation of many body systems, and, at the same time, also one of the best tools for wave function optimization. The delicate procedure of wave function optimization, in particular, is a fundamental step for any subsequent application of DMC, especially in fermionic systems. The availability of efficient VMC algorithms therefore represents a crucial issue for the QMC treatment of many body problems.

Standard VMC implementations (*18*) make use of an explicit integration over space coordinates, while treating spin variables as static labels. Neglecting the summation over the spin degrees of freedom, however, is only possible for systems with spin rotation symmetry. In the case of Hamiltonians only depending on space coordinates, this procedure is certainly correct, and the expectation value of a general observable O could be mathematically expressed as:

$$\langle \varphi_T | O | \varphi_T \rangle = \frac{\int dR \varphi_T^*(R)\varphi_T(R)\dfrac{O\varphi_T(R)}{\varphi_T(R)}}{\int dR \varphi_T^*(R)\varphi_T(R)}$$

where R represents the set of space coordinates of the system. If a spin-orbit term is introduced in the Hamiltonian, the same procedure is no longer applicable, and, in general, an explicit summation over a complete spin basis set turns out to be necessary. Unfortunately, such an exact summation soon becomes too expensive, even for a relatively limited numbers of particles, due to the exponential dependence of the basis set dimension (scaling as 2^N). Some alternative strategy should therefore be applied in order to retain the overall VMC efficiency.

A particularly efficient method, recently proposed by our group (*19*), makes use of a mathematical equivalence between the integration over a set of continuous variables and complete spin basis set summation in order to reduce the whole computational effort. In order to illustrate the method we will restrict consideration to the two-electron case, considering a trial wave function composed of a single Slater determinant. Extensions to larger number of particles and to linear combinations of Slater determinants are trivial. In the following we will make use of the following single particle spinors:

$$\bar{\varphi}_1 = \begin{pmatrix} \varphi_1^1 \\ \varphi_2^1 \end{pmatrix} \qquad \bar{\varphi}_2 = \begin{pmatrix} \varphi_1^2 \\ \varphi_2^2 \end{pmatrix}$$

and of the following parameterization for the spin coordinates:

$$\bar{s}_1 = \begin{pmatrix} \sin(\alpha_1)e^{i\delta_1} \\ \cos(\alpha_1) \end{pmatrix} \qquad \bar{s}_2 = \begin{pmatrix} \sin(\alpha_2)e^{i\delta_2} \\ \cos(\alpha_2) \end{pmatrix}$$

By using the above definitions, the two-body wave function Ψ (made of a single Slater determinant) could be explicitly expressed as:

$$\begin{aligned} \Psi(\bar{r}_1,\bar{s}_1,\bar{r}_2,\bar{s}_2) &= \left[\varphi_1^1(\bar{r}_1)e^{i\delta_1}\sin(\alpha_1) + \varphi_2^1(\bar{r}_1)\cos(\alpha_1)\right]\times \\ &\times\left[\varphi_1^2(\bar{r}_2)e^{i\delta_2}\sin(\alpha_2) + \varphi_2^2(\bar{r}_2)\cos(\alpha_2)\right] - \\ &-\left[\varphi_1^2(\bar{r}_1)e^{i\delta_1}\sin(\alpha_1) + \varphi_2^2(\bar{r}_1)\cos(\alpha_1)\right]\left[\varphi_1^1(\bar{r}_2)e^{i\delta_2}\sin(\alpha_2) + \varphi_2^1(\bar{r}_2)\cos(\alpha_2)\right] \end{aligned} \qquad (1)$$

Considering now a second Slater determinant Ψ′ (with corresponding single particle spinors φ′), the overlap integral $\langle \Psi | \Psi' \rangle$ could be expanded over a complete spin basis set:

$$\begin{aligned}\langle \Psi | \Psi' \rangle &= \langle \Psi | \uparrow\uparrow \rangle \langle \uparrow\uparrow | \Psi' \rangle + \langle \Psi | \uparrow\downarrow \rangle \langle \uparrow\downarrow | \Psi' \rangle + \\ &+ \langle \Psi | \downarrow\uparrow \rangle \langle \downarrow\uparrow | \Psi' \rangle + \langle \Psi | \downarrow\downarrow \rangle \langle \downarrow\downarrow | \Psi' \rangle\end{aligned} \qquad (2)$$

Making use of simple trigonometric relations, it is possible to show (see ref. (*19*)) the equivalence of the above expression with the following integral:

$$\langle \Psi | \Psi' \rangle = Const \cdot \int\int\int_0^{2\pi}\int_0^{2\pi} \Psi(\bar{r}_1,\bar{s}_1,\bar{r}_2,\bar{s}_2)\psi'(\bar{r}_1,\bar{s}_1,\bar{r}_2,\bar{s}_2)d\alpha_1 d\alpha_2 d\bar{r}_1 d\bar{r}_2$$

In fact, among all terms deriving from the product of the two Slater determinants (such as (1)), only those containing either $\cos(\alpha_i)^2$ or $\sin(\alpha_i)^2$ will give a non-zero contribution. It is then easy to prove that these terms exactly correspond to those contained in . Furthermore, integration over the δ_i variables is not necessary due to the occurrence of phase cancellation.

The mapping of spin summation over a continuous integration allows for a simple extension of the Metropolis integration, which now will not only include space coordinates, but also the spin parameters ai. The computation of the expectation value of physical observables over a given trial wave function relies exactly on the same scheme as (2) and could easily be achieved without a particularly significant increase of computational cost with respect to standard VMC.

C and Pb Atoms

An obvious first application of this algorithm certainly is to the study of realistic spin-orbit splittings in atoms. These indeed represent particularly favorable benchmark systems, due to the availability of both theoretical (*20*) and experimental (*21*) results. In order to investigate both the two limiting cases of weak and strong SO interaction, isolated carbon and lead atoms will be taken into account, respectively corresponding to the *LS* and *jj* SO couplings.

Due to its low atomic number (*Z*=6), the C atom shows very tiny SO splittings, induced by the presence of p valence electrons. Though much lower than the other energy scales, SO splittings are a clearly observable non-trivial feature of the C spectrum. Therefore, due to the small energy differences and the peculiar ordering of the spectral lines, the C atom is a valuable candidate for assessing the accuracy of the proposed method. The all electron Hamiltonian considered is the following:

$$H = \sum_{i=1}^{N} \frac{P_i^2}{2m} + V_{SO}{}^{i} - \frac{Z}{r_i} + \sum_{i<j}^{N} \frac{1}{|\bar{r}_i - \bar{r}_j|}$$

containing as the only relativistic correction, the SO potential

$$V_{SO}{}^{i}\varphi = -\frac{\hbar^2}{4m^2c^2}\bar{\sigma}_i\cdot\left[\left(\bar{\nabla}_i V\right)\times\bar{\nabla}_i\varphi\right] \tag{3}$$

Other relativistic corrections are intentionally neglected, not being directly involved in the splitting effect.

A possible choice for tackling the problem of SO splitting in the C atom consists of using a trial wave function built as a single Slater determinant of HF single particle orbitals. In Figure 1 VMC results are reported for the SO splitting computed using the reference HF orbital obtained by Clementi and Roetti (*20*) within a *LS* coupling approach. Comparison is also given between the results obtained by using the realistic SO potential (3) and a commonly used approximated version (*22*) $\frac{1}{2m^2c^2}\frac{1}{r}\frac{dV_{eff}{}^{i}}{dr}\bar{L}_i\cdot\bar{S}_i$ obtained by using an averaged spherically symmetrized effective potential V_{eff}. As a general result, the correct ordering and order of magnitude is obtained in both cases, being however the results obtained from the realistic SO potential in better agreement with the experimental data (*21*). This is due to an improved screening with respect to the averaged effective potential.

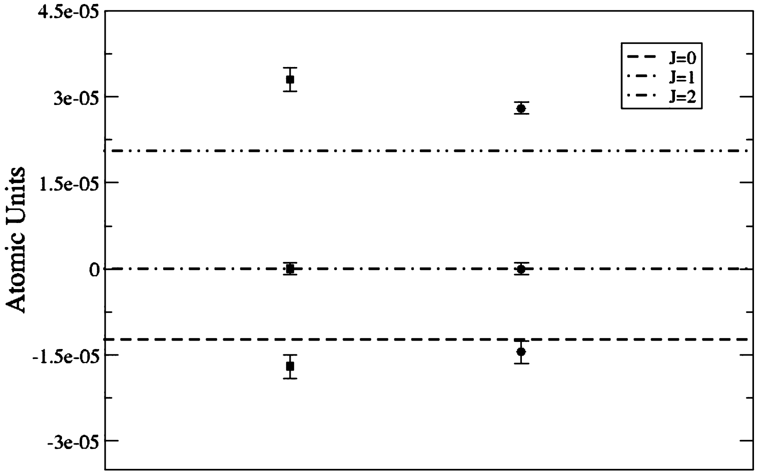

Figure 1. SO splittings for the C atom, defined as E(J)-E(0). Lines represent experimental data (21) . Squares and circles correspond to VMC results with effective and realistic SO interaction, respectively.

Moreover, the reported VMC data clearly show that the theoretical ratio 1:2 between the splittings $E(J{=}1)$-$E(J{=}0)$ and $E(J{=}2)$-$E(J{=}1)$ predicted by the *LS* coupling is correctly reproduced, though implying an imperfect agreement with experimental data.

As a second example, a VMC calculation of SO splittings in the Pb atom is reported. Though the method is certainly applicable to all electron calculations, given the large atomic number (Z=82), an optimal choice, enabling for a drastic reduction of the computational cost, is the use of a pseudopotential (*4*).

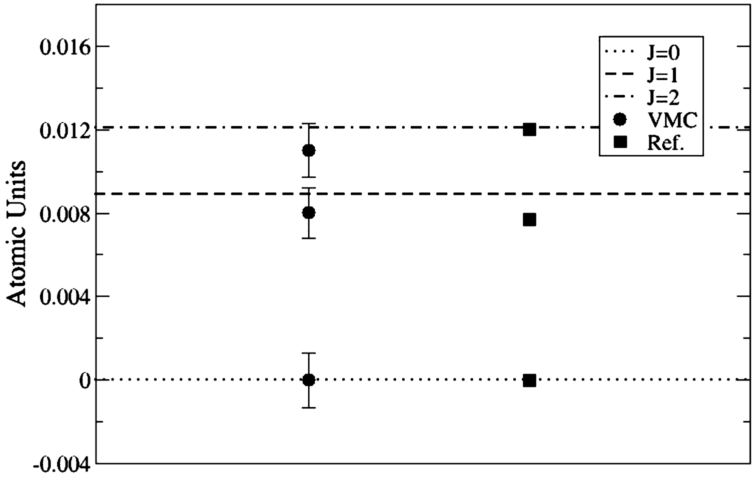

Figure 2. SO splittings for Pb. Lines correspond to experimental data (21). VMC results are reported as circles, HF data (21) is also given for comparison as squares.

Within this approach only valence electrons are explicitly considered, while keeping track of the inner electrons through an effective interaction. This approximation still allows for an accurate description of SO effects, being those induced by the p valence orbitals. Given the importance of SO effects in Pb, in this case a VMC wave function optimization procedure was applied (*19*, *23*, *24*).

In Figure 2 VMC *jj* coupling results are reported for the three lowest states of Pb, together with HF (*4*) and experimental (*21*) results. Correct ordering of the different states is found, together with a good compatibility with both HF and experimental data.

DMC+SO: Two-Dimensional Electron Gas in Presence of Rashba Interaction

Hamiltonian

A two dimensional (2D) model is considered in this section in order to give a description of an infinite system of electrons strongly confined along the z direction (*13*). Such a system is experimentally realized in quantum wells, typically based on semiconductor heterostructures. In this kind of systems electrons have been experimentally proved (*5*) to undergo the effect of a SO-like interaction

(Rashba interaction) having the form: $V_{Rashba} = \lambda \sum_{i=1}^{N} \left(p_y^i \sigma_x^i - p_x^i \sigma_y^i \right)$ where the σ^i indicate the Pauli matrices and the p^i the momentum operators. The constant λ is the SO coupling strength, which is experimentally tunable by means of a gate potential.

In order to simplify the description, we will consider the electrons in the semiconductor as a homogeneous electron gas in which the effects of the surrounding medium is included through an effective mass $m=m^*m_e$ and a dielectric constant ε.

The resulting 2D effective Hamiltonian, which includes a kinetic term, the Rashba spin-orbit interaction, and Coulomb interaction, reads:

$$H = \sum_{i=1}^{N} \frac{(p_x^i)^2 + (p_y^i)^2}{2m} + \lambda \sum_{i=1}^{N} \left(p_y^i \sigma_x^i - p_x^i \sigma_y^i \right) + \frac{e^2}{\varepsilon} \sum_{i<j}^{N} \frac{1}{|\bar{r}_i - \bar{r}_j|}$$

Hereafter effective atomic units will be used, defining $\hbar = e^2 \varepsilon = m^* m_e = 1$, $a_0^* = a_0 \varepsilon / m^*$ and $H^* = H m^* / \varepsilon^2$.

Although the Rashba SO interaction certainly appears simpler than the realistic SO interaction (3), the procedure illustrated in the following should be intended as a general approach, that can be extended to a broad variety of systems.

Diffusion Monte Carlo

The imaginary--time τ propagation that is commonly implemented in Diffusion Monte Carlo calculations relies on the knowledge of the imaginary time propagator G defined by: $\psi(R,\tau+\Delta\tau) = \int dR' G(R,R',\Delta\tau) \Psi(R',\tau)$

The standard approach is based on applying the Trotter-Suzuki approximation, valid in the limit of short imaginary time steps:

$$G(R,R',\Delta\tau) \approx e^{-[V(R)-E\_0]\Delta\tau} G_0(R,R',\Delta\tau) =$$

$$= e^{-[V(R)-E\_0]\Delta\tau} \left(2\pi\Delta\tau\right)^{-N} e^{-\frac{(R-R')^2}{2\Delta\tau}}$$

where E_0 is a constant introduced in order to preserve the wave function normalization. When restricting to local potentials the exponential factor containing $V(R)$ is interpreted as a weight, and is typically applied after the space propagation given by the free imaginary time propagator G_0. In this case only space coordinates are treated in a dynamical fashion, while spin appears as a static label. In standard DMC implementations, therefore, walkers will be displaced according to the Gaussian propagator G_0 and weighted according to the potential computed in the coordinates relative to the walkers themselves. Such an implementation, however, is not possible in the case of potentials carrying momentum dependence. The fundamental reason is that walkers basically are local objects, only carrying information about the system coordinates. Since no information about the wave function derivatives is present in the walkers, an alternative approach is required.

In the case of the Rashba potential, an extended DMC implementation (*13*, *14*) is achieved by an explicit separation of the local and SO potential prior to the use of the Trotter's formula.

Three separate factors are thus obtained, containing local potential, SO potential and kinetic energy, respectively:

$$e^{-H\Delta\tau} \approx e^{-V_{local}\Delta\tau} e^{-V_{SO}\Delta\tau} e^{-T\Delta\tau} \tag{4}$$

Notice that the ordering of these three factors does not affect the result up to order $\Delta\tau$. The most convenient ordering is therefore chosen as in (4), placing the exponential of V_{SO} right after the Gaussian free imaginary time propagator. The momentum operators contained in V_{SO} will now act as derivatives on the G_0 factor. The exponential of V_{SO} is thus turned into a factor, depending on space displacements and spin operators, which act rotating the spin components of the single electron spinors. The third (local) factor is then used as a weight in the standard way. The full propagator is expressed as:

$$G(R,R',\Delta\tau) = e^{-\left(V_{Coul}(R)-E_0-N\lambda^2\right)\Delta\tau} e^{-i\sum_{j=1}^{N}\Delta r_j^y\sigma_j^x-\Delta r_j^x\sigma_j^y} G_0(R,R',\Delta\tau) \tag{5}$$

R and *R′* respectively indicate the new and old coordinates of the *N* electrons, V_{Coul} the Coulomb potential and Δr_j^i ($j=x,y$) the *x* and *y* components of the *j*-th electron space displacement.

The walkers should now carry both information regarding space and spin coordinates, since both will be sampled along the imaginary time propagation.

At each propagation step, spatial displacements are sampled according to G_0 and spin coordinates are modified depending on rotation matrix in (5). Finally the weighting factor is applied.

Results

The infinite two dimensional electrons gas, described by the Hamiltonian (3) is modeled through a periodic two-dimensional cell, containing 58 electrons. Ewald summation is applied in order to efficiently account for the Coulomb interaction in the extended system and twist-averaged boundary conditions are implemented in order to significantly reduce finite size effects (*24*, *25*).

The many body trial wave function is built as a Slater determinant of single particle orbitals multiplied by a two-body Yukawa-type (*13*) Jastrow factor.

Single particle orbitals were chosen as solutions of the Hamiltonian of the system in absence of Coulomb interaction:

$$\left\langle r,s\,|\,\varphi_{T,\bar{k},\pm}\right\rangle = \left[\pm\alpha\frac{k_x + ik_y}{|\,\bar{k}\,|} + \beta\right]e^{i\bar{k}\cdot\bar{r}}$$

where α and β are the spin coordinates along the z axis of the electrons.

As clearly visible from the previous equation, for each wave vector $\underline{k}$ two distinct non degenerate single particle states exist, carrying a + or a - sign in the z up component. The former class of states, (+ sign) will be referred to as "quasi-up" states, while the latter (- sign) will be named "quasi-down" states.

Given the intrinsic imaginary character of the trial wave function, the fixed node approximation (*26*) cannot be employed. For this reason the fixed phase approximation (*27–29*) was used instead. This approximation constrains the projected distribution of walkers to the state of lowest energy having the same phase as the trial wave function.

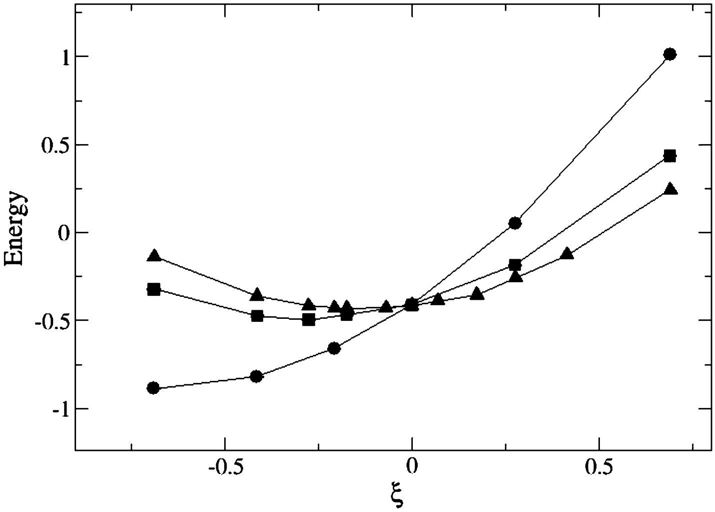

Figure 3. Energy values (in Ry) obtained at r_S=1 for three different values of λ respectively 0.1 (triangles), 0.2 (squares) and 0.5 (circles).

In Figure 3 DMC energy values are reported for three different values of the SO coupling constant λ at fixed density (Wigner-Seitz radius r_S=1) as a function of the so-called quasi-polarization, defined as $\xi = \frac{N_- - N_+}{N}$ where N_+ and N_- correspond to the number of *quasi-up* and *quasi-down* spin particles in the Slater determinant.

From the three curves a tendency for the system clearly appears to assume an increasing (in modulus) quasi polarization for larger λ values, respecting somehow the independent particle picture even in presence of the Coulomb two-body interaction.

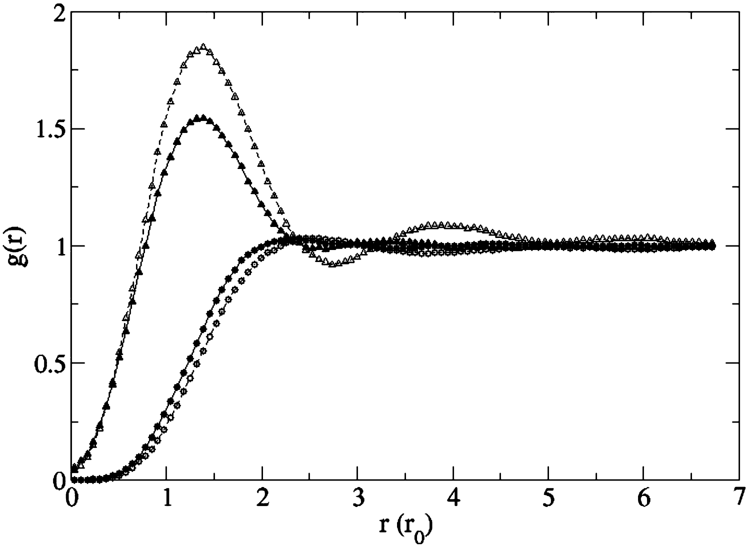

Figure 4. Pair correlation function g(r) decomposed into singlet and triplet channels for r_s=5 with and without spin-orbit interaction. Empty triangles and empty circles correspond to triplet and singlet channels at λ=0. Full triangles and full circles correspond to triplet and singlet channels at λ=0.

Figure 4 shows the two body distribution function with separated singlet and triplet contributions (*13*), corresponding to the probability of finding two particles at a given distance in either singlet or triplet total spin configuration.

Comparing the curves in presence and in absence of Rashba interaction it is possible to notice how the first peaks of the singlet and triplet channels get closer to each other when the SO interaction is considered, suggesting a decreased antiferromagnetic character of the electron gas.

Conclusions

Extensions of the VMC and DMC methods capable of dealing with SO interacting systems were presented together with the results of applications to two different classes of physical systems.

Both algorithms are based on a stochastic integration over the electron spin variables, thus implying a dynamical treatment of spin coordinates and, consequently, slightly more complex and demanding codes. The additional computational cost due to the use of a single Slater determinant for all the electrons and of complex numbers is not seriously impairing the possibility of performing simulations with a considerable number of electrons. The methods here exposed represent highly accurate tools for the study of SO effects in a variety of physical systems. These first encouraging applications will certainly be followed by a more systematic study of the still largely unexplored field of the phenomenology of SO interactions.

Acknowledgments

Calculations were performed on the Wiglaf cluster of the Physics department of the University of Trento and on CINECA computers under grants of the University of Trento. L.M. acknowledges support by ARO and NSF grants DMR-0804549 and OCI-0904794.

We want to thank Stefano Gandolfi, Francesc Malet, and Jose Maria Escartin for useful discussions.

References

1. Dirac, P. A. M. *Proc. R. Soc. London, Ser. A* **1928**, *117*, 610.
2. Thomas, L. H. *Nature (London)* **1926**, *117*, 514.
3. Condon, E. U.; Shortley, G. H. *The Theory of Atomic Spectra*; Cambridge University Press: Cambridge, U. K., 1935.
4. Küchle, W.; Dolg, M.; Stoll, H.; Preuss, H. *Mol. Phys.* **1991**, *74*, 1245–1263.
5. Rashba, E. I. *Phys. Rev. B* **2004**, *70*, 201309.
6. Bychov, Yu. A.; Rashba, E. I. *J. Phys. C* **1994**, *17*, 6039.
7. Dresselhaus, G. *Phys. Rev.* **1955**, *100*, 580.
8. Kouwenhoven, L. P.; Oosterkamp, T. H.; Danoesastro, M. W. S.; Eto, M.; Austing, D. G.; Honda, T.; Tarucha, S. *Science* **1997**, *278*, 1788.
9. Steward, D. R.; Sprinzak, D.; Marcus, C. M.; Duruöz, C. I.; Harris, J. S., Jr. *Science* **1997**, *278*, 1784.
10. Nitta, J.; Akazaki, T.; Takayanagi, H.; Enoki, T. *Phys. Rev. Lett.* **1997**, *78*, 1335.
11. Engels, G.; Lange, J.; Schäpers, T.; Lüth, H. *Phys. Rev. B* **1997**, *55*, R1958.
12. Kohda, M.; Nihei, T.; Nitta, J. *Phys. E* **2008**, *40*, 1194–1196.
13. Ambrosetti, A.; Pederiva, F.; Lipparini, E.; Gandolfi, S. *Phys. Rev. B* **2009**, *80*, 125306.
14. Ambrosetti, A.; Pederiva, F.; Lipparini, E. *Phys. Rev. B* **2011**, *83*, 1.
15. Lipparini, E.; Barranco, M.; Malet, F.; Pi, M. *Phys. Rev. B* **2009**, *79*, 115310.
16. Maksym, P. A.; Chakraborty, T. *Phys. Rev. Lett.* **1990**, *65*, 108.
17. Aleiner, L.; Fal'ko, V. *Phys. Rev. Lett.* **2001**, *87*, 256801.
18. See e.g. W. M. C. Foulkes, L. Mitas, R. J. Needs and G. Rajagopal, *Rev. Mod. Phys.* (2001) 73, 33.
19. Ambrosetti, A.; Silvestrelli, P. L.; Toigo, F.; Mitas, L.; Pederiva, F., **2001**, arXiv:1103.6209v1.
20. Clementi, E.; Roetti, C. *Nucl. Data Tables* **1974**, *14*, 177.
21. Sansonetti, J. E.; Martin, W. C. *J. Phys. Chem. Ref. Data* **2005**, *34*, 1559.
22. Slater, J. C. *Quantum Theory of Atomic Structure*; McGraw-Hill: New York, 1960.
23. Bitzek, E.; Koskinen, P.; Gaehler, F.; Moseler, M.; Gumbsch, P. *Phys. Rev. Lett.* **2006**, *97*, 170201.
24. Sorella, S.; Casula, M.; Rocca, D. *J. Chem. Phys.* **2007**, *127*, 014105.
25. Lin, C.; Zhong, F. H.; Ceperley, D. M. *Phys. Rev. E* **2001**, *64*, 016702.
26. Bajdich, M.; Mitas, L.; Drobny, G.; Wagner, L. K. *Phys. Rev. B* **2005**, *72*, 075131.

27. Bolton, F. *Phys. Rev. B* **1996**, *54*, 4780.
28. Colletti, L.; Pederiva, F.; Lipparini, E.; Umrigar, C. J. *Eur. Phys. J. B* **2002**, *27*, 385.
29. Gandolfi, S.; Pederiva, F.; Fantoni, S.; Schmidt, K. E. *Phys. Rev. Lett.* **2007**, *98*, 102503.

Downloaded by UNIV OF GUELPH LIBRARY on May 28, 2012 | http://pubs.acs.org
Publication Date (Web): February 6, 2012 | doi: 10.1021/bk-2012-1094.ch011

Chapter 11

High-Energy Electron Scattering from Selected Diatomics Using Monte Carlo Methods

S. A. Alexander,[*,a] Sumita Datta,[b] and R. L. Coldwell[c]

[a]Department of Physics, Southwestern University, Georgetown, Texas 78626
[b]Department of Theoretical Physics,
Indian Association for the Cultivation of Science,
2A and 2B Raja S. C. Mullick Road, Jadavpur, Kolkata 700 032, India
[c]Department of Physics, University of Florida, Gainesville, Florida 32611
[*]E-mail: alexands@southwestern.edu

Using highly-accurate trial wavefunctions optimized by Filippi and Umrigar (*J. Chem. Phys.* **1996**, *105*, 213), we compute cross sections for the elastic and inelastic scattering of fast electrons and X-rays by the diatomics Li_2, Be_2, B_2, C_2, N_2, O_2 and F_2. Our results are in good agreement with previous calculations but previously observed discrepancies with experiment remain.

Introduction

In the first Born approximation (*1*, *2*) the cross sections for the elastic scattering of high energy (>25 keV) electrons off a molecule is normally written as

$$\frac{\sigma^{e}_{el}}{\sigma_R} = \frac{1}{4\pi} \int d\Omega_{\mathbf{q}} \left| \sum_{A} Z_A \, e^{i\mathbf{q}\bullet\mathbf{R}_A} - F(\mathbf{q}) \right|^2 \qquad (1)$$

the Waller-Hartree cross section for the elastic scattering of X-rays is

$$\frac{\sigma^{xr}_{el}}{\sigma_T} = \frac{1}{4\pi} \int d\Omega_{\mathbf{q}} \left| F(\mathbf{q}) \right|^2 \qquad (2)$$

© 2012 American Chemical Society
In Advances in Quantum Monte Carlo; Tanaka, S., et al.;
ACS Symposium Series; American Chemical Society: Washington, DC, 2012.

Downloaded by UNIV OF GUELPH LIBRARY on May 28, 2012 | http://pubs.acs.org
Publication Date (Web): February 6, 2012 | doi: 10.1021/bk-2012-1094.ch011

the inelastic cross section is

$$\frac{\sigma_{in}^{e}}{\sigma_R} = \frac{\sigma_{in}^{xr}}{\sigma_T} = \frac{1}{2\pi} \int d\Omega_{\mathbf{q}} <\Psi| \sum_{j<k} e^{i\mathbf{q}\bullet|\mathbf{r}_j - \mathbf{r}_k|} |\Psi> - \frac{\sigma_{el}^{xr}}{\sigma_T} \tag{3}$$

and the form factor is defined as

$$F(\mathbf{q}) = <\Psi| \sum_{j} e^{i\mathbf{q}\bullet\mathbf{r}_j} |\Psi> \tag{4}$$

Here σ_R is the Rutherford cross section, σ_T is the Thompson cross section, **q** is the momentum transfer, R_A is the distance from the center of mass of the molecule to atom A, Z_A is the atomic charge of atom A, and r_i is the distance from the center of mass of the molecule to electron i. The internuclear axis is aligned with the polar (z) axis and the origin is at the center of mass. In such cases the angular integration $d\Omega_{\mathbf{q}}$ simplifies to $d(\cos\theta)$ and this spherical integration for a fixed value of q is normally done using Gauss-Legendre quadrature.

Equations 1-4 have been used to calculate scattering cross sections for a number of molecules (see, for example, Refs. (*3–14*)). The wavefunctions in these calculations almost always assume the Born-Oppenheimer approximation near the molecular equilibrium because this choice usually produces reasonable agreement with experiment.

One molecule that has received considerable attention is H_2 because the results from a variety of high-quality theoretical calculations (*15–27*) can be compared with the results from several experiments (*28–32*). For this system a high-quality Born-Oppenheimer wavefunction produces cross sections that exhibit small but detectable deviations from experiment. In 1982 Kolos, Szalewicz and Monkhorst used a set of 36-term correlated Gaussians to determine the ground state energy of H_2 as well as the elastic, inelastic and total cross sections at several internuclear distances (*20*). They then calculated the rovibrationally-average of each cross section and got excellent agreement with experiment.

In this paper we use Monte Carlo integration techniques to compute cross sections for the elastic and inelastic scattering of fast electrons and X-rays by the diatomics Li_2, Be_2, B_2, C_2, N_2, O_2 and F_2. Because no analytic integrals need be determined, these techniques enable us to evaluate all of these expectation values using highly accurate, explicitly correlated wavefunctions. Where available we will compare our results with those computed by other theoretical methods and with experiment. Unless otherwise indicated, all values in this paper are given in atomic units.

Calculations

Variational Monte Carlo is a method of computing the expectation value of an operator

$$<A> = \sum_{i} [\, \Psi(\mathbf{x}_i)\, A\, \Psi(\mathbf{x}_i) \,/\, w(\mathbf{x}_i) \,] \,/\, \sum_{i} [\, \Psi(\mathbf{x}_i)^2 \,/\, w(\mathbf{x}_i) \,] \tag{5}$$

Downloaded by UNIV OF GUELPH LIBRARY on May 28, 2012 | http://pubs.acs.org
Publication Date (Web): February 6, 2012 | doi: 10.1021/bk-2012-1094.ch011

and its standard deviation (i.e. statistical error)

$$\sigma^2 = \sum_i \left[(A\Psi(\mathbf{x}_i) - \langle A\rangle \Psi(\mathbf{x}_i))^2 \, \Psi(\mathbf{x}_i)^2 / w(\mathbf{x}_i)^2 \right] / \left\{ \sum_i \left[\Psi(\mathbf{x}_i)^2 / w(\mathbf{x}_i) \right] \right\}^2 \qquad (6)$$

sing Monte Carlo integration. Here $\psi(\mathbf{x}_i)$ is the value of the trial wavefunction at the Monte Carlo integration point $\mathbf{x}_i$ and the weight function $w(\mathbf{x}_i)$ is the relative probability of choosing this point. The adjustable parameters in the trial wavefunction are often optimized with respect to a functional, usually some combination of the energy and its standard deviation (*33*, *34*). The Monte Carlo integration points used in these calculations are generated from a guiding function that can also be optimized with respect to the standard deviation of the local energy or any other property (*35*).

In Ref. (*36*) Filippi and Umrigar used the explicitly correlated multideterminental trial wavefunction form

$$\Psi = \left[\sum_k \det_k \right] \exp^{\text{Jastrow}} \qquad (7)$$

to calculate the energy of several homonuclear diatomics. Although these wavefunctions have fewer than 100 adjustable parameters, we show in Table 1 that they clearly capture a large percentage of the correlation energy. These values have been computed with 4096000 Monte Carlo integration points that were generated from a guiding function that minimizes the variance in the local energy of each molecule and a selection process that includes information about the position of the nodes (*37*, *38*). With the exception of the two largest diatomics our energies are statistically equivalent to the variational results given in Ref. (*36*). Despite our using the exact same wavefunctions as in that reference, we found that our O2 energy is lower by almost three standard deviations and that our F2 energy is higher by more than eight standard deviations. Extensive testing has not revealed any error in our program so for the moment the cause of this discrepancy remains unknown.

In Tables 2-4 we list the values obtained for the elastic electron, elastic X-ray and inelastic scattering cross sections, respectively, using these same wavefunctions. As in Ref. (*27*) we use from 6 to 22 Gaussian integration points to rotationally average each cross section at the equilibrium geometry prior to the Monte Carlo sampling. With this number of integration points we are able to obtain converged cross sections to at least three significant figures with a small statistical error in the last significant digit.

Downloaded by UNIV OF GUELPH LIBRARY on May 28, 2012 | http://pubs.acs.org
Publication Date (Web): February 6, 2012 | doi: 10.1021/bk-2012-1094.ch011

Table 1. Comparison of our molecular energies with estimates of the Hartree-Fock energy limit and the Born-Oppenheimer energy limit (both from Ref. (*36*)). Our energies were calculated using 4 096 000 Monte Carlo integration points and the wavefunctions in Ref. (*36*). The number in the parenthesis is the statistical error. R is the internuclear distance. All values are in a.u.

System	*R*	*Number of determinants*	*Molecular Energy*	*Hartree-Fock Energy*	*Born-Oppenheimer Energy*	*Correlation Energy*
Li_2	5.051	5	-14.98844(6)	-14.87152	-14.9945	95%
Be_2	4.63	16	-29.3130(2)	-29.13242	-29.33854(5)	88%
B_2	3.005	11	-49.3603(4)	-49.09088	-49.415(2)	83%
C_2	2.3481	16	-75.8291(7)	-75.40620	-75.923(5)	82%
N_2	2.068	17	-109.437(1)	-108.9928	-109.5423	81%
O_2	2.282	7	-150.194(2)	-149.6659	-150.3268	80%
F_2	2.68	2	-199.351(7)	-198.7701	-199.518925	78%

Downloaded by UNIV OF GUELPH LIBRARY on May 28, 2012 | http://pubs.acs.org
Publication Date (Web): February 6, 2012 | doi: 10.1021/bk-2012-1094.ch011

Table 2. Elastic electron scattering cross sections (Eqn. 1) for several diatomics at select values of the momentum transfer variable, q. These results have been computed using 4 096 000 Monte Carlo integration points. The number in the parenthesis is the statistical error. All values are in a.u.

q	Li_2	Be_2	B_2	C_2	N_2	O_2	F_2
0.10	0.002287(5)	0.003097(6)	0.002469(4)	0.001644(3)	0.001570(3)	0.001454(4)	0.001131(4)
0.20	0.03217(7)	0.04458(9)	0.03736(6)	0.02545(4)	0.02443(5)	0.02260(6)	0.01753(5)
0.30	0.1326(3)	0.1900(4)	0.1727(2)	0.1222(2)	0.1182(3)	0.1096(3)	0.0849(2)
0.40	0.3196(6)	0.4756(9)	0.4822(7)	0.3591(5)	0.3512(7)	0.3264(8)	0.2524(7)
0.50	0.5677(9)	0.874(2)	1.009(1)	0.799(1)	0.792(2)	0.739(2)	0.571(2)
0.60	0.836(1)	1.317(2)	1.745(2)	1.484(2)	1.494(3)	1.400(3)	1.078(3)
0.70	1.103(1)	1.757(3)	2.634(3)	2.420(3)	2.480(5)	2.333(5)	1.795(5)
0.80	1.3778(9)	2.208(3)	3.594(4)	3.579(4)	3.737(7)	3.533(7)	2.715(7)
0.90	1.684(1)	2.746(3)	4.548(4)	4.903(5)	5.221(9)	4.96(1)	3.81(1)
1.00	2.041(1)	3.468(4)	5.445(5)	6.317(5)	6.86(1)	6.55(1)	5.05(1)
1.20	2.884(2)	5.628(4)	7.068(5)	9.139(6)	10.29(2)	9.94(2)	7.79(2)
1.40	3.677(2)	8.297(5)	8.786(6)	11.676(8)	13.49(2)	13.23(2)	10.84(3)
1.60	4.128(2)	10.384(6)	11.080(6)	13.958(9)	16.24(2)	16.34(3)	14.52(3)
1.80	4.200(2)	11.168(6)	14.121(7)	16.32(1)	18.76(2)	19.65(3)	19.49(3)
2.00	4.177(2)	10.886(6)	17.606(7)	19.17(1)	21.52(2)	23.80(3)	26.36(4)
2.20	4.444(2)	10.432(6)	20.919(8)	22.705(8)	25.00(2)	29.32(3)	35.27(5)

Continued on next page.

Downloaded by UNIV OF GUELPH LIBRARY on May 28, 2012 | http://pubs.acs.org
Publication Date (Web): February 6, 2012 | doi: 10.1021/bk-2012-1094.ch011

Table 2. (Continued). Elastic electron scattering cross sections (Eqn. 1) for several diatomics at select values of the momentum transfer variable, q. These results have been computed using 4 096 000 Monte Carlo integration points. The number in the parenthesis is the statistical error. All values are in a.u.

q	Li_2	Be_2	B_2	C_2	N_2	O_2	F_2
2.40	5.151(3)	10.620(6)	23.437(9)	26.844(7)	29.47(2)	36.39(4)	45.63(6)
2.60	6.073(3)	11.640(5)	24.79(1)	31.237(9)	34.92(2)	44.67(4)	56.28(7)
2.80	6.803(4)	13.018(6)	24.97(1)	35.39(1)	41.01(2)	53.44(5)	65.79(9)
3.00	7.125(4)	14.052(6)	24.31(1)	38.80(1)	47.21(2)	61.72(6)	73.0(1)
3.20	7.219(4)	14.354(7)	23.35(1)	41.12(1)	52.94(2)	68.64(6)	77.5(1)
3.40	7.493(4)	14.124(7)	22.64(1)	42.22(2)	57.64(2)	73.54(7)	79.6(1)
3.60	8.193(4)	13.969(7)	22.593(9)	42.19(2)	60.96(2)	76.20(7)	80.2(1)
3.80	9.160(5)	14.423(6)	23.360(9)	41.33(2)	62.75(2)	76.80(8)	80.6(1)
4.00	9.971(6)	15.542(6)	24.813(9)	40.05(2)	63.08(2)	75.92(7)	82.0(1)
4.20	10.334(6)	16.871(6)	26.61(1)	38.82(2)	62.23(3)	74.32(7)	85.0(1)
4.40	10.368(6)	17.810(6)	28.32(1)	38.03(2)	60.63(3)	72.82(7)	89.9(1)
4.60	10.484(6)	18.081(6)	29.55(1)	37.96(2)	58.74(3)	72.10(6)	95.9(1)
4.80	10.996(6)	17.938(6)	30.12(1)	38.71(2)	57.06(3)	72.62(6)	102.2(1)
5.00	11.827(6)	17.951(7)	30.04(1)	40.20(2)	55.96(3)	74.48(6)	107.5(1)
5.20	12.578(6)	18.551(8)	29.58(1)	42.21(2)	55.73(3)	77.49(6)	111.0(1)
5.40	12.912(6)	19.691(8)	29.11(1)	44.42(2)	56.45(3)	81.22(6)	112.4(1)

Downloaded by UNIV OF GUELPH LIBRARY on May 28, 2012 | http://pubs.acs.org
Publication Date (Web): February 6, 2012 | doi: 10.1021/bk-2012-1094.ch011

q	Li_2	Be_2	B_2	C_2	N_2	O_2	F_2
5.60	12.867(6)	20.887(8)	28.99(1)	46.49(2)	58.08(2)	85.08(6)	111.7(1)
5.80	12.813(6)	21.613(8)	29.45(1)	48.11(2)	60.39(2)	88.47(6)	109.7(1)
6.00	13.103(7)	21.712(8)	30.53(1)	49.08(2)	63.09(2)	90.91(6)	107.5(1)

Downloaded by UNIV OF GUELPH LIBRARY on May 28, 2012 | http://pubs.acs.org
Publication Date (Web): February 6, 2012 | doi: 10.1021/bk-2012-1094.ch011

Table 3. Elastic X-ray scattering cross sections (Eqn. 2) for several diatomics at select values of the momentum transfer variable, q. These results have been computed using 4 096 000 Monte Carlo integration points. The number in the parenthesis is the statistical error. All values are in a.u.

q	Li_2	Be_2	B_2	C_2	N_2	O_2	F_2
0.10	34.6952(7)	61.9925(9)	98.2641(7)	142.3755(7)	194.199(1)	253.679(1)	320.867(2)
0.20	31.119(2)	56.413(3)	93.275(3)	137.630(3)	188.917(5)	246.860(6)	311.669(7)
0.30	26.130(4)	48.421(6)	85.636(5)	130.127(6)	180.49(1)	235.96(1)	296.99(1)
0.40	20.742(5)	39.482(8)	76.200(8)	120.417(9)	169.45(2)	221.62(2)	277.72(2)
0.50	15.796(5)	30.923(9)	65.89(1)	109.16(1)	156.43(2)	204.66(3)	255.01(3)
0.60	11.790(4)	23.638(9)	55.57(1)	97.06(1)	142.13(3)	185.95(4)	230.11(4)
0.70	8.899(3)	18.020(8)	45.88(1)	84.76(2)	127.25(3)	166.39(4)	204.28(5)
0.80	7.065(3)	14.052(8)	37.27(1)	72.82(2)	112.38(4)	146.81(5)	178.72(6)
0.90	6.106(2)	11.472(7)	29.96(1)	61.68(2)	98.06(4)	127.91(5)	154.44(7)
1.00	5.784(2)	9.928(6)	24.00(1)	51.62(2)	84.67(4)	110.26(5)	132.22(7)
1.20	6.090(2)	8.639(5)	15.707(8)	35.29(1)	61.63(4)	80.08(5)	95.84(7)
1.40	6.416(2)	8.212(5)	11.119(7)	23.91(1)	44.07(3)	57.58(5)	70.99(6)
1.60	6.048(2)	7.683(5)	8.844(6)	16.64(1)	31.58(3)	42.20(4)	56.11(6)
1.80	5.148(2)	6.814(5)	7.827(5)	12.331(9)	23.14(2)	32.41(3)	48.12(5)
2.00	4.265(2)	5.800(4)	7.389(5)	9.943(7)	17.66(2)	26.44(3)	43.84(4)
2.20	3.766(2)	4.985(4)	7.129(4)	8.695(5)	14.16(2)	22.79(3)	40.80(5)

Downloaded by UNIV OF GUELPH LIBRARY on May 28, 2012 | http://pubs.acs.org
Publication Date (Web): February 6, 2012 | doi: 10.1021/bk-2012-1094.ch011

q	Li_2	Be_2	B_2	C_2	N_2	O_2	F_2
2.40	3.600(2)	4.577(4)	6.832(5)	8.054(4)	11.95(1)	20.37(3)	37.58(5)
2.60	3.475(3)	4.518(3)	6.411(5)	7.688(4)	10.51(1)	18.50(3)	33.65(6)
2.80	3.175(3)	4.549(3)	5.869(5)	7.401(5)	9.54(1)	16.80(3)	29.14(6)
3.00	2.711(3)	4.420(4)	5.271(5)	7.089(5)	8.83(1)	15.14(3)	24.43(6)
3.20	2.243(2)	4.060(4)	4.706(5)	6.705(6)	8.253(9)	13.48(3)	20.00(6)
3.40	1.906(2)	3.582(4)	4.254(4)	6.246(6)	7.734(8)	11.85(3)	16.18(5)
3.60	1.710(2)	3.164(3)	3.955(4)	5.735(6)	7.231(7)	10.32(3)	13.18(5)
3.80	1.571(2)	2.904(3)	3.802(4)	5.210(6)	6.726(7)	8.93(3)	11.01(4)
4.00	1.408(2)	2.772(2)	3.746(4)	4.715(6)	6.217(8)	7.73(2)	9.59(4)
4.20	1.205(2)	2.659(2)	3.718(4)	4.288(6)	5.713(8)	6.76(2)	8.74(4)
4.40	1.001(2)	2.477(2)	3.653(4)	3.955(6)	5.234(8)	6.01(2)	8.25(3)
4.60	0.842(2)	2.217(2)	3.513(4)	3.724(6)	4.800(9)	5.48(2)	7.95(3)
4.80	0.737(1)	1.938(2)	3.293(3)	3.586(6)	4.428(8)	5.13(2)	7.69(3)
5.00	0.662(1)	1.708(2)	3.017(3)	3.517(5)	4.131(8)	4.94(1)	7.37(3)
5.20	0.591(1)	1.554(2)	2.724(3)	3.483(5)	3.911(8)	4.84(1)	6.96(3)
5.40	0.510(1)	1.451(2)	2.455(3)	3.452(5)	3.763(7)	4.80(1)	6.46(3)
5.60	0.429(1)	1.355(2)	2.236(3)	3.396(5)	3.672(6)	4.77(1)	5.92(3)
5.80	0.361(1)	1.235(2)	2.076(3)	3.298(5)	3.621(6)	4.71(1)	5.39(3)
6.00	0.313(1)	1.093(2)	1.964(3)	3.151(5)	3.588(5)	4.61(1)	4.93(3)

Downloaded by UNIV OF GUELPH LIBRARY on May 28, 2012 | http://pubs.acs.org
Publication Date (Web): February 6, 2012 | doi: 10.1021/bk-2012-1094.ch011

Table 4. Inelastic scattering cross sections (Eqn. 3) for several diatomics at select values of the momentum transfer variable, q. These results have been computed using 4 096 000 Monte Carlo integration points. The number in the parenthesis is the statistical error. All values are in a.u.

q	Li_2	Be_2	B_2	C_2	N_2	O_2	F_2
0.10	0.10211(8)	0.09027(9)	0.08278(8)	0.06384(8)	0.05037(9)	0.0493(1)	0.0445(1)
0.20	0.3776(3)	0.3444(3)	0.3180(3)	0.2495(3)	0.1986(4)	0.1946(5)	0.1759(5)
0.30	0.7515(4)	0.7196(6)	0.6710(5)	0.5404(6)	0.4363(8)	0.428(1)	0.388(1)
0.40	1.1427(5)	1.1632(9)	1.0977(8)	0.913(1)	0.751(1)	0.738(2)	0.672(2)
0.50	1.4944(6)	1.629(1)	1.557(1)	1.341(1)	1.128(2)	1.111(3)	1.015(2)
0.60	1.7830(8)	2.084(1)	2.018(1)	1.798(2)	1.550(2)	1.531(3)	1.406(3)
0.70	2.0094(9)	2.510(2)	2.466(2)	2.265(2)	2.003(3)	1.984(4)	1.833(4)
0.80	2.187(1)	2.897(2)	2.893(2)	2.726(3)	2.473(3)	2.458(5)	2.284(5)
0.90	2.330(1)	3.239(2)	3.300(2)	3.174(3)	2.949(4)	2.941(5)	2.749(6)
1.00	2.454(1)	3.535(2)	3.688(2)	3.605(4)	3.422(4)	3.427(6)	3.222(7)
1.20	2.678(1)	3.996(2)	4.406(3)	4.416(4)	4.342(4)	4.383(7)	4.170(9)
1.40	2.901(1)	4.317(3)	5.029(3)	5.166(4)	5.207(4)	5.300(8)	5.10(1)
1.60	3.129(1)	4.552(3)	5.542(3)	5.855(4)	6.009(5)	6.170(8)	6.01(1)
1.80	3.361(1)	4.746(2)	5.942(4)	6.474(5)	6.743(6)	6.989(9)	6.89(1)
2.00	3.592(1)	4.925(2)	6.249(4)	7.009(6)	7.409(7)	7.75(1)	7.73(1)
2.20	3.816(1)	5.096(2)	6.491(4)	7.456(6)	8.004(7)	8.46(1)	8.53(1)

Downloaded by UNIV OF GUELPH LIBRARY on May 28, 2012 | http://pubs.acs.org
Publication Date (Web): February 6, 2012 | doi: 10.1021/bk-2012-1094.ch011

q	Li_2	Be_2	B_2	C_2	N_2	O_2	F_2
2.40	4.028(1)	5.265(2)	6.691(4)	7.820(5)	8.528(8)	9.11(1)	9.28(2)
2.60	4.227(1)	5.434(2)	6.866(4)	8.113(5)	8.982(8)	9.69(1)	9.98(2)
2.80	4.413(1)	5.601(2)	7.027(4)	8.353(5)	9.372(8)	10.20(2)	10.63(2)
3.00	4.586(1)	5.765(2)	7.178(4)	8.555(5)	9.703(9)	10.66(2)	11.22(2)
3.20	4.743(2)	5.924(2)	7.321(3)	8.729(5)	9.984(9)	11.05(2)	11.75(2)
3.40	4.885(2)	6.077(2)	7.458(3)	8.886(5)	10.22(1)	11.39(2)	12.23(2)
3.60	5.014(2)	6.224(2)	7.591(2)	9.029(5)	10.43(1)	11.68(2)	12.64(2)
3.80	5.129(1)	6.364(2)	7.721(2)	9.163(5)	10.612(9)	11.93(2)	13.00(2)
4.00	5.232(1)	6.495(3)	7.847(3)	9.290(5)	10.772(9)	12.15(2)	13.31(2)
4.20	5.323(1)	6.619(2)	7.972(3)	9.414(5)	10.916(9)	12.35(2)	13.58(2)
4.40	5.404(1)	6.734(2)	8.094(4)	9.536(6)	11.047(9)	12.52(2)	13.81(2)
4.60	5.475(1)	6.841(2)	8.212(4)	9.654(6)	11.169(9)	12.67(2)	14.01(2)
4.80	5.537(1)	6.942(2)	8.325(4)	9.769(6)	11.284(8)	12.80(2)	14.19(2)
5.00	5.593(1)	7.035(2)	8.433(4)	9.880(6)	11.393(8)	12.93(2)	14.35(2)
5.20	5.642(1)	7.122(2)	8.535(3)	9.986(6)	11.499(8)	13.04(2)	14.49(2)
5.40	5.685(1)	7.201(2)	8.633(3)	10.088(6)	11.603(8)	13.15(2)	14.63(2)
5.60	5.722(2)	7.275(2)	8.726(3)	10.186(6)	11.703(8)	13.25(2)	14.75(2)
5.80	5.755(2)	7.341(2)	8.813(3)	10.282(6)	11.801(8)	13.35(1)	14.87(2)
6.00	5.784(2)	7.402(2)	8.895(3)	10.375(6)	11.895(8)	13.45(1)	14.97(2)

Downloaded by UNIV OF GUELPH LIBRARY on May 28, 2012 | http://pubs.acs.org
Publication Date (Web): February 6, 2012 | doi: 10.1021/bk-2012-1094.ch011

Of the seven diatomics examined here, the cross sections of N_2, O_2 and F_2 have previously been studied using other theoretical methods (*3*, *7*, *8*, *10–13*). A detailed comparison of our results with these earlier studies is greatly complicated by the fact that the cross sections produced by these other calculations are almost always presented as difference functions in graphical form. Fortunately in Ref. (*13*) Hoffmeyer *et al.* list the values of their MR-SDCI cross sections in tables so we were able to confirm that all of our values are in very good agreement with theirs. For N_2 all of our elastic electron scattering results are smaller than those in Ref. (*13*) (the percentage difference between these two calculations is 2.5% or less). In contrast, all of our X-ray scattering results are slightly larger, but the percentage difference is less than 1%. When we compare our inelastic results with those of Hoffmeyer *et al.* we find that they are larger in the region $0.1 \leq q \leq 2.0$ (where the percentage difference varies between 1.0% and 4.9%) and smaller in the region $2.2 \leq q \leq 6.0$ (where the percentage difference is 1.5% or less). For O_2 our elastic electron scattering results are slightly larger in the region $0.1 \leq q \leq 1.6$ and slightly smaller in the region $1.8 \leq q \leq 6.0$. The percentage difference in all these calculations is less than 1%. When we compare our X-ray scattering results with those in Ref. (*13*) we find that they are slightly smaller in the region $0.1 \leq q \leq 1.6$ (where the percent difference is less than 1%) and larger in the region $1.8 \leq q \leq 6.0$ (where the percentage difference is 1.2% or less). Similarly our inelastic scattering results are larger in the region $0.1 \leq q \leq 2.0$ (where the percent difference varies between 1.0% and 3.8%) and smaller in the region $2.2 \leq q \leq 6.0$ (where the percentage difference is 1.5% or less).

In Figures 1 and 3 of Ref. (*13*), Hoffmeyer *et al.* plot their elastic electron and inelastic difference curves for N_2 and O_2 alongside those from earlier theoretical calculations (*10–12*) and experiment (*39–42*). They attribute the small, but visible differences between their curves and those produced by the other computational studies to their use of a modest Sadlej basis. This reasonably good agreement between the different theoretical methods (and by extension with our Monte Carlo results) is in stark contrast to the larger discrepancies between the computational difference curves and the experimental curves. Hoffmeyer *et al.* attribute these discrepancies to either experimental errors (and point out that the experimental measurements for N_2 in Refs. (*41*) and (*42*) disagree) or to the neglect of higher-order Born corrections (*13*). We concur with this assessment and believe that the reason for the differences between theory and experimental will remain unresolved until such time as more accurate experimental and/or theoretical determinations are performed on these diatomics.

Conclusions

Accurate molecular cross sections require accurate molecular wavefunctions. For such calculations Meyer and coworkers recommend that the basis set should approach the Hartree-Fock limit (with up to g Gaussian-type orbitals), all electrons should be correlated and all singly and doubly excited configurations should be included as well as a selection of triply and quadruply excited configurations (*12*). The explicitly-correlated wavefunctions defined in Ref. (*36*) have a very different form than those previously used to calculate molecular cross sections. They automatically include the effect of all excitations and are able to capture a large percentage of the correlation energy with roughly a hundred adjustable parameters. Despite these differences the cross sections computed in this study are in generally good agreement with earlier calculations. This suggests that Monte Carlo methods and explicitly-correlated wavefunctions can play a useful role in calculating the scattering cross sections of larger molecules.

Acknowledgments

We wish to thank Drs. Claudia Filippi and Cyrus Umrigar for generously sharing with us the details of their wavefunctions. This work was supported in part by the Department of Science and Technology, India (Award No. SR/WOS A/PS-32/2009).

Downloaded by UNIV OF GUELPH LIBRARY on May 28, 2012 | http://pubs.acs.org
Publication Date (Web): February 6, 2012 | doi: 10.1021/bk-2012-1094.ch011

References

1. Bonham, R. A.; Fink, M. *High Energy Electron Scattering*; Van Nostrand: Princeton, NJ, 1974.
2. Tripathi, A. N.; Smith, V. H., Jr. In *Comparison of ab Initio Quantum Chemistry with Experiment for Small Molecules*; Bartlett, R. J., Ed.; D. Reidel: New York, 1985.
3. Liu, J. W. *J. Chem. Phys.* **1973**, *59*, 1988.
4. Szabo, A.; Ostland, N. S. *J. Chem. Phys.* **1974**, *60*, 946.
5. Pulay, P.; Mawhorter, R.; Kohl, D. A.; Fink, M. *J. Chem. Phys.* **1983**, *79*, 185.
6. Kohl, D. A.; Pulay, P.; Fink, M. *J. Mol. Struct.: THEOCHEM* **1984**, *108*, 149.
7. Breitenstein, M.; Endesfelder, A.; Meyer, H.; Schweig, A. *Chem. Phys. Lett.* **1984**, *108*, 430.
8. Liu, J. W. *Phys. Rev. A* **1985**, *32*, 1384.
9. Tripathi, A. N.; Smith, V. H., Jr.; Thakkar, A. J. *Int. J. Quantum Chem.* **1989**, *35*, 869.
10. Liu, J. W.; Thakkar, A. J.; Tatewaki, H. *J. Phys. B* **1993**, *26*, L185.
11. Meyer, H.; Muller, T.; Schweig, A. *Chem. Phys. Lett.* **1995**, *236*, 497.
12. Meyer, H.; Muller, T.; Schweig, A. *Mol. Phys.* **1996**, *88*, 1563.
13. Hoffmeyer, R. E.; Bundgen, P.; Thakkar, A. J. *J. Phys. B: At., Mol. Opt. Phys.* **1998**, *31*, 3675.
14. Smith, G. T.; Tripathi, A. N.; Smith, V. H., Jr. *J. Chem. Phys.* **1999**, *110*, 9390.
15. Liu, J. W.; Bonham, R. A. *Chem. Phys. Lett.* **1972**, *14*, 346.
16. Liu, J. W.; Smith, V. H., Jr. *J. Phys. B* **1973**, *6*, L275.
17. Liu, J. W. *J. Chem. Phys.* **1973**, *59*, 1988.
18. Bentley, J. J.; Stewart, R. F. *J. Chem. Phys.* **1975**, *62*, 875.
19. Liu, J. W.; Smith, V. H., Jr. *Chem. Phys. Lett.* **1977**, *45*, 59.
20. Kolos, W.; Monkhorst, H. J.; Szalewicz, K. *J. Chem. Phys.* **1982**, *77*, 1323.

21. Szalewicz, K.; Kolos, W.; Monkhorst, H. J.; Jackson, C. *J. Chem. Phys.* **1984**, *80*, 1435.
22. Thakkar, A. J.; Tripathi, A. N.; Smith, V. H., Jr. *Phys. Rev. A* **1984**, *29*, 1108.
23. Liu, J. W. *Phys. Rev. A* **1985**, *32*, 1384.
24. Liu, J. W. *Phys. Rev. A* **1987**, *35*, 591.
25. Sharma, B. S.; Thakkar, A. J. *Phys. Rev. A* **1987**, *36*, 5151.
26. Komasa, J.; Thakkar, A. J. *Phys. Rev. A* **1994**, *49*, 965.
27. Alexander, S. A.; Coldwell, R. L.; Hoffmeyer, R. E.; Thakkar, A. J. *Int. J. Quantum Chem.* **1995**, *S29*, 627.
28. Kohl, D. A.; Bonham, R. A. *J. Chem. Phys.* **1967**, *47*, 1634.
29. Jaegle, A.; Duguet, A. *J. Chem. Phys.* **1971**, *68*, 1154.
30. Ulsh, R. C.; Wllenstein, H. E.; Bonham, R. A. *J. Chem. Phys.* **1974**, *60*, 103.
31. Ketkar, S. N.; Fink, M. *Phys. Rev. Lett.* **1980**, *45*, 1551; **1981**, *47*, 1678, errata.
32. Zhang, Y.; Ross, A. W.; Fink, M. *Phys. Rev. A* **1991**, *43*, 3548.
33. Coldwell, R. L. *Int. J. Quantum Chem.* **1977**, *S11*, 215.
34. Alexander, S. A.; Coldwell, R. L.; Monkhorst, H. J.; Morgan, J. D., III *J. Chem. Phys.* **1991**, *95*, 6622.
35. Alexander, S. A.; Coldwell, R. L.; Morgan, J. D., III *J. Chem. Phys.* **1992**, *97*, 8407.
36. Filippi, C.; Umrigar, C. J. *J. Chem. Phys.* **1996**, *105*, 213.
37. Alexander, S. A.; Coldwell, R. L. *J. Chem. Phys.* **1995**, *103*, 2572.
38. Datta, Sumita; Alexander, S. A.; Coldwell, R. L. *J. Chem. Phys.* **2004**, *120*, 3642.
39. Fink, M.; Moore, P. G.; Gregory, D. *J. Chem. Phys.* **1979**, *71*, 5227.
40. Fink, M.; Schmiedekamp, C. *J. Chem. Phys.* **1979**, *71*, 5243.
41. Zhang, Y.; Ross, A. W.; Fink, M. *Z. Phys. D* **1991**, *18*, 163.
42. Barbieri, R. S.; Bonham, R. A. *Phys. Rev. A* **1991**, *44*, 7361.

Downloaded by UNIV OF GUELPH LIBRARY on May 28, 2012 | http://pubs.acs.org
Publication Date (Web): February 6, 2012 | doi: 10.1021/bk-2012-1094.ch011

Chapter 12

Studying Properties of Floppy Molecules Using Diffusion Monte Carlo

Anne B. McCoy,*, Charlotte E. Hinkle, and Andrew S. Petit

Department of Chemistry, The Ohio State University,
100 W. 18th Ave., Columbus, Ohio 43210
***E-mail: mccoy@chemistry.ohio-state.edu**

Downloaded by CORNELL UNIV on May 28, 2012 | http://pubs.acs.org
Publication Date (Web): February 6, 2012 | doi: 10.1021/bk-2012-1094.ch012

Recent extensions to the Diffusion Monte Carlo approach are presented and discussed in the context of polyatomic molecules that undergo large amplitude vibrational motions, even in their ground states. The methods specifically involve the evaluation of rotationally excited state energies and wave functions, and are discussed in the context of fixed-node studies of H_3O^+ and CH_5^+.

Introduction

An area in which Diffusion Quantum Monte Carlo (DMC) provides great promise and one for which the methodology has not been fully exploited is in studies of molecules or clusters that contain one or more vibrational degrees of freedom that sample large regions of the potential surface even in the vibrational ground state (*1–3*). The advantage of using DMC to study these systems, that is not realized in electronic structure calculations, comes from the fact that the analysis of the results of calculations of the bosonic (nodeless) ground state provides insights into properties of the molecules of interest. While most of the contributions to this volume focus on Quantum Monte Carlo approaches for electronic structure calculations, several have used DMC approaches to study rotation-vibration states. Initially this line of investigation focused on hydrogen bonded clusters (*1–8*). In many of these studies, the intramolecular degrees of freedom were kept fixed, and the studies focused on the intermolecular degrees of freedom (*9*). An attractive feature of these systems was the availability of potential surfaces, which could be readily evaluated for dimer systems and extended to larger clusters using sums of pair-wise and perhaps higher order interactions.

In Advances in Quantum Monte Carlo; Tanaka, S., et al.;
ACS Symposium Series; American Chemical Society: Washington, DC, 2012.

Downloaded by CORNELL UNIV on May 28, 2012 | http://pubs.acs.org
Publication Date (Web): February 6, 2012 | doi: 10.1021/bk-2012-1094.ch012

Over the past decade, interest in using DMC in studies of vibrational properties has moved from molecular clusters to protonated systems, like CH_5^+ (*2*, *6*, *7*, *10*) and protonated water clusters (*2*, *6*, *11*, *12*). These are systems that include several large amplitude vibrations and in which many of the 3N-6 vibrational degrees of freedom are strongly coupled. Often the ground state is delocalized over multiple minima on the potential surface with significant amplitude in the region of the transition states that connect these minima. This type of system is difficult to treat by conventional methods since most of these approaches require a well-defined reference structure.

On the other hand, the delocalization of the ground state wave function along the vibrational degrees of freedom is not nearly as extensive as is seen in electronic structure problems. In the most extreme case of CH_5^+, the ground state wave function has similar amplitude in all 120 equivalent minima and in the region of the 180 low-energy saddle points that connect these minima (*10*). This would lead one to expect that a particle on a sphere basis might be effective for describing the vibrational dynamics in CH_5^+ (*13*). On the other hand, while the amplitudes of the displacements sampled in the coordinates that interconnect the minima are large even in the vibrational ground state, the overall envelope of the CH stretch region of the spectrum is well-described by the average of the harmonic spectra obtained at these 300 stationary points (*14*). The above characteristics of CH_5^+, which make it difficult to treat by conventional methods also make it well-suited for studies based on Diffusion Monte Carlo approaches.

Two sets of challenges are posed by these systems. First, unlike molecular clusters, the potential needs to be separately constructed for each molecule of interest. Second, DMC, in its purest form, provides a method for obtaining the zero-point energy and a Monte Carlo sampling of the ground state wave function. How can a ground state method be used to provide insights into molecules for which much of our understanding of their properties is based on spectroscopic and kinetic studies, which sample rotationally and vibrationally excited states?

The first challenge has been overcome, at least in part, through sophisticated methodologies for obtaining multi-dimensional potential surfaces from numerous electronic energies, and in some cases gradients and Hessians (*15–17*). All of this required data can be generated by any one of a number of commonly available electronic structure programs, and can be evaluated at a variety of levels of theory, depending on the size of the system and the level of accuracy that is desired. With this information in hand, Braams, Bowman and their co-workers fit the electronic energies to high-order polynomial expansions in functions of the atom-atom distances. The fit is constrained to ensure that the potential energy is not affected by exchange of identical particles (*17*). This is the form of the potentials used in the studies of CH_5^+ (*18*) and H_3O^+ (*19*), described below. In an alternative approach, Collins, Jordan and co-workers *GROW* their potential by generating a series of quadratic expansions of the potential in terms of inverse bond-lengths and using Shephard Interpolation to obtain electronic energies at intermediate points (*15*, *16*). This latter approach is ideally suited for DMC studies, since, while the interpolation can lead to artificial *wiggles* in the potential, the statistical sampling of the wave function, generated by the DMC approach, tends to be insensitive to these small oscillations.

The challenge of evaluating excited states using a fundamentally ground state method is more fundamental. This has been a focus of our research over the past decade. Ways in which we have addressed some of these questions is the focus of the present article. In the previous volume of this series (*20*), we outlined our use of the fixed-node treatment, as described by Anderson (*21*, *22*) to calculate vibrational excited states. In the present article we turn our attention to the calculation of rotationally excited states. As mentioned above, the focus of this work will be on systems that display large amplitude excursions from the equilibrium structure, even in the rotational and vibrational ground state, specifically H_3O^+ and CH_5^+.

Downloaded by CORNELL UNIV on May 28, 2012 | http://pubs.acs.org
Publication Date (Web): February 6, 2012 | doi: 10.1021/bk-2012-1094.ch012

General Background

Diffusion Monte Carlo approaches and their applications to a variety of systems are described throughout this volume. In our work we use the simplest form of DMC. We base our implementation on the two early studies of Anderson (*21*)(*22*). Specifically, we take advantage of the fact that when the time-dependent Schrödinger equation is expressed in terms of an imaginary time variable, $\tau = it/\hbar$, the long-time solution converges to the lowest energy solution to the time-independent Schrödinger equation, and the amplitude of the wave function decays with a rate that is proportional to the ground state energy. If the wave function that is being propagated is expressed by an ensemble of δ-functions (or walkers), the positions of which are allowed to move in space under the influence of the imaginary-time time-dependent Schrodinger equation, the resulting equilibrium distribution of walkers represents a Monte-Carlo sampling of the ground state wave function. A more detailed description of this approach and our implementation may be found in our earlier publications (*2*, *23–25*).

As described in Refs. (*20*) and (*22*), one way to generate excited states is through a fixed-node treatment. Here we exploit the fact that if the nodal surface can be described by a simple functional form, the wave function in the vicinity of the nodal surface has similar properties to a wave function in the vicinity of an infinite potential barrier. As such, within our implementation of the fixed-node treatment, we divide configuration space into two parts using the nodal surface as the dividing surface. The two parts correspond to the regions in which the wave function has positive and negative amplitude. The “true” potential surface is used in one region, while the potential is made to be infinite in the other. Because the amplitude of the wave function is zero in regions of configuration space where the potential is infinite, any walker that moves into the region of configuration space where the potential is infinite is removed from the simulation. In practice, when the nodal surfaces divide the wave function into three or more parts, we choose to treat each region separately.

Since we use finite time steps in the simulation, typically 1-10 atomic units, there is a finite probability that a walker that appears to have remained on the same side of the dividing surface could have crossed over to the forbidden region and back within a single time step. If the trajectory had been divided into smaller time increments, this walker would have been removed from the simulation. A statistical measure of the probability of this occurring, based on the distance of the walker from the dividing surface before and after a time step in the simulation, was developed by Anderson (*22*), and this recrossing correction is included in most of our simulations. We have demonstrated the effectiveness of this approach for vibrational problems through direct comparison of DMC calculations of vibrationally excited states to variational results obtained for the same surfaces for Ne_2OH, Ne_2SH (*26*) and $H_3O_2^-$ (*12*).

Direct Evaluation of Rotationally Excited States

The approach described above can be readily extended to rotationally excited states since all that is required is knowledge of the functional form for the nodal surfaces, and, if the recrossing correction is to be used, an expression for the reduced mass associated with motion perpendicular to the nodal surface. The solutions to the rotational Hamiltonian for a rigid molecular system are well-known, and are expressed as functions of the three Euler angles that relate the molecule- and space-fixed Cartesian coordinate systems. Specifically, if the rotational Hamiltonian is expressed as

$$H_{\mathrm{rot}} = AJ_a^2 + BJ_b^2 + CJ_c^2 \tag{1}$$

analytic solutions exist in three cases:

- When J=0, $E_{\mathrm{rot}} = 0$ and the wave functions are isotropic.
- When J=1, there are three solutions with energies of $A+B$, $A+C$ and $B+C$. The corresponding wave functions have analytical solutions that are independent of the values of A, B, and C.
- For symmetric (or spherical) tops with higher values of J, the wave functions can be expressed by the Tesseral harmonics, which are the set of real functions that are eigenfunctions of Eq. (1) when either $A = B$ or $B = C$.

With the excpetion of the J = 0 case, the definitions of the rotational wave functions require definitions for the arguments of the Tesseral harmonics, θ and χ, which in turn require an embedding of a body-fixed axis system.

At first thought the embedding of a body-fixed axis system in a highly fluxional molecule seems like an insurmountable problem. In earlier studies of CH_5^+ (*27*), Ne_nOH (*28*) and $H_5O_2^+$ (*2*), we have demonstrated that application of the Eckart conditions (*29*) through a series of linear algebra manipulations provides a robust internal coordinate system that minimizes the presence of rotation-vibration coupling. The procedure is relatively straight-forward and can be easily applied to the DMC wave functions.

To start, we choose a reference geometry, translate it so the center of mass is at the origin and rotate the molecule to a principle axis frame by ensuring that the moment of inertia tensor is diagonal in this coordinate system. The *3N* Cartesian

Downloaded by CORNELL UNIV on May 28, 2012 | http://pubs.acs.org
Publication Date (Web): February 6, 2012 | doi: 10.1021/bk-2012-1094.ch012

Downloaded by CORNELL UNIV on May 28, 2012 | http://pubs.acs.org
Publication Date (Web): February 6, 2012 | doi: 10.1021/bk-2012-1094.ch012

coordinates that define the reference geometry are denoted by the vectors $\vec{a}_i$. Following Louck and Galbraith (*30*), for an arbitrary structure denoted by a set of *N* vectors $\vec{r}_i$ we define a set of vectors

$$F_{\alpha\beta} = \sum_{i=1}^{N} m_i a_{i,\beta} r_{i,\alpha} \tag{2}$$

where the α and β indices represent the Cartesian components of the vectors (x,y,z). From these we generate a set of unit vectors

$$f_{\alpha,\beta} = \sum_{\gamma} F_{\alpha,\gamma} \left(\Phi^{-1/2}\right)_{\gamma,\beta} \tag{3}$$

where

$$\Phi_{\alpha,\beta} = \sum_{\gamma} F_{\gamma,\alpha} \cdot F_{\gamma,\beta} \tag{4}$$

These vectors provide the three coordinate axes in the Eckart frame so that the Cartesian coordinates of the atoms in the Eckart frame are

$$r_{i,\alpha}^{\text{eck}} = \sum_{\beta} r_{i,\beta} f_{\beta,\alpha} \tag{5}$$

One of the most rigorous tests of Eckart embedding was a study of vibrationally averaged rotational constants for CH_5^+ and its deuterated analogues (*27*). In that study, we calculated the values of $\langle A \rangle_0$, $\langle B \rangle_0$, and $\langle C \rangle_0$ for the ground state of these ions by averaging the values of the elements of the inverse moment of inertia tensor, evaluated using an Eckart frame defined using the procedure described above. We showed that we obtained the same values for the rotational constants independent of the reference geometry used to define the body-fixed axis system. There were examples where this broke down, but they corresponded to using stationary point structures that were not sampled by the ground state wave function as the reference geometry.

With the embedding in hand, we use standard fixed-node approaches in which we assume that the nodal structure is defined by the solutions to the Hamiltonian for a rigid rotor. Specifically, the nodes are placed at the zero's of the Tesseral Harmonics:

$$\begin{aligned} \left\langle \theta, \chi, \phi \middle| J, |K|, M = 0 \right\rangle_{\pm} &= \frac{T_J^{|K|,\pm}(\theta,\chi)}{\sqrt{2\pi}} \\ &= \frac{Y_J^{|K|}(\theta,\chi) \pm (-1)^K Y_J^{-|K|}(\theta,\chi)}{\sqrt{4\pi\left(1+\delta_{K,0}\right)}} \end{aligned} \tag{6}$$

for chosen values of *J* and *K*. For simplicity, we require that *M*=0, although calculations were performed for *J*=1 and non-zero values of *M* (*24*). The values of θ and χ used to define these functions (and the nodes) are extracted from the Eckart rotation matrix (**f**) in Eq. (3). Specifically

$$\begin{aligned} f_{3,1} &= -\sin\theta\cos\chi \\ f_{3,2} &= \sin\theta\sin\chi \\ f_{3,3} &= \cos\theta \end{aligned} \tag{7}$$

Before introducing the nodal surfaces, we run a long equilibration simulation for the $J = 0$ wave function. This simulation needs to be propagated for sufficiently long times to ensure that the wave function is isotropic.

The final ingredient in the DMC simulations is the introduction of the recrossing correction. Specifically, the probability of a walker crossing and then recrossing a nodal surface within a single time step is given by

$$P_{recross} = \exp\left[-\frac{2m_{eff}d(\tau)d(\tau+\Delta\tau)}{\Delta\tau}\right] \tag{8}$$

where $d(\tau)$ and $d(\tau+\Delta\tau)$ are the perpendicular distances of the walker from the nodal surface at the start and end of the time step (*22*). In our studies on H_3O^+, we introduced the following definitions for the effective mass for a node in θ

$$m_{eff} = \sqrt{\left[\frac{I_{AA}(\tau)+I_{AA}(\tau+\Delta\tau)}{2}\right]\left[\frac{I_{BB}(\tau)+I_{BB}(\tau+\Delta\tau)}{2}\right]} \tag{9}$$

and in χ

$$m_{eff} = \sqrt{I_{CC}(\tau)I_{CC}(\tau+\Delta\tau)} \tag{10}$$

where $\mathbf{I}(\tau)$ is the instantaneous moment of inertia tensor for a given walker evaluated in the Eckart frame. Based on our studies on H_3O^+, we found that this correction does not affect the calculated energies for the J=1 levels, and, as a result, it was not used in the calculations involving CH_5^+ where the definitions of the separate rotational constants are less straight-forward (*24*).

Applications to H_3O^+ and CH_5^+

The approach, described above, has been recently applied to studies of H_3O^+ (*24*), CH_5^+ (*25*), and their deuterated analogues. One challenge that we encountered results from the fact that both systems explore broad regions of the potential surface. Specifically, consider the equilibrium structures of these two molecules, shown in the left column of Figure 1, as well as the low-energy saddle points, shown to the right of the corresponding minimum energy structure. In the case of CH_5^+, the structures on the left and right each represent one of 120 equivalent structures, while the one in the center represents one of 60 equivalent structures. The symmetry is lower for H_3O^+, but here there are two equivalent minima on the potential separated by a saddle point.

Downloaded by CORNELL UNIV on May 28, 2012 | http://pubs.acs.org
Publication Date (Web): February 6, 2012 | doi: 10.1021/bk-2012-1094.ch012

Downloaded by CORNELL UNIV on May 28, 2012 | http://pubs.acs.org
Publication Date (Web): February 6, 2012 | doi: 10.1021/bk-2012-1094.ch012

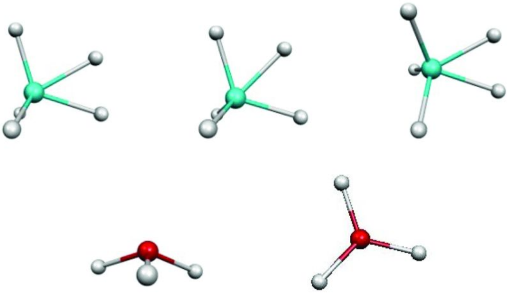

Figure 1. Equilibrium (left) and low-energy transition state (center and right) structures of CH_5^+ (top) and H_3O^+ (bottom).

Without doing any calculations we can anticipate the delocalization of the ground state wave function by comparing the energies of these saddle points, relative to the potential minimum, to the harmonic zero-point energy associated with the mode that connects the minimum to the saddle point geometry. For CH_5^+, the energies of the two saddle points are 29.1 and 340.7 cm^{-1} above the global minimum, while the harmonic zero-point energy in the associated modes are 99.9 and 419.7 cm^{-1} as determined from the potential surface of Jin, Braams and Bowman (*18*). For H_3O^+, the energy of the saddle point is 690 cm^{-1} while the zero-point energy in the out-of-plane vibration is 445.5 cm^{-1} (*19*). In both cases the zero-point energy is close to or larger than the energy of the corresponding saddle point.

If we analyze the fully anharmonic ground state probability amplitude obtained from DMC, we find that there is significant amplitude in all of the equivalent minima and at the saddle points that connect the minima (*10*, *24*), as was anticipated in the harmonic analysis. This behavior is also reflected in the lowest energy vibrationally excited state in both systems being substantially non-zero (46.4 cm^{-1} for H_3O^+ (*24*) and 10.4 cm^{-1} for CH_5^+ (*31*)) but considerably smaller than the lowest calculated harmonic frequency of 891 cm^{-1} in H_3O^+ (*19*) and 199.9 cm^{-1} in CH_5^+ (*18*). Such behavior is indicative of a sizable tunneling splitting of the ground state and is consistent with the ground state wave function having amplitude at the saddle point as well as the minimum energy structures.

This large delocalization of the ground state wave function, on its own, does not cause any problems for the evaluation of rotationally excited states. On the other hand, if we identify the atoms in each of these ions, as is done when we imposed a numbering scheme in Eqs. (2) to (5), the equilibrium structures are chiral, and, based on the above discussion, the ground state wave function has amplitude along the path that connects sets of chiral pairs. The reason this becomes a complicating factor in evaluating rotationally excited states is due to the fact that when a walker samples certain regions of configuration space, the algorithm for the Eckart embedding not only rotates the molecule, it also inverts the axis system. This is more easily seen for H_3O^+, and is illustrated in Figure 2. The top two diagrams represent the reference structure for H_3O^+ (left) and the structure that one would obtain with excitation of the out-of-plane (umbrella) mode. No rotation of the axis system will bring the structure on the right close to that on the left. If instead we first inverted the axis system then performed a 180° rotation (following the arrows through the intermediate structure), we return to the structure on the left. Numerically, the algorithm that we use for the Eckart embedding generates a rotation matrix that has a determinant of –1, and we cannot use this matrix to determine the Euler angles used to define the nodal surfaces. While the problem is easily identified, the solution is less obvious. The only one we have found to be uniformly effective is to use a reference structure that does not contain a chiral center. This can be achieved by using the transition state structure for H_3O^+, shown in the lower right of Figure 1. However, there are no such achiral, energetically accessible stationary point structures for CH_5^+.

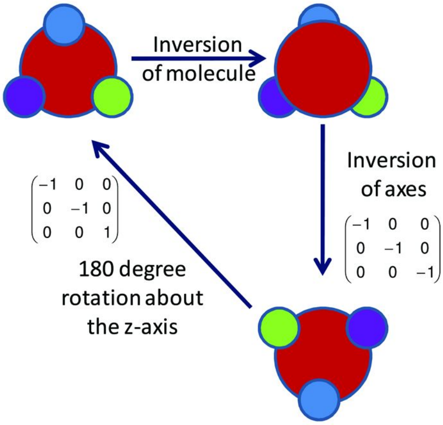
Inversion of molecule
Inversion of axes
$\begin{pmatrix}-1&0&0\\0&-1&0\\0&0&-1\end{pmatrix}$
$\begin{pmatrix}-1&0&0\\0&-1&0\\0&0&1\end{pmatrix}$
180 degree rotation about the z-axis

Figure 2. An illustration of the relationship between "inversion" of H_3O^+ and an inversion of the axis system.

Energies for CH_5^+ and H_3O^+, calculated by this method, for J=0 and J=1 are reported in Table I. For comparison, we also report the energies that are obtained for J=0 when we remove all inverted walkers. To differentiate these states, we denote this state with a superscripted (-) and the ground state with a (+). For comparison, results performed using variational approaches with the same potential surface are also reported (*19*, *31*). Calculations for the deuterated analogues of both species have been performed and the results can be found in the original publications (*24*, *25*). As indicated by the notation, and discussed above, since there is no achiral reference structure that could be chosen for calculations of CH_5^+, the rotationally excited states for CH_5^+ have a vibrational wave function that is antisymmetric with respect to inversion (*25*).

We have also performed calculations for higher J levels in H_3O^+ (*24*), and, more recently on H_3^+ and D_3^+. Generally the agreement remains good at all values of J and we are investigating whether the origins of any break-downs that are observed can be attributed to problems with the model that we employ for defining the nodal surfaces or rotation-vibration interactions that are not well-described by this model. While the agreement is much less good at J=10 than for $J < 6$, to our knowledge these systems have more nodes in the rotation-vibration wave function than any previous fixed-node studies of nuclear dynamics.

Downloaded by CORNELL UNIV on May 28, 2012 | http://pubs.acs.org
Publication Date (Web): February 6, 2012 | doi: 10.1021/bk-2012-1094.ch012

Downloaded by CORNELL UNIV on May 28, 2012 | http://pubs.acs.org
Publication Date (Web): February 6, 2012 | doi: 10.1021/bk-2012-1094.ch012

Table I. $J = 0$ and 1 energies for H_3O^+ (*24*) and CH_5^+ (*25*) calculated using DMC are compared to previously reported energies obtained using the same potential surfaces

Molecule	*State*[a]	*DMC* (cm^{-1})	*Variational*[b] (cm^{-1})
H_3O^+	$\left\|0,0,0\right\rangle^{(+)}$	7452±2	7450.6
	$\left\|0,0,0\right\rangle^{(-)}$	44±5	46.4
	$\left\|1,0,0\right\rangle^{(+)}$	23±4	22.3
	$\left\|1,1,0\right\rangle_{+}^{(+)}$	20±3	17.4
	$\left\|1,1,0\right\rangle_{-}^{(+)}$	19±3	17.4
CH_5^+	$\left\|0,0,0\right\rangle^{(+)}$	10916±5	10926.5
	$\left\|0,0,0\right\rangle^{(-)}$	11±2	10.4
	$\left\|1,0,0\right\rangle^{(-)}$	19±1	
	$\left\|1,1,0\right\rangle_{+}^{(-)}$	20±1	
	$\left\|1,1,0\right\rangle_{-}^{(-)}$	19±1	

[a] The states are labeled as $\left|J,|K|,M\right\rangle_{\pm}^{(\pm)}$, where $\left|0,0,0\right\rangle^{(+)}$ and $\left|0,0,0\right\rangle^{(-)}$ correspond to the lower and upper members of the ground state tunneling doublet respectively and the subscript ± provide the parity of the rotational level. [b] References (*19*) and (*31*).

Concluding Remarks

In this paper, we discuss a method for describing rotationally excited states of molecules that undergo large amplitude motions that was recently developed in our group. The above approach has several advantages over correlation function-based approaches, previously employed by Whaley and Roy and their co-workers to study rotationally excited states of molecules embedded in helium droplets (*4*, *5*). Most important, within the context of floppy molecular systems, the present approach allows for a non-rigid molecule. Further, in contrast to approaches that are based on linear response theory, we are able to obtain the probability amplitude associated with the excited states in a straightforward manner. We are presently working to further characterize the properties of this algorithm through studies of

H_3^+ and D_3^+ and NH_3 for which rotation vibration energies for $J > 5$ have been evaluated using the same potential surfaces.

Acknowledgments

Support for this work by the National Science Foundation (CHE-0848242) is gratefully acknowledged, as is allocation of computational resources from the Ohio Supercomputing Center with which many of the calculations described above were performed.

Downloaded by CORNELL UNIV on May 28, 2012 | http://pubs.acs.org
Publication Date (Web): February 6, 2012 | doi: 10.1021/bk-2012-1094.ch012

References

1. Suhm, M. A.; Watts, R. O. *Phys. Rep.* **1991**, *204*, 293.
2. McCoy, A. B. *Int. Rev. Phys. Chem.* **2006**, *25*, 77.
3. Sandler, P.; Buch, V.; Sadlej, J. *J. Chem. Phys.* **1996**, *105*, 10387.
4. Moroni, S.; Blinov, N.; Roy, P.-N. *J. Chem. Phys.* **2004**, *121*, 3577.
5. Blume, D.; Lewerenz, M.; Whaley, K. B. *J. Chem. Phys.* **1997**, *107*, 9067.
6. Cho, H. M.; Singer, S. J. *J. Phys. Chem. A* **2004**, *108*, 8691.
7. Thompson, K. S.; Crittenden, D. L.; Jordan, M. J. T. *J. Am. Chem. Soc.* **2005**, *127*, 4954.
8. Severson, M. W.; Buch, V. *J. Chem. Phys.* **1999**, *111*, 10866.
9. Buch, V. *J. Chem. Phys.* **1992**, *97*, 726.
10. Brown, A.; McCoy, A. B.; Braams, B. J.; Jin, Z.; Bowman, J. M. *J. Chem. Phys.* **2004**, *121*, 4105.
11. McCoy, A. B.; Huang, X.; Carter, S.; Landeweer, M. Y.; Bowman, J. M. *J. Chem. Phys.* **2005**, *122*, 061101.
12. McCoy, A. B.; Huang, X.; Carter, S.; Bowman, J. M. *J. Chem. Phys.* **2005**, *123*, 064317.
13. Deskevich, M. P.; McCoy, A. B.; Hutson, J. M.; Nesbitt, D. J. *J. Chem. Phys.* **2008**, *128*, 094306.
14. Huang, X.; McCoy, A. B.; Bowman, J. M.; Johnson, L. M.; Savage, C.; Dong, F.; Nesbitt, D. J. *Science* **2006**, *311*, 60.
15. Ischtwan, J.; Collins, M. A. *J. Chem. Phys.* **1994**, *100*, 8080.
16. Jordan, M. J. T.; Crittenden, D. L.; Thomson, K. C. Quantum Effects in Loosely Bound Complexes. In *Advances in Quantum Monte Carlo*; Anderson, J. B., Rothstein, S. M., Eds.; ACS Symposium Series 953; American Chemical Society: Washington, DC, 2006; pp 101−142.
17. Braams, B. J.; Bowman, J. M. *Int. Rev. Phys. Chem.* **2009**, *28*, 577.
18. Jin, Z.; Braams, B. J.; Bowman, J. M. *J. Phys. Chem. A* **2006**, *110*, 1569.
19. Huang, X.; Carter, S.; Bowman, J. *J. Chem. Phys.* **2003**, *118*, 5431.
20. McCoy, A. B. Diffusion Monte Carlo Approaches for Studying Systems That Undergo Large Amplitude Vibrational Motions. In *Advances in Quantum Monte Carlo*; Anderson, J. B., Rothstein, S. M., Eds.; ACS Symposium Series 953; American Chemical Society: Washington, DC, 2007; pp 147−164.
21. Anderson, J. B. *J. Chem. Phys.* **1975**, *63*, 1499.

22. Anderson, J. B. *J. Chem. Phys.* **1976**, *65*, 4121.
23. McCoy, A. B. *Chem. Phys. Lett.* **2000**, *321*, 71.
24. (a) Petit, A. S.; McCoy, A. B. *J. Phys. Chem. A* **2009**, *113*, 12706. (b) Petit, A. S.; McCoy, A. B. *J. Phys. Chem. A* **2011**, *115*, 9325.
25. Hinkle, C. E.; Petit, A. S.; McCoy, A. B. *J. Mol. Spectrosc.* **2011**, *268*, 189–198.
26. Lee, H.-S.; McCoy, A. B. *J. Chem. Phys.* **2002**, *116*, 9677.
27. Johnson, L. M.; McCoy, A. B. *J. Phys. Chem. A* **2006**, *110*, 8213.
28. Lee, H.-S.; McCoy, A. B. *J. Chem. Phys.* **2001**, *114*, 10278.
29. Eckart, C. *Phys. Rev.* **1935**, *47*, 552.
30. Louck, J. D.; Galbraith, H. W. *Rev. Mod. Phys.* **1976**, *48*, 69.
31. Wang, X.-G.; Carrington, T., Jr. *J. Chem. Phys.* **2008**, *129*, 234102.

Downloaded by CORNELL UNIV on May 28, 2012 | http://pubs.acs.org
Publication Date (Web): February 6, 2012 | doi: 10.1021/bk-2012-1094.ch012

Chapter 13

Quantum Monte Carlo Study of the Binding of a Positron to Polar Molecules

Yukiumi Kita* **and Masanori Tachikawa**

Quantum Chemistry Division, Yokohama-city University, 22-2 Seto,
Kanazawa-ku, Yokohama 236-0027, Japan
***E-mail: ykita@yokohama-cu.ac.jp**

We report the theoretical investigations of the positron binding to alkali-metal hydrides (LiH, NaH, and KH) and hydrogen cyanide molecule (HCN) using quantum Monte Carlo (QMC) methods. We have obtained the lowest variational energies of positron-attached NaH, KH, and HCN systems so far, and larger positron affinities of these molecules than the theoretical predictions by previous configuration interaction calculations. Our study also confirms the strong correlation between the positron affinity and dipole moment of alkali-metal hydrides and the binding of a positron in the electrostatic field of the HCN molecule. In this report, we have described our methodology for analyzing a positron-attached molecule (positronic compound) using QMC techniques, and have reviewed our recent results of QMC calculations of the positron binding to these polar molecules.

1. Introduction

The positron (e^+) is the anti-particle of the electron (e^-) and therefore has the same mass and spin, but the opposite charge. Positrons injected into a liquid or solid induce processes such as ionization or electronic excitation of atoms/molecules, the formation of a meta-stable bound state of a positron and an electron (positronium or Ps), and the formation of positronic compounds which are bound states of a positron and atoms or molecules, etc., before the positron undergoes pair-annihilation with an electron (*1*, *2*). A number of positron annihilation experiments on molecular species have recently been reported by

In Advances in Quantum Monte Carlo; Tanaka, S., et al.;
ACS Symposium Series; American Chemical Society: Washington, DC, 2012.

Surko and co-workers (*3*–*5*). They have measured positron binding energies (positron affinity, PA) for many molecular species such as alkanes and aromatic molecules, etc., and have discussed the relationship between the positron binding and the properties of the parent molecule. However, since it is difficult to directly measure the properties of positronic compounds such as the electronic/positronic structures, the stable geometry, etc., theoretical calculations for positronic compounds have an important role (*6*–*15*).

Theoretical analyses of positronic compounds have shown that an accurate description of correlation effects, especially electron-positron correlation, is indispensable for obtaining reliable values of the PA and other properties (*6*–*15*). For example, Hartree-Fock (HF) theory gives too small a binding energy for Ps and too small a PA for even the simplest positronic compound, [H^-;e^+] (*9*). Conventional quantum chemical approaches based on *ab initio* molecular orbital methods such as many-body perturbation theory (*10*) and configuration interaction (CI) methods (*9*) etc., are frequently used to describe correlation in positronic compounds. It is, however, desirable for the electronic and positronic wave functions to be constructed within a more sophisticated theoretical framework, because even full-CI calculations using H-centered Gaussian type basis functions have not given accurate results for the [H^-;e^+] system (*9*).

Two accurate theoretical approaches are known for studying positronic compounds: variational calculations with explicitly correlated Gaussian (ECG) wave functions (*11*–*13*) and *ab initio* quantum Monte Carlo (QMC) calculations (*14*, *15*). Although variational calculations with ECG wave functions have given the most accurate results obtained to date for small systems, this method cannot in practice be applied to large systems because the required computational effort grows very rapidly with the number of particles. Two types of QMC approach are typically used: the variational Monte Carlo (VMC) and diffusion Monte Carlo (DMC) methods (*16*). The DMC method is also variational in the sense that the DMC energy is always higher than or equal to the exact energy and, in addition, it is always lower than or equal to the VMC energy calculated with the same trial wave function. The cost of QMC calculations grows much less rapidly with the number of particles than in CI and ECG methods, and they are therefore well suited for applications to positronic compounds.

Theoretical work by Crawford (*17*) suggests that a molecule with a dipole moment larger than a critical value of 1.625 Debye (D) is able to bind either an e^- or an e^+ in its electrostatic field. This estimate is based on the long-range form of the electrostatic potential of a dipole. Weakly bound positronic molecular states have large positronic orbitals and the short-range repulsion between the positron and nuclei does not necessarily prevent the formation of a positronic molecular complex. Recently, Chojnacki and Strasburger have theoretically analyzed the positron binding to the hydrogen cyanide (HCN) molecule, which has the permanent dipole moment of 3.3 D, using the CI method with single- and double-particles excited configurations (*18*). Buenker *et al.* have also analyzed positron binding to the alkali-metal hydrides, XH (X=Li, Na, K, etc.), using an *ab initio* multireference double-excitation configuration interaction (MRD-CI) method (*19*, *20*). Although they obtained PAs for these molecules, which are larger than the HF values, the theoretical accuracy is insufficient due to the small configuration space.

Recently, we have investigated the positron binding to these molecular systems, that is, hydrogen cyanide molecule and alkali-metal hydrides (LiH, NaH, and KH) using VMC and DMC methods (*21*, *22*). In these theoretical analyses, we obtained the lowest variational energies of positronic HCN, NaH, and KH systems so far, and larger positron affinities of these molecules than the previous theoretical predictions by the CI methods. In this report, we have described our methodology for analyzing a positron-attached molecule (positronic compound) using QMC techniques, and have reviewed our recent results of QMC calculations of the positron binding to these polar molecules.

At the end of this section, we note that the atomic units are used throughout this report ($\hbar = 1$, $m_{e^-} = m_{e^+} = 1$, $|q_{e^-}| = |q_{e^+}| = 1$).

2. Method

2.1. Non-Relativistic Hamiltonian of a Positronic Compound

The large mass ratios justify the use of the Born-Oppenheimer (BO) approximation to separate the nuclear motion from the electronic and positronic motions. The non-relativistic Hamiltonian operator for a molecular system containing N_e electrons, N_{nuc} nuclei, and a positron is

$$H = -\frac{1}{2}\sum_{i}^{N_e} \nabla_i^2 - \frac{1}{2}\nabla_p^2 + V(\boldsymbol{R}), \qquad [1]$$

where the first and second terms are the kinetic energy operators of the electrons and positron, respectively. We employ an all-electron description of the atoms and the nuclei are treated as point charges. The term $V(\boldsymbol{R})$ is the Coulomb interaction between the particles,

$$V(\boldsymbol{R}, \boldsymbol{R}_{nuc}) = \sum_{i}^{N_e}\sum_{j>i}^{N_e}\frac{1}{r_{ij}} - \sum_{i}^{N_e}\sum_{I}^{N_{nuc}}\frac{Z_I}{r_{iI}} - \sum_{i}^{N_e}\frac{1}{r_{ip}} + \sum_{I}^{N_{nuc}}\frac{Z_I}{r_{pI}}, \qquad [2]$$

where Z_I is the charge of the I-th nucleus, $\boldsymbol{R} = (\boldsymbol{R}_e, \boldsymbol{r}_p)$ is the $3(N_e+1)$-dimensional position vector (configuration) consisting of the electronic coordinates $\boldsymbol{R}_e = (\boldsymbol{r}_1, \ldots, \boldsymbol{r}_{N_e})$ and the positron coordinate $\boldsymbol{r}_p$, and the variables of r_{ij}, r_{ip}, etc. are the distances between particles.

2.2. Slater-Jastrow Trial Wave Functions

In our QMC calculations we have used trial wave functions of the Slater-Jastrow form,

$$\Psi_T(\boldsymbol{R}) = \exp\{J(\boldsymbol{R})\} \times D_e^{\uparrow}\left(\boldsymbol{R}_e^{\uparrow}\right) D_e^{\downarrow}\left(\boldsymbol{R}_e^{\downarrow}\right) \varphi_p\left(\boldsymbol{r}_p\right), \qquad [3]$$

where $\exp\{J(\boldsymbol{R})\}$ is the Jastrow factor described in the section 2.2.2, $D_{\mathrm{e}}^{\uparrow\downarrow}$ are Slater determinants for the up/down-spin electrons and φ_{p} is the positronic orbital, which are obtained by the method described in the section 2.2.1.

2.2.1. Multi-Component Molecular Orbital Method

In order to generate the orbital part in the trial wave function, that is, $D_{\mathrm{e}}^{\uparrow}D_{\mathrm{e}}^{\downarrow}\varphi_{\mathrm{p}}$, we used the multi-component molecular orbital (MC_MO) method within Hartree-Fock (HF) approximation. The MC_MO method is described in detail in the literature (*10*) and is discussed only briefly here.

In the MC_MO method for an electronic closed-shell system, the Fock operators for an electron and a positron are written as

$$f^{\mathrm{e}}(e) \;=\; h^{\mathrm{e}}(e) + \sum_{i}^{N_{\mathrm{e}}/2} [2J_i(e) - K_i(e)] - J_{\mathrm{p}}(e), \qquad [4]$$

$$f^{\mathrm{p}}(p) \;=\; h^{\mathrm{p}}(p) - \sum_{i}^{N_{\mathrm{e}}/2} 2J_i(p), \qquad [5]$$

where $h^{\mathrm{e,p}}$ is the one-particle operator which contains the kinetic energy and Coulomb interaction potential with the nuclei, $J_{i,p}$ is the Coulomb operator and K_i is the exchange operator.

Expanding the molecular orbitals of the electrons and positron in linear combination of Gaussian basis functions $\{\chi_n\}$,

$$\phi_i^{\mathrm{e}} \;=\; \sum_n C_{ni}^{\mathrm{e}}\chi_n^{\mathrm{e}}, \qquad [6]$$

$$\varphi^{\mathrm{p}} \;=\; \sum_n C_n^{\mathrm{p}}\chi_n^{\mathrm{p}}, \qquad [7]$$

we obtain the Roothaan equations for the electrons and positron are

$$\boldsymbol{F}^{\mathrm{e}}\boldsymbol{C}^{\mathrm{e}} \;=\; \boldsymbol{S}^{\mathrm{e}}\boldsymbol{C}^{\mathrm{e}}\boldsymbol{\epsilon}^{\mathrm{e}}, \qquad [8]$$

$$\boldsymbol{F}^{\mathrm{p}}\boldsymbol{C}^{\mathrm{p}} \;=\; \boldsymbol{S}^{\mathrm{p}}\boldsymbol{C}^{\mathrm{p}}\boldsymbol{\epsilon}^{\mathrm{p}}. \qquad [9]$$

Equations 8 and 9 are solved simultaneously using conventional self-consistent-field procedures, giving the multi-component electron-positron wave function.

2.2.2. Orbital Cusp Corrections and the Jastrow Factor

Exact many-body wave functions have cusps when particles interacting via the Coulomb interaction come into contact, as the divergence in the potential energy must be cancelled by an equal and opposite divergence in the kinetic energy. In the MC_MO we describe the electron and positron orbitals by linear combinations of Gaussian-type functions, which cannot satisfy the electron-nucleus or positron-nucleus Kato cusp conditions. Although an accurate description of the cusps is not important for obtaining a reasonable variational energy, violating the Kato cusp conditions (*23*) can cause serious numerical problems in quantum Monte Carlo calculations. The problem is particularly serious for particles of opposite charge because the potential energy diverges to minus infinity, which increases the serial correlation of the energies and can even lead to instabilities in diffusion Monte Carlo calculations. We enforce the electron-nucleus cusp conditions by modifying the electron molecular orbitals using the scheme developed by Ma *et al.* (*24*). In this scheme the orbitals close to the nuclei are replaced by forms which obey the cusp conditions. In practice introducing these cusp corrections reduces the variational energy and its variance (*24*).

The correction to satisfy other cusp conditions and to take the correlation effect for interparticle such as e^{-}-e^{-}, e^{-}-e^{+}, and e^{+}-nuc. are achieved by Jastrow factor. We use the Jastrow factor developed by Drummond *et al.* (*25*) which contains two- and three-body terms,

$$\begin{aligned} J(\boldsymbol{R}) &= \sum_{i}^{N_e}\sum_{j(>i)}^{N_e} u_{ij}(r_{ij}) + \sum_{i}^{N_e}\sum_{I}^{N_{\mathrm{nuc}}} \chi_I(r_{iI}) + \sum_{i}^{N_e}\sum_{j(>i)}^{N_e}\sum_{I}^{N_{\mathrm{nuc}}} f_{ijI}(r_{iI}, r_{jI}, r_{ij}) \\ &\quad + \sum_{i}^{N_e} \tilde{u}_{ip}(r_{ip}) + \sum_{I}^{N_{\mathrm{nuc}}} \tilde{\chi}_{pI}(r_{pI}), \end{aligned} \qquad [10]$$

The functions $u, \tilde{u}, \chi, \tilde{\chi}$, and f are expressed as power series with variable coefficients which are constrained to satisfy the cusp conditions and the functions are smoothly truncated at suitable cutoff distances, as described in the literature (*25*). The u term describes pairwise homogeneous and isotropic electron-electron correlation, while the f term describes pairwise electron-electron correlation which depends on the positions of the nuclei. The χ term describes electron-nucleus correlation which amounts to varying the electron orbitals by multiplying each of them by a positive position-dependent function. The $\tilde{u}$ term describes pairwise homogeneous and isotropic electron-positron correlation, and the $\tilde{\chi}$ term multiplies the positron orbital by a positive position-dependent function. All of the variational parameters in $J(\boldsymbol{R})$ were optimized by minimizing either the reweighted (*26*, *27*) or un-reweighted (*28*) variances of the energy minimization.

We have implemented the methodology described above for including positrons in QMC calculations within the CASINO code, which we have used for all the QMC calculations reported here (*29*).

2.3. Variational and Diffusion Monte Carlo Methods

In variational Monte Carlo (VMC) method, the energy is calculated as the expectation value of the Hamiltonian H . Assuming a real trial wave function we have

$$\langle H\rangle_{\text{VMC}} = \frac{\int \Psi_{\text{T}}(\boldsymbol{R}) H \Psi_{\text{T}}(\boldsymbol{R})\, d\boldsymbol{R}}{\int \Psi_{\text{T}}(\boldsymbol{R})\Psi_{\text{T}}(\boldsymbol{R})\, d\boldsymbol{R}} = \frac{\int \Psi_{\text{T}}^2(\boldsymbol{R})\, E_{\text{L}}(\boldsymbol{R})\, d\boldsymbol{R}}{\int \Psi_{\text{T}}^2(\boldsymbol{R})\, d\boldsymbol{R}}, \qquad [11]$$

where E_{L} is the local energy defined as $\Psi_{\text{T}}^{-1}(\boldsymbol{R}) H \Psi_{\text{T}}(\boldsymbol{R})$. To evaluate this expectation value, we use the Metropolis algorithm (*30*) which generates a set of configurations distributed according to Ψ_{T}^2, and average the corresponding local energies. VMC is a conceptually simple method. Any form of trial wave function can be used and it does not suffer from a fermion sign problem.

We use VMC mainly to optimize the parameters in trial wave functions, while our most accurate results are obtained with the diffusion Monte Carlo (DMC) method. In the DMC method the wave function is evolved in imaginary time, which substantially reduces the bias inherent in VMC which arises from the particular choice of trial wave function. Projector methods such as DMC suffer from a fermion sign problem which results in a rapid decay towards the lower energy bosonic ground state. Stable fermionic behavior is achieved using the fixed-node approximation (*16*) in which the nodal surface of the DMC wave function $\Psi_{\text{DMC}}(R, \tau)$ is fixed to that of a guiding function $\Psi_{\text{Guide}}(R)$ which is taken to be the optimized trial wave function of eq 3. The importance sampled DMC method generates the distribution $f(\boldsymbol{R},\tau) = \Psi_{\text{Guide}}(\boldsymbol{R})\Psi_{\text{DMC}}(\boldsymbol{R},\tau)$. The total energy is given by

$$\langle H\rangle_{\text{DMC}} = \frac{\int f(\boldsymbol{R},\tau)\, E_{\text{L}}(\boldsymbol{R})\, d\boldsymbol{R}}{\int f(\boldsymbol{R},\tau)\, d\boldsymbol{R}}, \qquad [12]$$

and the average energy is accumulated after a period of equilibration.

3. Computational Details

We performed all-electron+positron VMC and DMC calculation for positron-attached alkali-metal hydrides (LiH, NaH, and KH) and hydrogen cyanide molecule (HCN). The lowest variational energy obtained so far for LiH and [LiH;e$^+$] systems are reported by Strasburger (*11*) with the ECG calculations. In order to confirm our implementations, we used the optimized inter-nuclear separations obtained from their ECG calculations, 3.348 Bohr for [LiH;e$^+$] and 3.015 Bohr for LiH, while the calculations of other alkali-metal hydrides were performed using the optimized inter-nuclear separations obtained from the MRD-CI calculations by Buenker *et al.* (*19*), 3.566 Bohr for NaH, 4.095 Bohr for [NaH;e$^+$], 4.246 Bohr for KH, and 5.061 Bohr for [KH;e$^+$]. On the other hand, in the calculation of positronic hydrogen cyanide molecule, we employed the same molecular geometry as HCN molecule obtained at MP2/aug-cc-pVTZ level, because there are no reliable reports available for the geometry of [HCN;e$^+$].

Slater-Jastrow trial wave functions were used with orbitals generated at the HF level of MC_MO theory described in the section 2.2.1. Gaussian type functions (GTFs) of 6-311++G(*3d2f,3p2d*) and [*15s15p6d2f*] quality were employed for the electronic and positronic basis sets, respectively. The exponents of the positronic GTFs were chosen to form even-tempered sets. The smallest exponents for the *s*-, *p*-, *d*- and *f*-type positronic GTFs were 0.00010, 0.00010, 0.001, and 0.001 a.u., respectively, because very diffuse-type GTFs are required to represent the weakly bound positron orbital. The Jastrow factor contained two- and three-body terms, that is, electron-electron, electron-nucleus, electron-positron, positron-nucleus, and electron-electron-nucleus terms. The wave function contained 96 optimizable parameters for [LiH;e^+], 136 for [NaH;e^+], 124 for [KH;e^+], and 123 for [HCN;e^+].

We performed DMC calculations with several imaginary timesteps $\Delta\tau$ ranging from 0.001 to 0.010 a.u. The target population of walkers was chosen to be 2000 for [LiH;e^+], 5000 for the [NaH;e^+], 8000 for [KH;e^+], and 4000 for [HCN;e^+]. These numbers are sufficient to make the population control error completely negligible.

4. Results and Discussion

4.1. Positron Binding to Alkali-Metal Hydrides

Figure 1 shows the electronic and positronic molecular orbitals of [LiH;e^+], [NaH;e^+], and [KH;e^+] systems obtained at the Hartree-Fock level using the MC MO method. The positronic orbitals in both systems are much more diffuse than the electronic highest-occupied molecular orbital (HOMO) due to the strong repulsion between the nuclei and the positron. The positronic orbitals of all positronic alkali-metal hydrides are located at the H-end of the molecule due to the negative charge on the hydrogen atom.

4.1.1. Lithium Hydride

Table 1 gives total energies for LiH and [LiH;e^+] and PAs obtained in various calculations. The VMC calculations give lower variational total energies than the CISD calculations (*31*), but slightly poorer results than the MRD-CI method (*19*). Our DMC energies are slightly higher than the ECG ones, by 0.00049(4) Hartree for LiH and 0.0003(1) Hartree for [LiH;e^+]. These energy differences presumably arise from the fixed-node error in our DMC calculations. The dependence of the PA of LiH on the timestep is shown in Figure 2. Although the weak dependence of the PA on timestep indicates that our calculations are of very high quality, we can obtain slightly more reliable value by extrapolating to zero timestep. Our result for the PA extrapolated to zero timestep is 1.010(3) eV, which is only 0.005(3) eV higher than the ECG result.

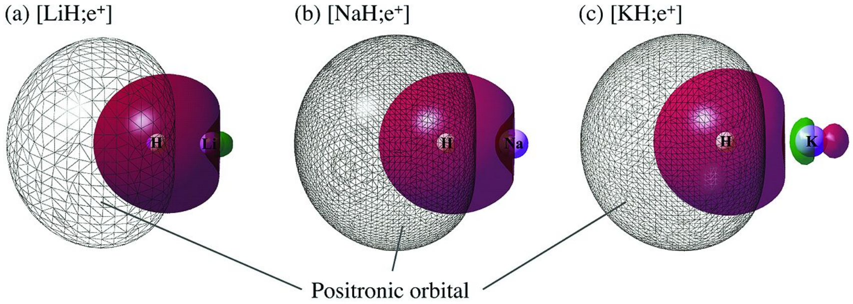

Figure 1. The electronic and positronic molecular orbitals of (a) [LiH;e$^+$], (b) [NaH;e$^+$], and (c) [KH;e$^+$], obtained at the Hartree-Fock level using the MC MO method. Contours of isovalue 0.015 are drawn. The meshed region denotes the contour of the positronic orbital, while the solid black and gray regions denote contours of the positive and negative parts of the electronic HOMO, respectively. The percentages of the positron charge within the meshed region are 44.7 % for [LiH;e$^+$], 63.3 % for [NaH;e$^+$], and 75.3 % for [KH;e$^+$].

Table 1. Total energy (E_X, Hartree), inter-nuclear separations (R_{LiH}, Bohr), and positron affinity (PA, eV) for LiH and [LiH;e$^+$] systems with various schemes

		LiH		*[LiH;e$^+$]*		
Method		E_{LiH}	R_{LiH}	$E_{[LiH;e^+]}$	R_{LiH}	*PA*
HF		-7.98584	3.015	-7.99036	3.348	0.123
VMC		-8.06307(34)	3.015	-8.08034(36)	3.348	0.47(1)
FN-DMC	$\Delta\tau$=0.001	-8.070015(24)	3.015	-8.107172(71)	3.348	1.011(2)
	extrapolated	-8.070045(38)	3.015	-8.10718(11)	3.348	1.010(3)
CISD	Ref. (*31*)	-8.03830	3.015	-8.05530	3.015	0.463
MR-CI	Ref. (*19*)	-8.068266	3.019	-8.097643	3.324	0.800
FN-DMC	Ref. (*37*)	-8.0704(1)	3.015	-8.1072(2)	3.458	1.001(6)
ECG	Ref. (*11*)	-8.070538	3.015	-8.107474	3.348	1.005

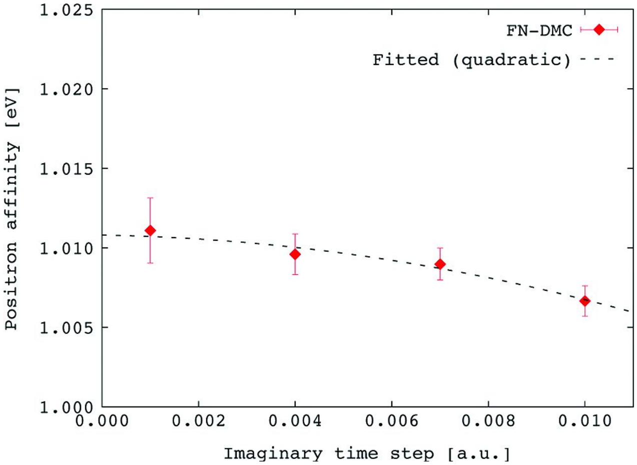

Figure 2. Timestep dependence of the positron affinity (PA) of the LiH molecule ($PA_{LiH} = E_{LiH} - E_{[LiH;e+]}$). The standard error of each DMC energy is shown and the solid line is a quadratic fit to the DMC data.

4.1.2. Sodium Hydride

Table 2 gives the total energies of NaH and [NaH;e^+] obtained from our QMC calculations. The values from the MRD-CI calculations of Buenker *et al.* (*19*) are also given. For both systems, our VMC energies are substantially lower than both the Hartree-Fock and MRD-CI energies, where a frozen core approximation was employed for the Na 1s electrons in the MRD-CI calculations. DMC calculations use a short-time approximation and the energies should be extrapolated to zero timestep. The variation of the DMC energy with timestep is smooth and the extrapolation is well-behaved. The DMC energies of NaH and [NaH;e^+] at a timestep of $\Delta\tau = 0.001$ are, respectively, 0.0013(2) and 0.0009(4) a.u. lower than the values extrapolated to zero timestep (see Table 2). These energy differences are comparable with the scale of interest but, as explained below, the timestep dependence of the difference between the energies of NaH and [NaH;e^+], which gives the PA, is much smaller.

To compare the accuracy of our DMC calculation for NaH with the MRD-CI calculation of Buenker *et al.* (*19*) we estimated the percentages of the correlation energies retrieved. We used an accurate value of the non-relativistic energy of the Na atom of -162.2546 a.u. (*32*), the experimental dissociation energy of the NaH molecule of 0.07206 a.u. (*33*), the Hartree-Fock (HF) energy of a Na atom of -161.8587 a.u. (*32*) and the HF energy of the NaH molecule of -162.3923 a.u. (*34*). Using this data we deduce that our DMC calculation for NaH retrieves 95.7% of the total correlation energy, which is considerably larger than the 39.8% retrieved in the MRD-CI calculation. We note that this large difference is mainly due to the frozen core approximation used for the Na 1s electrons in the MRD-CI calculations.

Table 2. Total energy (E_X, Hartree) and positron affinity (PA, eV) for NaH and [NaH;e^+] systems with various schemes

Method		*Total energy*		*PA*
		E_{NaH}	$E_{[NaH;e^+}$	
HF		-162.380271	-162.389916	0.262
VMC		-162.721(2)	-162.751(2)	0.80(7)
FN-DMC	$\Delta\tau$=0.001	-162.809260(89)	-162.86113(17)	1.412(5)
	extrapolated	-162.80798(18)	-162.86025(35)	1.422(10)[a]
MRD-CI	Ref. (*19*)	-162.5653	-162.60332	1.035

[a] The extrapolated PA and its uncertainty due to timestep bias are estimated from a quadratic fit to the timestep data shown in Figure 3.

Table 2 gives the PA of the NaH molecule and Figure 3 shows the timestep dependence of the PA. The VMC value of the PA of 0.80(7) eV is slightly smaller than the MRD-CI value of 1.035 eV and is further from the DMC result, even though VMC gives a lower variational energy than MRD-CI. Such a result is typical of VMC calculations as the inherent bias due to the choice of trial wave function can be substantial. DMC energies are much less sensitive to the trial wave function. The timestep-extrapolated DMC value of the PA of 1.422(10) eV is substantially larger than the VMC value of 0.80(7) eV. Even at the largest timestep used of $\Delta\tau = 0.007$ the DMC value of the PA of the NaH molecule is 1.339(4) eV, which is close to the extrapolated value. The PA increases by only 0.00037(4) a.u. (0.01 eV) on going from the value for $\Delta\tau = 0.001$ to the extrapolated value, see Figure 3. This cancellation of timestep errors in the NaH molecule and positronic complex occurs because of the similarity of the two systems and because the timestep error arises mainly from the core orbitals, which vary rapidly in space but are very similar in the molecule and positronic complex. We conclude that the timestep error in our extrapolated DMC value of the PA of NaH is smaller than 0.01 eV.

When the ionization potential (IP) of the parent molecule is greater than the formation energy of Ps of 6.8 eV, the structure of the [NaH;e^+] system is closer to the configuration of NaH$\cdots e^+$ rather than $NaH^+\cdots$Ps, due to the strong attraction of the electron to the parent molecule. The first IP of the NaH is estimated to be 7.037 eV, which is a little larger than 6.8 eV. To estimate the total energy of NaH^+ we used the accurate total energy of the Na atom (*32*), the IP of the Na atom of 5.139 eV, and the binding energy of NaH^+ of 0.061 eV reported by Melius *et al* (*35*). The energy of infinitely separated NaH + e^+ is -162.8266 a.u., which is lower than the energy of NaH^+ + Ps of -162.81798 a.u. We also found another feasible dissociation channel of [NaH;e^+] to Na^+ + [H^-;e^+], which has an energy of -162.85494 a.u. Therefore the lowest-energy channel for dissociation of [NaH;e^+] is to Na^+ + [H^-;e^+] rather than NaH + e^+ or NaH^+ + Ps. The zero-point vibration of NaH^+ and NaH molecules does not change the order of the energies of these dissociation channels, because the zero-point energy (ZPE) of NaH^+ can be neglected and that of NaH is very small (0.072 eV (*20*)). The lowest-energy dissociation channel for [LiH;e$^+$] system is also to form Li$^+$ + [H$^-$;e$^+$], but LiH + e$^+$ is less stable due to the ZPE of the LiH molecule as discussed by Mitroy *et al.* (*36*) and Mella *et al.* (*37*).

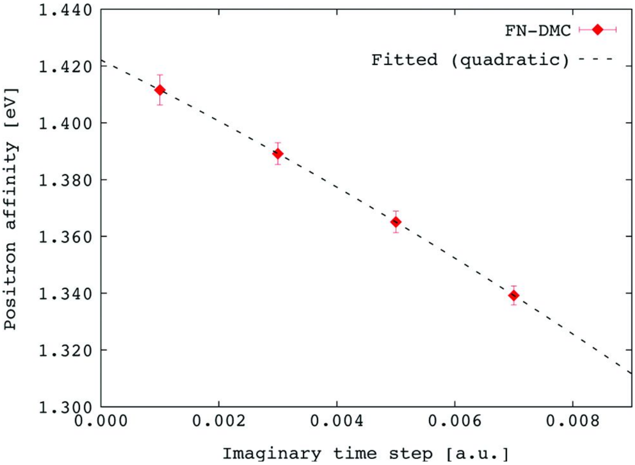

Figure 3. Timestep dependence of the positron affinity (PA) of the NaH molecule ($PA_{NaH} = E_{NaH} - E_{[NaH;e+]}$). The standard error of each DMC energy is shown and the dotted line is a quadratic fit to the DMC data.

4.1.3. Potassium Hydride

Results for KH and [KH;e$^+$] are shown in Table 3. The DMC energies are significantly lower than the MRD-CI ones. The DMC energies of KH and [KH;e$^+$] extrapolated to zero timestep are -600.40028(39) and -600.47638(57) a.u., respectively. The timestep dependence of the PA of KH is shown in Figure 4. In this molecule the variation of the PA with timestep is larger than for NaH as the quality of the wave function is poorer because electronic orbitals with very different energies are present. In addition, the timestep error is not well-described by a linear form and therefore we have plot both linear and quadratic fits in Figure 4. We have estimated the extrapolated PA by averaging the values from the linear and quadratic fits and taking the error bar from the timestep bias to equal the difference between the linear and quadratic extrapolations, giving a PA of 2.051(39) eV. Our DMC value of the PA is much larger than the MRD-CI value and the uncertainty in the timestep error is small on the scale of the difference between them.

Figure 5 shows the PAs and dipole moments of LiH, NaH, and KH. We estimated the dipole moments of these molecules at the coupled cluster singles and doubles level augmented by a perturbative correction for connected triple excitations, CCSD(T), with 6-311++G(*3d2f,3p2d*) Gaussian basis sets. Figure 5 clearly shows that a polar molecule with a larger dipole moment binds a positron more strongly.

Table 3. Total energy (E_X, Hartree) and positron affinity (PA, eV) for KH and [KH;e^+] systems with various schemes

Method		*Total energy*		*PA*
		E_{KH}	$E_{[KH;e^+}$	
HF		-599.680525	-599.703078	0.614
VMC		-600.072(3)	-600.130(3)	1.6(1)
FN-DMC	$\Delta\tau$=0.002	-600.43605(11)	-600.51044(17)	2.024(6)
	extrapolated	-600.40028(39)	-600.47638(57)	2.051(39)[a]
MRD-CI	Ref. (*19*)	-600.069358	-600.116143	1.273

[a] The value of the PA is taken to be the average of those from the linear and quadratic fits at zero timestep shown in Figure 4. The uncertainty in the PA due to timestep bias is estimated from difference between the values of the PA obtained from the two extrapolations.

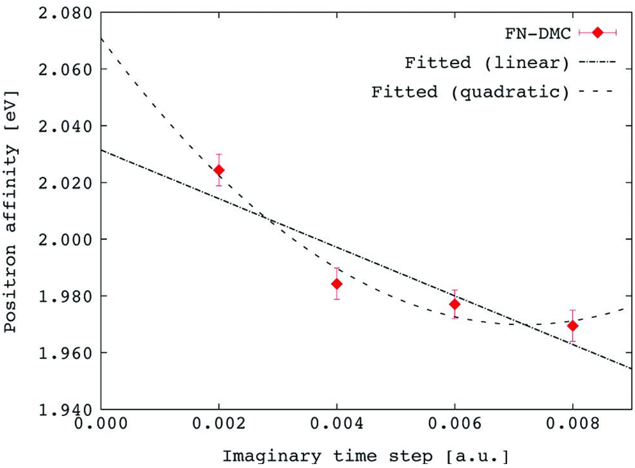

Figure 4. Timestep dependence of the positron affinity (PA) of the KH molecule ($PA_{KH} = E_{KH} - E_{[KH;e+]}$). The standard error of each DMC energy is shown. The dashed-dotted line is a linear fit to the DMC data while the dotted line is a quadratic fit.

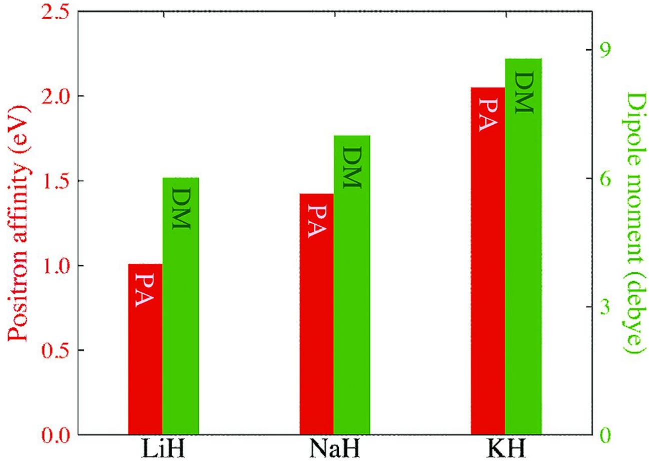

Figure 5. Positron affinities (PAs) and dipole moments (DMs) of LiH, NaH, and KH. The PAs and DMs are estimated using DMC and CCSD(T) calculations, respectively.

4.2. Positron Binding to Hydrogen Cyanide Molecule

Figure 6 shows the electronic HOMO and positronic orbital in [HCN;e^+] by the MC_MO method. The figure shows that the positron orbital being spatially more diffuse than that in the positron-attached alkali-metal hydrides, implying the weak binding. Results for HCN and [HCN;e^+] are reported in Table 4. The QMC total energies are substantially lower than the CISD ones in this case (*18*) even at the VMC level. The VMC estimate of the PA is poor, presumably because the trial wave function of [HCN;e^+] is of lower quality than for HCN. The timestep dependence of the PA of the HCN molecule is shown in Figure 7. The variation of the PA with timestep is significant in this molecule, and the PA at the largest timestep (0.010 a.u.) is negative, suggesting that the HCN molecule does not bind a positron. The variation of the PA with timestep is, however, smooth and the PA can readily be extrapolated to zero timestep, giving a PA of 0.0378(48) eV.

We have shown that the DMC method can give a reliable description of correlation effects in positronic molecules, although the accuracy is limited by the fixed-node approximation. Our results suggest that the HCN molecule is capable of capturing a positron, although further investigations would be helpful, considering effects such as relaxing the geometry of [HCN;e^+], including the nuclear zero-point energy, and estimating positron life-times. Including the relaxation energy of [HCN;e^+] can only increase the PA, strengthening our conclusions.

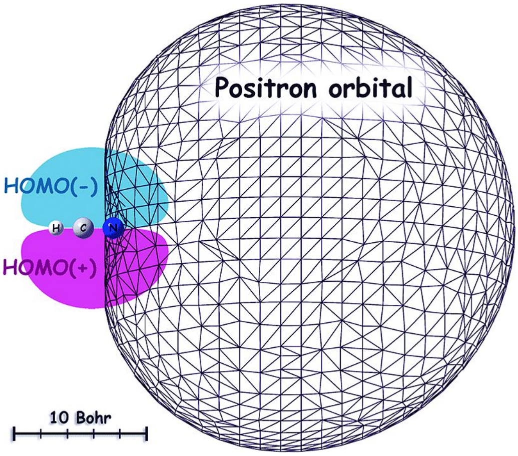

Figure 6. The electronic and positronic molecular orbitals in [HCN;e^+] system, obtained by Hartree-Fock level of calculation in MC_MO method. The meshed contour means certain amplitude of the positronic orbital, and the solid black and gray regions mean that of the highest occupied molecular orbital (HOMO) of electrons.

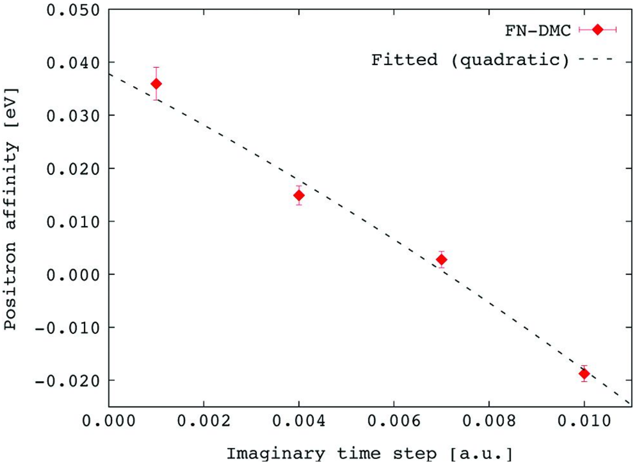

Figure 7. Timestep dependence of the positron affinity (PA) of the HCN molecule ($PA_{HCN} = E_{HCN} - E_{[HCN;e+]}$). The standard error of each DMC energy is shown. The dashed-dotted line is a linear fit to the DMC data while the solid line is a quadratic fit.

Table 4. Total energy (E_X, Hartree) and positron affinity (PA, eV) for HCN and [HCN;e$^+$] systems with various schemes

Method		*Total energy*		*PA*
		E_{HCN}	$E_{[HCN;e^+}$	
HF		-92.900743	-92.900818	0.0020
VMC		-93.26758(25)	-93.26753(25)	-0.001(9)
FN-DMC	$\Delta\tau$=0.001	-93.399407(73)	-93.400727(86)	0.0359(30)
	extrapolated	-93.39986(12)	-93.40121(13)	0.0378(48)
CISD	Ref. (*18*)	-92.901242	-92.901915	0.0183[a]

[a] The value of PA with the CISD calculations giving the lowest variational energy in their report.

5. Summary

In this report, we have briefly described the molecular theory to analyze a positron-attached complex (positronic compound) using quantum Monte Carlo (QMC) techniques. Our implementation is proved to give satisfactory quantitative accuracy for positron affinity estimation on the benchmark calculations on [LiH;e$^+$], giving the consistent result with previous works by the explicitly correlated Gaussian basis sets11 evaluation. We have applied the QMC methods to the positron-attached alkali-metal hydrides, [XH;e$^+$] (X=Na and K), for which accurate theoretical predictions have not previously been made. Our fixed-node diffusion Monte Carlo (DMC) calculations for [NaH;e$^+$] and [KH;e$^+$] give the lowest variational energies obtained so far for both systems. The values of the positron affinities obtained in our DMC calculations for the NaH and KH molecules are 1.422(10) eV and 2.051(39) eV, respectively. These values are considerably larger than those from multireference double-excitation configuration interaction (MRD-CI) calculations (*19*) of 1.035 eV and 1.273 eV, respectively. Our DMC calculations confirm the strong correlation between the positron affinity and dipole moment of alkali-metal hydrides. The mechanism of positron binding in the molecular dipole field was investigated many years ago by Crawford (*17*), and recent MRD-CI calculations (*19*) have yielded quantitative estimates of positron affinities. We believe, however, that our DMC positron affinities are substantially more accurate. Our implementation is also applied to the positronic hydrogen cyanide molecule, [HCN;e$^+$], and we obtained the positron affinity of 0.0378(48) eV under the assumption that the geometry of [HCN;e$^+$] is not relaxed from that of HCN. The positive affinity predicted with DMC calculations supports the capability of HCN molecule to capture a positron in its electrostatic field.

The DMC method can provide an excellent description of the electron-electron and electron-positron correlation in positronic complexes. The present study shows that this accurate methodology can be applied to systems containing atoms with atomic numbers up to at least 19. The polynomial scaling of the algorithm should make it feasible to perform accurate DMC calculations for substantially larger positronic complexes.

Acknowledgments

Financial support was provided by Grant-in-Aid for Scientific Research and for the priority area by Ministry of Education, Culture, Sports, Science and Technology, Japan for Y.K. and M.T. The authors, Y.K. and M.T. highly appreciate Dr. Ryo Maezono in Japan Advanced Institute of Science and Technology, Japan, Dr. Mike D. Towler, Prof. Richard J. Needs in University of Cambridge, UK for their insightful and helpful comments and suggestions.

References

1. *New Directions in Antimatter Chemistry and Physics*; Surko, C. M., Gianturco, F. A., Eds.; Kluwer Academic Publishers: Dordrecht, The Netherlands, 2001.
2. Gribakin, G. F.; Young, J. A.; Surko, C. M. *Rev. Mod. Phys.* **2010**, *82*, 2557.
3. Danielson, J. R.; Young, J. A.; Surko, C. M. *J. Phys. B* **2009**, *42*, 235203.
4. Young, J. A.; Surko, C. M. *Phys. Status Solidi C* **2009**, *6*, 2265.
5. Danielson, J. R.; Gosselin, J. J.; Surko, C. M. *Phys. Rev. Lett.* **2010**, *104*, 233201.
6. Schrader, D. M.; Yoshida, T.; Iguchi, K. *J. Chem. Phys.* **1993**, *98*, 7185.
7. Saito, S. L. *Chem. Phys. Lett.* **1995**, *245*, 54.
8. Strasburger, K. *Chem. Phys. Lett.* **1996**, *253*, 49.
9. Tachikawa, M. *Chem. Phys. Lett.* **2001**, *350*, 269.
10. Tachikawa, M.; Sainowa, H.; Iguchi, K.; Suzuki, K. *J. Chem. Phys.* **1994**, *101*, 5925.
11. Strasburger, K. *J. Chem. Phys.* **2001**, *114*, 00615.
12. Bubin, S.; Adamowicz, L. *J. Chem. Phys.* **2004**, *120*, 6051.
13. Mitroy, J. *Phys. Rev. A* **2006**, *73*, 054502.
14. Bressanini, D.; Mella, M.; Morosi, G. *J. Chem. Phys.* **1998**, *108*, 4756.
15. Mella, M.; Casalegno, M.; Morosi, G. *J. Chem. Phys.* **2002**, *117*, 1450.
16. Foulkes, W. M. C.; Mitas, L.; Needs, R. J.; Rajagopal, G. *Rev. Mod. Phys.* **2001**, *73*, 33.
17. Crawford, O. H. *Proc. Phys. Soc.* **1967**, *91*, 279.
18. Chojnacki, H.; Strasburger, K. *Mol. Phys.* **2006**, *104*, 2273.
19. Buenker, R. J.; Liebermann, H.-P.; Melnikov, V.; Tachikawa, M.; Pichl, L.; Kimura, M. *J. Phys. Chem. A* **2005**, *109*, 5956.
20. Gianturco, F. A.; Franz, J.; Buenker, R. J.; Liebermann, H.-P.; Pichl, L.; Rost, J.-M.; Tachikawa, M.; Kimua, M. *Phys. Rev. A* **2006**, *73*, 022705.
21. Kita, Y.; Maezono, R.; Tachikawa, M.; Towler, M.; Needs, R. J. *J. Chem. Phys.* **2009**, *131*, 134310.
22. Kita, Y.; Maezono, R.; Tachikawa, M.; Towler, M.; Needs, R. J. *J. Chem. Phys.* **2011**, *135*, 054108.

23. Kato, T. *Commun. Pure Appl. Math.* **1957**, *10*, 151.
24. Ma, A.; Towler, M. D.; Drummond, N. D.; Needs, R. J. *J. Chem. Phys.* **2005**, *122*, 224322.
25. Drummond, N. D.; Towler, M. D.; Needs, R. J. *Phys. Rev. B* **2004**, *70*, 235119.
26. Umrigar, C. J.; Wilson, K. G.; Wilkins, J. W. *J. Chem. Phys.* **1988**, *60*, 1719.
27. Kent, P. R. C.; Needs, R. J.; Rajagopal, G. *Phys. Rev. B* **1999**, *59*, 12344.
28. Drummond, N. D.; Towler, M. D.; Needs, R. J. *Phys. Rev. B* **2005**, *72*, 085124.
29. Needs, R. J.; Towler, M. D.; Drummond, N. D.; Lopez Rios, P. *J. Phys.: Condens. Matter* **2010**, *22*, 023201.
30. Metropolis, N.; Rosenbluth, A. W.; Rosenbluth, M. N.; Teller, A. M.; Teller, E. *J. Chem. Phys.* **1953**, *21*, 1087.
31. Strasburger, K. *Chem. Phys. Lett.* **1996**, *253*, 49.
32. (a) O'Neill, D. P.; Gill, P. M. W. *Mol. Phys.* **2005**, *103*, 763. (b) Chakravorty, S. J.; Gwaltney, S. R.; Davidson, E. R. *Phys. Rev. A* **1993**, *47*, 3649.
33. Huang, H.-Y.; Lu, T.-L.; Whang, T.-J.; Chang, Y.-Y.; Tsai, C.-C. *J. Chem. Phys.* **2010**, *133*, 044301.
34. Feller, D.; Peterson, K. A. *J. Chem. Phys.* **1998**, *108*, 154.
35. Melius, C. F.; Numrich, R. W.; Truhlar, D. G. *J. Phys. Chem.* **1979**, *83*, 1221.
36. Mitroy, J.; Ryzhikh, G. G. *J. Phys. B* **2000**, *33*, 3495.
37. Mella, M.; Morosi, G.; Bressanini, D.; Elli, S. *J. Chem. Phys.* **2000**, *113*, 6154.

Chapter 14

Molecular Dynamics and Hybrid Monte Carlo Algorithms for the Variational Path Integral with a Fourth-Order Propagator

Shinichi Miura[*]

School of Mathematics and Physics, Kanazawa University,
Kakuma, Kanazawa 920-1192, Japan
[*]E-mail: smiura@mail.kanazawa-u.ac.jp

Downloaded by CORNELL UNIV on May 28, 2012 | http://pubs.acs.org
Publication Date (Web): February 6, 2012 | doi: 10.1021/bk-2012-1094.ch014

In the present study, molecular dynamics (MD) and hybrid Monte Carlo (HMC) methods have been developed for the variational path integral with a fourth-order propagator. Two types of hybrid Monte Carlo are introduced. One is based on a straightforward use of the MD with the fourth-order approximation, which is called HMC I. The other is based on a two level description avoiding the evaluation of time consuming part regarding higher order terms in MD and HMC I, which is called HMC II. These methods are applied to the liquid helium-4 in the ground state as a benchmark system. The calculated results indicate that for the present system, the HMC II is a better choice from the point of view of the computational efficiency.

Introduction

Quantum Monte Carlo (QMC) methods provide computational tools for accurately calculating ground state properties of many body systems (*1*–*4*). Variational Monte Carlo (VMC) method (*5*), for example, is used to calculate expectation values of physical quantities using a trial wavefunction of the target system. The more sophisticated diffusion Monte Carlo (DMC) method (*6*, *7*) is a projector approach in which a stochastic imaginary time evolution is used to improve a starting trial wavefunction. The QMC methods including the VMC and DMC methods have successfully been applied to various quantum systems

In Advances in Quantum Monte Carlo; Tanaka, S., et al.;
ACS Symposium Series; American Chemical Society: Washington, DC, 2012.

ranging from quantum liquids like helium to electronic structure of atoms and molecules (*1–4*).

Recently, we have developed a molecular dynamics algorithm for a variational path integral method (*1*) that is closely related to the diffusion Monte Carlo method. The variational path integral method, which is also called path integral ground state (*8*, *9*), is another method to numerically generate exact ground state of many body systems. We have constructed the molecular dynamics algorithm to carry out the variational path integral calculations (*10–12*) on the basis of path integral molecular dynamics method developed for finite temperature quantum systems (*13*, *14*). We call it a variational path integral molecular dynamics (VPIMD) method. In the present study, VPIMD method is extended to handle a fourth-order approximation of a density operator (*15*) that is utilized to obtain a discretized path integral expression. Based on VPIMD, hybrid Monte Carlo method for the variational path integral is also developed. Variational path integral calculations using these methods have been performed for the liquid helium-4 as a benchmark system.

Downloaded by CORNELL UNIV on May 28, 2012 | http://pubs.acs.org
Publication Date (Web): February 6, 2012 | doi: 10.1021/bk-2012-1094.ch014

Method

The Variational Path Integral

We start to consider a system consisting of N identical particles whose coordinates are collectively represented to be R. The Hamiltonian of the system is written by H = T + V where T and V are the kinetic and potential energy operators, respectively. A quantity playing a central role in the variational path integral method is the following (*1*):

$$Z_0 = \int\int dRdR'\Phi_T(R)\langle R|e^{-\beta\hat{H}}|R'\rangle\Phi_T(R')$$

where Φ_T is a trial wavefunction of the system considered. The above quantity Z_0, which is called a pseudo partition function (*16*), becomes the inner product of the exact wavefunction when an imaginary time β is large enough. To obtain the discretized path integral expression of Z_0, the operator $e^{-\beta H}$ is written by M-fold product of a short time propagator $e^{-\tau H}$ where τ = β/M. Then, an approximation is applied to the short time propagator. The standard primitive approximation can be written by (*1*)

$$e^{-\tau\hat{H}} = e^{-\frac{\tau}{2}\hat{V}}e^{-\tau\hat{T}}e^{-\frac{\tau}{2}\hat{V}} + \mathcal{O}(\tau^3).$$

The above approximation is accurate up to the second order of τ. On the other hand, a more accurate approximation can be utilized: a fourth-order approximation can be written by (*15*)

$$e^{-2\tau\hat{H}} = e^{-\frac{\tau}{3}\hat{V}_e}e^{-\tau\hat{T}}e^{-\frac{4\tau}{3}\hat{V}_m}e^{-\tau\hat{T}}e^{-\frac{\tau}{3}\hat{V}_e} + \mathcal{O}(\tau^5)$$

with

$$\hat{V}_e = \hat{V} + \frac{\tau^2 \alpha}{6}\hat{C}, \qquad \hat{V}_m = \hat{V} + \frac{\tau^2(1-\alpha)}{12}\hat{C}.$$

Here, α is an arbitrary constant in the range of [0, 1] and C is the following commutator:

$$\hat{C} = [\hat{V}, [\hat{T}, \hat{V}]] = \sum_{i=1}^{N} \frac{\hbar^2}{m}(\nabla_i \hat{V})^2$$

where m is a particle mass. Then, using the primitive or fourth-order approximation, we can obtain the following path integral expression of Z_0:

$$Z_0 \propto \int \cdots \int \left\{ \prod_{s=0}^{M} dR^{(s)} \right\} \Phi_T(R^{(0)}) e^{-S(\{R^{(s)}\};\tau)} \Phi_T(R^{(M)})$$

where S is an imaginary time action. The explicit expression of S is dependent on the approximation adopted. As in the standard path integral method for finite temperature systems (*17*), the pseudo partition function Z_0 can be regarded as a configurational integral of classical polymers. Here, in the variational path integral, the classical isomorphic systems consist of open chain polymers. Furthermore, distributions of end-point coordinates at s = 0 and M are affected by the trial wavefunction $\Phi_T(R^{(0)})$ and $\Phi_T(R^{(M)})$, respectively.

Molecular Dynamics and Hybrid Monte Carlo

We next consider a molecular dynamics method to sample configurations of the isomorphic polymers. First, we define the following classical Hamiltonian:

$$H_{\text{VPIMD}} = \sum_{s=0}^{M} \frac{\left(P^{(s)}\right)^2}{2m'} + \frac{S(\{R^{(s)}\})}{\beta} - \frac{\ln \Phi_T(R^{(0)})}{\beta} - \frac{\ln \Phi_T(R^{(M)})}{\beta}$$

where $P^{(s)}$ collectively denotes fictitious momenta of particles at an s-th time slice and m′ is a fictitious mass of the particle. Using the above Hamiltonian, we can derive equations of motion based on the Hamilton equation. Then, in order to generate the distribution compatible with Z_0, we attach a single Nosé-Hoover chain thermostat to each degree of freedom (*13*, *14*, *18*). The resulting equations of motion are basic equations for the variational path integral molecular dynamics (VPIMD) method.

We also consider a hybrid Monte Carlo (*13*, *19*, *20*) method for the variational path integral calculations. The hybrid Monte Carlo is a method that combines molecular dynamics (MD) and Monte Carlo (MC) techniques. Unlike the standard MC, whole system coordinates are simultaneously updated by equations of motion. The trial configuration is then accepted by an appropriate Metropolis criterion as in MC. The HMC algorithm has been proved to yield the canonical

Downloaded by CORNELL UNIV on May 28, 2012 | http://pubs.acs.org
Publication Date (Web): February 6, 2012 | doi: 10.1021/bk-2012-1094.ch014

distribution as long as a time-reversible and area-preserving numerical integration algorithm is employed to solve the equations of motion; this condition is needed so as to guarantee the microscopic detailed balance (*20*). To construct the HMC method for the variational path integral, the above Hamiltonian H_{VPIMD} is used for introducing the equations of motion. The variational path integral hybrid Monte Carlo (VPIHMC) method is outlined as follows. We start with an initial state of the system ($\{R^{(s)}\}$, $\{P^{(s)}\}$) and re-sample momenta $\{P^{(s)}\}$ from a Maxwell distribution. Molecular dynamics is then used to move the whole system for time increment of $n_{MD}\times\Delta t$ where Δt is the time step of the MD calculation and n_{MD} is the number of MD step in one HMC cycle. The trial configuration is then accepted or rejected based on the following Metropolis criterion:

$$\min\left\{1, e^{-\beta\Delta H_{\mathrm{VPIMD}}}\right\}$$

where ΔH_{VPIMD} is the change in the total Hamiltonian H_{VPIMD} as a result of the move. In the present study, the method is referred to be HMC I. When we adopt the fourth-order approximation, the effective interaction among polymers includes the square of the gradient of the potential function. Then, the Hessian matrix of the potential have to be calculated for evaluating the force in MD and HMC I. Here, we consider a method to avoid the calculation of the Hessian matrix in the HMC method. First, we decompose the action into two parts:

$$S(\{R^{(s)}\}) = S_0(\{R^{(s)}\}) + \beta V_{\mathrm{corr}}(\{R^{(s)}\})$$

where V_{corr} includes the terms regarding the gradient of the potential and the remaining terms are expressed to be S_0. Then, we define the following classical Hamiltonian using S_0:

$$H'_{\mathrm{VPIMD}} = \sum_{s=0}^{M} \frac{\left(P^{(s)}\right)^2}{2m'} + \frac{S_0(\{R^{(s)}\})}{\beta} - \frac{\ln \Phi_T(R^{(0)})}{\beta} - \frac{\ln \Phi_T(R^{(M)})}{\beta}.$$

We can derive equations of motion using the above H'_{VPIMD}. As in the HMC I, the system coordinates are evolved with time increment $n_{MD}\times\Delta t$ using the equations of motion. The trial configuration is then accepted or rejected by the following Metropolis criterion:

$$\min\left\{1, e^{-\beta\Delta H'_{\mathrm{VPIMD}}-\beta\Delta V_{\mathrm{corr}}}\right\}$$

where $\Delta H'_{VPIMD}$ and ΔV_{corr} respectively denote the change in the corresponding quantities as a result of the move. The method is referred to be HMC II. Since the terms regarding the gradient of the potential do not appear in H'_{VPIMD}, we do not need to evaluate the Hessian matrix. Thus, the computational cost is virtually equivalent with that by the primitive approximation using the same M. The bias introduced by using S_0 is then removed by the above Metropolis function.

Downloaded by CORNELL UNIV on May 28, 2012 | http://pubs.acs.org
Publication Date (Web): February 6, 2012 | doi: 10.1021/bk-2012-1094.ch014

In the HMC methods, intermediate configurations in n_{MD} steps are usually discarded. However, we can use the intermediate configurations to evaluate physical quantities (*21*). The procedure is that the configurations generated by the equations of motion are simply accepted or rejected according to the above Metropolis criteria at every n_{sample} steps ($n_{sample} \leq n_{MD}$). Here, the acceptance or rejection of the intermediate configurations must not give any effect on the system evolution of n_{MD} steps (*21*).

The above formulation is based on the real space coordinates R. In the present study, we use staging coordinates (*13*) to describe the polymer configurations for enhancing sampling efficiency. The standard definition (*14*, *22*) on the staging variables and associated staging masses $m^{(s)}$ are adopted. The fictitious masses for the staging variables $m'^{(s)}$ are set to be equal to the corresponding staging masses except end-point coordinates (at s = 0 and M) where $m'^{(0)} = m'^{(M)} = \gamma \times m$. In the preset study, the parameter γ is chosen to be about 4 / M.

Downloaded by CORNELL UNIV on May 28, 2012 | http://pubs.acs.org
Publication Date (Web): February 6, 2012 | doi: 10.1021/bk-2012-1094.ch014

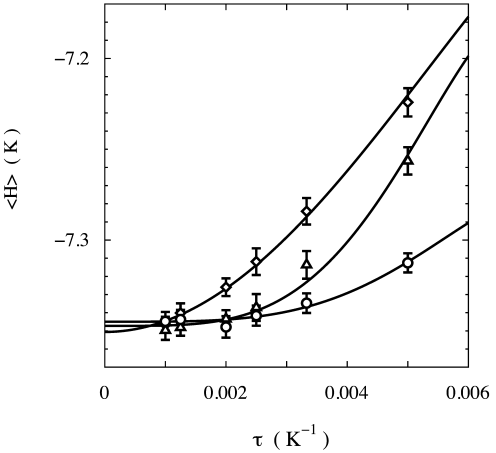

Figure 1. Total energy per ^{4}He atom as a function of the imaginary time step τ. Total projection time is $\beta = 0.4\ K^{-1}$. Open diamonds, triangles, and circles denote the calculated results by the primitive, fourth order (α = 1/3), and fourth-order (α = 0) approximations, respectively. The curves are fitted results of the energy where the corresponding τ dependence is assumed.

Downloaded by CORNELL UNIV on May 28, 2012 | http://pubs.acs.org
Publication Date (Web): February 6, 2012 | doi: 10.1021/bk-2012-1094.ch014

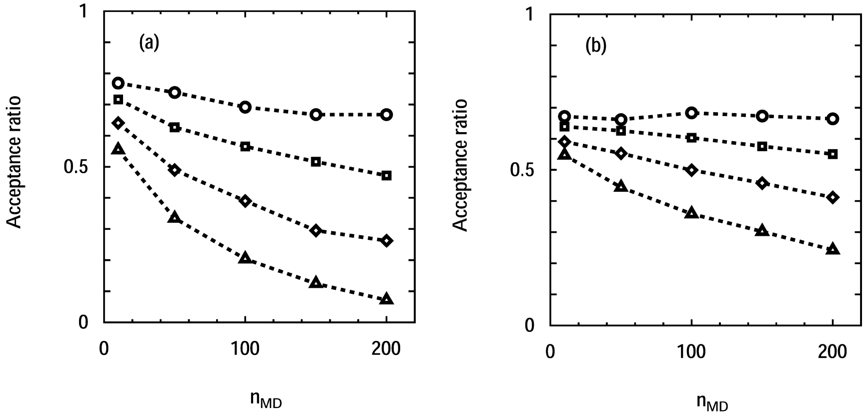

Figure 2. Acceptance ratio of the hybrid Monte Carlo I (left panel (a)) and the hybrid Monte Carlo II (right panel (b)) as a function of n_{MD} that is the number of the molecular dynamics steps in one hybrid Monte Carlo cycle. Open circles, squares, diamonds, and triangles are the results using the time increment of one molecular dynamics step Δt = 12, 13, 14, and 15 fs, respectively.

Results

In the present study, the liquid helium-4 is adopted as a model system to examine computational efficiencies of the methods. The density of the system is set to be the experimental equilibrium value $\rho = 0.0218$ Å^{-3}. The system consists of N = 64 ^{4}He atoms in a cubic box under the periodic boundary condition. The interatomic interaction is represented by the pair interaction developed by Aziz and coworkers (*23*). The following trial wavefunction is adopted:

$$\Phi_T(R) = \prod_{i<j}^{N} \exp\left\{-\frac{1}{2}\left(\frac{b}{r_{ij}}\right)^5\right\}$$

where b = 3.07 Å (*9*).

We first show the total energy of the liquid helium-4 as a function of the imaginary time increment τ. The total projection time β is fixed to be 0.4 K^{-1}. The energy has been evaluated using the mixed estimator. Calculations have been performed by the VPIMD method. Regarding the fourth-order approximation, we test the cases of the parameter $\alpha = 0$ and 1/3. As seen in Figure 1, the energy approaches a converged value with decreasing τ. The faster convergence is achieved using the fourth-order approximations compared with the primitive counterpart. Regarding the fourth-order approximation, the case with $\alpha = 0$ shows better performance. The calculated energies are described by the following relation (*9*):

$$E(\tau) = E_0 + A_\delta \tau^\delta + A_{\delta+2}\tau^{\delta+2}$$

where E_0 is an extrapolated ground-state energy and δ depends on the approximation employed: δ = 2 for the primitive approximation and δ = 4 for the fourth-order approximation. As seen in the figure, the τ dependence of the energy for each approximation is well fitted by the above equation, confirming the second and 4-th order convergence of the energy.

We next examine the computational efficiency on the HMC I and II methods. Hereafter, the total projection time β is fixed to be 0.25 K^{-1} with M = 100. The value α = 0 for the fourth-order approximation is adopted. The number n_{sample} is 10 for all the calculations. Molecular dynamics calculation with Δt = 10 fs has been performed for comparison. In Figure 2, we show acceptance ratio for the HMC calculations for various n_{MD} that is the number of MD steps in one HMC step. As expected, the acceptance ratio decreases with increasing n_{MD} for each Δt, since the rejection arises from the Hamiltonian error as a result of the move. For given n_{MD}, the acceptance ratio decreases with increasing Δt. In the case of the HMC II, the similar trend is observed, however, the trend is found to be milder.

Downloaded by CORNELL UNIV on May 28, 2012 | http://pubs.acs.org
Publication Date (Web): February 6, 2012 | doi: 10.1021/bk-2012-1094.ch014

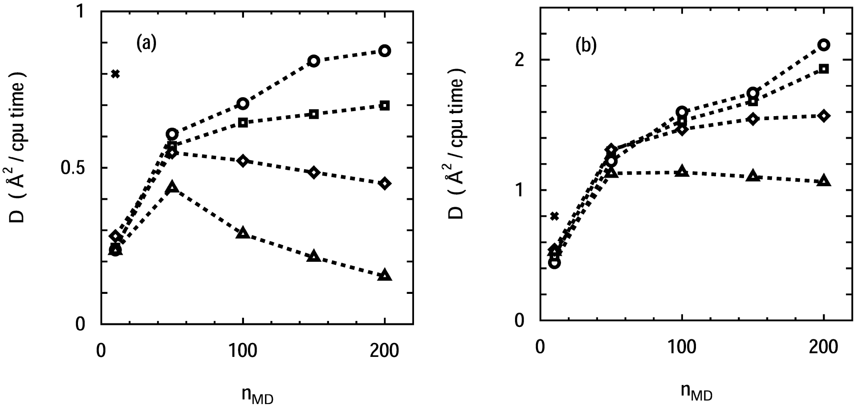

Figure 3. Diffusion constant of a tagged particle as a function of n_{MD}. Left panel (a) indicates the hybrid Monte Carlo I results and right panel (b) the hybrid Monte Carlo II results. Open circles, squares, diamonds, and triangles are the results using the time increment of one molecular dynamics step Δt = 12, 13, 14, and 15 fs, respectively. Crosses are the molecular dynamics results.

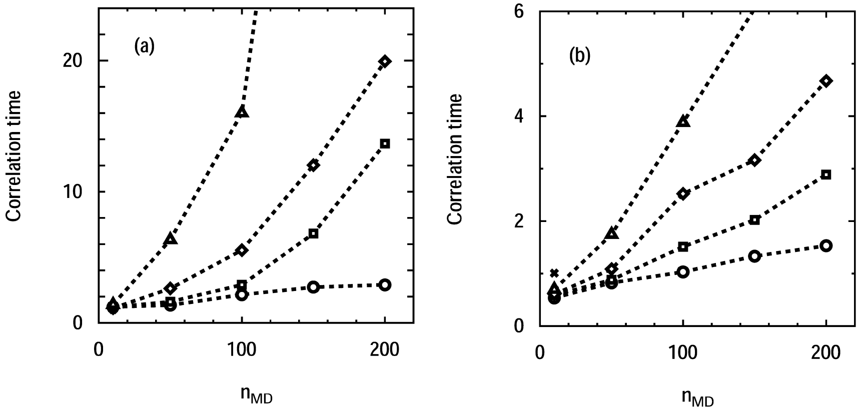

Figure 4. Correlation time in total energy as a function of n_{MD}*. The correlation time is defined by the number of correlated steps multiplied with the CPU time of one step. Left panel (a) indicates the hybrid Monte Carlo I results and right panel (b) the hybrid Monte Carlo II results. Open circles, squares, diamonds, and triangles are the results using the time increment of one molecular dynamics step* Δt *= 12, 13, 14, and 15 fs, respectively. Crosses are the molecular dynamics results.*

In Figure 3, we show a diffusion constant D to measure the sampling efficiency of the method. The diffusion constant is defined by the slope of the root mean square displacement of a tagged isomorphic polymer as a function of the elapsed CPU time. It is noted that the above diffusion constant is not related with the experimentally observable diffusion constant of the helium atoms. This is artificially introduced to measure the sampling efficiency of the isomorphic polymers in phase space; the larger diffusion constant yields faster convergence of physical quantities, indicating more efficient sampling. In the case of the HMC I, the diffusion constant increases with increasing n_{MD} for smaller Δt ($\Delta t = 12$ and 13 fs), while n_{MD} dependence shows a maximum around $n_{MD} = 50$ for larger Δt ($\Delta t = 14$ and 15 fs). Compared with MD, the sampling efficiency is almost comparable using large n_{MD} with small Δt. Note that the computation time by HMC I was found to be 64 % of the corresponding MD. The extra computation time comes from the integration of thermostat's equations of motion. With respect to HMC II, larger D is found in the case of larger n_{MD} except in the case of largest Δt examined. Much better efficiency is observed in comparison with MD. In the case of the HMC II, the computation time was found to be 28 % of the corresponding MD, due to avoiding the evaluation of the Hessian matrix. We next show another quantity regarding the correlation in successive HMC steps. This corresponds to the correlation time or statistical inefficiency (*24*, *25*). Correlation time in the total energy, which is defined by the number of correlated steps multiplied by the CPU time for one step, is presented in Figure 4. For both methods, the correlation time monotonically increases with increasing n_{MD}. However, much longer correlation time is found in the case of the HMC I.

Downloaded by CORNELL UNIV on May 28, 2012 | http://pubs.acs.org
Publication Date (Web): February 6, 2012 | doi: 10.1021/bk-2012-1094.ch014

Downloaded by CORNELL UNIV on May 28, 2012 | http://pubs.acs.org
Publication Date (Web): February 6, 2012 | doi: 10.1021/bk-2012-1094.ch014

As seen in Figures 3 and 4, the sampling efficiency and the statistical efficiency show the opposite trend. The HMC parameters should be chosen with considering the balance between the sampling efficiency and the statistical inefficiency. For example, in the case of $\Delta t = 12$ fs and $n_{MD} = 100$, D(HMC I) / D(MD) = 0.9 where D(HMC I) and D(MD) denote the diffusion constant by HMC I and MD, respectively. This indicates the sampling efficiency of the HMC I is comparable with that of MD. On the other hand, τ_{cor}(HMC I) / τ_{cor}(MD) = 2.1 where τ_{cor}(HMC I) and τ_{cor}(MD) denote the correlation time by HMC I and MD, respectively, which means the HMC I method is twice as statistically inefficient as MD. Regarding the HMC II, D(HMC II) / D(MD) = 2.0 and τ_{cor}(HMC II) / τ_{cor}(MD) = 1.0. While the sampling efficiency of the HMC II is twice in comparison with MD, the correlation time is almost the same. It indicates that the HMC II is a better choice for the above HMC parameters.

Summary and Outlook

In the present study, molecular dynamics and hybrid Monte Carlo (HMC) methods have been developed for the variational path integral using a fourth-order propagator. Two types of the HMC methods have been introduced. One is constructed by a standard way of introducing the HMC using the VPIMD method with a fourth-order propagator. This is called HMC I. The other is that a two level description is introduced by separating higher order terms from the action. Then, time consuming part in MD and HMC I can be avoided. The method is called HMC II. The methods have been applied to the liquid helium-4 to examine the computational efficiency. The HMC II is found to be a better choice for the present system.

Future applications of the present methods include nuclear fluctuations in hydrogen-bonded clusters like water molecules. For these systems, the description of the intermolecular interaction is a key to understand the molecular properties accurately. As in the path integral simulations for finite temperature systems (*26–28*), systematic improvement of the adiabatic potential energy surface is possible by directly combining the variational path integral with electronic structure calculations. As seen in the present study, the fourth-order approximation is useful to reduce the number of the imaginary time slices M. However, the evaluation of the Hessian matrix is computationally highly expensive for the electronic structure calculations. From this point of view, the HMC II method will be useful for the *ab initio* variational path integral calculations.

Acknowledgments

This work was partially supported by the Grant-in-Aid for Scientific Research (C) (No. 23550011) from the Japan Society for the Promotion of Science and by the Next Generation Super Computing Project, Nanoscience Program, MEXT, Japan.

Downloaded by CORNELL UNIV on May 28, 2012 | http://pubs.acs.org
Publication Date (Web): February 6, 2012 | doi: 10.1021/bk-2012-1094.ch014

References

1. Ceperley, D. M. *Rev. Mod. Phys.* **1995**, *67*, 279.
2. Lester, W. A., Ed. *Recent Advances in Quantum Monte Carlo Methods*; World Scientific: Singapore, 1997.
3. Nightingale, M. P.; Umrigar, C. J., Eds. *Quantum Monte Carlo Methods in Physics and Chemistry*; Kluwer Academic: Dordrecht, 1999.
4. Foulkes, W. M. C; Mitas, L.; Needs, R. J.; Rajagopal, G. *Rev. Mod. Phys.* **2001**, *73*, 33.
5. McMillan, W. L. *Phys. Rev.* **1965**, *138*, A442.
6. Anderson, J. B. *J. Chem. Phys.* **1975**, *63*, 1499.
7. Anderson, J. B. *J. Chem. Phys.* **1976**, *65*, 4121.
8. Sarsa, A.; Schmidt, K. E.; Magro, W. R. *J. Chem. Phys.* **2000**, *113*, 1366.
9. Cuervo, J. E.; Roy, P.-N.; Boninsegni, M. *J. Chem. Phys.* **2005**, *122*, 114504.
10. Miura, S. *Chem. Phys. Lett.* **2009**, *482*, 165.
11. Miura, S. *Comp. Phys. Commun.* **2011**, *182*, 274.
12. Miura, S. *Mol. Simul.*in press.
13. Tuckerman, M.; Berne, B. J.; Martyna, G. J.; Klein, M. L. *J. Chem. Phys.* **1993**, *99*, 2796.
14. Tuckerman, M. E.; Hughes, A. In *Classical and Quantum Dynamics in Condensed Phase Simulations*; Berne, B. J., Ciccotti, G., Coker, D. F., Eds.; World Scientific: Singapore, 1999; p 311.
15. Jang, S.; Jang, S.; Voth, G. A. *J. Chem. Phys.* **2001**, *115*, 7832.
16. Baroni, S.; Moroni, S. *Phys. Rev. Lett.* **1999**, *82*, 4745.
17. Chandler, D.; Wolynes, P. G. *J. Chem. Phys.* **1981**, *74*, 4078.
18. Martyna, G. J.; Klein, M. L.; Tuckerman, M. *J. Chem. Phys.* **1993**, *98*, 2796.
19. Duane, S.; Kennedy, A. D.; Pendleton, B. J.; Roweth, D. *Phys. Lett. B* **1987**, *195*, 216.
20. Mehlig, B.; Heermann, D. W.; Forrest, B. M. *Phys. Rev. B* **1992**, *45*, 679.
21. Matubayasi, N.; Nakahara, M. *J. Chem. Phys.* **1999**, *110*, 3291.
22. Miura, S.; Tanaka, J. *J. Chem. Phys.* **2004**, *120*, 2161.
23. Aziz, R. A.; Janzen, A. R.; Moldover, M. *Phys. Rev. Lett.* **1995**, *74*, 1586.
24. Friedberg, R.; Cameron, J. E. *J. Chem. Phys.* **1970**, *52*, 6049.
25. Allen, M. P.; Tildesley, D. J. *Computer Simulation of Liquids*; Clarendon Press: Oxford, 1987.
26. Marx, D.; Parrinello, M. *J. Chem. Phys.* **1996**, *104*, 4077.
27. Shiga, M.; Tachikawa, M.; Miura, S. *Chem. Phys. Lett.* **2000**, *332*, 396.
28. Shiga, M.; Tachikawa, M.; Miura, S. *J. Chem. Phys.* **2001**, *115*, 9149.

Downloaded by PENNSYLVANIA STATE UNIV on May 27, 2012 | http://pubs.acs.org
Publication Date (Web): February 6, 2012 | doi: 10.1021/bk-2012-1094.ch015

Chapter 15

Ab Initio Path Integral Molecular Dynamics and Monte Carlo Simulations for Water Trimer and Oligopeptide

Takatoshi Fujita,*,[1] Masa-Aki Kusa,[2] Takayuki Fujiwara,[2]
Yuji Mochizuki,[2,3] and Shigenori Tanaka*,[1]

[1]Graduate School of System Informatics, Kobe University,
1-1 Rokkodai, Nada, Kobe 657-8501, Japan
[2]Department of Chemistry and Research Center for Smart Molecules,
Faculty of Science, Rikkyo University, 3-34-1 Nishi-ikebukuro,
Toshima-ku, Tokyo 171-8501, Japan
[3]Institute of Industrial Science, The University of Tokyo,
4-6-1 Komaba, Meguro-ku, Tokyo 153-8505 Japan
***E-mails: fujita@insilico.h.kobe-u.ac.jp (T. Fujita);**
tanaka2@kobe-u.ac.jp (S. Tanaka)

We have performed *ab initio* path integral molecular dynamics and Monte Carlo simulations for water trimer and oligopeptide. In the first part, we illustrate the path integral molecular dynamics method based on fragment molecular orbital (FMO-PIMD) method. The FMO-PIMD method is applied to water trimer and glycine pentamer to investigate nuclear quantum effects on the structure and molecular interactions. In the second part, we employ the Møller-Plesset perturbation theory and discuss interplay of nuclear quantum effects and electron correlations.

In Advances in Quantum Monte Carlo; Tanaka, S., et al.;
ACS Symposium Series; American Chemical Society: Washington, DC, 2012.

Downloaded by PENNSYLVANIA STATE UNIV on May 27, 2012 | http://pubs.acs.org
Publication Date (Web): February 6, 2012 | doi: 10.1021/bk-2012-1094.ch015

Introduction

Hydrogen-bonded systems are important in various fields of chemistry and biology. Theoretical treatments of hydrogen-bonded systems require accurate calculations of potential energy surface and consideration of quantum effects of nuclei. Earlier studies have shown that nuclear quantum effects (NQEs) of hydrogen atoms influence the structural and dynamical properties of these systems (*1–9*).

Ab initio path integral simulation is one of the useful simulation methods suitable to treat hydrogen-bonded systems. Marx and Parrinello (*10*) and Tuckerman et al. (*11*) originally formulated *ab initio* path integral molecular dynamics (PIMD) method based on the density functional theory and the Car-Parrinello molecular dynamics (MD) method. This approach has been used in the studies of various hydrogen-bonded systems (*12–16*). Shiga, Tachikawa, and co-workers (*17–19*) later developed an *ab initio* PIMD method employing molecular orbital theory. Semiempirical molecular orbital theories have also been combined with the PIMD methods as an alternative approach to treat large systems (*20*). While most path integral simulations have employed the MD method to sample the nuclear configuration space, a path integral Monte Carlo (PIMC) (*21*) have also been employed by several authors (*22–24*). Pierleoni have formulated the PIMC method with quantum Monte Carlo method and applied it to the study of metallic hydrogen (*24*).

In the first part of this article, we report the PIMD method to treat large hydrogen-bonded systems with high accuracy (*25*). Our approach is based on the fragment molecular orbital (FMO) method. The FMO method (*26–33*) is a highly parallelizable quantum-chemical method suitable for the accurate electronic structure calculations of large systems. The FMO-based molecular dynamics (FMO-MD) method have also been developed (*34*) and applied to hydrated molecular systems (*35*). The incorporation of three-body term (*30*, *31*) in the FMO method improves the accuracy of the FMO-MD (*36*, *37*). Nagata et al. (*38*) have developed fully analytical gradients in the FMO method, in which the self-consistent **Z**-vector method is derived for solving the response term due to the external potentials. Mochizuki et al. (*39*) have implemented the energy gradient of the second-order Møller–Plesset perturbation theory in conjunction with the FMO method. Fujita et al. (*40*) have recently introduced the periodic boundary condition on the FMO method and calculated the radial distribution functions of liquid water. With these developments of the FMO-MD methods in mind, FMO-based PIMD method is expected to be a useful simulation method to treat large hydrogen-bonded systems with inclusion of NQE.

In the present study, we develop and implement the *ab initio* PIMD using the FMO method (FMO-PIMD). This FMO-PIMD method will provide an *ab initio* tool to simulate large hydrogen-bonded systems with high accuracy. Water trimer and glycine pentamer are studied using the FMO-PIMD method, where the electronic structure is first considered at the Hartree-Fock (HF) level. Analyzing the NQEs on the structure and the molecular interactions in these systems, we discuss the usefulness of the FMO-PIMD method.

In the second part of this article, the PIMC calculation together with Møller-Plesset (MP) perturbation theory is carried out and compared with the previous HF-based PIMD results so as to examine the dependence of the NQEs on the approximation level of molecular orbital theories. This *ab initio* comparison is analogous to that by Habershon et al. (*7*). They have analyzed the NQEs on the dynamics of liquid water using several force fields for water and shown that the PIMD simulations that employ rigid water models and flexible water models where intramolecular interactions are described by simple harmonic functions overestimate the NQEs on the diffusivities in liquid water. They have also remarked that the NQEs on the hydrogen bonds (HBs) consist of two competing effects: Intermolecular zero-point energies and tunneling effects destabilize the HBs, which is canceled by intramolecular zero-point energies that lead to the increase in the O-H bond lengths and result in the stabilization of the HBs. This picture has recently been supported by Li et al. (*9*). They have analyzed the NQEs on the HBs in several hydrogen-bonded systems and suggested that the NQEs weaken the weak HBs but strengthen the relatively strong HBs.

The electronic structure was considered at the HF level in the first part, while the HF method overestimates the O-H harmonic frequencies (*41*) and underestimates the hydrogen-bond interactions (*42*). Consequently, the PIMD methods with the HF may overestimate the NQE that destabilizes the HBs. The tendency similar to that by Habershon (*7*) may also be observed in the case of molecular orbital theories. To analyze this issue, the PIMC method with the MP perturbation theory was applied to water trimer and compared with previous PIMD-HF results. Since we are interested in interplay between electron correlations and the NQEs, the FMO method is not employed in this study. We then discuss how the NQEs depend on the level of molecular orbital theories.

Methods

Path Integral Molecular Dynamics Based on Fragment Molecular Orbital Method

In the FMO method, the calculated system is first divided into a lot of fragments, and molecular orbital calculations for fragment monomers and dimers are performed to approximate the total energy and other properties (*26–29*). The Born-Oppenheimer (BO) energy of the system can be calculated as follows:

$$E = \sum_{I}^{N_f} E_I + \sum_{I>J}^{N_f} \left(E_{IJ} - E_I - E_J \right),$$

where N_f is the number of fragments; E_I and E_{IJ} denote the energies of fragment monomer and dimer, respectively, which are calculated under the electrostatic potentials from other fragments. The atomic forces acting on the nuclei are obtained by taking the derivatives of the BO energy (*28*, *38*). We have then developed the PIMD methods based on the FMO method. Detailed

Downloaded by PENNSYLVANIA STATE UNIV on May 27, 2012 | http://pubs.acs.org
Publication Date (Web): February 6, 2012 | doi: 10.1021/bk-2012-1094.ch015

Downloaded by PENNSYLVANIA STATE UNIV on May 27, 2012 | http://pubs.acs.org
Publication Date (Web): February 6, 2012 | doi: 10.1021/bk-2012-1094.ch015

implementation of our method is found elsewhere (*25*). ABINIT-MPX program package was employed for FMO calculations (*27*, *29*, *32*, *33*).

FMO-MD and FMO-PIMD methods are applied to water trimer and glycine pentamer in the present study. In both simulations, electronic structure calculations were carried out at the HF level, and temperature was set at 300 K. In the calculations of water trimer, 6-31G** basis set was employed, and the imaginary time slice of 32 was used in the PIMD calculation. For glycine pentamer, STO-3G basis set was employed, and the imaginary time slices of 16 was applied. Other details of the calculations are found in Ref . (*25*).

Path Integral Monte Carlo with Møller-Plesset Perturbation Theory

In the second part of this article, we show the results of the PIMC simulations with MP perturbation theory for water trimer. Here, we employ the PIMC methods because the gradient calculation of the MP perturbation theory is expensive. The second-order MP perturbation (MP2) theory was used to take account of electron correlations at the least computational cost. In addition to the MP2, we employ third-order MP perturbation (MP3) theory. The O-O distances of the water trimer optimized at the MP2 level are shorter than those optimized at the post MP2 level (*41*, *43–46*). We discuss the effects of higher-order electron correlations on the structure in connection with the NQEs.

We have employed the normal-mode sampling of PIMC (*22*, *23*) which relies on the following effective potential:

$$V_{eff} = \sum_{s=1}^{P}\left[\sum_{I=1}^{N}\frac{M_I^{(s)} w_P^2}{2}\left(\mathbf{q}_I^{(s)}\right)^2 + \frac{1}{P}E\left(\mathbf{R}_I^{(s)}\left(\mathbf{q}_I^{(1)},\ldots,\mathbf{q}_I^{(P)}\right)\right)\right],$$

where P is imaginary time slices, N is the number of atoms, and s and I refer to the indices of P and N, respectively. $w_P = P^{1/2}/k_B T$, where k_B is the Boltzmann constant, and T is temperature. $\mathbf{q}$ are normal mode coordinates and related to atomic Cartesian coordinates $\mathbf{R}$ through a linear transformation, where zero-frequency mode (s=1) correspond to centroid coordinates which describe the center of mass motions of the polymer. The normal mode masses $M_I^{(s)}$ is related to the atomic masses M_I through $M_I^{(s)} = M_I \lambda^{(s)}$, where $\lambda^{(s)}$ is given by

$$\lambda^{(s)} = 2P\left(1 - \cos\left[\frac{2\pi(s-1)}{P}\right]\right).$$

E is the Born-Oppenheimer potential energy calculated by quantum mechanical methods.

Following procedure was employed as a trial displacement. First, centroid coordinates (s=1) or other coordinates (s≠1) are chosen with each probability of 0.5. In the movements of centroid coordinates, we attempt to move the centroid coordinates of one atom. In the movements of other coordinates, we attempt to simultaneously move several normal mode coordinates other than the centroid coordinates. We performed this trial move in such a way that the acceptance ratio becomes 0.4-0.5 in the system of water trimer.

Water trimer was employed also in this study. MC and PIMC simulations using MP2 and MP3 were performed at the temperature of 300K, where 6-31G** basis sets was employed. Simulations were carried out for 300000 steps; equilibration runs were carried out for 100000 steps, and following 200000 steps were used for calculations of physical properties. The imaginary time slices of 16 was employed for the PIMC simulations. We compare the MP2 and the MP3 results with that of the former HF and discuss the dependence of the NQEs on the level of molecular orbital theories.

Results and Discussion

FMO-PIMD for Water Trimer

We first show the optimized structure of the water trimer, before illustrating the results of the MD and the PIMD simulations. Figure 1 represents the global minimum (GM) structure of the water trimer optimized by the FMO-HF/6-31G** method. It is well established (*47*) that the GM structure of the water trimer is a cyclic structure where each water monomer simultaneously acts as both hydrogen-bond donor and acceptor. The O-O distances, O-O-O angles, and the interfragment interaction energies (IFIEs) of the FMO method are also shown in Fig. 1. Since each water molecule was assigned as one fragment, the IFIEs describe the intermolecular interactions between the water molecules.

Downloaded by PENNSYLVANIA STATE UNIV on May 27, 2012 | http://pubs.acs.org
Publication Date (Web): February 6, 2012 | doi: 10.1021/bk-2012-1094.ch015

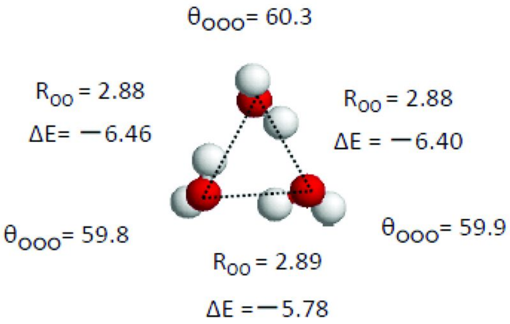

*Figure 1. Optimized structure of water trimer calculated by FMO-HF/6-31G** method. The O-O distances (R_{OO}), the O-O-O angles (θ_{OOO}), and the interfragment interaction energies (ΔE) are shown in units of Å, degrees, and kcal/mol, respectively.*

In order to examine the NQEs on the structure of water trimer, probability distributions of the O-O distances and the O-O-O angles were calculated and are shown in Figs. 2(a) and 2(b), respectively. In the quantum system, the extended separation of the O-O distance was found up to the range longer than 4.5Å, which is not observed in the classical system.

The differences between the quantum and the classical systems for nuclear degrees of freedom are also found in the distribution of the O-O-O angles. The maximum peaks are located at around 60 degrees in both the MD and the PIMD simulations, hence the cyclic structures are dominant. The distribution of the O-O-O angles in the MD simulations extends within the range of 60±20 degrees, indicating that the cyclic structure was maintained throughout the simulation. On the other hand, in the PIMD simulation, the distribution is also observed in the range of 20< θ_{OOO} <40 degrees and 100< θ_{OOO}<120 degrees as well, showing that the NQEs induce the significant fluctuations from the cyclic structure.

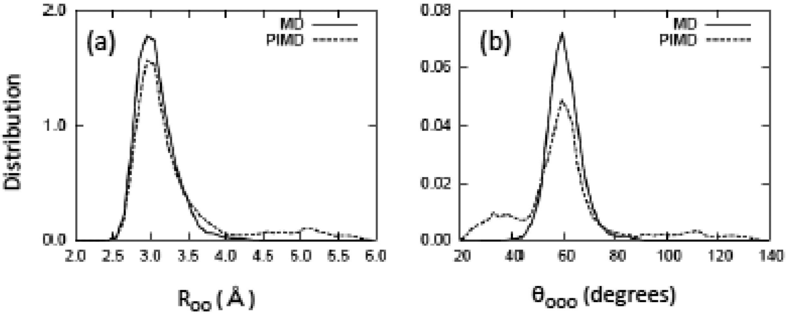

Figure 2. The probability distribution of (a) the O-O distances (R_{OO}) and (b) the O-O-O (θ_{OOO}) angles in the water trimer calculated by the MD (solid line) and the PIMD (dashed line) simulations. The results are shown in units of Å and degrees.

Downloaded by PENNSYLVANIA STATE UNIV on May 27, 2012 | http://pubs.acs.org
Publication Date (Web): February 6, 2012 | doi: 10.1021/bk-2012-1094.ch015

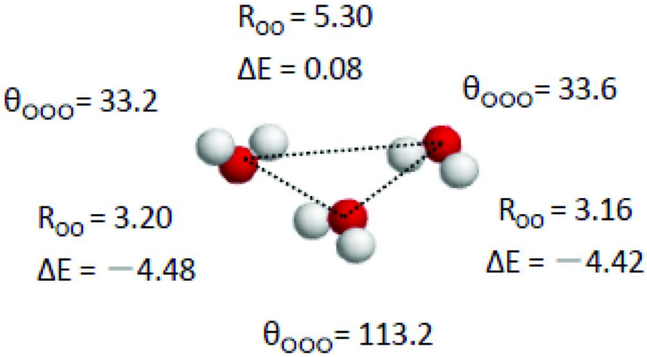

Figure 3. One of snapshots in the PIMD simulation for water trimer. The picture only shows the centroid coordinates, which is averages of all beads. The O-O distances (R_{OO}), the O-O-O angles (θ_{OOO}), and the interfragment interaction energies (ΔE) are shown in units of Å, degrees, and kcal/mol, respectively.

Figure 3 represents one of snapshots from the PIMD simulation. Here, only the centroid coordinates of the atoms are shown. In this structure, the O-O distance and the corresponding IFIE of a pair of water molecules are 5.30Å and 0.08 kcal/mol, respectively, thus showing that their HB is considered to be broken. The three O-O-O angles are 33.2, 33.6, and 113.2 degrees. These values of the O-O

Downloaded by PENNSYLVANIA STATE UNIV on May 27, 2012 | http://pubs.acs.org
Publication Date (Web): February 6, 2012 | doi: 10.1021/bk-2012-1094.ch015

distances and the O-O-O angles correspond to the distributions found only in the PIMD simulation as in Figs. 2(a) and 2(b). The observations thus indicate that the differences between the classical and quantum systems consist in whether or not the structures similar to Fig. 3 are found. The NQEs considerably enhance the structural fluctuations so that one of the hydrogen bonds would be broken.

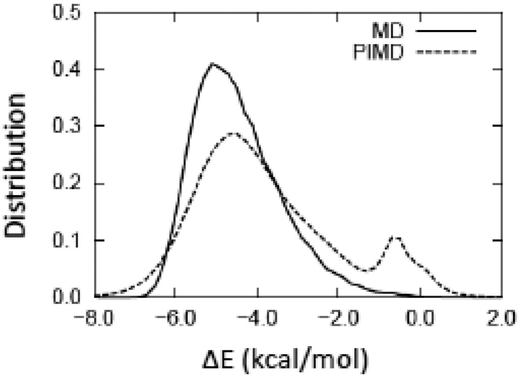

Figure 4. The probability distribution of the interfragment interaction energy (ΔE) between water molecules calculated by the MD (solid line) and the PIMD (dashed line) simulations for water trimer. The IFIE values are shown in units of kcal/mol.

Figure 4 shows the distributions of the IFIEs between water molecules. Maximum peaks are observed at around -5.4 and -4.9 kcal/mol in the MD and the PIMD simulations, respectively. The peak found at around -0.5 kcal/mol in the PIMD simulation corresponds to the interactions of the pair of water molecules where the HB is broken. These results indicate that the NQEs enhance the fluctuations in the intermolecular interactions. The distribution in the range of $-8 < \Delta E < -7$ kcal/mol in the PIMD simulation, which is not found in the MD simulation, indicates that in some configurations the NQEs stabilize hydrogen-bond interactions. This stabilization of the HB is due to the intramolecular zero-point energies leading to the increase in the O-H bond lengths. Figure 4 shows that there are two competing NQEs on the hydrogen-bond interactions, which are ascribed to intermolecular and intramolecular vibrations. The results presented here are consistent with a physical picture of the NQEs on the HBs proposed by Habershon et al. (*7*) and Li et al. (*9*).

In summary, the NQEs destabilize the HB in water trimer on average: the NQEs induce the considerable fluctuations from the cyclic structure so that one HB would be broken. This result is owing to the zero-point energies of intermolecular vibrations and the tunneling effects. Although the NQEs primarily destabilize the HB, there is also another tendency that the HB between water molecules are stabilized by the NQEs. We have observed these two competing NQEs by calculating the distribution of intermolecular interaction between water molecules, which is consistent with the earlier studies (*7*, *9*).

Downloaded by PENNSYLVANIA STATE UNIV on May 27, 2012 | http://pubs.acs.org
Publication Date (Web): February 6, 2012 | doi: 10.1021/bk-2012-1094.ch015

FMO-PIMD for Glycine Pentamer

The structure of the glycine pentamer was optimized by the FMO-HF/STO-3G method, which is shown in Fig. 5. N-H…O and O-H…O hydrogen bonds are observed between the fragments 2-5 and 3-5, respectively. Geometrical properties in these HBs were then averaged over the MD and the PIMD simulations. IFIEs between fragment 2-5 and 3-5 are also shown. Since each glycine was assigned as one independent fragment, these IFIEs describe these hydrogen-bond interactions. As shown in Table 1, the NQEs seem to increase the N-O and O-O distances, and the IFIEs also indicate that the NQEs destabilize intramolecular interactions in the glycine pentamer. Nevertheless, the differences between the classical and the quantum systems were within the statistical uncertainties due to the limitation of computational cost.

Then, we compare the present results with the earlier study. Ishimoto et al. (*4*) have discussed the hydrogen/deuterium isotope effects on the HBs in glycine pentamer and octamer by combining the FMO and multi-component molecular orbital theory, in which only hydrogen atoms are treated quantum-mechanically. They have observed that the HBs in the glycine pentamer with hydrogen atoms, which have larger zero-point energies, are more stabilized than those with deuterium atoms. Therefore, their results indicate that the incorporation of the zero-point energies leads to the stabilization of the HBs in the glycine pentamer, which contradicts our results. Since quantization of only hydrogen atoms mainly includes the intramolecular zero-point energies, their calculations incorporate the NQEs that destabilize the HBs. The present results, which take account of quantum effects of all nuclei, suggest that the NQEs destabilize the HBs. Although there are considerable statistical errors in our results, present observations agree to the suggestion by Li et al. (*9*) that the NQEs weaken the weak HBs.

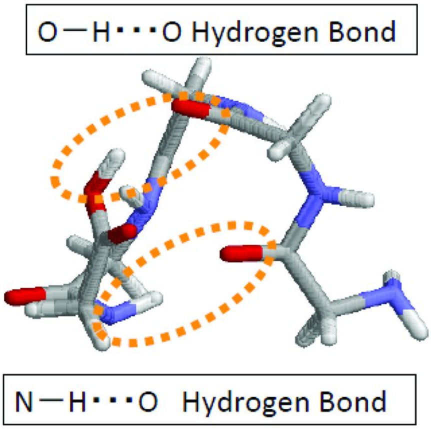

Figure 5. The structure of the glycine pentamer optimized by the FMO-HF/STO-3G method.

Downloaded by PENNSYLVANIA STATE UNIV on May 27, 2012 | http://pubs.acs.org
Publication Date (Web): February 6, 2012 | doi: 10.1021/bk-2012-1094.ch015

Table 1. Structural properties and interaction energies of the N-H…O and the O-H…O hydrogen bonds in glycine pentamer[a]

	Opt.	*MD*	*PIMD*
N-H…O			
$<R_{N\text{-}O}>$	2.94	3.06±0.07	3.28±0.21
$<R_{N\text{-}H}>$	1.03	1.03	1.04
$<R_{HO}>$	1.99	2.11±0.08	2.38±0.27
$<\Delta E_{2\text{-}5}>$	-4.44	-3.37±0.83	-2.54±1.01
O-H…O			
$<R_{OO}>$	2.63	2.90±0.25	3.06±0.30
$<R_{OH}>$	0.99	0.99	1.00
$<R_{HO}>$	1.73	2.22±0.48	2.62±0.57
$<\Delta E_{3\text{-}5}>$	-5.17	-2.20±2.91	-1.04±1.12

[a] Results are shown in units of Å and kcal/mol . ΔE are interfragment interaction energies between fragment 2-5 (N-H…O) and fragment 3-5 (O-H…O), respectively. Shown results are those of the optimized structure, and the thermal averages of the MD and the PIMD simulations. Statistical uncertainties of the results are also shown. Unless stated, the statistical uncertainty is smaller than the last digit.

PIMC for Water Trimer

In order to quantify the effects of electron correlations on the structure in the water trimer, O-H bond lengths and O-O distances are averaged in the PIMC simulation and presented in Table 2. Average O-H bond lengths increase in the following order: HF < MP3 < MP2. The HF overestimates the intramolecular harmonic frequencies and thus underestimates the O-H bond lengths. The incorporation of electron correlations by the MP2 increases the O-H bond lengths, but the MP2 rather overestimates them. The results at the MP3 level are smaller than those of the MP2.

We then examine the average O-O distances. Large differences between classical and quantum simulations obtained by the HF method is due to the breaking of the HB: quantum results include the large separation of water molecules. In contrast to the HF, such a large separation between water molecules is not observed in the cases of the MP2 and the MP3. This result shows that the considerable fluctuations induced by the NQEs in the HF are due to the underestimation of hydrogen-bond interactions; the HF method overestimates the NQEs that destabilize the hydrogen-bond interactions. This *ab initio* observation is analogous to that by Habershon et al. (*7*). The present results show that the incorporation of electron correlations is essential to perform the path integral simulations.

Figure 6 show the probability distribution of the O-O distances calculated by the (a) MP2 and the (b) MP3. The maximum peak are observed at around 2.85-2.86 Å for the MP2 and 2.86-2.87 Å for the MP3. The peak positions of the distributions correspond to the average O-O distance of vibrational ground states. Liu et al. (*48*) have estimated the O-O distance in the water trimer by vibrational-rotational-tunneling spectroscopy and found it is 2.86-2.87Å. The peak positions of the O-O distances are in good agreement in their estimation. In the case of the MP2, the consideration of the NQEs has slight effects on the O-O distribution, which may be due to the overestimation of the hydrogen-bond interactions by the MP2. On the other hand, the NQEs enhance the fluctuations in the O-O distances in the MP3. The detailed comparison between the MP2 and the MP3 will be published elsewhere (*49*).

Downloaded by PENNSYLVANIA STATE UNIV on May 27, 2012 | http://pubs.acs.org
Publication Date (Web): February 6, 2012 | doi: 10.1021/bk-2012-1094.ch015

Table 2. Average O-H bond lengths (R_{OH}) and O-O distances (R_{OO}) of water trimer calculated by the HF, the MP2, and the MP3 methods with 6-31G basis set[a]**

	Classical	*Quantum*
$<R_{OH}>$		
HF	0.948	0.961
MP2	0.970	0.983
MP3	0.965	0.978
$<R_{OO}>$		
HF	3.069±0.018	3.296±0.198
MP2	2.885±0.013	2.913±0.016
MP3	2.931±0.021	2.955±0.020

[a] Results are shown in units of Å. The results of the HF were calculated by the previous FMO-MD (Classical) and FMO-PIMD (Quantum) simulations. The results of the MP2 and the MP3 were calculated by the MC (Classical) and the PIMC (Quantum) simulations. Statistical uncertainties of the results are also shown. Unless stated, the statistical uncertainty is smaller than the last digit.

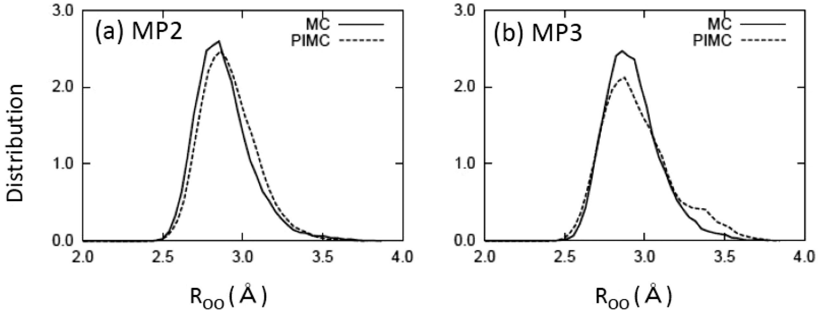

Figure 6. The probability distributions of the O-O distance (R_{OO}) in the water trimer calculated by (a) the MP2 and (b) the MP3. Solid and dashed lines refer to the results of MC and PIMC simulations, respectively. R_{OO} is measured in units of Å.

Downloaded by PENNSYLVANIA STATE UNIV on May 27, 2012 | http://pubs.acs.org
Publication Date (Web): February 6, 2012 | doi: 10.1021/bk-2012-1094.ch015

Summary and Perspective

In the first part of this article, we have presented the FMO-based PIMD method suitable to treat large systems and applied it to water trimer and glycine pentamer. In the FMO-PIMD study of the water trimer, we have shown that the NQEs enhance the fluctuations in the structure and the intermolecular interactions. We have also demonstrated the FMO-PIMD calculations of the glycine pentamer and shown that the NQEs in the glycine pentamer destabilize the intramolecular hydrogen-bond interactions. Although statistical errors are considerable in our calculations, the present results are consistent with the suggestion by Li et al (*9*) that the NQE weaken the weak HBs. To our knowledge, this is the first attempt to treat all (electronic and nuclear) degrees of freedom in polypeptides quantum mechanically.

In the second part of this article, the PIMC based on the MP2 and the MP3 has been applied to water trimer so as to investigate the dependence of the NQEs on the calculation level of molecular orbital theories. The considerable fluctuations induced by the NQEs in the HF are due to the underestimation of the hydrogen-bond interactions. The incorporation of electron correlations is thus essential to perform path integral simulations. Present *ab initio* observation is analogous to the classical one by Haberoshon et al. (*7*). The NQEs have slight effects on the distribution of the O-O distances in the MP2, while the NQEs induce the fluctuation of the O-O distance in the MP3. The detailed comparison between the MP2 and the MP3 will be published elsewhere (*49*).

The FMO-MD method has recently been improved through theoretical developments such as fully analytical gradients (*38*), FMO-MP2 gradient (*39*), and periodic boundary conditions (*40*). FMO-PIMD methods in conjunction with these developments will become a powerful simulation tool to describe HBs and proton transfer in condensed systems.

Acknowledgments

The authors greatly thank Dr. Motoyuki Shiga and Prof. Masanori Tachikawa for discussions concerning path integral simulations and nuclear quantum effects. T.F. (T. Fujita) appreciates a financial support from Research Fellowship of the Japan Society for the Promotion of the Science. T.F. (T. Fujiwara) would like to acknowledge financial support from a Special Fund for Research by Rikkyo University. This work was financially supported by the Core Research for Evolutional Science and Technology (CREST) project of the Japan Science and Technology Agency (JST).

References

1. Gregory, J. K.; Clary, D. C. *J. Phys. Chem.* **1996**, *100*, 18014.
2. Clary, D. C.; Benoit, D. M.; Van Mourik, T. *Acc. Chem. Res.* **2000**, *33*, 441.
3. Tachikawa, M. *Mol. Phys.* **2002**, *100*, 881.
4. Ishimoto, T.; Tachikawa, M.; Nagashima, U. *J. Chem. Phys.* **2006**, *124*, 014112.

5. Nakai, H.; Ikabata, Y.; Tsukamoto, Y.; Imamura, Y.; Miyamoto, K.; Hoshino, M. *Mol. Phys.* **2007**, *105*, 2649.
6. Paesani, F.; Voth, G. A. *J. Phys. Chem. B* **2009**, *113*, 5702.
7. Habershon, S.; Markland, T. E.; Manolopoulos, D. E. *J. Chem. Phys.* **2009**, *131*, 024501.
8. Paesani, F.; Yoo, S.; Bakker, H. J.; Xantheas, S. S. *J. Phys. Chem. Lett.* **2010**, *1*, 2316.
9. Li, X-Z.; Walker, B.; Michaelides, A. *Proc. Natl. Acad. Sci. U.S.A.* **2011**, *108*, 6369.
10. Marx, D.; Parrinello, M. *J. Chem. Phys.* **1996**, *104*, 4077.
11. Tuckerman, M. E.; Marx, D.; Klein, M. L.; Parrinello, M. *J. Chem. Phys.* **1996**, *104*, 5579.
12. Marx, D.; Tuckerman, M. E.; Hutter, J.; Parrinello, M. *Nature* **1999**, *397*, 601.
13. Raugei, S.; Klein, M. L. *J. Am. Chem. Soc.* **2003**, *125*, 8992.
14. Chen, B.; Ivanov, I.; Klein, M. L.; Parrinello, M. *Phys. Rev. Lett.* **2003**, *91*, 215503.
15. Swalina, C.; Wang, Q.; Chakraborty, A.; Hammes-Schiffer, S. *J. Phys. Chem. A* **2007**, *111*, 2206.
16. Morrone, J. A.; Car, R. *Phys. Rev. Lett.* **2008**, *101*, 017801.
17. Shiga, M; Tachikawa, M.; Miura, S. *J. Chem. Phys.* **2001**, *115*, 9149.
18. Tachikawa, M.; Shiga, M. *J. Am. Chem. Soc.* **2005**, *127*, 11908.
19. Ishibashi, H.; Hayashi, A.; Shiga, M.; Tachikawa, M. *ChemPhysChem* **2008**, *9*, 383.
20. Kakizaki, A.; Motegi, H.; Yoshikawa, T.; Takayanagi, T.; Shiga, M.; Tachikawa, M. *J. Mol. Struct.: THEOCHEM* **2009**, *901*, 1.
21. Ceperley, D. M. *Rev. Mod. Phys.* **1995**, *67*, 279.
22. Weht, R. O.; Kohanoff, J.; Estrin, D. A.; Chakravarty, C. *J. Chem. Phys.* **1998**, *108*, 8848.
23. Glaesemann, K. R.; Fried, L. E. *J. Chem. Phys.* **2003**, *118*, 1596.
24. Pierleoni, C.; Ceperley, D. M.; Holzmann, M. *Phys. Rev. Lett.* **2004**, *93*, 146402.
25. Fujita, T.; Watanabe, H.; Tanaka, S. *J. Phys. Soc. Jpn.* **2009**, *78*, 104723.
26. Kitaura, K.; Ikeo, E.; Asada, T.; Nakano, T.; Uebayasi, M. *Chem. Phys. Lett.* **1999**, *313*, 701.
27. Nakano, T.; Kaminuma, T.; Sato, T.; Akiyama, Y.; Uebayasi, M.; Kitaura, K. *Chem. Phys. Lett.* **2000**, *318*, 614.
28. Kitaura, K.; Sugiki, S.; Nakano, T.; Komeiji, Y.; Uebayasi, M. *Chem. Phys. Lett.* **2001**, *336*, 163.
29. Nakano, T.; Kaminuma, T.; Sato, T.; Fukuzawa, K.; Akiyama, Y.; Uebayasi, M.; Kitaura, K. *Chem. Phys. Lett.* **2002**, *351*, 475.
30. Fedorov, D. G.; Kitaura, K. *J. Chem. Phys.* **2004**, *120*, 6832.
31. Fujita, T.; Fukuzawa, K.; Mochizuki, Y.; Nakano, T.; Tanaka, S. *Chem. Phys. Lett.* **2009**, *478*, 295.
32. Mochizuki, Y.; Nakano, T.; Koikegami, S.; Tanimori, S.; Abe, Y.; Nagashima, U.; Kitaura, K. *Theor. Chem. Acc.* **2004**, *112*, 442.

Downloaded by PENNSYLVANIA STATE UNIV on May 27, 2012 | http://pubs.acs.org
Publication Date (Web): February 6, 2012 | doi: 10.1021/bk-2012-1094.ch015

33. Mochizuki, Y.; Yamashita, K.; Fukuzawa, K.; Takematsu, K.; Watanabe, H.; Taguchi, N.; Okiyama, Y.; Tsuboi, M.; Nakano, T.; Tanaka, S. *Chem. Phys. Lett.* **2010**, *493*, 346.
34. Komeiji, Y.; Nakano, T.; Fukuzawa, K.; Ueno, Y.; Inadomi, Y.; Nemoto, T.; Uebayasi, M.; Fedorov, D. G.; Kitaura, K. *Chem. Phys. Lett.* **2003**, *372*, 342.
35. Komeiji, Y.; Mochizuki, Y.; Nakano, T.; Fedorov, D. G. *J. Mol. Struct.: THEOCHEM* **2009**, *898*, 2.
36. Komeiji, Y.; Mochizuki, Y.; Nakano, T. *Chem. Phys. Lett.* **2010**, *484*, 380.
37. Fujiwara, T.; Mochizuki, Y.; Komeiji, Y.; Okiyama, Y.; Mori, H.; Nakano, T.; Miyoshi, E. *Chem. Phys. Lett.* **2010**, *490*, 41.
38. Nagata, T.; Brorsen, K.; Fedorov, D. G.; Kitaura, K.; Gordon, M. S. *J. Chem. Phys.* **2011**, *134*, 124115.
39. Mochizuki, Y.; Nakano, T.; Komeiji, Y.; Yamashita, K.; Okiyama, Y.; Yoshikawa, H.; Yamataka, H. *Chem. Phys. Lett.* **2011**, *504*, 95.
40. Fujita, T.; Nakano, T.; Tanaka, S. *Chem. Phys. Lett.* **2011**, *506*, 112.
41. Xantheas, S. S.; Dunning, T. H., Jr. *J. Chem. Phys.* **1993**, *99*, 8774.
42. Xantheas, S. S. *J. Chem. Phys.* **1994**, *100*, 7523.
43. Fowler, J. E.; Schaefer, H. E. *J. Am. Chem. Soc.* **1995**, *117*, 446.
44. Nielsen, I. M. B.; Seidl, E. T.; Janssen, C. L. *J. Chem. Phys.* **1999**, *110*, 9435.
45. Anderson, J. A.; Crager, K.; Fedoroff, L.; Tschumper, G. S. *J. Chem. Phys.* **2004**, *121*, 11023.
46. Wang, Y.; Shepler, B. C.; Braams, B. J.; Bowman, J. M. *J. Chem. Phys.* **2009**, *131*, 054511.
47. Keutsch, F. N.; Cruzan, J. D.; Saykally, R. J. *Chem. Rev.* **2003**, *103*, 2533.
48. Liu, K.; Cruzan, J. D.; Saykally, R. J. *Science* **1996**, *271*, 929.
49. Fujita, T.; Fujiwara, T.; Kusa, M.; Mochizuki, Y.; Tanaka, S. ; Shiga, M., in preparation.

Downloaded by PENNSYLVANIA STATE UNIV on May 27, 2012 | http://pubs.acs.org
Publication Date (Web): February 6, 2012 | doi: 10.1021/bk-2012-1094.ch015

Chapter 16

Beyond a Single Solvated Electron: Hybrid Quantum Monte Carlo and Molecular Mechanics Approach

D. Yu. Zubarev[a] and W. A. Lester, Jr.*[,a,b]

[a]Kenneth S. Pitzer Center for Theoretical Chemistry,
University of California, Berkeley, California 94720
[b]Chemical Sciences Division,
Lawrence Berkeley National Laboratory,
Berkeley, California 94720
*E-mail: walester@lbl.gov

Downloaded by OHIO STATE UNIV LIBRARIES on May 28, 2012 | http://pubs.acs.org
Publication Date (Web): February 6, 2012 | doi: 10.1021/bk-2012-1094.ch016

A hybrid computational approach that combines quantum Monte Carlo and molecular mechanics (QMC/MM) has been recently developed for the accurate treatment of electron correlation in systems that require a large number of explicit solvent molecules. Here, the results of QMC/MM calculations are reported of the binding among two excess electrons and a water cluster containing 31 molecules. This system is relevant to the study of the interaction of excess electrons with solvent molecules during electron and energy transfer in media. Strong sensitivity of QMC/MM prediction of the vertical detachment energy is observed with respect to the number of water molecules treated at the QMC level. Origins of this tendency are discussed.

Introduction

The application of quantum Monte Carlo (QMC) approaches to realistic molecular systems faces the common trade-off of ab initio quantum chemistry, namely, quality vs. feasibility. A recently developed hybrid methodology that combines QMC and force-field molecular mechanics (QMC/MM) (*1*) is perceived as a viable route to the treatment of challenging systems such as solute-solvent complexes in a way that preserves the accurate description of correlation for the

In Advances in Quantum Monte Carlo; Tanaka, S., et al.;
ACS Symposium Series; American Chemical Society: Washington, DC, 2012.

solute molecule treated by QMC and incorporates solvent effects as captured by MM. The present contribution describes a QMC/MM investigation of the interaction among two excess electrons and a cluster of water. Dianionic water clusters can be seen as a model of the elusive dielectron $(e^{-}{}_{2})_{\mathrm{aq}}$ whose existence is inferred from the results of pulse radiolysis experiments (*2*, *3*). Theoretical studies of $(e^{-}{}_{2})_{\mathrm{aq}}$ are also available (*4–10*). The stabilization of the electron pair in singlet or triplet spin-coupling by solvent can be an important aspect of multi-electron charge and energy transfer as well as electron capture by anionic systems resulting in dissociation of the latter.

The chemical context of the present problem is similar to that of bound states of a single solvated electron (*11–38*). The ability of water clusters to bind excess electrons depends largely on cluster geometry. The structural motifs of water clusters interacting with 2 excess electrons are available from a combined study utilizing force-field replica-exchange simulations and density functional theory (DFT) gradient optimization (*39*). Vertical detachment energies (VDEs) are used as a measure of binding. Dianions characterized by positive VDEs were found to bind electrons either in two cavities or one electron in a cavity and the other on a surface. The computation of VDEs is associated with certain difficulties approach. For example, DFT facilitates affordable computations but systematically overbinds excess electrons, although the calculations are readily affordable. With perturbation theory, more accurate results can be obtained but the computations become prohibitively expensive for large water clusters. The problem appears to be amenable to QMC/MM treatment, which has been pursued here with findings reported below. In view of the methodological emphasis of the present study, only one $(H_2O)_{31}{}^{2-}$ cluster is considered which is shown at Figure 1.

Downloaded by OHIO STATE UNIV LIBRARIES on May 28, 2012 | http://pubs.acs.org
Publication Date (Web): February 6, 2012 | doi: 10.1021/bk-2012-1094.ch016

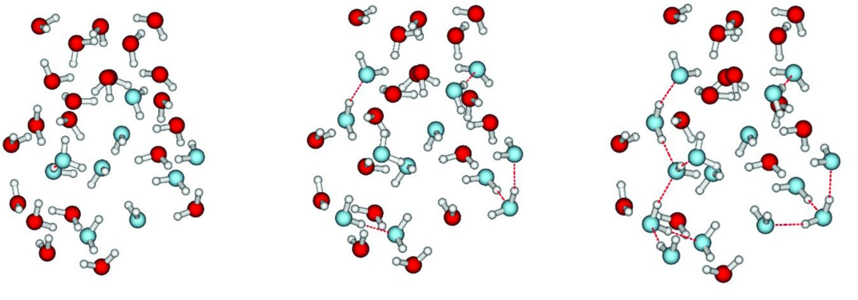

Figure 1. From left to right: 9-22, 12-19, and 15-16 partitioning of the $(H_2O)_{31}{}^{2-}$ cluster into QMC (O atoms in blue) and MM (O atoms in red) parts.

Downloaded by OHIO STATE UNIV LIBRARIES on May 28, 2012 | http://pubs.acs.org
Publication Date (Web): February 6, 2012 | doi: 10.1021/bk-2012-1094.ch016

Methodology

The application of QMC/MM implies that the system under consideration can be separated into two components. One of these requires a very accurate quantum treatment (QMC) and the other implies a lower level of theory (MM) due to lesser importance in the system. In the context of detachment of an excess electron from a dianionic water cluster, the assumption is that the interaction of the two water molecules with the excess electron is not equivalent which raises the question of how to treat this distinction in water molecules. One notes that a heuristic approach is used typically to distinguish between QMC and MM fragments. Here, it is based on the change of cumulative Mulliken charge of water molecules upon loss of one electron by the dianion. The assumption is that the molecules undergoing the largest change of charge are more involved in the interaction and should be treated at the quantum level. Following this direction, QMC/MM calculations were carried out for cases with 9, 12, and 15 water molecules in the QMC component of the cluster. The remaining 22, 19, and 16 molecules were described by the TIP3P force-field (*40*).

QMC/MM calculations were performed with the Zori code (*41*) according to the methodology described in Ref. (*1*). Trial wave functions for fixed-node diffusion Monte Carlo (FNDMC) calculations were constructed in the product form of an independent particle function and correlation function. The former included B3LYP (*41*, *42*) determinants obtained from calculations with Burkatzki-Fillipi-Dolg (BFD) (*43*) pseudo-potential and basis set augmented with 3 diffuse s exponents on H. These calculations were carried out using GAMESS software (*44*). Correlation functions (CF) were in the form of a 17-term Schmidt-Moscowitz-Boys-Handy (SMBH) expansion (*45–47*). The CF parameters were energy optimized using variational Monte Carlo (VMC). For each partitioning of the cluster, the determinants describing QMC component were obtained in the absence of the MM component so that the nodal structure of the trial wave functions used in the FNDMC/MM runs does not reflect the presence of solvent. The effect of the solvent is accounted for only by the total energy shift due to coupling between QMC and MM components, not by the fixed-node approximation. The QMC/MM runs were performed with time steps of 0.02, 0.04, 0.08, and 0.16 a.u.$^{-1}$ and subsequent weighted quadratic extrapolation to zero time step. The simulation ensemble included ~200K walkers for 9-22, 12-18, and 15-16 partitioning of the cluster into QMC and MM components, respectively.

Results and Discussion

The first VDE of a singlet dianion $(H_2O)_{31}^{2-}$ is 0.16 eV at the B3LYP/6-31++G** level of theory and -0.24 eV at the MP2/6-31++G** level of theory (*39*). Results of FNDMC/MM calculations are summarized in Table 1. The largest QMC (with water) component of the cluster is vertically unbound with a VDE comparable to MP2 value. The VDEs with the smallest QMC (with water) component considerably underestimate the strength of the interaction in view of the other results.

Table 1. First VDE of $(H_2O)_{31}^{2-}$ cluster from FNDMC/MM calculations for selected partitioning into QMC and MM components

Size of QMC component	*Size of MM component*	*$VDE_{QMC/MM}$ (eV)*
9	22	-2.42±0.08
12	19	-0.52±0.09
15	16	-0.17±0.09

The main conclusion is that FNDMC/MM calculations demonstrate high sensitivity to the number of water molecules present in the component of the cluster that is treated at FNDMC level. First possible explanation of the observed tendency is that the present methodology does not account for the effect of the MM component on the nodes of trial wave function describing the QMC component. The effect of the MM component is exclusively an energy shift due to the field of external charges. This aspect can be investigated further by preparing determinants in the presence of the solvation shell molecules represented, for example, by point charges or effective fragment potentials (EFP). FNDMC/MM runs with such determinants encountered heavy instabilities associated with the locality approximation of ECPs. Alternatively, the highest occupied molecular orbital of the dianion can be optimized in the course of VMC/MM calculations. A second possible explanation is inadequacy of the current approach to cluster partitioning into the central QMC component and MM solvation shell. Mulliken charges are crude and can yield inadequate results especially in calculations with basis sets with diffuse functions. The source of such inadequacy might be intrinsic relevance of all molecules of a cluster to the interaction with highly delocalized excess electrons, especially for small clusters. This matter can be clarified if FNDMC/MM calculations are performed for increasingly large QMC components in the limit of FNDMC treatment of the entire cluster. The considerations outlined are perceived as directions for future research that aims to clarify and improve the methodology of QMC/MM calculations.

Downloaded by OHIO STATE UNIV LIBRARIES on May 28, 2012 | http://pubs.acs.org
Publication Date (Web): February 6, 2012 | doi: 10.1021/bk-2012-1094.ch016

Acknowledgments

DYZ was supported by the National Science Foundation under grant NSF CHE-0809969. This research used computational resources of the National Energy Research Scientific Computing Center, which is supported by the Office of Science of the U.S. Department of Energy under Contract No. DE-AC02-05CH11231. WAL was supported by the Director, Office of Energy Research, Office of Basic Energy Sciences, Chemical Sciences, Geosciences and Biosciences Division of the US Department of Energy, under Contract No. DE-AC03-76F00098. The authors would like to thank Professor Teresa Head-Gordon and Dr. Gary Clark for useful discussions.

Downloaded by OHIO STATE UNIV LIBRARIES on May 28, 2012 | http://pubs.acs.org
Publication Date (Web): February 6, 2012 | doi: 10.1021/bk-2012-1094.ch016

References

1. Cho, H. M.; Lester, W. A. *J. Phys. Chem. Lett.* **2010**, *1*, 3376.
2. Basco, N.; Kenney-Wallace, G. A.; Vidyarthi, S. K.; Walker, D. C. *Can. J. Chem.* **1972**, *50*, 2059.
3. Schmidt, K. H.; Bartels, D. M. *Chem. Phys.* **1995**, *190*, 145.
4. Feng, D. F.; Feuki, K.; Kevan, L. *J. Chem. Phys.* **1973**, *58*, 3281.
5. Kaukonen, H. P.; Barnett, R. N.; Landman, U. *J. Chem. Phys.* **1992**, *97*, 1365.
6. Chuev, G. N.; Fedorov, M. V. *Int. J. Quantum. Chem.* **2004**, *100*, 539.
7. Larsen, R. E.; Schwartz, B. J. *J. Phys. Chem. B* **2004**, *108*, 11760.
8. Larsen, R. E.; Schwartz, B. J. *J. Phys. Chem. B* **2006**, *110*, 9681.
9. Larsen, R. E.; Schwartz, B. J. *J. Phys. Chem. B* **2006**, *110*, 9692.
10. Larsen, R. E.; Schwartz, B. J. *J. Phys. Chem. B* **2006**, *110*, 1006.
11. Hart, E. J.; Boag, J. W. *J. Am. Chem. Soc.* **1962**, *84*, 4090.
12. Migus, A.; Gauduel, Y.; Martin, J. L.; Antonetti, A. *Phys. Rev. Lett.* **1987**, *58*, 1559.
13. Long, F. H.; Lu, H.; Eisenthal, K. B. *Phys. Rev. Lett.* **1990**, *64*, 1469.
14. Coe, J. V.; Lee, G. H.; Eaton, J. G.; Arnold, S. T.; Sarkas, H. W.; Bowen, K. H.; Ludewigt, C.; Haberland, H.; Worsnop, D. R. *J. Chem. Phys.* **1990**, *92*, 3980.
15. Silva, C.; Walhout, P. K.; Yokoyama, K.; Barbara, P. F. *Phys. Rev. Lett.* **1998**, *80*, 1086.
16. Tauber, M. J.; Mathies, R. A. *J. Am. Chem. Soc.* **2003**, *125*, 1394.
17. Bragg, A. E.; Verlet, J. R. R.; Kammrath, A.; Cheshnovsky, O.; Neumark, D. M. *Science* **2004**, *306*, 669.
18. Hammer, N. I.; Shin, J. W.; Headrick, J. M.; Diken, E. G.; Roscioli, J. R.; Weddle, G. H.; Johnson, M. A. *Science* **2004**, *306*, 675.
19. Verlet, J. R. R.; Bragg, A. E.; Kammrath, A.; Cheshnovsky, O.; Neumark, D. M. *Science* **2005**, *307*, 93.
20. Verlet, J. R. R.; Bragg, A. E.; Kammrath, A.; Cheshnovsky, O.; Neumark, D. M. *Science* **2005**, *310*, 1769b.
21. Tang, Y.; Shen, H.; Sekiguchi, K.; Kurahashi, N.; Mizuno, T.; Suzuki, Y. I.; Suzuki, T. *Phys. Chem. Chem. Phys.* **2010**, *12*, 3653.
22. Sagar, D. M.; Bain, C. D.; Verlet, J. R. R *J. Am. Chem. Soc.* **2010**, *132*, 6917.
23. Siefermann, K. R.; Liu, Y.; Lugovoy, E.; Link, O.; Faubel, M.; Buck, U.; Winter, B.; Abel, B. *Nat. Chem.* **2010**, *2*, 274.
24. Kevan, L. *Acc. Chem. Res.* **1981**, *14*, 138.
25. Barnett, R. N.; Landman, U.; Cleveland, C. L.; Kestner, N. R.; Jortner, J. *J. Chem. Phys.* **1988**, *88*, 6670.
26. Rossky, P. J.; Schnitker, J. *J. Phys. Chem.* **1988**, *92*, 4277.
27. Wallqvist, A.; Martyna, G.; Berne, B. J. *J. Phys. Chem.* **1988**, *92*, 1721.
28. Schwartz, B. J.; Rossky, P. J. *J. Chem. Phys.* **1994**, *101*, 6902.
29. Staib, A.; Borgis, D. *J. Chem. Phys.* **1995**, *103*, 2642.
30. Turi, L.; Borgis, D. *J. Chem. Phys.* **2002**, *117*, 6186.
31. Zhan, C. G.; Dixon, D. A. *J. Phys. Chem. B* **2003**, *107*, 4403.
32. Turi, L.; Sheu, W. S.; Rossky, P. J. *Science* **2005**, *309*, 914.

33. Herbert, J. M.; Head-Gordon, M. *J. Phys. Chem. A* **2005**, *109*, 5217.
34. Herbert, J. M.; Head-Gordon, M. *Proc. Natl. Acad. Sci. U.S.A.* **2006**, *103*, 14282.
35. Herbert, J. M.; Head-Gordon, M. *Phys. Chem. Chem. Phys.* **2006**, *8*, 68.
36. Sommerfeld, T.; DeFusco, A.; Jordan, K. D. *J. Phys. Chem. A* **2008**, *112*, 11021.
37. Jacobson, L. D.; Herbert, J. M. *J. Am. Chem. Soc.* **2010**, *132*, 10000.
38. Xu, J.; Jordan, K. D. *J. Phys. Chem. A* **2010**, *114*, 1364.
39. Larsen, R. E.; Glover, W. J.; Schwartz, B. J. *Science* **2010**, *329*, 65.
40. Zubarev, D. Yu.; Clark, G.; Head-Gordon, T.; Lester, W. A., Jr. , unpublished.
41. Jorgensen, W. L.; Chandrasekhar, J.; D, M. J.; Impey, R. W.; Klein, M. L. *J. Chem. Phys.* **1983**, *79*, 926.
42. Aspuru-Guzik, A.; Salomon-Ferrer, R.; Austin, B.; Perusquia-Flores, R.; Griffin, M.; Oliva, R. A.; Skinner, D.; Domin, D.; Lester, W. A., Jr. *J. Comput. Chem.* **2005**, *26*, 856.
43. Becke, A. D. *J. Chem. Phys.* **1993**, *98*, 1372.
44. Burkatzki, M.; Filippi, C.; Dolg, M. *J. Chem. Phys.* **2007**, *126*, 234105.
45. Schmidt, M. W.; Baldridge, K. K.; Boatz, J. A.; Elbert, S. T.; Gordon, M. S.; Jensen, J. H.; Koseki, S.; Matsunaga, N.; Nguyen, K. A.; Su, S. J.; Windus, T. L.; Dupuis, M.; Montgomery, J. J. A. *J. Comp. Chem.* **1993**, *14*, 1347.
46. Boys, S. F.; Handy, N. C. *Proc. R. Soc. London, Ser. A* **1969**, *310*, 63.
47. Schmidt, K. E.; Moskowitz, J. E. *J. Chem. Phys.* **1990**, *93*, 4172.

Downloaded by OHIO STATE UNIV LIBRARIES on May 28, 2012 | http://pubs.acs.org
Publication Date (Web): February 6, 2012 | doi: 10.1021/bk-2012-1094.ch016

Chapter 17

Quantum Monte Carlo and Zdenek Herman's Enchanted Psiland

James B. Anderson[*]

Department of Chemistry, Pennsylvania State University,
University Park, Pennsylvania 16802
[*] E-mail: jba@psu.edu

Downloaded by PENNSYLVANIA STATE UNIV on May 27, 2012 | http://pubs.acs.org
Publication Date (Web): February 6, 2012 | doi: 10.1021/bk-2012-1094.ch017

> "There are some enterprises
>
> in which a careful disorderliness
>
> is the true method."
>
> Herman Melville in Moby Dick, Chapter 82 (1851)

This chapter gives an outline of the advances in quantum chemistry provided by Quantum Monte Carlo methods since the 1970s. The account is based on a drawing made in 1976 by Zdenek Herman entitled The Enchanted Psiland which illustrates the principal methods, the chemical systems of interest, and the challenges at that time. Many of these challenges have been fully met by QMC, others have been partially met, others remain open, and still more have been newly revealed.

In Advances in Quantum Monte Carlo; Tanaka, S., et al.;
ACS Symposium Series; American Chemical Society: Washington, DC, 2012.

Downloaded by PENNSYLVANIA STATE UNIV on May 27, 2012 | http://pubs.acs.org
Publication Date (Web): February 6, 2012 | doi: 10.1021/bk-2012-1094.ch017

Introduction

In 1976, at the time when quantum Monte Carlo methods were first being developed for applications to the problems of quantum chemistry, a number of quantum chemists met for a Faraday Society Discussion of the Chemical Society on the topic of potential energy surfaces. One of the participants was Zdenek Herman of the Heyrovsky Institute of Physical Chemistry at Prague who, inspired by a talk given by Dudley Herschbach, prepared a wonderful drawing (*1*) depicting the status of quantum chemistry and carrying the title "The Enchanted Psiland." His drawing is reproduced here as Figure 1. In the lower right corner one can see Professor Herman's signature and a self-portrait.

The drawing shows a sampling of systems facing quantum chemists in 1976 along with the theoretical methods available at that time for attacking them. What is missing from the drawing is Quantum Monte Carlo which was then in its infancy (as were several other methods now available). We use this drawing as the base for discussion of the successes of QMC in treating the systems indicated and the many others which are now treatable by QMC methods (*2*).

The Enchanted Psiland

The drawing shows theoretical methods in the range all the way from semi-empirical to SCF to CI to ab initio and pseudopotentials as well as molecules and molecular ions from H_3^+ to $(HF)_2$. These are listed in Table 1. Many of them are numbered in the drawing. Near the center is simplest of the species shown, the ion H_3^+ represented by a small chapel. The largest structure is the H_3 Shrine, representing the intermediate in the reaction $H + H_2 \rightarrow H_2 + H$. To its right is the FH_2 Palace, representing the intermediate in the reaction $F + H_2 \rightarrow HF + H$. Other species involving H and F and Li atoms have smaller structures or construction sites. Varied other types of species are also indicated: van der Waals molecules, the electron gas, stiff and floppy molecules, and solvated molecules. Anyone working in the QMC area will recognize the climber scaling Mount Pauli as attacking the node problem.

Downloaded by PENNSYLVANIA STATE UNIV on May 27, 2012 | http://pubs.acs.org
Publication Date (Web): February 6, 2012 | doi: 10.1021/bk-2012-1094.ch017

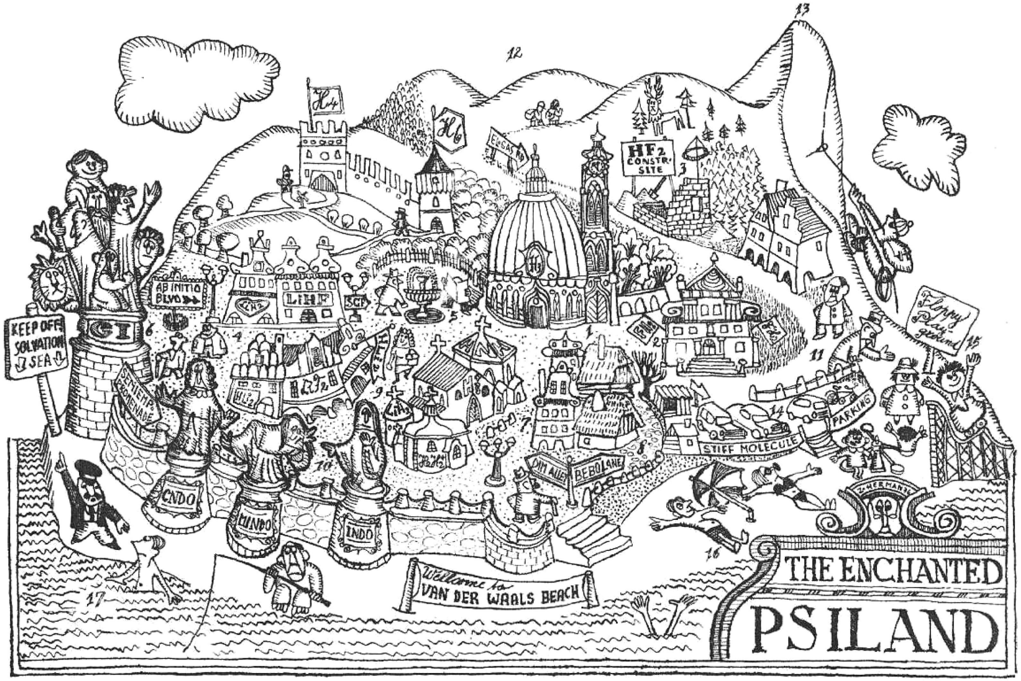
KEEP OFF SOLVATION SEA
GI
AB INITIO BLVD
LiHF
SCF
HF2 CONSTR. SITE
STIFF MOLECULE
PARKING
Floppy Play ground
DIM ALLEY
BEBO LANE
CNDO
MINDO
INDO
Welcome to VAN DER WAALS BEACH
THE ENCHANTED PSILAND
Z. HERMAN
1
2
3
4
5
6
7
8
9
10
11
12
13
14
15
16
17

The enchanted Potential Surface Island.
Inspired by Dudley Herschbach's talk at the Faraday Discussions 1976 and
in cooperation with him

Figure 1. The Enchanted Psiland, by Zdenek Herman of the Heyrovsky Institute (Prague,1976). See reference (1).

Downloaded by PENNSYLVANIA STATE UNIV on May 27, 2012 | http://pubs.acs.org
Publication Date (Web): February 6, 2012 | doi: 10.1021/bk-2012-1094.ch017

Table 1. Items in Figure 1

1. H_3 Shrine	also H_3^+ H_4 H_6 HeH_2^+
2. FH_2 Palace	FH_2 HF_2 $(HF)_2$
3. HF_2 Mansion	LiH LiHF HLi_2
4. Ab Initio Boulevard	HNH
5. SC Field	
6. CI Monument	CNDO MINDO INDO
7. DIM Alley	
8. BEBO Lane	
9. Pseudopotential Road	
10. Semiempirical Promenade	
11. Electron Gas Road	
12. Repulsion Range	
13. Mount Pauli	
14. Stiff Molecule Parking Lot	
15. Floppy Playground	
16. van der Waals Beach	
17. Solvation Sea	

Small Molecules

The first variational QMC calculations for molecular systems were carried out by Conroy (*3*) almost a decade before 1976 for several small hydrogenic systems. These included the species H_3^+ and HeH_2^+ shown in Herman's drawing. For these Conroy obtained energies more accurate than those of any earlier calculations. Our own diffusion QMC calculations (*4*) for H_3^+ in 1975 gave still better values, with –1.344 ± 0.013 hartrees for the triangular equilibrium structure. By 1992 the QMC value for that configuration had been improved to –1.343 835 ± 0.000 001 hartrees in 'exact' cancellation QMC calculations (*5*). This was the first quantum calculation of any type to reach an uncertainty of one microhartree for a polyatomic system. Nearly twenty years later analytic variational calculations Pavanello and Adamowicz (*6*) using spherical Gaussian functions have obtained the lowest yet reported upper bound of –1.343 835 625 02 hartrees. (Improvement on that value might be obtained with QMC correction calculations).

The saddle point for that simplest of neutral reactions, $H + H_2 \rightarrow H_2 + H$, is the collinear configuration H–H–H represented by the H_3 Shrine. In 1976 the best calculations of the barrier height to reaction were analytic variational calculations by Liu (*7*) with an upper bound of 10.28 kcal/mol and an estimate of 9.5 kcal/mol for the true value. Similar calculations by Liu (*8*) in 1984 gave an upper bound of 9.86 ± 0.12 kcal/mol and an estimate of 9.53 to 9.65 kcal/mol. Fixed-

Downloaded by PENNSYLVANIA STATE UNIV on May 27, 2012 | http://pubs.acs.org
Publication Date (Web): February 6, 2012 | doi: 10.1021/bk-2012-1094.ch017

node diffusion QMC calculations in our laboratory (*9*) gave an upper bound of 10.20 ± 0.20 kcal/mol (variational due to node location error). In the same year a transient released node calculation by Ceperley and Alder gave a barrier height of 9.65 ± 0.06 kcal/mol. A year later a fixed-node diffusion calculation by Barnett, Reynolds, and Lester (*10*) gave an upper bound of 9.70 ± 0.13 kcal/mol. After a hiatus of several years Diedrich and Anderson (*11*) reported an exact cancellation value of 9.61 ± 0.01 kcal/mol. If we accept this last value as the true value, then every single result listed here is correct (that is, below upper bounds or within error bars). Recent calculations by Mielke et al. (*12*) using multireference CI methods gave an upper bound of 9.661 kcal/mole and an estimated value of 9.608 ± 0.010 kcal/mole, and recent 'exact' cancellation calculations by Riley and Anderson (*13*) gave a value of 9.608 ± 0.001 kcal/mol.

"The reaction $F + H_2 \rightarrow HF + H$ is of special theoretical interest because it is one of the simplest examples of an exothermic chemical reaction" (*14*). This sentence has echoed through the literature of quantum chemistry and chemical kinetics ever since 1971 (*15*). The barrier to reaction has had its ups and downs. These have been described by Schaefer (*16*) in 1985 as "the ecstasy and the agony". The earliest QMC calculations were fixed-node calculations in 1987 (*17*) giving total energies 60 kcal/mol below the lowest analytic calculations at the time and only about 9 kcal/mol above exact values. The collinear barrier height found was 4.5 ± 0.6 kcal/mole, a value 3 to 4 kcal/mol too high to be compatible with crossed-beam scattering experiments (surely due to node-location error). There was a hint of a lower barrier for a bent F–H–H configuration. The next QMC calculation, reported by Lu (*18*) in 2005, specified the nodes with a multireference trial function of floating spherical Gaussian orbitals and obtained a barrier height of 1.09 ± 0.16 kcal/mole for a slightly bent configuration. Multi-reference coupled cluster calculations at about the same time by Kállay et al. (*19*) gave nearly identical results. These modern results are quite different from those leading to the "agony" of the 1980s.

The molecule LiH has served as a test case for quantum chemistry since the 1930s and it has continued to serve as a test case right up to the present time. About 1976 one of the lowest energies for the molecule at its equilibrium nuclear separation was that of Hylleraas-CI calculations by Clary and Handy (*20*) at –8.0630 hartrees. The first QMC calculation was a fixed-node diffusion QMC calculation in 1982 by Moskowitz, Schmidt, Lee, and Kalos (*21*) with an energy of about –8.07 hartrees. A number of fixed-node and released node QMC calculations from 1984 to 1992 (*22–26*) gave values of about –8.070 hartrees. Our own released node calculations in 1995, Chen and Anderson (*27*), gave an extrapolated value of –8.07021 ± 0.00005 hartrees, lower than any variational result up to that date, but found later to be 0.00034 hartrees above the variational energy of –8.07055 hartrees established by Cencek and Rychlewski (*28*) in 2000. Apparently, the extrapolation required in released node calculations is dangerous.

Wells (*29*) investigated difference methods for the dipole moment for LiH and Carlson, Moskowitz, and Schmidt (*30*) investigated model Hamiltonians for LiH. The most recent calculations for LiH are the reptation QMC calculations by Ospadov, Oblinsky, and Rothstein (*31*) to obtain static polarizabilities and hyperpolarizabilities for the ground state.

Downloaded by PENNSYLVANIA STATE UNIV on May 27, 2012 | http://pubs.acs.org
Publication Date (Web): February 6, 2012 | doi: 10.1021/bk-2012-1094.ch017

Other small species named in the drawing are H_4 and H_6. In the case of the H_4 square, a possible intermediate in the reaction $H_2 + D_2 \rightarrow 2\ HD$, shock tube experiments had suggested a barrier height of about 40 kcal/mol, but analytic variational calculations about 1976 indicated a height of more than 115 kcal/mol. A fixed-node QMC calculation (*32*) in 1979 indicated a barrier height of 150-180 kcal/mol. The experiments were subsequently reinterpreted.

In the case of the hydrogen-bonded dimer $(HF)_2$ Sun and Watts (*33*) and Quark and Suhm (*34*) reported in 1991-92 diffusion QMC calculations for the nuclear motions to make predictions and assignments of the spectral bands of $(HF)_2$ observed in earlier experiments. In both sets of calculations several different potential energy surfaces and treatments of nodes were employed to reproduce the measured spectra. The calculations revealed anharmonicity and strong mixing among the varied stretching and bending vibrational modes.

The Electron Gas

The development of earlier theoretical treatments of the electron gas was recently summarized by Mahan (*35*). By 1976 the treatments by Singwi and his coworkers (*36*, *37*) had provided predictions of the correlation energy and other properties. The first QMC calculations for the electron gas were those of Ceperley and Alder (*38*) in 1980, described in a paper which introduced the released node method for treating nodes in QMC. The calculations were carried out for 38 to 246 electrons to determine the fermion ground state over a wide range of densities. The results were in general agreement with earlier predictions and they have provided a solid basis for density functional theory.

More recent calculations by Ortiz and Ballone (*39*) provided further details on correlation energy and related properties. Kenny et al. (*40*) used both variational and fixed-node diffusion QMC to explore relativistic effects for the electron gas. They showed the importance of electron correlation, even for relativistic effects.

Pseudopotential Road

Three papers with different authors in 1987-88 were first to report the use of pseudopotentials, effective potentials, and model potentials in QMC calculations. The studies were carried out by Hammond, Reynolds, and Lester (*41*), by Hurley and Christiansen (*42*), and by Yoshida and Iguchi (*43*) to predict ionization potentials and electron affinities for ion-atom pairs such as K/K^{-} and Ca/Ca^{+}. The computation requirements were several orders of magnitude less than those of comparable all-electron calculations. Statistical uncertainties were typically 0.01 to 0.03 eV and differences from experimental values were generally within the uncertainties.

A number of QMC studies with pseudopotentials were reported very soon after the first three. Many of these are listed and reported elsewhere (*2*). The carbon cluster C_{20} was investigated using pseudopotentials in 1995 by Grossman, Mitas, and Raghavachari (*44*) to determine the relative values of the energies of its ring, bowl, and cage configurations. The bowl configuration was found the lowest in energy with the ring and cage energies 1.1 and 2.2 eV higher. Five years later, in 2000, Sokolova, Luchow, and Anderson (*45*) reported all-electron calculations with nearly identical results (i.e., the ring and cage energies 1.1 and 2.1 eV higher than the bowl). The close agreement gives confidence in both sets of calculations. Alternative methods of all types, some limited to small basis sets by the large number of electrons, gave widely varying results.

Stiff Molecule Parking Lot and Floppy Molecule Playground

Stiff molecules and floppy molecules and perhaps any and all polyatomic molecules can present difficulties in quantum chemistry. The typical problem is that of predicting rotation-vibration energy levels, especially for coupled anharmonic modes. QMC has provided a completely new way of attacking the problems. Many advances have been made, but only a few will be mentioned here.

An early QMC study in 1985 by Coker, Miller, and Watts (*46*) predicted infrared predissociation spectra of water clusters far better than earlier normal mode analyses. Early studies for the HF dimer were noted above. Buch (*47*) treated the loosely-bound ground states of ortho-H_2-H_2O and para-H_2-H_2O using rigid bodies for the molecules. Larger systems have also been the subject of such QMC studies. A string of 100 atoms in a polyethylene chain was treated by Tuzun, Noid, and Sumpter (*48*), and strings of more than 1000 atoms in protein chains were studied by Clary (*49*) in 2001. An "adiabatic" extension to diffusion QMC was devised by Lee, Herbert, and McCoy (*50*) in 1999 for treating excited states of several loosely bound van der Waals complexes. In 2007 Meredith, Crittenden, and Thompson (*51*) reported a means of combining potential energy surfaces for loosely bound complexes and its successful applications to several large hydrogen-bonded molecules.

van der Waals Beach

The earliest use of Metropolis sampling in QMC was in 1965 by McMillan (*52*) for calculations of liquid helium using pairwise-additive interaction potentials. This was the first of many QMC calculations for the study of van der Waals attractions and systems. Diffusion and Green's function calculations for helium droplets followed McMillan's calculations within a few years. These include, for example, calculations by Kalos et al. (*53*) in 1981, Pandharipande et al. (*54*) in 1983, Coker and Watts (*55*) in 1987, and Lewerenz (*56*) in 1997. Calculations for systems other than He dimers and clusters have been reported by Rick et al. (*57*) in 1991, Broude et al. (*58*) in 1999, and Lee and McCoy (*59*) in 2001.

Electronic structure calculations using QMC for van der Waals interactions began with a variational calculation for the helium dimer He-He by Coldwell and Lowther (*60*) in 1978 and continue for that dimer with fixed-node diffusion

Downloaded by PENNSYLVANIA STATE UNIV on May 27, 2012 | http://pubs.acs.org
Publication Date (Web): February 6, 2012 | doi: 10.1021/bk-2012-1094.ch017

calculations and several “exact” cancellation calculations to 2004 with a latest well depth (*61*) of 10.998 ± 0.005 degrees K. The neon dimer Ne-Ne presents a more difficult problem. The most successful QMC calculations to date for that system are those by Toulouse and Umrigar (*62*) reported in 2008.

(Keep Off) Solvation Sea

Until recently theoretical chemists, except for Onsager (*63*), kept off the Solvation Sea. Onsager’s ‘reaction field’ of 1938, which incorporated a continuum with a uniform dielectric constant, was available in 1976 and with improvements remains useful at present. QMC methods for treating solvation have used explicit solvent molecules surrounding a solvent molecule. First was the work of Dobrosavljevic, Henebry, and Stratt (*64*) in 1989 with a hydrogen atom in a hard sphere fluid. Later Brown, Gregory, and Clary (*65*) predicted vibrational frequency shifts of N_2^+ in helium clusters, while Cazzato et al. (*66*) calculated the infrared spectrum of CO in helium, and Moroni, Blinov, and Roy (*67*) considered NNO, also in helium.

Once the possibility of “on the fly” classical trajectory calculations in QMC was demonstrated in 2005 by Grossman and Mitas (*68*) QMC treatments of solvated molecules began to appear. In 2007 Maezano et al. (*69*) adapted fragment molecular orbital methods to variational QMC for treating clusters containing glycine molecules. In 2010 Cho and Lester (*70*) reported a QMC hybrid quantum mechanics/molecular mechanics approach with explicit solvent molecules that was successfully applied to hydrogen bonded systems. It appears there soon may be smooth sailing on the Solvation Sea.

Discussion

The quantum chemistry methods available in 1976 and listed in Table 1 include SC Field, CI Monument, DIM Alley, BEBO Lane, CINDO, MINDO, Pseudo Potential and Semiempirical Promenade. Of these, DIM, BEBO, CINDO, MINDO, and INDO are almost forgotten at present. New methods which have evolved since the 1960s and 1970s are CC, MP2, MP3, MP4, MCSCF, DFT, FCI, G2, G3, G4, a number of others and, of course, QMC.

A “tree” drawing from 1999 (*71*) also shows the growth and branching of methods from about 1976 up to 1999. In Figure 2, a similar “tree” shows the growth and branching of QMC from 1976 to the present. In another 35 years we should expect a few dead limbs, a lot more growth and branching, and perhaps even flowers and seeds.

Downloaded by PENNSYLVANIA STATE UNIV on May 27, 2012 | http://pubs.acs.org
Publication Date (Web): February 6, 2012 | doi: 10.1021/bk-2012-1094.ch017

Downloaded by PENNSYLVANIA STATE UNIV on May 27, 2012 | http://pubs.acs.org
Publication Date (Web): February 6, 2012 | doi: 10.1021/bk-2012-1094.ch017

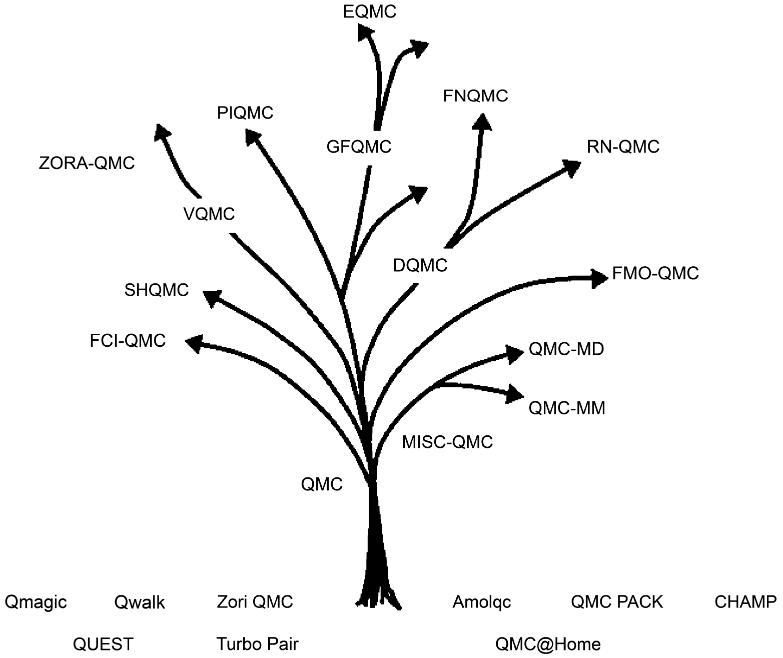
EQMC
FNQMC
PIQMC
GFQMC
RN-QMC
ZORA-QMC
VQMC
DQMC
FMO-QMC
SHQMC
FCI-QMC
QMC-MD
QMC-MM
MISC-QMC
QMC
Qmagic
Qwalk
Zori QMC
Amolqc
QMC PACK
CHAMP
QUEST
Turbo Pair
QMC@Home

Figure 2. A QMC tree of methods along with package programs.

Acknowledgments

Support by the National Science Foundation (IGERT Award No. 9987589) and by the Research Computing and Cyber Infrastructure (a unit of ITF) of the Pennsylvania State University is gratefully acknowledged.

References

1. Herman, Z. Heyrovsky Institute, 1976. The drawing may be found at www.jh-inst.cas.cz/~herman/files/vi-occas.pdf.
2. Anderson, J. B. *Quantum Monte Carlo: Origins, Development, Applications*; Oxford University Press: Oxford, U.K., 2006.
3. Conroy, H. *J. Chem. Phys.* **1964**, *41*, 1331.
4. Anderson, J. B *J. Chem. Phys.* **1975**, *63*, 1499.
5. Anderson, J. B *J. Chem. Phys.* **1972**, *96*, 3702.
6. Pavanello, M.; Adamowicz, L. *J. Chem. Phys.* **2009**, *130*, 034104.
7. Liu, B. *J. Chem. Phys.* **1973**, *58*, 1925.
8. Liu, B. *J. Chem. Phys.* **1984**, *80*, 581.
9. Mentch, F.; Anderson, J. B. *J. Chem. Phys.* **1984**, *80*, 2675.
10. Reynolds, P. J.; Barnett, R. N.; Lester, W. A. *Int. J. Quantum Chem., Symp. Ser.* **1984**, *18*, 709.
11. Diedrich, D. L.; Anderson, J. B. *Science* **1992**, *258*, 786.

Downloaded by PENNSYLVANIA STATE UNIV on May 27, 2012 | http://pubs.acs.org
Publication Date (Web): February 6, 2012 | doi: 10.1021/bk-2012-1094.ch017

12. Mielke, S. L.; Garrett, B. C.; Peterson, K. A. *J. Chem. Phys.* **2002**, *116*, 4142.
13. Riley, K. E.; Anderson, J. B. *J. Chem. Phys.* **2003**, *118*, 3437.
14. Jaffe, R. L.; Anderson, J. B. *J. Chem. Phys.* **1971**, *54*, 2224.
15. Anderson, J. B. *Adv. Chem. Phys.* **1995**, *91*, 381.
16. Schaefer, H. F. *J. Phys. Chem.* **1985**, *89*, 5336.
17. (a) Garmer, D. R; Anderson, J. B. *J. Chem. Phys.* **1987**, *86*, 7237. (b) Garmer, D. R; Anderson, J. B. *J. Chem. Phys.* **1988**, *89*, 3050.
18. Lu, S.-I. *J. Chem. Phys.* **2005**, *122*, 194323.
19. Kállay, M.; Gauss, J.; Szalay, P. J. *J. Chem. Phys.* **2003**, *119*, 2991.
20. Clary, D. C.; Handy, N. C. *Chem. Phys. Lett.* **1977**, *51*, 483.
21. Moskowitz, J. W.; Schmidt, K. E.; Lee, M. A.; Kalos, M. H. *J. Chem. Phys.* **1982**, *77*, 349.
22. Ceperley, D. M.; Alder, B. J. *J. Chem. Phys.* **1984**, *51*, 5833.
23. Harrison, R. J.; Handy, N. C. *Chem. Phys. Lett.* **1985**, *113*, 257.
24. Barnett, R. N.; Reynolds, P. J.; Lester, W. A. *J. Chem. Phys.* **1987**, *91*, 2005.
25. Caffarel, M.; Ceperley, D. M. *J. Chem. Phys.* **1992**, *97*, 8415.
26. Subramanium, R. P.; Lee, M. A.; Schmidt, K. E.; Moskowitz, J. W. *J. Chem. Phys.* **1992**, *97*, 2600.
27. Chen, B.; Anderson, J. B. *J. Chem. Phys.* **1995**, *102*, 4491.
28. Cencek, W.; Rychlewski, J. *Chem. Phys. Lett.* **2000**, *320*, 549.
29. Wells, B. H. *Chem. Phys. Lett.* **1985**, *115*, 89.
30. Carlson, J.; Moskowitz, J. W.; Schmidt, K. E. *J. Chem. Phys.* **1989**, *90*, 1003.
31. Ospadov, E.; Oblinsky, D. G.; Rothstein, S. M. *Phys. Chem. Chem. Phys.* **2011**, *13*, 8031.
32. Anderson, J. B. *Int. J. Quant. Chem.* **1979**, *15*, 109.
33. Sun, H.; Watts, R. O. *J. Chem. Phys.* **1990**, *92*, 603.
34. Quack, M.; Suhm, M. A. *J. Chem. Phys.* **1991**, *95*, 28.
35. Mahan, G. D. *Many Particle Physics*, 3rd ed.; Kluwer Academic/Plenum: New York, 2000.
36. Singwi, K. S.; Sjolander, A.; Tosi, M. P.; Land, R. H. *Phys. Rev. B* **1970**, *1*, 1044.
37. Vashista, P.; Singwi, K. S. *Phys. Rev. B* **1972**, *6*, 875.
38. Ceperley, D. M.; Alder, B. J. *Phys. Rev. Lett.* **1980**, *45*, 566.
39. (a) Ortiz, G.; Ballone, P. *Phys. Rev. B* **1994**, *50*, 1391. (b) Ortiz, G.; Ballone, P. *Phys. Rev. B* **1997**, *56*, 9970.
40. Kenny, S. D.; Rajagopal, G.; Needs, R. J.; Leung, W.-K.; Godfrey, M. J.; Williamson, A. J.; Foulkes, W. M. C. *Phys. Rev. Lett.* **1996**, *77*, 1099.
41. Hammond, B. L.; Reynolds, P. J.; Lester, W. A. *J. Chem. Phys.* **1987**, *87*, 1130.
42. Hurley, M. M.; Christiansen, P. A. *J. Chem. Phys.* **1987**, *86*, 1069.
43. Yoshida, T.; Iguchi, K. *J. Chem. Phys.* **1988**, *88*, 1032.
44. Grossman, J. C.; Mitas, L.; Raghavachari, K. *Phys. Rev. Lett.* **1995**, *74*, 3870.
45. Sokolova, S.; Luchow, A.; Anderson, J. B. *Chem. Phys. Lett.* **2000**, *323*, 229.
46. Coker, D. F.; Miller, R. E.; Watts, R. O. *J. Chem. Phys.* **1985**, *82*, 3554.
47. Buch, V. *J. Chem. Phys.* **1992**, *97*, 726.

48. Tuzun, R. E.; Noid, D. W.; Sumpter, B. G. *J. Chem. Phys..* **1996**, *105*, 5494.
49. Clary, D. C. *J. Chem. Phys.* **2001**, *114*, 9725.
50. Lee, H.-S.; Herbert, J. M.; McCoy, A. B. *J. Chem. Phys.* **1999**, *110*, 5481.
51. Jordan, M. J. T.; Crittenden, D. L.; Thompson, K. C. Quantum Effects in Loosely Bound Complexes. In *Advances in Quantum Monte Carlo*; Anderson, J. B., Rothstein, S. M., Eds.; ACS Symposium Series 953; American Chemical Society: Washington, DC, 2007; pp 101−140.
52. McMillan, W. L. *Phys. Rev.* **1965**, *138*, A442.
53. Kalos, M. H; Lee, M. A.; Whitlock, P. A.; Chester, G. V. *Phys. Rev. Lett.* **1981**, *46*, 728.
54. Pandharipande, V. R.; Zabolitzky, J. G.; Peiper, S. C.; Wiringa, R. B.; Helmbrecht, U. *Phys. Rev. Lett.* **1983**, *50*, 1676.
55. Coker, D. F.; Watts, R. O. *J. Chem. Phys.* **1987**, *86*, 5707.
56. Lewerenz, M. *J. Chem. Phys.* **1997**, *106*, 4596.
57. Rick, S. W.; Lynch, D. L.; Doll, J. D. *J. Chem. Phys.* **1991**, *95*, 3506.
58. Broude, S.; Jung, J. O.; Gerber, R. B. *Chem. Phys. Lett.* **1999**, *299*, 437.
59. Lee, H.-S.; McCoy, A. B. *J. Chem. Phys.* **2001**, *114*, 10278.
60. Coldwell, R. L.; Lowther, R. E. *Int. J. Quantum Chem., Symp. Ser.* **1978**, *12*, 329.
61. Anderson, J. B. *J. Chem. Phys.* **2004**, *120*, 9886.
62. Toulouse, J.; Umrigar, C. J. *J. Chem. Phys.* **2008**, *128*, 174101.
63. Onsager, L. *J. Am. Chem. Soc.* **1938**, *58*, 1486.
64. Dobrosavljevic, V.; Henebry, C. W.; Stratt, R. M. *J. Chem. Phys.* **1989**, *91*, 2470.
65. Brown, D. F. R.; Gregory, J. K.; Clary, D. C. *J. Chem. Soc., Faraday Trans.* **1996**, *92*, 11.
66. Cazzato, P.; Paolini, S.; Moroni, S.; Baroni, S. *J. Chem. Phys.* **2004**, *120*, 9071.
67. Moroni, S.; Blinov, N.; Roy, P.-N. *J. Chem.Phys.* **2004**, *121*, 3577.
68. Grossman, J. C.; Mitas, L. *Phys. Rev. Lett.* **2005**, *94*, 194323.
69. Maezono, R.; Watanabi, H.; Tanaka, S.; Towler, M. D.; Needs, R. *J. Phys. Soc. Jpn.* **2007**, *76*, 064301.
70. Cho, H. M.; Lester, W. A. *J. Phys. Chem. Lett.* **2010**, *1*, 3376.
71. Anderson, J. B. *Rev. Comput. Chem.* **1999**, *13*, 133.

Downloaded by PENNSYLVANIA STATE UNIV on May 27, 2012 | http://pubs.acs.org
Publication Date (Web): February 6, 2012 | doi: 10.1021/bk-2012-1094.ch017

Subject Index

A

Ab initio Monte Carlo simulations
  approximate potential method, 28
  hybrid Monte Carlo, 32, 36
  IMLS approach, 30
  interpolated potential energy surface
    H_2O, 33
    H_3O^+, 35
  overview, 27
  path integral Monte Carlo method, 31, 36
Ab initio path integral molecular dynamics, 187
Acceptance ratio
  function of time step in ab initio HMC simulation, 37*f*
  hybrid Monte Carlo I, 182*f*
    results, 183*f*
  hybrid Monte Carlo II, 182*f*
    results, 183*f*
  statistical errors of potential energies for H_2O and H_3O^+ molecules, 38*t*
Alkali-metal hydrides, positron binding
  lithium hydride, 163
  potassium hydride, 167
  sodium hydride, 165
α phase unit cell, 105*f*
Average of geometrical parameters and energies
  ab initio classical MC and ab initio PIMC, 34*t*
  ab initio simulations on H_3O^+, 36*t*

C

CH_5^+ and H_3O^+, equilibrium (left) and low-energy transition state structures, 151*f*
CH_5^+ applications, 150
Chemical structure of para-DIB molecule, 105*f*
Chromium dimer. *See* ground state chromium dimer
Computed energy differences, 108*f*, 109*f*
Correct node, wave functions, 85
Correlated DQMC
  C_{10} circle (R = 2.04 bohr) vs. C_{10} circle, 9*t*
  H_2 with R = 1.4000 bohr vs. H_2 with R = 1.4011 bohr, 8*t*
  (Ne + Ne) vs. Ne_2 (R = 5.8 bohr), 10*t*
  Ne vs. Ne shifted 0.02 bohr, 7*t*
Correlated wave functions
  correct node, 85
  interacting Hamiltonian function, 85
  noninteracting Hamiltonian function, 85
  noninteracting wave function, 85
Correlation time in total energy, 184*f*
C_{10} rings comparisons, 9

D

Delayed feedback DMC, 18
Density-functional theory (DFT), 101
DFT. *See* density-functional theory (DFT)
DFT predictions, 106
DFT structure optimization, 110
Diffusion constant of tagged particle, 183*f*
Diffusion Monte Carlo (DMC), 57, 124
  predictions, 106
  total energies of H_{4n+2} rings, 61*f*
Diffusion Monte Carlo (DMC) simulations, 25
Diffusion Quantum Monte Carlo
  C_{10} rings comparisons, 9
  correlation, 6
  H_2 molecules comparisons, 8
  neon dimer, 9
  neon *vs.* neon, 7
  overview, 3
  theoretical basis, 4
Distribution functions of distance
  O and H atoms, 35*f*
  O atom and H-H-H plane, 35*f*
DMC. *See* diffusion Monte Carlo (DMC)

E

Electron assignments, 67
Electron gas, 214
Electronic and positronic molecular orbitals, 164*f*, 170*f*
Electron scattering. *See* high-energy electron scattering
Enchanted Psiland
  electron gas, 214
  floppy molecules, 215

Downloaded by 89.163.35.42 on May 27, 2012 | http://pubs.acs.org
Publication Date (Web): February 6, 2012 | doi: 10.1021/bk-2012-1094.ix002

Downloaded by 89.163.35.42 on May 27, 2012 | http://pubs.acs.org
Publication Date (Web): February 6, 2012 | doi: 10.1021/bk-2012-1094.ix002

  - overview, 209
  - pseudopotentials, 214
  - small molecules, 212
  - solvation, 216
  - stiff molecules, 215
  - van der Waals attractions, 215
- Energy components
  - 2p^2 states for Coulomb potential, 83*t*
  - two- and four-electron atoms, 82*t*
- Energy differences in meV/unit cell, 107*t*
- Energy values, 127*f*
- Equivalence classes of symmetric group for 4 particles, S$_4$, 47*f*
- Exchange Truncated Grand Canonical PIMC, 49*f*

F

- Fermion-Boson gaps, 45*t*
- Fermion-Boson gaps, fermion treatment, 44
- Fermion treatment
  - finite temperature, permutation space structure, 47
  - zero temperature
    - fermion-boson gaps, 44
    - release node improvement, 45
    - released node quantum Monte Carlo, 42
- Finite feedback delay, 23
- Finite-size effect, 113
- First VDE of $(H_2O)_{31}^{2-}$ cluster, 204*t*
- Floppy molecules, 215
  - CH_5^+ applications, 150
  - H_3O^+ applications, 150
  - overview, 145
  - rotationally excited states, 148
- FMO method. *See* fragment molecular orbital (FMO) method
- Fourth-order propagator, variational path integral, 177
- Fragment molecular orbital (FMO) method, 189

G

- Glycine pentamer structure, 194, 194*f*
- Ground state chromium dimer
  - multi-determinant calculations, 94
  - overview, 91
  - quantum Monte Carlo methods, 93
  - single determinant calculations, 94

H

- Hartree-Fock symmetry breaking, 55
- Hartree-Fock symmetry dilemma
  - computational details, 59
  - overview, 53
  - symmetry breaking, 55
- HCN and [HCN;e$^+$] systems, total energy and positron affinity, 171*t*
- HCN molecule, timestep dependence of positron affinity (PA), 170*f*
- HF energy differences of H_{4n+2} rings, 57*t*
- High-energy electron scattering
  - calculations, 132
  - overview, 131
- Highest occupied molecular orbital, 170*f*
- H_2 molecules comparisons, 8
- $H_3O^{+,}$ inversion, 152*f*
- H_3O^+ applications, 150
- $(H_2O)_{31}^{2-}$ cluster, 9-22, 12-19, and 15-16 partitioning of, 202*f*
- Hybrid Monte Carlo, 32, 36, 179
- Hybrid path integral Monte Carlo method, 36
- Hydrogen cyanide molecule, 169

I

- Inelastic scattering cross sections, 140*t*
- Interacting Hamiltonian function, 85
- Interpolated potential energy surface
  - H_2O, 33
  - H_3O^+, 35
- Inversion of H_3O^+ and inversion of axis system, relationship, 152*f*
- Isosurfaces (60%)
  - single electrons of LiH, 69*f*
  - spin up single electron densities, 72*f*, 74*f*
  - spin up valence densities ethane, 70*f*

J

- J = 0 and 1 energies for H_3O^+ and CH_5+, 153*t*

K

- KH and [KH;e$^+$] systems, total energy and positron affinity, 168*t*
- KH molecule, timestep dependence of positron affinity (PA), 168*f*

Downloaded by 89.163.35.42 on May 27, 2012 | http://pubs.acs.org
Publication Date (Web): February 6, 2012 | doi: 10.1021/bk-2012-1094.ix002

L

LiH, NaH, and KH, positron affinities and dipole moments, 169*f*
LiH and [LiH;e^+] systems, total energy, inter-nuclear separations, and positron affinity, 181*f*
LiH molecule, timestep dependence of positron affinity (PA), 165*f*

M

Many-body nodal hypersurface, 77
Molecular crystal polymorphism
  DFT predictions, 106
  DFT structure optimization, 110
  DMC predictions, 106
  finite-size effect, 113
  methodology, 104
  overview, 101
  zero-point effect, 113
Molecular dynamics
  hybrid Monte Carlo, 179
  overview, 177
  variational path integral, 178
Møller-Plesset perturbation theory, 190
Multi-determinant calculations, 94
Munkres algorithm, 69*f*

N

NaH molecule, timestep dependence of positron affinity (PA), 167*f*
Neon dimer, 9
Neon vs. neon, 7
Noninteracting Hamiltonian function, 85
Noninteracting wave function, 85
Non-relativistic Hamiltonian, positron binding, 159

O

Optimal reference positions, 71
Optimized lattice constants
  α polymorph, 112*f*
  β polymorph, 113*f*
  and unit cell volumes, 111*t*
Optimized structure of water trimer, 191*f*
Optimized unit cell volumes, 110*f*

P

Pair correlation function g(r), 128*f*
Parallel diffusion Monte Carlo
  delayed feedback DMC, 18
  finite feedback delay, 23
  future, 13
  model system, 19
  review, 15
  simulations, practical recommendations, 25
  zero feedback delay, 21
9-22, 12-19, and 15-16 partitioning of $(H_2O)_{31}2^-$ cluster, 202*f*
Path integral molecular dynamics
  FMO method, 189
  glycine pentamer, 194
  Møller-Plesset perturbation theory, 190
  overview, 188
  water trimer, 191, 195
Path integral Monte Carlo method, 31, 36
Permutation space structure, fermion treatment, 47
Population control bias
  vs. combined population control parameter and update period, 22*f*
  vs. effective control parameter for standard and time delayed DMC, 24*f*
Population volatility vs. combined population control parameter and update period, 21*f*
Positron binding, polar molecules
  alkali-metal hydrides
    lithium hydride, 163
    potassium hydride, 167
    sodium hydride, 165
  computational details, 162
  DMC, 162
  hydrogen cyanide molecule, 169
  non-relativistic Hamiltonian, 159
  overview, 157
  Slater-Jastrow trial wave functions
    Jastrow factor, 161
    multi-component molecular orbital method, 160
    orbital cusp corrections, 161
  VMC, 162
Probability distributions
  interfragment interaction energy, 193*f*
  O-O distance, 192*f*, 196*f*
  O-O-O angles, 192*f*
Pseudopotentials, 214

Downloaded by 89.163.35.42 on May 27, 2012 | http://pubs.acs.org
Publication Date (Web): February 6, 2012 | doi: 10.1021/bk-2012-1094.ix002

Q

QMC tree of methods, 217*f*

R

Rashba interaction, 124
Release node improvement, fermion treatment, 45
Released node quantum Monte Carlo, fermion treatment, 42
Rotationally excited states, floppy molecules, 148

S

SCF, VMC, and DMC binding curves, 96*f*
Self-consistent centers, electron charge, 71
Single determinant calculations, 94
Single electron densities
  electron assignments, 67
  optimal reference positions, 71
  overview, 65
Single solvated electron
  methodology, 203
  overview, 201
Slater-Jastrow trial wave functions, positron binding
  Jastrow factor, 161
  multi-component molecular orbital method, 160
  orbital cusp corrections, 161
Small molecules, 212
Solvation, 216
SO splittings
  for C atom, 123*f*
  for Pb, 124*f*
Spin-orbit interaction
  DMC, Hamiltonian, 124
  overview, 119
  Rashba interaction, 124
  VMC, 119
    C and Pb atoms, 122
Stability vs. feedback delay and population control parameter, 24*f*
Stiff molecules, 215
Structural properties and interaction energies, N-H…O and O-H…O hydrogen bonds, 195*t*
Structure of one-particle density matrix
  HF symmetry-adapted (SA) solution, 56*f*
  symmetry-broken (SB-AC and SB-BC) solution, 56*f*

T

Timestep dependence of positron affinity (PA)
  HCN molecule, 170*f*
  KH molecule, 168*f*
  LiH molecule, 165*f*
  NaH molecule, 167*f*
Total energy and energy differences, per H_2 cell in mhartree, 61*t*
Total energy and positron affinity, HCN and [HCN;e^+] systems, 171*t*
Total energy per ^{4}He atom, 181*f*

U

Uncorrelated and correlated water wavefunction, maxima, 71*f*
Uncorrelated ethene wavefunction, maxima, 73*f*

V

van der Waals attractions, 215
Variational Monte Carlo (VMC), 57, 120
  total energies of H_{4n+2} rings, 60*f*
Variational path integral, 178
VMC. *See* variational Monte Carlo (VMC)

W

Water trimer, 191, 195
  O-H bond lengths (R_{OH}) and O-O distances (R_{OO}), 196*t*
  Optimized structure, 191*f*
  PIMD simulation, 192*f*
  probability distribution of O-O distance (R_{OO}), 196*f*
  probability distribution of O-O distance (R_{OO}) and O-O-O (q_{OOO}), 192*f*

Z

Zero-point effect, 113